Ultrafast dynamics in phase-change materials and chalcogenide glasses

Paloma Martinez

université de BORDEAUX

THÈSE PRÉSENTÉE

POUR OBTENIR LE GRADE DE

DOCTEURE

DE L'UNIVERSITÉ DE BORDEAUX

ECOLE DOCTORALE SCIENCES PHYSIQUE ET DE L'INGÉNIEUR

LASERS, MATIÈRE, NANOSCIENCES

Par **Paloma Martinez**

Ultrafast dynamics in phase-change materials and chalcogenide glasses

Dynamique ultra-rapide dans les matériaux à changement de phase et verres chalcogénures

Soutenue le 9 décembre 2021

Membres du jury :

Mme Alessandra Benuzzi-Mounaix	Directrice de Recherche	Univ. Sorbonne (LULI)	Présidente
M. Christophe Bichara	Directeur de Recherche	Univ. Aix-Marseille (CINaM)	Rapporteur
M. Stéphane Guizard	Directeur de Recherche	Univ. Paris-Saclay (LIDYL)	Rapporteur
Mme Andrea Piarristeguy	Maîtresse de Conférences	Univ. Montpellier (ICGM)	Examinatrice
M. Fabien Dorchies	Directeur de Recherches	Univ. Bordeaux (CELIA)	Directeur
M. Jérôme Gaudin	Maître de Conférences	Univ. Bordeaux (CELIA)	Co-Directeur
M. Pierre Noé	Ingénieur-Chercheur	Univ. Grenoble (LETI)	Invité
M. Jean-Yves Raty	Maître de Recherches	Univ. Liège (CESAM)	Invité

CONTENTS

REMERCIEMENTS

Je crois que chaque doctorant commence sa thèse dans le même état d'esprit, l'esprit léger par la fin des études, en se disant que quand même, trois ans c'est long, j'aurais largement le temps. Et puis...

"Le temps passe et passe et passe et beaucoup de choses ont changé
Qui aurait pu s'imaginer que le temps se serait si vite écoulé
[Je] fai[s] le Bilan calmement en [m]'remémorant chaque instant" Nèg'Marrons©

Et je me dis qu'effectivement la thèse n'est pas un long fleuve tranquille... Il y a des hauts, il y a débat (pun intended), mais j'aurais réussi à porter ce projet jusqu'au bout, bien sûr pas sans l'aide de nombreuses personnes à qui je tiens à exprimer ma reconnaissance.

Tout d'abord un grand merci à Jérôme, qui je suis sûre aura grandement apprécié la haute qualité de cette introduction (hey j'ai pas commencé par depuis l'aube de l'humanité, l'honneur est sauf). Toujours prêt à me dire quand mes graphes sont moches ou "pas adaptés à des yeux de vieux", mais surtout toujours disponible et toujours prêt à répondre à mes questions, j'aurai énormément appris grâce à toi, que ce soit sur le plan scientifique, ou bien dans la vie quotidienne, comme le fait de ne pas mettre un téléphone dans une tasse de café pendant une réunion. Ou en tout cas s'assurer qu'elle est bien parfaitement vide avant ça. Certains se diront "mais pourquoi donc?" et je répondrais à ça que c'est là clairement l'esprit créatif du scientifique aguerri qui s'exprime en trouvant une solution pratique à un problème (tel que : devoir tenir à la main un combiné pendant 2h de réunion : non. Avec une tasse : oui). Merci pour toutes les opportunités d'expériences, que ce soient le parcours d'obstacles d'Aurore 2, ou les expériences à SOLEIL et SACLA, j'ai pu découvrir des gens et des structures formidables. En conclusion un encadrement de grande qualité du début à la fin, encore merci.

Fabien, mon directeur de thèse "sur le papier", avec ton oeil vif pour spotter tous mes "s" manquants, merci pour tes bons conseils, et ta non-râlerie quant au fait d'avoir dû découvrir le sujet et affronter ce (petit) manuscrit dans le désordre (désolée pour ça haha).

Merci à nos collaborateurs de haute qualité, Jean-Yves et Pierre, pour votre expertise des chalcos et les discussions intéressantes qui en découlent, mais également pour votre acceuil chaleureux lors mes visites à Liège et Grenoble ! Une bonne partie de cette thèse n'aurait pas pu être possible sans toi Jean-Yves, car se lancer dans les simulations de chalcos, amorphes, sans expert à l'appui, je dirais juste "aïe aïe aïe", encore merci pour tout.

Je tiens à remercier tous ceux qui ont contribué à rendre cette thèse possible : Valérie qui a sauvé le NOPA à de multiples reprises, Céline, Sonia et Sophie, toujours au top de l'efficacité, Gaëtan et Richard, qui résolvent mes problèmes informatiques par magie, Fabrice pour sa relecture et son livre plein d'équations indigestes mais néanmoins très utiles, Dominique et sa gestion de la chaine laser et toutes les personnes que j'ai pu croisé au CELIA qui contribuent à la bonne humeur qui y règne en permanence.

Valentin, toi qui m'as supportée et supportée (dans les deux sens). Comme dirait un certain Perceval, "la patience est un plat qui se mange sans sauce", et il en faut de la patience pour une thèse. Le problème c'est que moi j'aime pas les pâtes sans sauce. Donc un grand merci à toi qui m'a accompagnée dans cette aventure.
Mes chers parents, qui avez toujours cru aveuglément en mes capacités, et m'avez permis d'aller aussi loin, je ne saurai trop vous remercier.

Finalement, je tiens quand même à remercier Freyja, qui ne lira pas ses lignes (car c'est un chat) mais dont la contribution doit être reconnue. M'obliger à me lever à 6h tous les matins de la semaine était une ruse de sioux de haute qualité, augmentant ainsi grandement ma productivité, et pour ça je t'en remercie.

Je vous souhaite donc une bonne lecture de ce manuscrit, certifié "adapté à des yeux de vieux".

INTRODUCTION

Data storage

Modern societies are now based on a digital way of living. From social interactions to administration paperwork, all this data needs to be stored. The Global Datasphere (every bit of data from clouds datacenters, enterprise-hardened infrastructure and all PCs/smartphone/...) is estimated to grow from 33 Zettabytes (ZB) in 2018 to 175 ZB in 2025 [1]. This impressive expansion goes with the concomitant rise of demands level: ever faster access speed, largest possible memory capacities, at the lowest cost, motivating the research for ever new types of storage.

In the domain of computer science, memory hierarchy is often represented with a pyramidal shape as in Figure 1. From top to bottom, the memories (short for "data storage memories") are listed from the fastest to the slowest. But this can also be seen in terms of cost per byte, which goes in the same direction as the speed, or in terms of storage capacities, which evolves in the opposite direction. At the top, we find the *static random-access memory* (SRAM) and the CPU memories (cache, registers). This is the fastest memory to access, with about 50 ns of latency, but the storage capacities are limited to about 16 MB [2]. In second, we find the *dynamic random-access memory* (DRAM), with higher storage capacities: 64 GB per RAM stick, but the access time is doubled. These two first ranks are both *volatile* memories, meaning that they only preserve the data as long as there is power supplied. As soon as the power is cut off, memory is lost. At the opposite of the pyramid, we find *solid state drive* (SSD) as well as the flash memory, with the highest storage capacity nowadays, 30 TB, but the speed to get access to data is also slowed by a factor 10^3. They both are non-volatile types of memories, enabling data storage, even long after power is cut off. The problem is that we end up with two very contrasted types of memories: on the one hand, low access time, but associated with a non-volatile character and very limited in terms of capacities and on the other hand a large storage capacity, persistent but greatly limited in terms of speed.

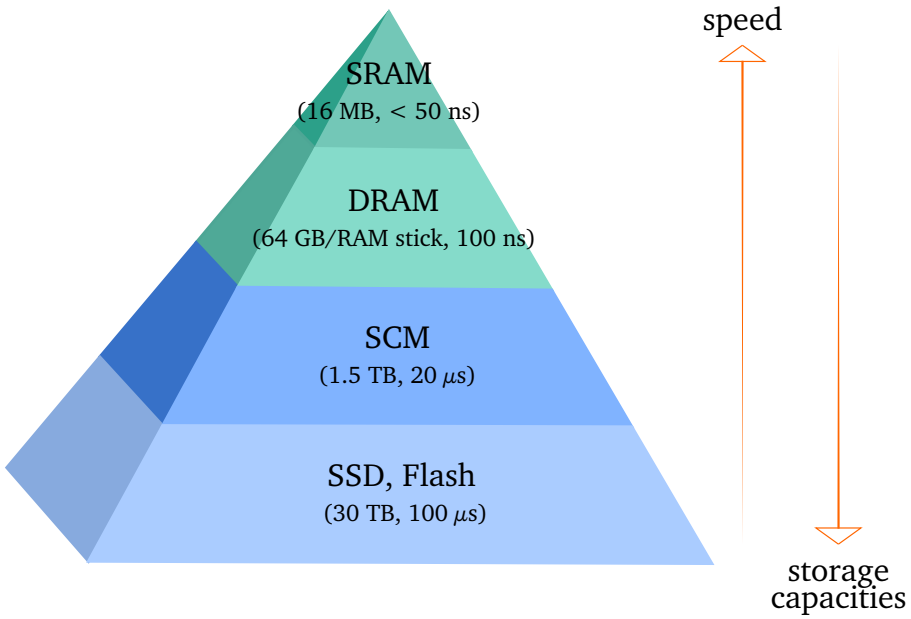

Figure 1 – *Memory hierarchy. Non-volative memories are represented in blue (bottom of the pyramid) while the volatile ones are in green (top of the pyramid). Latency and storage capacities values are taken from Reference [2].*

Storage class memories

To bridge the gap between both extremes, *storage class memories* (SCM) were developed with emerging technologies [3]. In SCM, memory is persistent as in SSD devices, but latency is a better compromise, giving rise to an intermediate case with storage capacities of about 1.5 TB, and access time estimated of 20 µs. The ultimate goal would be a universal memory, based on the development of neuromorphic capacities [4]: only one memory componant would be required as all the computation and storage part would be dealt with in the same element, surpassing the Von Neuman architecture [5].

The 3D crossbar architecture emerged, with the development and commercialization of the *phase change random access memory* (PCRAM) Optane^{TM} product, developed by Intel and Micron [6]. This so-called Xpoint technology enables to circumvent the physical lack of place encountered in previous devices when trying to increase storage density [7]. Indeed, increasing the storage capacities was mainly dealt with by miniaturizing the system, however, this has obviously a limit given the fact that fabrication methods (of transistors for example) are themselves limited by the size of the tools. Adding one dimension increases the storage density and therefore paves the way to a whole new set of memories, with enhanced capacities, in terms of storage, but also in terms of operating concept.

The 3D crossbar technology, represented in Figure 2, consists in a stack of two types of elements, with different roles: the memory cells and the selectors. Each memory cell encodes one bit of data (a "0" or a "1" in binary computer science language). In practice, these logical states are represented by two states that the memory cells can adopt: the *SET* state ~ "1", and the *RESET* state ~ "0". The switching from one state to another occurs on the nanosecond scale, and can be reversed [8, 9]. As for the selectors, their role is to choose precisely which memory cell to write, erase or just read. Before explaining how it works more thoroughly and the phenomenon at play, it is necessary to speak about the materials constituting both types of elements, and their outstanding properties: the chalcogenides.

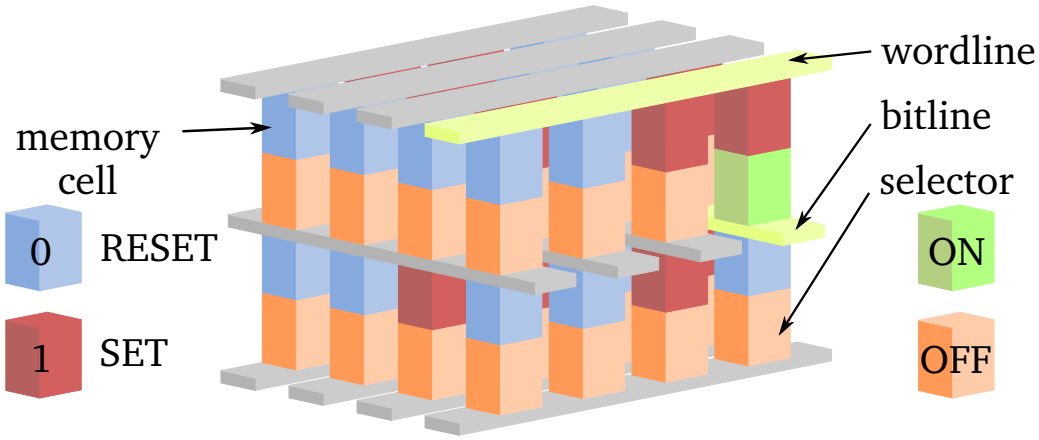

Figure 2 – *3D XPoint technology. It consists in a stack of memory cells (blue and red) and selectors elements (orange and green). Voltage is applied between a word line and bit line (metal rod) to switch the selector from its OFF state to its ON state, which then changes the state of the chosen memory cell from zero to one or conversely by Joule effect.*

Chalcogenides

The term of *chalcogenide* corresponds to semiconductor alloys based on S, Se or Te, chalcogen elements from the 16^{th} column of the Mendeleev periodic table (see Figure 3), with one or several electropositive elements. These latter are mostly chosen from the 14^{th} and 15^{th} column with the main (but not only) associated elements being As, Ge, Sn or Sb.

Their diverses properties make them key-components in several domains. For instance, their thermoelectric properties [10, 11], as well as their non-linear optical properties [12, 13] make them materials of choice for energy and optics applications. Another domain in which they are widely used is the interest of this thesis: data storage applications. Chalcogenides have a long history with memories. Starting with the CDs, then the DVDs, Blu-rays [8], it goes on nowadays with the emerging SCM technologies [9].

First, their outstanding optical and electrical properties makes them particularly well-suited for data storage applications. For instance, Germanium Telluride (GeTe), a typical chalcogenide, exhibits a reflectivity ratio of 2 between its crystalline and amorphous phases and about four orders of magnitude in terms of conductivity. This particularity is not common for most semiconductors in which, though the properties are different, the contrast is not as striking. This high contrast was exploited in memory devices, in which it is crucial to differentiate two logical states that binary encode all data. The "1" and "0" states were then associated respectively to the crystalline phase and the amorphous state. Now, with the crossbar architecture, the memory cells are not the only element that exploit these interesting properties: as it will be explained slightly later, the contrasted electrical properties of chalcogenide glasses makes them particularly well-suited for the selector elements.

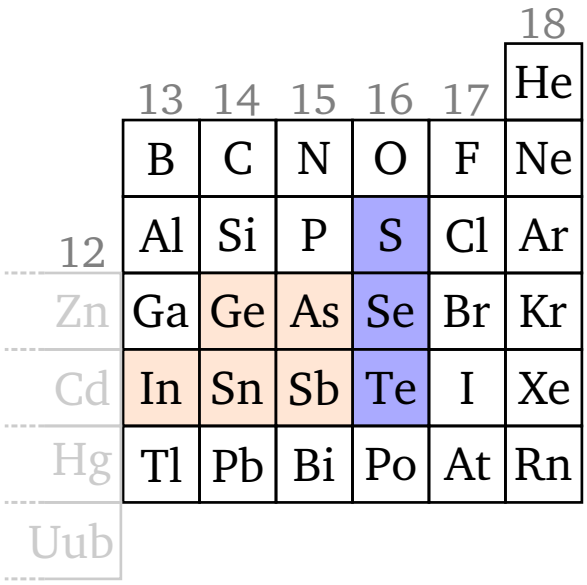

Figure 3 – *Close up of the Mendeleiev periodic table on the main elements associated in chalcogenide compounds. The purple colored elements S, Se and Te are the three chalcogens used in chalcogenides, while the elements in light orange are the electropositive elements most alloyed with them.*

Three different types of chalcogenide solid phases are used in memories: crystalline, amorphous, and glassy. However, they are not used for the same elements. It is therefore important to differentiate one from another to take into account all possible parameters when studying them.

The crystalline phase is characterized by a long range order. It is constituted of a repeated pattern of atoms, molecules or ions. The evolution of the enthalpy H of the system as a function of atomic configuration and temperature T is represented in Figure 4 [14]. The crystalline phase is formed when the melted phase is cooled very slowly under the crystallization temperature T_c and results in a configuration with lowest possible enthalpy. Several crystalline phases are possible for one compound (as will be evoked in Chapter 1 for GeTe), with different stability, yet compared to

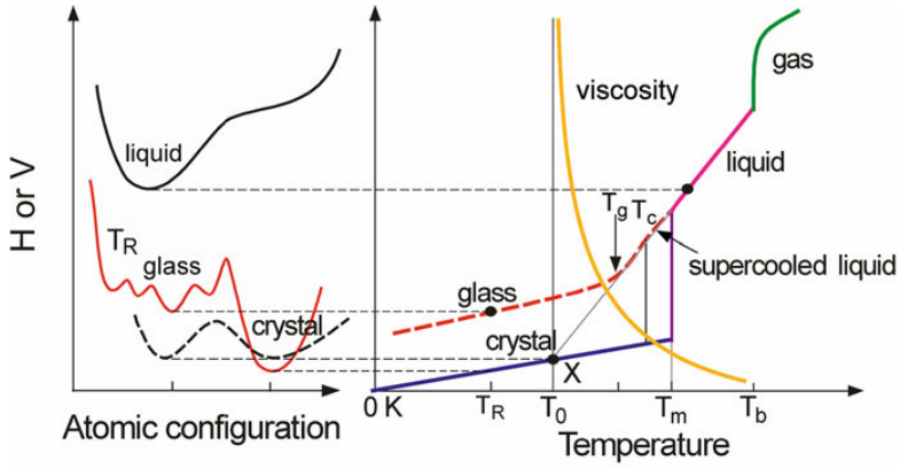

Figure 4 – *General representation of the enthalpy H/ Volume V of a system as a function of atomic configuration and temperature, from [14].*
T is the temperature, and the indexes g, c, m, b and R correspond respectively to glass transition, crystallisation, melting, boiling and room temperatures. (T_0 is an example temperature, not used here).

other types of phases that will be evoked, they are overall the most stable.

The real ambiguity lies in the difference between an amorphous and a glassy state, which are both disordered phases. A first definition was given by Mott and Davis in 1979 [15], defining the glass state as a non-crystalline phase obtained from the melt, in opposition to the other amorphous phases obtained from vapor/plasma phases. A second definition emerged and is now the most used, as Philips and Elliott [16, 17] separated the amorphous and glassy states depending on their capability to exhibit or not the phenomena of glass transition. When a liquid is cooled below the melting temperature of the material, rapidly enough to prevent crystallization (generally about hundreds of °C/s), it reaches a metastable disordered configuration, a kind-of "frozen" liquid state called a *glass* [18]. The *glass transition* refers to the gradual transition from this glassy state to a supercooled liquid state when it is heated. This is not a phase transition in the thermodynamical sense as there are no discontinuity in any physical property, but the material changes from a hard, brittle glassy state to a viscous and rubbery state. The glass transition temperature T_g is therefore difficult to determine. An approximate value can be obtained by using the empirical relation that links the value of T_g with the melting temperature T_m such that $T_g = 2/3T_m$ [19]. Any "frozen" state that does not show this transition is defined as an amorphous state.
Amorphous and glassy phases are then meta-stable phases, corresponding to local minima of the enthalpy landspace. Similarly to the crystalline state, there can be several glasses and amorphous phases, but the glassy states are the ones with lowest enthalpy.

Chalcogenides demonstrate great optical and electrical contrast, but this is not the only reason

why they are well-adapted to memory applications. On the long term, encoding information is great, but being able to do it at high frequency, in a reversible way is much better. This is actually possible thanks to the underlying phenomenon called *threshold switching*, that takes effect in two different ways.

Threshold switching

The *threshold switching* (TS) effect was presented by Ovshinky in the late 60's [20]. He studied the I-V curve (current-voltage) of an amorphous Te-As-Si-Ge semiconductor alloy and shed light on a repeatable switching between the initially high resistive state and a conductive state when the voltage applied exceeds a certain threshold value V_{th}.
The phenomena was then investigated more thoroughly leading to two important conclusions. First, the switching can be triggered either by electrical or light pulses. The second conclusion is that the TS occurs in two different ways, which lead to the categorization of the materials depending on how the effect manifests itself, as represented in Figure 5.

1. The first type of threshold switching is the one that Ovshinsky encountered, and gave rise to the name of **ovonic threshold switching** (OTS)[1]. The OTS occurs between an initially highly resistive amorphous state (OFF state) which switches to another amorphous state, with lower resistivity (ON state), when the voltage applied is higher than a threshold value. This is a volatile effect: as soon as the power is cut off, the current will drop below a certain value, called the *holding current* I_h and the material reverts to the initial OFF state.

2. The second one is the one that has been the most exploited in memories until now. Sometimes called *memory switching*, it is the permanent (non-volatile), yet reversible, transition between the highly resistive amorphous (RESET) state and the conductive crystalline (SET) state encountered in the memory cells, leading to the name of **phase change memory** (PCM) materials to designate those that fall into this category. What differs between the OTS and the PCM is mainly the value of the threshold voltage V_{th}, and whether or not the material can crystallize after the threshold switching.
   Other materials than chalcogenides can be PCM materials, for instance Ge-Sb, Ga-Sb or InSb alloys have been found to demonstrate PCM properties [21, 22]. However, chalcogenide alloys are the ones that are the best suited to both OTS selectors and memory cells required properties in the domain of data storage.

Now we can understand the overall mechanism in crossbars memories that use chalcogenides. As an example, we consider the writing process of a bit, as shown in Figure 6. Writing a bit means

[1]The term 'ovonics' derives from the contraction of two words: the name of the researcher Ov-shinsky, and the techniques of electr-onics based on the use of thin films of chalcogenides that he developed

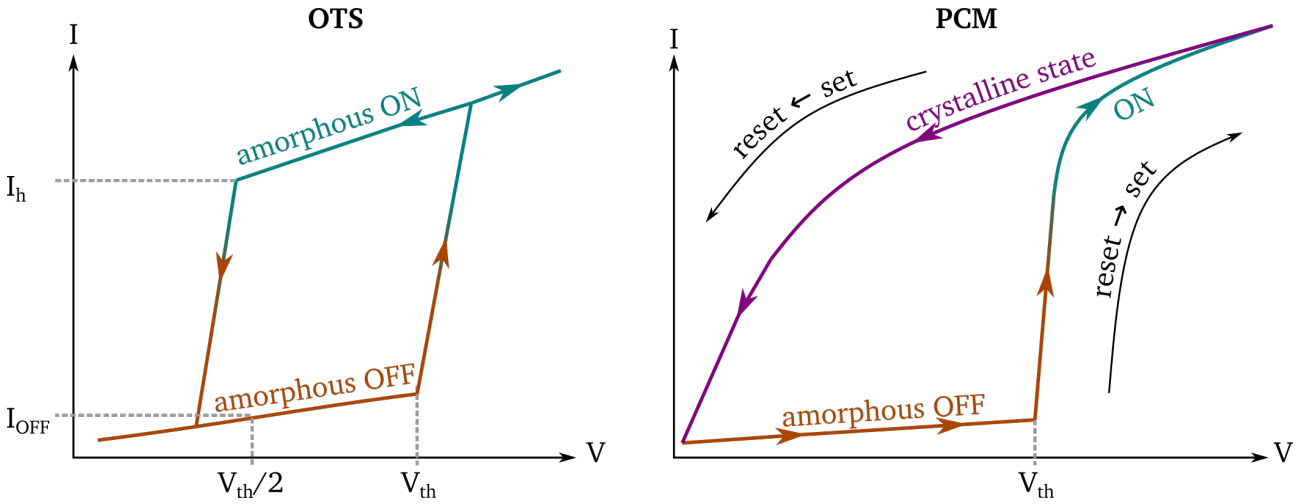

Figure 5 – *Schematic representation of typical current-voltage (I-V) curve for an OTS material (left) and a PCM material (right) submitted to a voltage V*

changing a RESET (amorphous) state into a SET (crystalline) state. Memory cells are made of chalcogenide PCMs, so the transition is done by exploiting the threshold switching cited above. A voltage V is applied through crossed metal rods to select the column and row of the memory cell of interest (in yellow in the Figure 6). Of course, as the OTS selectors and the PCM memory cells are stacked together, current also flows through the selectors, which are made of chalcogenide glasses. If the voltage applied V exceeds the threshold value $V_{th,OTS}$, the selector switches from the OFF to the ON state. Current flow, which was limited by the high resistive character of the selector OFF state, is now passing more efficiently through the conductive ON state. Similarly, the PCM memory cell sees the current flow increase when the selector is switched on. When the resulting voltage exceeds a certain threshold value, it will also switch from the initially resistive RESET (OFF) state to a conductive state, and Joule heating will be enhanced. This increase of temperature in the memory cell, such that $T_g < T < T_m$, induces then its transition towards the crystalline phase (SET).

Once the electrical pulse has stopped, the selector is finally able to escape from the out-of-equilibrium ON state and recovers its initial stable OFF state, while the memory cell stays in the SET state. To erase this bit (changing it back to the RESET state), a similar process needs to be used. In that case, the intensity of the electrical pulse is increased, such that the melting temperature T_m of the material constituting the memory cell is reached, but its duration is shortened, inducing a high cooling rate from the neighbouring cold cells.

Chalcogenide phase-change memory materials are nowadays the best option for memory cells [8,9]. The requirement for materials used in memory crossbar arrays are listed in Table 1. As discussed previously, PCM materials exhibit a reversible transition between an amorphous phase with low reflectivity and high resistivity and a crystalline phase with high reflectivity and high conductivity.

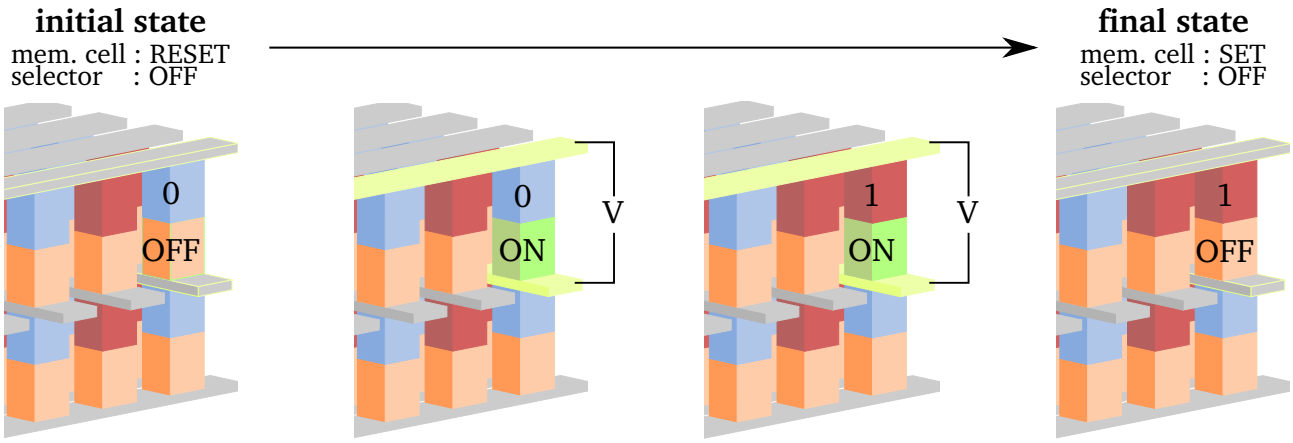

Figure 6 – *Schematic representation of the writing process of a particular bit in a crossbar memory device.*

With the limiting process (crystallization) it only takes a few hundreds of nanoseconds. As for the other properties, though they are not always ideal in PCMs, solutions are developed to circumvent the issues encountered [9]: data retention (stability of the amorphous phase over the years, also called *aging*) can be dealt with by doping the PCM for example (discussed in Chapter 1), miniaturizing the memory cells reduces its power consumption and the high cyclability has been investigated by studying different compounds. The two main families of chalcogenide PCM used in memories are the Ge-Sb-Te (GST) alloys, with the prototypical $Ge_2Sb_2Te_5$ and GeTe compounds, and the Ag/In-doped Sb_2Te_3 (AIST) alloys, with compositions close to $Ag_5In_5Sb_{60}Te_{30}$ being the most used. Both have been used in memory devices such as DVDs-RW or Blu-rays, but GST alloys have been found to be more promising, with a faster crystallization, and a better electrical contrast between the two logical states used in memories. GST compounds are now the ones that are mainly used in all memory devices.

Memory cells	• A high electrical/optical contrast between the two encoding states • A fast transition between those two states • A low power consumption required for the switching • At least 10 years of data retention • A high cyclability (at least 10^6 write/erase cycles)
Selectors	• V_{th} limiting unwanted memory cells switching • Holding current I_h compatible with the memory cell • low OFF state current I_{OFF} • thermal stability against crystallization

Table 1 – *Necessary properties of the materials constituting the memory cells and selectors [7–9].*

As for the selectors, OTS glassy chalcogenide have been shown to be very promising [7, 9, 23, 23], with a high current density in the ON state, low OFF-state current limiting the power consumption

of unselected memory cells, good thermal stability against crystallization and threshold current $V_{th,OTS}$ compatible with that of the memory cells, meaning that memory cells that are not both row and column selected do not change phase.

Mechanism of the transition

Though chalcogenides are well-suited for memory applications, there is still room for improvement. The need for better memory devices, with higher storage capacities, and faster access rate has motivated researches. Besides the search for optimal compounds, the effect of various external stimuli were investigated: light pulses [24–26], heat [27], electric field [28], pressure [29–31]... Beyond the discovery that the changes are occurring on a local scale, the underlying mechanism of the TS phenomenon has not been clearly elucidated. In fact, even the structures of the most used chalcogenides, such as the amorphous phase of GeTe or $Ge_2Sb_2Te_5$, are still debated [32–36].

On the way to improve memory devices, optimizing the compounds in themselves has not been the only research direction. As previously evoked, electrical triggering is not the only way to induce the TS. Light pulses of diverse wavelength, intensity, and especially duration have also proved their efficiency [37]. With the development of ultrafast optical sources, femtosecond lasers became routinely used in laboratory, and the study of their effects on PCM has become more common. Reducing the pulses duration in this regime induces new phenomena (discussed in Chapter 1), in particular the generation of transient out-of-equilibrium states where the electronic temperature $T_e \neq T_i$ the ionic temperature. The concept of non-thermal transition emerged, and was proved in semiconductors such as Si, C, ... [38–43]. Obtaining a phase with same properties as the liquid without heating up to T_m obviously became very attractive for PCM applications, and the possibility of such a transition was then also tackled and seen in chalcogenides and PCM compounds such as amorphous GeSb [44] or $Ge_2Sb_2Te_5$ [45]. The transposition of this phenomenon into memory devices would revolutionize the domain, overcoming the speed limits during the writing and erasing processes imposed by the heating that is predominant now.

Investigation of electronic excitation

Improving memory devices requires to understand how the underlying mechanisms work. Both memory cells and selectors transitions are based on the threshold switching, which supposedly takes its roots into electronic excitation. Besides, chalcogenides are particularly sensitive to optical techniques thanks to their contrasted properties. It seems then that studying the effect of light under the form of femtosecond pulses on thin films of amorphous GeTe, a much-studied PCM [46], and of three chalcogenide glasses: $Ge_{31}Se_{69}$ (GS), $Ge_{23}Se_{57}Sb_{20}$ (GSS) and $Ge_{23}Se_{53}Sb_{19}N_5$ (GSSN), chosen for their potential as future OTS selectors [23, 47] could be relevant. All four

are disordered phases, however, as they do not belong to the same categories (PCM *vs* OTS), we expect that their response to electronic excitation will presumably be different.

In the Chapter 1, ultrafast methods of investigation often used to probe chalcogenides are detailed, then the structures of chalcogenide glasses as well as phase-change materials (with a focus on GeTe) are discussed. The Chapter 2 presents the concepts of density functional theory (DFT) used for the *ab initio* molecular dynamics (AIMD) simulations as well as the protocol used to generate initial configurations and their out-of-equilibrium excitation. In the last part of this chapter, subsequent structural analysis methods will be detailed. After that, the Chapter 3 will explain the experimental optical technique used in this work: frequency-domain interferometry (FDI), information that can be extracted, and the set-up used for these measurements. Finally, the Chapters 4 and 5 will discuss the results of excitation on amorphous GeTe and on the chalcogenide glasses respectively, obtained both experimentally and *via* simulations.

I had the great opportunity to participate in several other projects during my phD: studying the generation of sub-micrometer wrinkles in GeTe [48], coincidence experiments of the fragmentation of carbon nanodots at the DESIRS beamline in SOLEIL synchrotron facility (collaboration CELIA (V. Blanchet), INSP (A. Lévy), ISM (D. Bassani)), characterization of the non-thermal graphitization of diamond with two color X-ray pulses at the SACLA XFEL facility (collaboration SLAC (P. Heiman), DESY (S. Toleikis), CELIA (F. Dorchies), HZDR (H. Hoeppner), and a little contribution in the study of the ultrafast electron energy transport in laser heated warm dense copper in high flux regime (Grolleau *et al.* [49]).
Although it would be very interesting to detail all these projects, the size of this manuscript would then be unreasonable. Hence, it will be focused only on the main subject of my thesis introduced here before.

CHAPTER 1

PHASE-CHANGE MATERIALS AND CHALCOGENIDE GLASSES

Chalcogenide materials have demonstrated a great potential for memory devices applications. The two categories of *phase-change memory* (PCM) materials and *ovonic threshold switching* (OTS) materials are though not interchangeable. Indeed, the memory switching encountered by PCM materials is permanent, which is absolutely not the case of the threshold switching (TS) in OTS ones. Those two mechanisms have been studied quite a lot, and while it is now clear that it happens on a local scale, the details of the mechanism are still unknown. Besides the TS in itself, the quest for answers has led numerous researchers to focus on the atomic structure of the chalcogenides, with the subsequent aim at understanding how the transition can be so fast.

To understand a transition as fast as hundreds of femtoseconds as there is in PCM memory devices, following it in a time-resolved manner might be a good idea. However, as it is happening on a very short timescale, and seems to be due to changes on the local order [50], it requires a probe that is actually able to follow on this short timescale and with an adequate space and time resolution: nanometric and sub-picosecond resolutions are a pre-requisite.

I Techniques of ultrafast investigation

Triggering and probing processes that are happening on an atomic scale require adequate techniques. Space and time scales needs to be consistent with the phenomenon of interest. In the case of threshold switching, the transition has been measured on the pico/nanosecond timescale and on a local scale. PCMs and OTS undergo the threshold switching by application of an electrical

or a light pulse. To have more insight about the mechanism and the structure of the material, a lot of studies chose this latter technique to reproduce the process in laboratory. This section will present several techniques of "ultrafast" investigation, which we locate on the timescale between femtoseconds and hundreds of picoseconds.

I.1 General picture of the ultrafast photo-excitation of semi-conductors

As it will be detailed in the Section IV, people turned to femtosecond laser aiming at developing a non-thermal transition in memory devices. The processes triggered by a nanosecond-laser and a sub-nanosecond laser are completely different. The main reason is due to the electron-phonon coupling. This latter is at best on the picosecond timescale for semi-conductors, which means that when using ns-pulses triggering, the lattice and electrons have the time necessary to get back to equilibrium, while it is not possible for ps- or even fs-laser pulses.
The ultrafast photo-excitation of a semiconductor results in different mechanisms that we can associate with the following encompassing categories [51–53]: carrier excitation, thermalization, relaxation and structural effects. All the mechanisms they involve are not necessarily successive, most of them are overlapping in time.

I.1.1 Carrier excitation

The first category consists in the processes of carriers excitation. It refers to the actual excitation of carriers in the material (electrons/holes) and scales with the laser duration. We will consider the example of electrons carriers for the rest of the explanation. The absorption of photons leads to the promotion of electrons from the valence band to the conduction band. This process can be a *single photon absorption* if the photon energy E_{ph} is larger than the band gap E_g or a *multi-photon absorption* if $E_{ph} \lesssim E_g$ (see Figure 1.1A). In any case, it is difficult to prevent the multi-photon absorption from occurring.

Excited electrons that are already in the conduction band are not exempted of photon absorption. This *free-carrier absorption* occurs with either the emission or the absorption of a phonon, as represented in Figure 1.1B. The electron undergoes the change of momentum corresponding to the phonon, and is therefore transferred to another excited state. As they are far from the nuclei, these excited electrons act as free-electrons, and may be described using a Drude model.

Another carrier excitation phenomenon consists in the *impact ionization*. Highly excited electrons may posses a kinetic energy sufficient to transfer electrons from the valence band to the conduction band. In the case of semiconductors and insulators, this effect is used to trigger avalanche breakdown and carrier multiplication [54].

I.1.2 Thermalization - Relaxation

The photo-excitation of the material leads to an out-of-equilibrium state where the electron temperature T_e and the lattice temperature T_i are completely different. As this state is thermodynamically not stable, the material will relax to a state which is more energetically favorable if the excitation is not maintained. The first step is the *thermalization* which occurs under two differents ways: *carrier-carrier scattering* and *carrier-phonon scattering*.

Carrier-carrier scattering corresponds to the two-body electrostatic interaction that leads to a Fermi-Dirac distribution in a few hundred of femtosecond whereas the carrier-phonon interaction is the transfer of energy between the carriers and the lattice *via* emission or absorption of a phonon. Right after excitation, the electron-phonon interaction is completely negligible. Only after some time, characterized by the *electron-phonon coupling constant*, this scattering will be important enough to be taken into account. This coupling constant $\gamma_{e/ph}$ depends on several parameters: electronic temperature (linked to the intensity of excitation), intrinsic properties of the material such as its structural configuration (crystal, amorphous, ..). It is therefore difficult to infer. Yet it can be deduced from time-resolved lattice temperature measurement for example. For $Ge_2Sb_2Te_5$ it is estimated to be about 2 ps [45]. Another way is to solve the two-temperature model (TTM). This latter, which was proposed by Anisimov in 1974 [55], describes the electron and lattice behaviours following a femtosecond laser irradiation, *via* the system of Equation 1.1. The indexes e and i refer respectively to the electrons and the lattice. T is the temperature of the sub-system considered, κ its heat conductivity and C its specific heat. The electron-phonon interaction is denoted by γ.

$$\begin{cases} C_e(T_e)\dfrac{\partial T_e}{\partial t} = \nabla\left[\kappa_e(T_e,T_i)\nabla T_e\right] - \gamma(T_e)(T_e - T_i) + S(\vec{r},t) \\ C_i(T_i)\dfrac{\partial T_i}{\partial t} = \nabla\left[\kappa_i(T_i)\nabla T_i\right] + \gamma(T_e)(T_e - T_i) \end{cases} \tag{1.1}$$

This method effectively retrieves the thermalization behaviour of a metal or a semiconductor [56–59], but requires to have measured beforehand the parameters that are used (or at least be able to derive them from other parameters).

Whether *via* numerical computation or measurements, this thermalization is in all cases estimated to be on the picosecond timescale.

The electron-phonon interaction results in the thermal equilibrium of carriers and lattice. However, the material is still not in a relaxed state: for instance in the case of electron carriers, at this stage there are still too many electrons in the conduction band compared to the thermal equilibrium configuration. The material will naturally tend to a more relaxed state, as it will be more energetically stable. This process will be achieved *via* several phenomena: electron-hole recombination (Figure 1.1C), Auger recombination (Figure 1.1D), diffusion.

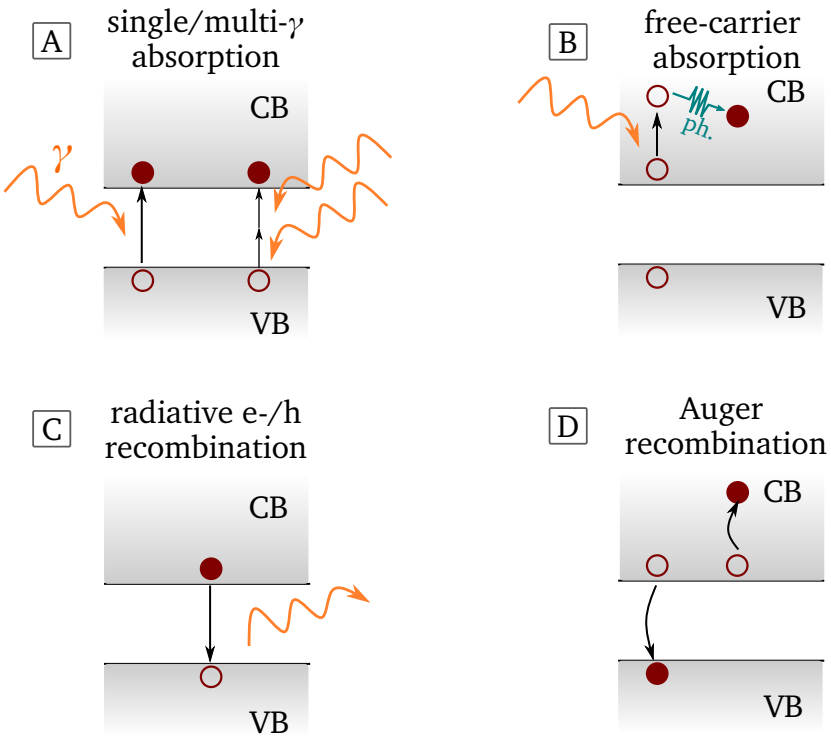

Figure 1.1 – *Schematic representation of: single and multi-photon absorption (A), free-carrier absorption (B), radiative electron-hole recombination (C) and Auger recombination (D).*

I.1.3 Structural effects

After the end of these relaxation phenomena, the state of the material can be compared to that of a material heated in a more conventional way. The main difference stems from the nature of laser excitation: that latter leads to an isochoric transition, which is not the case for the conventional heating. Depending on the parameters of excitation, the material could melt, boil or just revert to its initial state or yet another one. This last category is concerned with thermal phenomena, that can last up to several microseconds.

I.2 Probing an ultrafast phenomenon

For a phenomenon which is happening on a short timescale, for instance hundreds of femtoseconds, the response should be measured with appropriate probes, otherwise the interesting dynamics would be missed. The main probing methods used on chalcogenides are presented briefly below with some examples of studies in which they were used. These methods are actually suitable for static and time-resolved measurement, which makes them very powerful.

I.2.1 Optical probes

Reflectometry

The first technique is the *reflectometry* [44, 60–64]. As chalcogenides exhibit strong optical constrast between their different phases, the measurement of their reflectivity is greatly justified. When reflected on a material with reflectivity R, the intensity I_{inc} of the incident light beam will be modified as $I_{refl} = I_{inc}\, R$ for the reflected beam and $I_{trans} = I_{inc}T$ for the transmitted one, T being the transmissivity. Both physical quantities are linked such that $R + T + A = 1$, with A the absorption of the sample. This is the basics of this technique, it can be done in several forms (simple measurement of the intensity, interferometry,...). From this measurement of reflectivity, it may be possible to retrieve more specific properties of the material such as the dielectric function as will be shown in Chapter 3 and References [62, 65].

Raman spectroscopy

Raman spectroscopy [23, 29, 66, 67] uses the phenomena called Raman scattering to retrieve information about the vibrational states of a material. Raman scattering, represented in Figure 1.2, is a type of inelastic scattering. Two configurations are encountered, yet the second one is much less probable. For the first one, called *Stokes scattering*, an incident electromagnetic wave, characterized by a photon energy $h\nu_L$ is absorbed (with ν its frequency and h the Planck constant). This absorption results in the emission of a new photon $h\nu_R$ whose energy depends on how much of the incident energy was converted in vibrational energy. This latter, E_{vib}, depends directly on the vibrational modes of the material.
In the second configuration, called anti-Stokes scattering, the incident photon energy is associated to energy given by the system such that the scattered photon has a greater energy than the incident one: $h\nu_R > h\nu_L$.

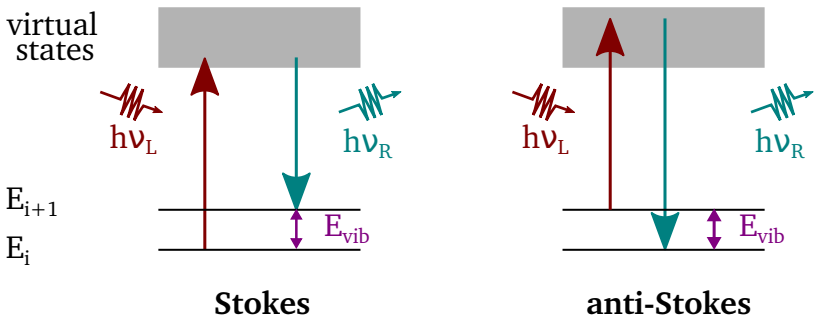

Figure 1.2 – *Stokes and anti-Stokes Raman scattering. The quantity $h\nu_L$ corresponds to the energy of the incoming photon, $h\nu_R$ to the energy of the scattered photon (measured with the Raman spectroscopy technique) and E_{vib} to the energy of the vibrational transition between the states of energy E_i and E_{i+1}.*

The incident photon comes from a monochromatic laser of known energy $h\nu_L$. In practice, the

phenomena of Rayleigh scattering, also called laser rejection, is present and corresponds to the case where $h\nu_R = h\nu_L$. After interaction with the sample of interest, this laser rejection is filtered out by means of notch or filters, and a spectrometer analyzes the spectrum of scattered photons. The energy of the vibrational transitions can be deduced as:

$$E_{\text{vib}} = h\nu_L - h\nu_R \tag{1.2}$$

The measured Raman peaks are mostly coming from Stokes process, as the anti-Stokes ones are much less probable.
Similarly to the reflectometry, Raman scattering is a measure of both the electronic and structure contribution, and it is not possible to disentangle both with this method either. However, this method is a powerful tool to identify the phonon modes of a material and thus study the bonds of a given material.

I.2.2 Diffraction

The second category shown here regroups the diffraction techniques with the three main types: x-ray, electron and neutron diffraction.

X-ray diffraction

X-ray diffraction (XRD) [67–73] relies on the application of the Bragg's law [74] with d the interlayer distance in the crystal, θ the angle of incidence, λ the wavelength of the incoming beam and n the diffraction order:

$$n\lambda = 2dsin\theta \tag{1.3}$$

An incident beam is sent onto the sample of interest. For this technique to be conclusive, it is necessary for the wavelength of the incident beam to be similar to the atoms interdistances inside the sample. Photons from the incident beam interact with the electrons of the sample's atoms. Incoming x-ray beam waves are then scattered elastically. The interest lies in the interferences that occur between all the scattered beams. Indeed, constructive and destructive interferences will give rise to a certain pattern depending on the internal structure of the sample. In the end, only when the Bragg's condition is fulfilled, does a so-called diffraction *Bragg peak* appear, with an intensity that is also dependent on the interference of the scattered waves. As d is usually on the nanometer scale, x-rays are the best wavelengths to be able to respect Bragg's condition. Varying the angle of incidence θ gives an XRD diffractogram from which all peaks maxima can be linked to crystal planes. Basically, XRD allows to retrieve the structure on a long range order of a material of interest [70, 72, 75–78].
From the mechanism of this technique, it is obviously easier to get conclusive results by studying

a crystal sample rather than an amorphous/glassy one, which are disordered phases and would give either very broad peaks (diffusion rings) or no peaks at all.

Neutron diffraction

Neutron diffraction (ND) [73, 78–81, 81–85] consists in the interaction of an incoming neutron beam with the atoms nuclei. Following the same principle as for XRD, the incoming beam will be scattered. The structure factor, which is deduced from this scattered beam is used to deduce information about the material. The main difference with XRD is the penetration depth of neutrons which enables to probe bulk materials much deeper than with X-rays.

Electron diffraction

*Electron diffractio*n [45,86] is similar to the two above techniques. Here, it is the lattice structure that acts as an optical diffraction grating, thus scattering the electrons in a statistically predictive way. Coulomb forces $F = \sum_i \frac{q_i e}{|r_i - r|}$ constitute the main interaction, with e the elementary charge, q_i the surrounding charges, $|r_i - r|$ the distance between the incoming electron and the sample's surrounding charged particles. This probing method is mostly used *via* a transmission electron microscope (TEM) or a scanning electron microscope (SEM). Shorter wavelengths are used compared to XRD giving a better range of measurement. Similarly to XRD, the structure of the lattice can be retrieved thanks to the diffraction pattern.

I.2.3 X-ray absorption spectroscopy

X-ray absorption spectroscopy (XAS) is a technique that measures the absorption coefficient of a sample depending on the energy of the incoming beam [31, 83, 87]. When the incident energy is above that required to excite inner-shell electrons of a particular type of atom from the sample, absorption is measured. The Figure 1.3 depicts a typical spectrum obtained by XAS. At the absorption threshold (minimal energy required for a transition to the lowest unoccupied states), there is an *absorption edge* which corresponds to a sharp rise of the absorption coefficient of a given element.
The analysis of this edge refers to the *X-ray absorption fine structure* (XAFS). Two nomenclatures are defined:

- Within about 30-50 eV of the edge, the analysis is called *X-ray absorption near-edge structure* (XANES) [88–90]. XANES is more sensitive to the electronic structure but is also the region where there are strong scattering processes, making the spectrum harder to decipher.
- Above these 30-50 eV, the *extended X-ray absorption fine structure* (EXAFS) [47,67,89,91–94] is more sensitive to the local atomic order, and gives information about the interatomic distances or coordination numbers.

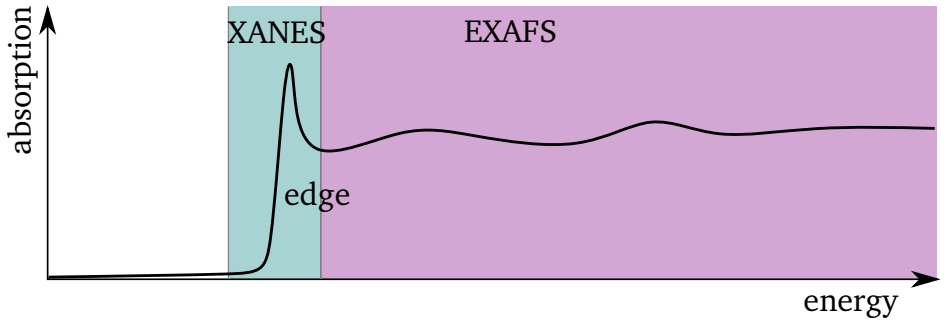

Figure 1.3 – *Schematic representation of a XAFS spectrum for a given atom. XANES refers to energies close the edge while for higher energies it is the EXAFS.*

The probing methods are diverse. The results obtained from their measurements are often complementary. For example, the structure of the GST compounds has been highly debated. This issue actually reflected the importance of understanding what is actually measured by a technique and the interest of cross-analyzing with different methods.
At first, diffraction methods were the main tools to investigate the structure of these materials [79]. Simulations were scarce as the calculation capacities were limited. After some time, other techniques (experimental and computational) enable to elucidate the structure on a global and local scale), notably X-ray absorption spectroscopy (XAS), then extended X-ray absorption fine structure (EXAFS) as well as X-ray absorption near-edge structure (XANES) techniques were developed and improved. A problem stood out: the results found with diffraction methods, such as coordination numbers, were not completely consistent with those found with EXAFS.
The difference lied in what was measured: EXAFS is a local probe while diffraction such as XRD averages on the whole probed structure. As the Ge-Sb-Te (GST) compounds feature a great amount of disorder [71, 94–96], even in the overall ordered crystalline phase, the averaged structure is not exactly the same as the local one [97].

II Ge-Sb-Te phase-change materials

GST alloys have been found to be the best family of PCM for data storage applications [9]. They demonstrate a fast crystallization, a high optical/electrical contrast between amorphous and crystalline states, a high endurance of cyclability. The two main prototypical materials are $Ge_2Sb_2Te_5$ and GeTe. Akola *et al.* [98] proved that both alloys possess similar local structure. There are obviously quantitatives differences in terms of vacancies, homopolar (like-atoms) bonds, interatomic distances, atomic mobility and electronic structure due to the presence of Sb atoms in $Ge_2Sb_2Te_5$ as it was also shown in the same article; yet they are characterized by the same phenomena (Peierls distortion, total coordination number that exceeds the 8-N rule, similar long-range radial

distribution for the Te atoms...).

II.1 Crystalline phase and the Peierls distortion

II.1.1 Crystal structure

Low temperature crystalline GeTe is a rhombohedral stable phase with space group *R3m*, often denoted as α-GeTe (Figure 1.4, left). When heated above the Curie temperature, this ferro-electric α-GeTe undergoes a transition towards a para-electric cubic phase, often denoted β-GeTe, with space group $Fm\bar{3}m$ [99–101] (Figure 1.4, right). This Curie temperature T_c is dependant on the exact composition of the alloy. While Steigmeier *et al.* [99] and Wiedemeier *et al.* [102] used X-ray diffraction to understand the change of structure during $\alpha - \beta$-GeTe transition and estimated the corresponding Curie temperature to be 670 K and 648 K respectively using X-ray diffraction , Chattopadhyay *et al.* [79] determined T_c to be about 705 K for a Ge-rich composition using neutron diffraction. Then, Fons *et al.* estimated it to be about 533 K using Extended X-ray Absorption Fine Structure (EXAFS) [96].

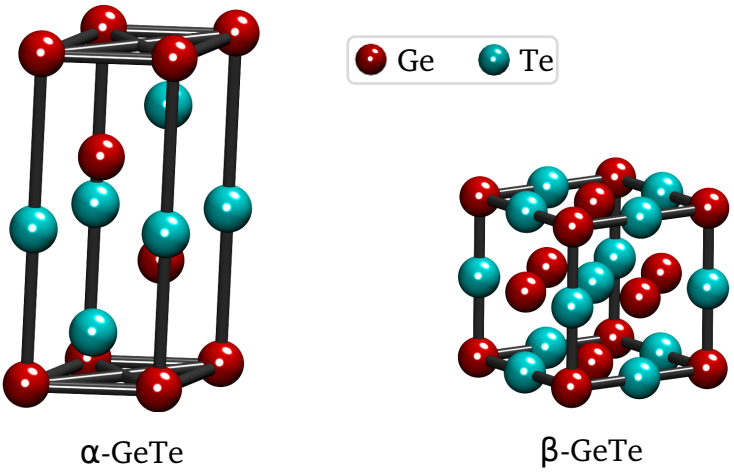

Figure 1.4 – *Rhombohedral (α-) and cubic (β-) crystalline GeTe.*

When switching to and from the amorphous phase in memory devices, it is this rhombohedral phase that intervene. This phase can be described as a NaCl structure with a shear along the [1,1,1] direction, with off-centering of the Ge and Te atoms along this direction. In this description, the distorted cube has angles and edges equal to 88.17° and 5.985 Å respectively at room temperature 295 K [79]. The off-centering of the Ge atom results in distorted octahedral local environments giving rise to three short and three long bonds (see Figure 1.6A for ideal octahedral structure properties). This distortion actually results from the phenomenon called Peierls transition.

II.1.2 Peierls distortion

The phenomenon responsible from the distorted environment of Ge atoms in GeTe is the so-called *Peierls distortion*, or *Peierls transition* [103], similar to the Jahn-Teller effect in molecules [104]. Here, the Peierls distortion results from electronic effects [105, 106]. The slight displacement of an atom results in a more energetically stable configuration by the opening of the gap.

Fowler [107] derived this using quantum perturbation theory for a one-dimensional chain of atoms. First, we consider the "conventional" case, with a chain of atoms equally spaced by a distance a, as represented in the Figure 1.5. Taking into account the interaction with the ionic lattice results in using the nearly-free electron model. In that model, the Bloch's theorem [74] states that the wave function ψ of the system should have the same periodicity as the lattice:

$$\psi_{\boldsymbol{k}}(\boldsymbol{r}) = u_{\boldsymbol{k}} e^{i\boldsymbol{k}\cdot\boldsymbol{r}} \tag{1.4}$$

with the function $u_{\boldsymbol{k}}(\boldsymbol{r}) = u_{\boldsymbol{k}}(\boldsymbol{r} + \boldsymbol{R})$ having same periodicity as the lattice[1] .
The lattice potential V has a periodicity of a. Therefore, as it can be written as $V(x) = \sum_n V_{nk} e^{iqx}$ with $n \in \mathbb{Z}$, the allowed values are $q_n = 2\pi/a$. The allowed values of k are constrained by the length $L = Na$ of the crystal, with N the number of atoms. Therefore allowed energy states E_n are also constrained in the same way:

$$\begin{aligned} k_n &= \frac{2\pi}{L} n \text{ with } n \in \mathbb{Z} \\ \Rightarrow E_n &= \frac{\hbar^2 k_n^2}{2m_e} = \frac{\hbar^2}{2m_e}\frac{4\pi^2}{L^2} n^2 \end{aligned} \tag{1.5}$$

The rest of the calculation consists in solving the Hamiltonian within the perturbation theory by diagonalizing it in the subspace determined by the two states of same energy:

$$\begin{vmatrix} \frac{\hbar^2(k-q)^2}{2m_e} - E_{k-q} & V_q^* \\ V_q & \frac{\hbar^2(k)^2}{2m_e} - E_k \end{vmatrix} = 0 \tag{1.6}$$

The corresponding eigenvalues are:

$$E_\pm = \frac{1}{2}\left(E_k + E_{k-q}\right) \pm \sqrt{\left(\frac{E_k - E_{k-q}}{2}\right)^2 + |V_q|^2} \tag{1.7}$$

As a consequence, as $k \to \pi/a$, the degeneracy is lifted and a band gap opens at $k = \pi/a$. This model is true for all crystals. As our interest lies in the understanding of the Peierls distortion,

[1] $\boldsymbol{R} = m_1\boldsymbol{a}_1 + m_2\boldsymbol{a}_2 + m_3\boldsymbol{a}_3$ defines the lattice, see Appendix A

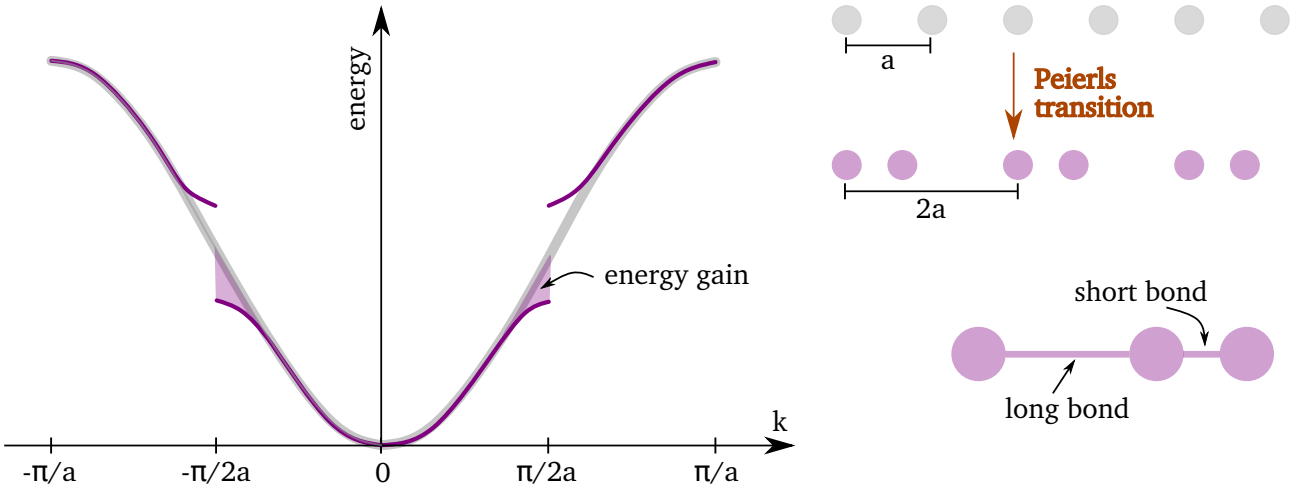

Figure 1.5 – *Representation of the energy dispersion curve in the nearly-free electron model (gray curve) and in a case with Peierls distortion (purple curve). The periodicity a of the lattice is increased to 2a which opens a band gap in the energy at $k = \pi/2a$. This rearrangement stems from the energy that they gain in doing so. Indeed, near the band gap at $k = \pm\pi/2a$, the curvature of the band leads to a lowering of the energy states, and therefore a gain in energy compared to the conventional case (area filled in purple).*

we consider now the dimerization of the chain of atoms. The new lattice periodicity is $a' = 2a$. The same reasoning as before applies, except that the allowed values for q are now $q_n = \pi/a$. Therefore, instead of opening a gap at $k = \pi/a$, a gap opens at $k = \pi/2a$.
In the first case, the lowest band spans from $k = \pm\pi/a$, and $\Delta k = 2\pi/L$, so the total number of energy states in this interval is $L/a = N$. Each atom contributes with two electrons, and one band can contain two electrons (with opposite spin) so this lower band will be completely filled. To move an electron, the only available states are those above the band gap, requiring an energy input of at least $2|V_q|$.
If the atoms are monovalent, *i.e.* they contribute with one electron, the lowest band would be only half-filled, resulting in a metal. Indeed, the free available states would be in the same band, allowing the electrons to move more easily

With the Peierls transition, an interesting phenomenon occurs. In cooled metals, it was observed that the atoms move slightly, resulting in a dimerization, and the opening of the gap at $k = \pm\pi/2a$ [108]. However, as the band was initially half filled, this new gap actually opens right where the electrons now fill completely the lowest band. The cooled metal behaves now as an insulator!

II.2 Amorphous phases: as-deposited and melt-quenched

Even though the structure of the crystalline phase is now pretty well-known, the amorphous one is still very debated. There are two main reasons for that:

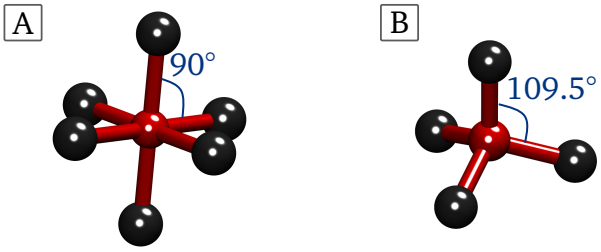

Figure 1.6 – *Ideal octahedral (A) and tetrahedral (B) configurations*

- A lot of studies have been done using diffraction techniques. While completely justified for the crystalline phase, it is much more complicated to use them for an amorphous phase which does not have a long range order.

- *Ab initio* molecular dynamics (AIMD) simulations have greatly help in the understanding of the structure of GST. However, amorphous phases are more difficult to generate than their crystalline counterpart.

    1. The first reason is the complexity to generate a simulation cell that resembles the real amorphous material.

    2. The second reason is due to the high number of atoms required to generate an accurate configuration. As an amorphous state has no symmetry, the simulation cell should be representative of the real material properties without having to use 10^{23} atoms (one mol), as it would clearly be impossible with the actual computer capabilities. To circumvent this, periodic boundary conditions (see Appendix A) allow to reduce greatly the number of atoms required. However, if this number is too low, these periodic conditions induce an unwanted periodicity in the simulation. Therefore, a compromise has to be made between accuracy and simulation time to get structures in a reasonable amount of time and that are effectively consistent with the experimental ones.

    3. The intrinsic structure of the amorphous phase is also a trouble. PCMs are mostly obtained *via* a physical vapor deposition method (PVD). Yet even with this method, the resulting film can be different from another one depending on the sputtering conditions. The resulting configuration is the so-called "as-deposited" (AD) phase. This phase is the most studied experimentally. However, it is difficult to reproduce this mechanism in simulations. The phase generated *via* simulations in almost all cases is the "melt-quenched" (MQ) one: the simulation cell is heated above the melting temperature, then quenched rapidly to obtain an amorphous phase.

The issue here is that the as-deposited and the melt-quenched amorphous phases are not exactly equivalent [109]. Raoux *et al.* [110] and De Bastiani *et al. via* micro-Raman/time-resolved

reflectivity measurements [111] showed that the AD and the MQ phases of amorphous GeTe have different crystallisation speed. This first observation already lead to the expectation of a difference of structure between the two phases. Akola *et al.* [112] analyzed both local structures, and found that the AD phase is characterized by Ge atoms predominantly in tetrahedral units (see Figure 1.6B for tetrahedral representation) whereas in the MQ phase they are mostly in distorted octahedral units. A subsequent consequence of this difference of Ge local environment is the amount of Ge-Ge homopolar bonds which is different in both phases. As this type of bonds is mostly found in tetrahedral environments [113], the AD phase is therefore more rich in Ge-Ge bonds than the MQ one. This has a great importance in terms of stability, as will be the seen in Section III.2.

Table 1.1 – *Bond lengths of GeTe from literature*

T_i (K)	r_{Ge-Ge} [Å]	r_{Ge-Te} [Å]	r_{Te-Te} [Å]	Method
299 K	2.479	2.649		EXAFS [114]
300 K	2.60	2.78	2.87	DFT [98]
300 K	2.473	2.628		EXAFS [92]
300 K	2.48	2.60	2.71	RMC [83]
300 K	2.53	2.60	2.73	RMC [115]
300 K	2.48-2.50	2.66-2.70	2.89	DFT [116]
965 K	2.57	2.74	2.91	DFT [69]
1032 K	2.57	2.74	2.93	XRD [69]

In the general picture for our material of interest, *a*-GeTe (amorphous-GeTe) is characterized by homopolar Ge-Ge bonds of 2.47-2.60 Å and Ge-Te bonds of 2.60-2.78 Å (see Table 1.1 that lists the bonds lengths values from literature). No Te-Te bond is detected in the first neighbouring shell [92, 98, 114, 117, 118]. As previously stated, Ge atoms are found either in tetrahedral environment with angles close to 110°, or in distorted octahedra with angles of about 90°. Te atoms are found in 2-fold configurations with angles close to 90°.

While we count a non negligible number of vacancies in the crystalline phase (defect where an atom was expected): about 6% [98], the amorphous one does not have any. One hypothesis is that they are intrinsic to the crystalline structure and are the key element that allows to have

such a fast transition between amorphous and crystalline phase. Vacancies are then believed to be replaced by Ge-Ge bonds. But this hypothesis may not hold as the number of Ge-Ge bonds compared to vacancies does not match.
Peierls distortion is still present in the amorphous phase, yet it is not as pronounced as in the crystalline phase [113].

It should also be noted that a large proportion of four-fold rings can be found, which are believed to be one of the reasons why the transition crystal ↔ amorphous is so fast [112, 119, 120] as they are the starting blocks of the crystal.

II.3 Liquid phase

The melting temperature T_m of stoichiometric, bulk GeTe was determined to be $T_m^{bulk} = 998$ K [121] *via* XRD. For thin films between 2 and 10 nm, T_m is slightly lower: between 825 K and T_m^{bulk}, increasing as the film thickness increases [121].

Different compositions of liquid GeTe and GST have been analyzed both experimentally and with simulations [69, 72, 81, 122–127].
Before a deep analysis of the structure, it is the characteristics of the molten GeTe phase that attracted attention. For most materials, the volume increases when it is heated above their melting temperature. However, for GeTe compounds close to the eutectic composition $Ge_{15}Te_{85}$[2], Tsuchiya demonstrated that an "anomalous" shrinkage occurs upon melting [128]. GeTe is not the only material to exhibit this kind of property: immediately we think of water [129]. For this latter, as for other materials exhibiting this shrinkage [130], it has been demonstrated that it is the nature of the bonding, more precisely the tetrahedral character of the bonding that is responsible for the anomalous density. Still, Bichara *et al.* showed *via* AIMD simulations that for GeTe, it is not the same origin [122]. An hypothesis in the same article suggests that the Peierls distortion present in the crystalline state, which induces a larger atomic volume than in an equivalent non-distorted structure, fades when melting, and the result of symmetry recovery is this volume decrease.

GST compounds are characterized by a re-entrance of the Peierls distortion when melting [69, 72, 131] then as the temperature is risen far above T_m, it fades away. In GeTe, both atoms are mainly found with angles of 90°, with coordinations numbers of 5.43 (Ge) and 3.98 (Te). There are still no Te-Te bonds, the majority of the bonds are Ge-Te ones, but Ge-Ge bonds are also present in this liquid state [69, 81].

[2] A *eutectic system* is characterized by the fact that all elements constituting the mixture melt/solidifies at the same temperature (eutectic point). For other compositions, the temperatures of each element are different, leading to a mixture of liquid and solid.

In addition to that Peierls re-entrance, another characteristic of GeTe liquid phase is its strong-fragile transition [69, 132–134]. The fragile/strong character corresponds to the behaviour of a liquid as it is cooled to the glass temperature. The viscosity of a strong liquid can be described with an Arrhenius law while fragile ones cannot. A typical glass obeys this Arrhenius law, but when heating above a certain temperature T^*, PCM have been seen to depart from it, and instead adopt a super-exponential behavior.

The description of the phases of GeTe leads to one main conclusion: the local scale has a considerable importance if we want to investigate its phase change.

III Chalcogenide glasses

Chalcogenide glasses have also been widely studied, for applications in photonics, opto-electronics, sensing, and as stated before memory applications by exploiting the ovonic threshold switching phenomenon [12]. In this thesis, three chalcogenide glasses derived from Selenium will be the object of interest (Ge-Se, Ge-Sb-Se, and N-doped Ge-Sb-Se). Those three are not phase-change materials. In general, it has been measured that the optical contrast between crystalline and amorphous phase in selenide chalcogenides is not sufficient to consider them as PCMs [135]. Though the phenomena of threshold switching is occuring in both PCMs and these OTS candidates, their structures and properties are fairly different.

III.1 Local configuration

Covalent network Various types of experiments and simulations were conducted to probe the structure of chalcogenide glasses. Interestingly, though it is here non-crystalline phases, diffraction methods (neutrons [80, 84, 136–138], electrons [139, 140], X-ray [75, 76, 141–143]) were widely used. Other techniques such as Raman spectroscopy [144–148], EXAFS [89, 149], anomalous x-ray scattering or even nuclear magnetic resonance (NMR) [150–153] were also methods of choice. What stems out of these studies is the counter-intuitive existence of a covalent network in these expected disordered glasses. This network contributes to the presence of rings constituted of a large number of atoms [154].

Pretty early, it was established that chalcogenide glasses are constrained to the 8-N rule[3] by analyzing the radial distribution function obtained from X-ray or neutron diffraction [139]. For

[3]This rule is a crystallographic concept stating that elements from the Group IVB (14^{th} column) to the Group VIIIB (18^{th}) tend to have $8 - N$ close neighbours, with N the group number of the element. [155]

example, the analysis for amorphous GeSe reveals coordination numbers of 2 for Se and 4 for Ge. The 8-N rule is respected here, so a great degree of covalency is expected. Yet it is not only the existence of covalent bonding that is interesting, but how the local structure is organized in the glasses.

Experiments and simulations (reverse Monte-Carlo (RMC) and AIMD) performed on various compositions of germanium selenides, especially the prototypical $GeSe_2$, revealed that the glasses are made of a majority of tetrahedral units ($GeSe_4$), connected with each other on two scheme: edge-sharing and corner-sharing (see Figure 1.7), resulting in angles of 80°and 100°. Ge-Se bonds as well as homopolar Se-Se bonds are present in the first neighbouring shell, but almost no Ge-Ge bonds.

With the addition of Sb-doping, Se-Sb bonds as well as Sb-Sb and Ge-Sb bonds are formed [47]. Though the first type of bonds cited has no particular drawbacks, the two latter have the major disadvantage of introducing band gap defects (unwanted in the aim of memory devices applications). The addition of Nitrogen dopants helps with this issue, by favoring the formation of Sb-N and Ge-N bonds over the Ge-Sb and Sb-Sb [47] bonds. Bond lengths from literature are listed in Tables 1.2, 1.3 and 1.4. The main bonds Ge-Se are found with similar distances: between 2.35 Å and 2.48 Å.

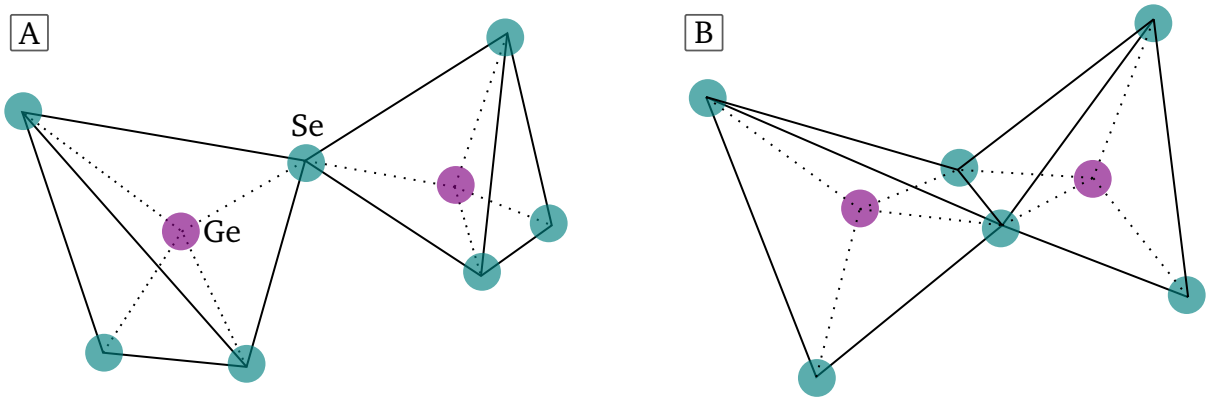

Figure 1.7 – *Schematic representation of corner- (A) and edge- (B) sharing tetrahedral configurations.*

Another surprising point, is that this covalent nature of the bonding is subject to change under application of a constraint. Notably, while in the study conducted by Wuttig *et al.* [32] GeSe clearly appeared as part of the covalent materials, it was shown later [156] that excitation could change the nature of bonding, giving it a more metavalent nature. It is actually what we observe under other constraint such as temperature or pressure where glasses bonding exhibit a character between ionic, covalent or even quite metallic [31, 157].

Table 1.2 – *Bond lengths in glassy GS from literature.*

Material	r_{Ge-Ge} [Å]	r_{Ge-Se} [Å]	r_{Se-Se} [Å]	Method
$Ge_{30}Se_{70}$	2.53	2.41	2.38	AIMD [47]
$Ge_{30}Se_{70}$	2.69	2.44	2.38	AIMD [47]
$Ge_{30}Se_{70}$		2.38		XAS [47]
$Ge_{25}Se_{75}$	2.46	2.36	2.37	AIMD [31]
$Ge_{25}Se_{75}$		2.366	2.35	XAFS [89]
$GeSe_3$	2.42	2.36	2.36	AIMD [154]
$Ge_{33}Se_{67}$		2.364		XAFS [89]
$GeSe_2$	2.42	2.36	2.32	ND [158]
$GeSe_2$	2.44	2.36	2.37	AIMD [154]
$GeSe_2$	2.42	2.36	2.32	ND [80]
$GeSe_2$	2.45	2.37	2.37	AIMD [159]
l-GeSe (727°C)	2.36	2.54	2.34	ND [158]
l-$GeSe_2$ (784°C)	2.33	2.41	2.30	ND [158]

Table 1.3 – *Bond lengths in glassy GSS from literature.*

Material	r_{Ge-Ge} [Å]	r_{Ge-Se} [Å]	r_{Ge-Sb} [Å]	Method
$Ge_{24}Se_{56}Sb_{20}$		2.39	2.64	XAS [47]
$Ge_{27}Se_{60}Sb_{13}$	2.45	2.35	2.50	RMC [73]
$Ge_{20}Se_{60}Sb_{20}$	2.45	2.35	2.50	RMC [73]
$Ge_{15}Se_{25}Sb_{20}$	2.50	2.35	2.52	RMC [73]
Material	r_{Se-Se} [Å]	r_{Se-Sb} [Å]	r_{Sb-Sb} [Å]	**Method**
$Ge_{24}Se_{56}Sb_{20}$		2.63	2.87	XAS [47]
$Ge_{27}Se_{60}Sb_{13}$	2.30	2.55	2.60	RMC [73]
$Ge_{20}Se_{60}Sb_{20}$	2.30	2.53	2.60	RMC [73]
$Ge_{15}Se_{25}Sb_{20}$	2.33	2.55	2.55	RMC [73]

Liquid phase The melting temperature of the three compounds of interest is not easy to determine, more precisely, it depends on the definition of this melting temperature. Analysis of the phase diagram of GeSe reveals that $Ge_{30}Se_{70}$ undergoes an incongruent (inhomogeneous)

Table 1.4 – *Bond lengths in glassy GSSN from literature.*

Material	r_{Ge-Ge} [Å]	r_{Ge-Se} [Å]	r_{Ge-Sb} [Å]	r_{Ge-N} [Å]	r_{Se-Se} [Å]	Method
N-$Ge_{24}Se_{56}Sb_{20}$		2.37		1.84		XAS [47]
N-$Ge_{24}Se_{56}Sb_{20}$	2.65	2.48	2.77	1.97	2.42	AIMD [47]
Material	r_{Se-Sb} [Å]	r_{Se-N} [Å]	r_{Sb-N} [Å]	r_{Sb-Sb} [Å]	r_{N-N} [Å]	Method
N-$Ge_{24}Se_{56}Sb_{20}$		2.63			2.00	XAS [47]
N-$Ge_{24}Se_{56}Sb_{20}$	2.66	2.96	2.07			AIMD [47]

melting at T_{m1} = 485 K [160–162] which leads to a mixture of liquid and solid $GeSe_2$. A second melting, congruent this time, occurs at T_{m2} = 976-978 K [160–162] leading to a fully molten $Ge_{30}Se_{70}$ compound. The same is expected for the two other chalcogenides that we are interested in. Compounds with compositions close to the GSS one can be found in the literature to have multiple melting temperature also. Phase diagram of tie-line Sb_2Se_3-GeSe shows that $Ge_{24}Sb_{21}Se_{55}$ melts at 726, 745 and 787 K [160]. Other studies focused on the crystallization and melting kinetics analyzed the thermal behaviour of $Ge_2Sb_2Se_5$ [163] and $Ge_{18}Sb_{28}Se_{54}$ [164] by differential scanning calorimetry (DSC). Similarly to the first alloy we talked about, both of these compounds demonstrate multiple incongruent and congruent melting temperatures from 665 K to 760 K [163, 164].
No literature can be found on GSSN, but as the composition is also close to all the other compounds, the same melting behaviour is expected.

Both Se-Se and Ge-Ge homopolar bonds are present in the liquid phase of Ge-Se [158, 165]. The characteristics of the liquid phase are very similar to the glassy one [166].

III.2 Structural relaxation

A crucial issue with the use of amorphous/glasses states in memory devices is the data retention. Over the years, the structure of the amorphous state of the PCM is not stable. The *resistance drift* phenomenon, which correspond in other words to the aging of material, leads to an increase of the electrical resistance [167] and of the band gap [168, 169] which hinders the storage of information. The mechanism at play is not much understood and theories proposed are sometimes clearly contradictory: for example, it could be due either to an increase of disorder [168] or to its decrease [170, 171]. An interesting model was suggested by Ielmini *et al.* [170]: this structural relaxation would be the thermal excitation of electrons trapped in defect states in the electronic gap. With aging, these trap states move to the conduction band. This model is for now the best hypothesis as other groups found results in adequation with it: evolution of the

trap states [172, 173], correlation between the drift coefficient ν, characterizing the evolution of resistance, and the activation energy [174].

The origin of aging phenomena depends on the material: for Si and similar standard glasses, it seems to be due to a decrease of the Urbach tails (slope of the density of states close to the band gap) [175, 176] while for PCMs, it is not the case as shown for GeTe by Raty *et al.* [113]. This latter study was the first *ab initio* molecular dynamics simulation able to describe the structural evolution during aging. Indeed, the aging phenomenon is not accessible with conventional simulations due to its timescale: several hours are needed to measure the aforementioned drift. To avoid this issue, multiple cells were simulated, representing the expected evolution of GeTe when aging. This structure which, as stated in Section II.2, is characterized by a great proportion of Ge atoms in tetrahedral sites, see this number decrease as the Ge atoms move toward a 3-fold configuration with angles of 90°. This is not without recalling the octahedral environment present in the crystalline state. With this change of configuration comes the reinforcement of the Peierls distortion and the opening of the band gap. Finally, the amount of homopolar Ge-Ge bonds are shown to be clearly linked to that of the tetrahedral configuration, and thus also disappearing with aging. Still, an experimental study contests this last result as they obtained the exact opposit: an increasing number of Ge-Ge bonds by EXAFS experiments [92], another metadynamics simulation [177] resulted in the same structural evolution as in Reference [113]. It is then questionable whether it is due to an experimental artifact (inhomogeneity of the sample, influence of the substrate or the capping, ..) or if simulations fail to represent accurately this phenomenon as they cannot be extended on a sufficient timescale.

III.3 Doping

To counter or at least limit the aforementioned negative impact of aging, one solution is to dope the materials. In embedded memory applications, the operating temperature is about 150 °C [9]. The thermal stability of the amorphous phase is therefore crucial for data retention. In practice, improving this stability means increasing the crystallization temperature T_x. The addition of dopant such as N [21, 23, 178–182], C [118, 182–185], Zn [186], Ni [187] for example has been proven to be very efficient. GeTe doped with 10% C increases its temperature from 180 °C to 340 °C. This increase of crystallizaton temperature is often accompanied by a decrease of the programming current, in particular for the RESET operation [23, 182, 183] and an increase of the band gap [188].

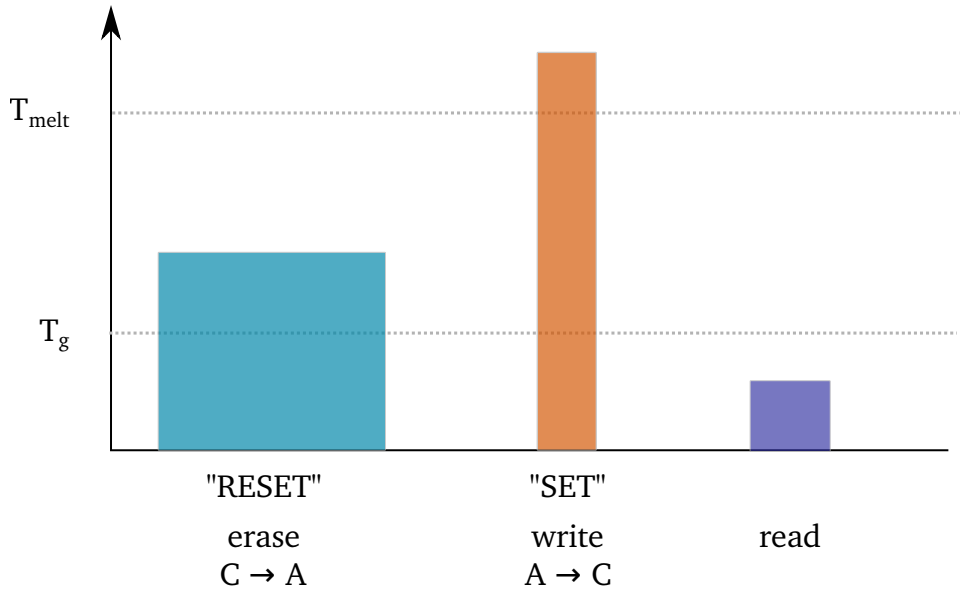

Figure 1.8 – *Amorphization ("RESET") and crystallization ("SET") procedures in DVDs, Blu-rays... with T_{melt} the melting temperature and T_g the glass temperature. The memory cell needs to be heated with a long electrical or light pulse of moderate intensity (the cell should be heated up to $T_g < T < T_{melt}$) to transition to the crystalline state while a short and intense pulse is required for the amorphization. Reading the memory cell state is possible thanks to a low intensity pulse such that it does not disturb the actual state.*

IV An ultrafast transition

Since the 90's, chalcogenide have had a renewed popularity with the realization that they could be materials of choice for storage memory devices. Phase-change disk in 1994, CD-RW in 1997, DVD-RAM in 1999, and so on... [8], all working on the basis on the irradiation of a PCM by a laser, triggering the phase transition. The physics that was at play was not fully understood, yet there was a need to improve the transition. While it was already fast for the time, the increasing need of data storage required the fastest possible.

The step forward was to investigate the materials while it is transitioning with the aim to see what is subject to improvement. In optical data storage devices (apart from the Xpoint technology and PCMs), the memory cell switches from one state to the other under application of a laser pulse. The duration of this latter is not short: mostly cw-laser are used, and the real application time is about a few hundreds of nanoseconds for the limiting step of recrystallisation. As a consequence, their utility is clearly to heat the material rather than anything else, as represented in Figure 1.8. Still, the question was how to improve this process as it is thermally driven, and thus cannot be reduced below a certain point as such.
With the development of new architectures of laser, shorter pulse durations were accessible to investigate chalcogenides behaviour in laboratory. Picosecond [189], and even femtosecond [61]

pulses have paved the way to new perspectives: the role of the laser was not anymore heating, but photo-exciting the sample, as detailed in Section I.1.

Measurement of reflectivity (optical probe) using this improved time resolution revealed interesting phenomena: the presence of ultrafast transient states. The irradiation of an amorphous GeSb (*a*-GeSb) film with a 100-fs laser pulse [44] showed a pronounced increase in reflectivity from 0.57-0.58 to 0.71 in less than a picosecond, followed by a decrease towards a transient state in 20 ps, and finally another increase up to the reflectivity of the crystal. The study of Callan *et al.* [62], consisting in pumping *a*-GeSb film with 50 fs laser pulses also revealed a similar two-timescales dynamics: the dielectric function shifts in 200 fs to a transient stationary value, then only after 5 ps it changes again.
This type of dynamics was seen in other studies [45, 60]. Waldecker *et al.* [45] revealed the decorrelation of the optical variation measured in photo-excited crystalline $Ge_2Sb_2Te_5$ and its lattice dynamics. Right after being pumped by a 35-fs pulse at 800 nm, the dielectric function shows a sudden decrease in 100 fs. The real part saturates to a corresponding to 70% of the initial one, which corresponds to that of the amorphous state. The imaginary part has a different response, with a transient saturation value on the same timescale as the real part, but continues to evolve on a longer timescale. This first ultrafast variation cannot be linked to a structural dynamics: when looking at the lattice temperature, it shows an exponential rise, with a characteristic time of 2.2 ps, and reaches a saturation regime after about 5 ps, so the electron-phonon coupling clearly has not taken place yet on the sub-picosecond timescale considered.

IV.1 A non-thermal transition ?

Non-thermal transitions have attracted a lot of attention over the last few decades. The idea of being able to get the same properties as the melted phase without heating it up to the melting temperature T_m is very attractive, especially in the domain of data storage. Indeed, data writing and erasing should be the fastest possible, especially with the increasing amount of information over the years.

In Figure 1.9, the difference of potential energy landscape between a thermal and a non-thermal transition from a phase 1 to a phase 2 is illustrated. This transition is only possible if the energetic barrier can be overcome, in other words, the transition requires an *activation energy* E_a. This latter can be obtained under different ways, in the example of nanosecond (ns) pulses lasers, it is heat. The important thing is that this transition occurs in the ground state. For femtosecond (fs) lasers pulses, the situation is different: the system is promoted to an excited state, whose potential energy landscape can reduce greatly the energy barrier from phase 1 to 2. Therefore, it might be possible to transition without any additional heat input.

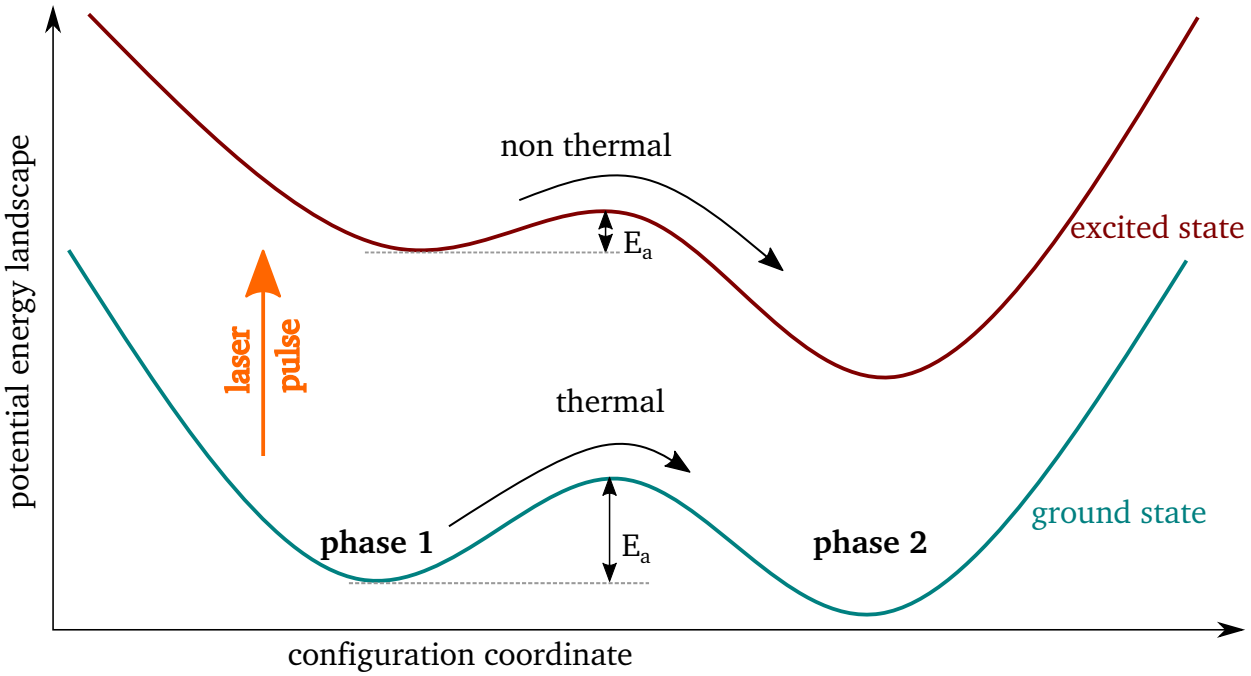

Figure 1.9 – *Schematic representation of the potential energy landscape for a thermal and a non-thermal transition. Adapted from [190].*

While previous attempts and the theory behind it have been subject to controversy [191–194], Shank *et al.* unambiguously demonstrated that Si could undergo such a non-thermal transition under photo-excitation with a 90-fs pulse at 620 nm [38]. After that, it was also demonstrated for other materials [39–43].

The concept of non-thermal transition was tackled in numerous studies dealing with photo-excited chalcogenides glasses or phase-change [44, 45, 90, 195, 195–199]. Kolobov *et al.* [195] reported that the photo-induced changes in band structure of trigonal Se were corresponding to its amorphous/liquid phase, while the temperature was still under T_m. Waldecker *et al.* [45] studied the photo-excitation of crystalline $Ge_2Sb_2Te_5$with electron diffraction and optical measurements of the reflectivity. The striking result they obtained is the detection of a change in the optical properties of the sample (*via* the dielectric function) while the ionic part of the material was still at room temperature. Only after 5 ps, the lattice reaches a stabilized heated value. The rise of temperature was fitted with an electron-phonon coupling of 2.2 ps. Therefore any variation measured before is not due to thermal effects (from the lattice) and can be considered as a non-thermal effects.

IV.2 Threshold switching mechanism

The actual mechanism of the *threshold switching* phenomenon, responsible the phase-transition discovered in phase-change materials and chalcogenide glasses is still debated. How can it be

this fast, along with an optical constrast this high ? Considering Ge-Sb-Te alloys, is it essentially a displacement of Ge atoms [67]? Or then Te atoms [60] ? Or maybe it is completely different ? The two main hypothesis are detailed here.

Umbrella flip model

A first hypothesis was the *umbrella flip* model suggested by Kolobov *et al.* in 2004 [67] (Figure 1.10) by studying the amorphization of $Ge_2Sb_2Te_5$ *via* experimental EXAFS and simulated XANES. Their conclusion is that the transition is due to the slight displacement of Ge atoms. These latter are initially in octahedral sites of three long and three short bonds in the crystalline sites and the weakening of the three long (already weak) bonds causes the reinforcement of the fourth closest bonds with the displacement of Ge towards a vacancy in the structure to form tetrahedral sites. This theory was questioned by Lang *et al.* [200] who performed Monte-Carlo simulations, inconsistent with the model as they resulted in the consideration that Ge and Sb atoms were actually relaxing away from that vacancy and it was in fact the Te atoms that were moving towards the vacancy in question. That was not the only disagreement: in fact further analyzes showed that all the variations observed between the amorphous and the crystalline phase cannot be accounted for with the umbrella flip model: Huang *et al.* [201] and Shportko *et al.* [63] investigations of the medium range order (MRO) showed that this one should change upon transition, yet that cannot be explained by the simple change of coordination suggested by the umbrella flip model.

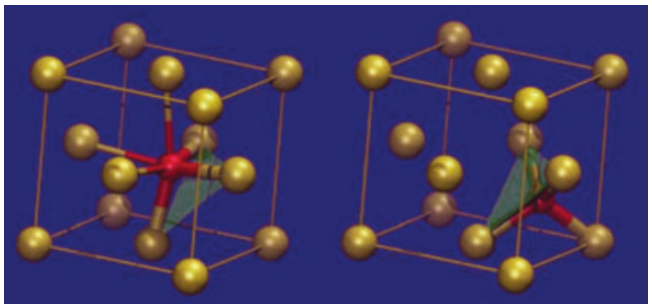

Figure 1.10 – *Illustration of the umbrella model. The Ge atoms supposedly switch from octahedral to tetrahedral local environment with their bonds that flip, similarly to an umbrella when there is too much wind. From Reference [67].*

Metavalent bonding

On the contrary to typical covalent solids [202], GeTe (and other PCMs) has a crystalline and an amorphous phase that are quite different in terms of local environments. Yet, the transition back and forth from the crystalline or amorphous phase is really fast, fast enough to be very interesting for the developement of data storage memories. The most stricking is the optical/electrical contrast. The unique nature of the bonding in PCMs may to be the key to the transition. Indeed, very soon,

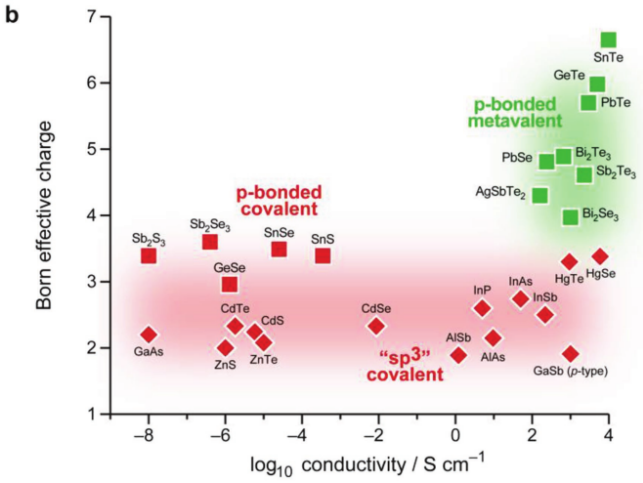

Figure 1.11 – *Chemical bond polarizability (via the Born effective charge) for a broad set of materials. The metavalent materials clearly separate themselves from the others. From Reference [32].*

the concept of *resonant bonding* emerged for IV-VI compounds [203]. The crystalline phases of these chalcogenide compounds demonstrated properties such as large Born effective charge or high lattice and electronic polarizabilities, that are not characteristic of ionic nor covalent bonding.

One remarkable feature of the GST family is the presence of short and long bonds in the crystalline phase. The initial hypothesis was that this resonant bonding was responsible for the fast character of the transition. However, vocabulary speaking, the term of "resonant bonding" is not satisfactory. Indeed, the term resonant bonding was first defined in the case of benzene, and we actually also refer to aromatic bonding as *resonant bonding*, while both types of materials (and their bonding properties) demonstrate completely different behaviours.

Recently, this concept of resonant bonding has been questioned and *via* a deep analysis of the nature of the bonds in lots of materials, the uniqueness of the PCMs bonds became clear: they are not fully covalent nor metallic, but a mix of the both, being at the same time delocalized and covalent. The term that now should refer to it is *metavalent* bonding [32, 33, 204].

This is what we see in the quantum mechanical maps established by Wuttig *et al.* to elaborate their theory [32, 33]. As shown in Figure 1.11, in terms of Born effective charges, which characterizes the chemical bond polarisability (sensitivity of a material to distortion here), covalent and metavalent materials do not mingle.

This unique type of bonding which shows up in the crystalline phase of PCMs and in the configuration of excited chalcogenides [156] could be the key to the rapidity of switching and to the large contrast in optical and electrical properties. While chalcogenides from the Se family

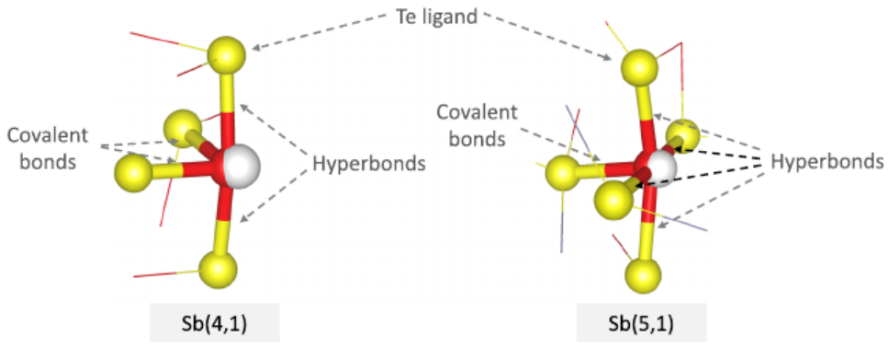

Figure 1.12 – *Hyperbonding of Sb atom from [35]. The number of bonds expected by the 8-N rule is four, but with the hyperbonds, the total exceeds the rule in both configurations shown here.*

seem to be purely covalent material and do not display the properties expected of metavalent bonding presence [32, 33, 205, 206], Raty *et al.* showed that upon excitation the chalcogenide glasses derived of Ge-Se alloys exhibit some of these characteristic properties [156].

Hypervalent bonding

This view of thinking is challenged by the *multicenter hyperbonding model* which regroups some of the similarities from the metavalent bonding, but claims to better describe the overall phenomenon as it gives a description of both crystalline and amorphous states [34, 35, 207]. This view is based on a molecular-orbital approach. Lone pairs in PCMs (pair of electrons not involved in a bonding) have a tendency to interact with unoccupied antibonding orbitals around them. This interaction results in an extra bonding compared to the maximum number expected with the octet rule as illustrated in Figure 1.12.

For now, no theory regarding the threshold switching mechanism is consually accepted, either in the case of PCM, nor in the case of OTS.

CHAPTER 2

OUT-OF-EQUILIBRIUM *AB INITIO* SIMULATIONS

Simulations are a great tool to understand the many-body physics that is not always accessible experimentally. Density functional theory (DFT) is a very powerful method to perform such simulations with a great accuracy. Still, it is not an easy task to compare the results obtained from that method with those measured during experiments. In this chapter, the basics of DFT and why it is used so much will be exposed. Then a description of the procedures and parameters used to mimick our fs-laser excitation will be detailed. Finally, a brief list of structural analyzes that are used to characterize a configuration will be given.

I Density functional theory

I.1 DFT fundations: Schrödinger's equation

The quantum mechanics description of a system of several atoms is complex. Considering a system of N nuclei and N_e electrons, the corresponding Hamiltonian H is expressed as:

$$H = \underbrace{\sum_{n}^{N} \frac{\boldsymbol{p}_n^2}{2M_n} + \sum_{i}^{N_e} \frac{\boldsymbol{p}_i^2}{2m_e}}_{\text{nuclei \& e- kinetic operators}} + \underbrace{\sum_{i>j}^{N_e} \frac{e^2}{|\boldsymbol{r}_i - \boldsymbol{r}_j|}}_{\text{e-/e- interaction}} + \underbrace{\sum_{n>m}^{N} \frac{Z_n Z_m e^2}{|\boldsymbol{R}_n - \boldsymbol{R}_m|}}_{\text{nuclei/nuclei interaction}} \underbrace{- \sum_{i,n} \frac{Z_n e^2}{|\boldsymbol{R}_n - \boldsymbol{r}_i|}}_{\text{e-/nuclei interaction}} \tag{2.1}$$

In this formula, $\boldsymbol{p}$ is the momentum operator, e the elementary charge and Z the nuclei charges. The nuclei (resp. the electrons) with masses M (resp. m_e) are represented with the indexes n, m (resp. i, j and e), and their positions with the symbol $\boldsymbol{R}$ (resp. $\boldsymbol{r}$).

The first two terms correspond to the kinetic operators of the nuclei T_n and electrons T_e respectively. Then the following terms in the equation refers to the electron-electron (V_{ee}), nuclei-nuclei (V_{nn}) and electron-nuclei (V_{en}) interactions in this order.
The full description of the system is equivalent to solving the Schrödinger Equation 2.2, with the many-body wave function of the system designated as $|\Psi\left(\{\boldsymbol{r}_i\},\{\boldsymbol{R}_n\},t\right)\rangle$.

$$i\hbar\frac{\partial}{\partial t}|\Psi\rangle = H|\Psi\rangle \Leftrightarrow \boxed{i\hbar\frac{\partial}{\partial t}|\Psi\rangle = \left[T_n + T_e + V_{ee} + V_{nn} + V_{en}\right]|\Psi\rangle} \tag{2.2}$$

I.1.1 Time-independent Schrödinger's equation

Considering that spatial and temporal terms are independent in the solution to Equation 2.2, these latter can be written as: $\Psi(r,t) = \psi(r)\varphi(t)$. This enables to separate the spatial and temporal components in the aforementioned equation, yielding:

$$i\hbar\frac{1}{\varphi(t)}\frac{\partial\varphi(t)}{\partial t} = \frac{1}{\psi(r)}\left[T_e + V_{ee} + V_{en} + E_{NN}\right]\psi(r) \tag{2.3}$$

As the left-hand and the right-hand side must be equal, though they are functions of two different variables, it means they are equal to a constant. This latter must have the dimension of an energy, such that we find the time-independent Schrödinger equation by considering the right-hand side: The system is then characterized by the eigenvalues E that are deduced *via* the time-independent Schrödinger equation:

$$\boxed{\left[T_n + T_e + V_{ee} + V_{en} + E_{NN}\right]\psi(r) = E\psi(r)} \tag{2.4}$$

I.1.2 Born-Oppenheimer (BO) approximation

The Schrödinger's equation can be solved exactly only for a few systems: H, H_2, He, using the free iterative complement interaction (ICI) method [208]. The common characteristic of these systems is the very small number of electrons. However, when it comes to larger systems, the number of degrees of freedom becomes too large to be solved with the current computer capacities.
A first simplification can be made to the Equation 2.4 with the adiabatic approximation stated by Born and Oppenheimer in 1927 [209]. The huge difference of mass between nuclei and electron (typically $M \sim 10^3 m_e$) implies that their motion can be decoupled: electrons are very fast compared to the nuclei. This has the direct consequence of considering that the nuclei have a fixed position, and justifies to write the electronic wave functions and eigenvalues as depending parametrically on the nuclear positions $\boldsymbol{R}$ and not on their dynamics [210].

First, we consider the Schrödinger equation of the electrons in the system, and find the *electronic wave equation*, see Equation 2.5, with $H_e = T_e(r) + V_{en}(r,R) + V_{ee}(r,R)$ the electronic hamiltonian, $\phi_q(\{R_n\},\{r_i\})$ and E_q respectively the wavefunctions and energies of each electronic state q:

$$\boxed{H_e\phi_q(\{\boldsymbol{R}_n\},\{\boldsymbol{r}_i\}) = E_q(\boldsymbol{R_n})\phi_q(R,r)} \tag{2.5}$$

The electronic wave functions $\{\phi_q\}$ form a complete basis set, which can be taken orthonormal such that $\langle\phi_q|\phi_p\rangle = \delta_{pq}$, with δ_{pq} the Kronecker delta function giving 1 if $p = q$ and 0 otherwise. This condition of completeness implies that the wave function of the total system can be expanded on this basis such that:

$$\psi(\{R_n\},\{r_i\}) = \sum_q F_q(\{R_n\})\phi_q(\{R_n\},\{r_i\}) \tag{2.6}$$

In this expression, the nuclear motion of the system in the electronic state q is represented by the wave functions F_q. The corresponding eigenvalue of V_{nn} applied on ψ, E_{nn}, is a constant due to the fixed nuclei. As a consequence, using the development 2.6 for the wave function, the Schrödinger Equation 2.4 for the complete system is now expressed as:

$$[T_n + H_e]\sum_q F_q(R)\phi_q(\{R_n\},\{r_i\}) = E\sum_q F_q(R)\phi_q(\{R_n\},\{r_i\}) \tag{2.7}$$

This latter equation is projected on each $\phi_p(\{R_n\},\{r_i\})$ electronic wave function of the basis such that:

$$\begin{aligned} &\sum_q \langle\phi_p|\left[T_n + H_e - E\right]|\phi_q\rangle F_q = 0 \qquad \text{for each } p \\ \Rightarrow &\boxed{\sum_q \langle\phi_p|T_n|\phi_q\rangle F_q + \left(E_p - E\right)F_p = 0 \qquad \text{for each } p} \end{aligned} \tag{2.8}$$

The kinetic operator of the nuclei T_n will now be expressed in terms of spherical coordinates (see Figure 2.1) rather than cartesian ones, with $\boldsymbol{L}$ the orbital angular momentum operator:

$$T_n = -\sum_n \frac{\hbar^2}{2M_n}\left[\frac{1}{R^2}\frac{\partial}{\partial R}\left(R^2\frac{\partial}{\partial R}\right) + \frac{1}{R^2}\underbrace{\left[\frac{1}{sin\theta}\frac{\partial}{\partial\theta}\left(sin\theta\frac{\partial}{\partial\theta}\right) + \frac{1}{sin^2\theta}\frac{\partial^2}{\partial\phi^2}\right]}_{=L^2/\hbar}\right] \tag{2.9}$$

As the motion of the electrons is very fast compared to that of the nuclei, the variation of the electronic wave functions ϕ_q with respect to R is negligible compared to that of F_q and allows to derive the set of uncoupled *nuclear wave equations*, describing the vibrational and rotational

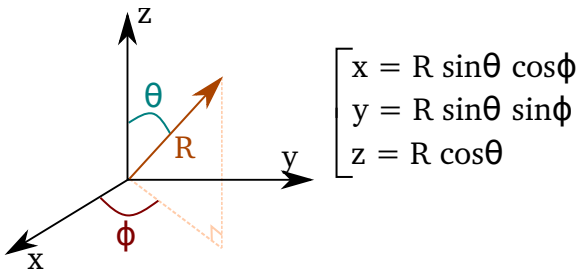

Figure 2.1 – *Reminder of the spherical coordinates.*

motions of the molecules when the electronic part is in the state p:

$$-\sum_n \frac{\hbar^2}{2M_n}\left[\frac{1}{R^2}\frac{\partial}{\partial R}\left(R^2\frac{\partial}{\partial R}\right)+\frac{\langle\phi_p|L^2|\phi_p\rangle}{2M_nR^2}+E_p-E\right]F_p(\boldsymbol{R})=0 \tag{2.10}$$

This last equation establishes the Born-Oppenheimer approximation. For each electronic state p, the total wave function reduces to $\boxed{\psi_p = F_p(\boldsymbol{R})\phi_p(\{\boldsymbol{R_n}\},\{r_i\})}$.
Practically, in order to solve the many-body problem in the Born-Oppenheimer approximation, the electronic eigenvalues $E_p(\boldsymbol{R})$ are retrieved thanks to the electronic wave Equation 2.5. They are then used under the form of a potential to solve the nuclear wave Equation 2.10.

I.1.3 Hartree-Fock model

The *Hartree-Fock* (HF) *approximation*, also known as the *self-consistent field method*, is based on the *independent-particle model* formulated by Hartree in 1928. The method of resolution introduced concepts that are at the base of DFT. The HF approximation consists in looking for wave functions that are solutions of the electronic wave Equation 2.5, in the form of a Slater determinant. The electronic hamiltonian of the N_e-body electronic system H_e, is written here as a sum of two terms denoted H_i and H_{ij}. The first one, H_i, is a sum of N_e one-body electronic hamiltonians, expressed with the electronic kinetic operator T_i of the electron i and the potential energy $V_{i,n}$ due to the interaction of the i^{th} electron with the n^{th} nucleus. The second term, H_{ij}, is the sum of two-body interactions of the electron i with the electron j:

$$\begin{aligned} H_e &= \sum_i \left(T_i - \sum_n V_{i,n}\right) + \sum_{i<j} V_{ij} \\ &= \sum_i h_i + H_{ij} \end{aligned} \tag{2.11}$$

As stated before, the solutions ψ are expressed as a Slater determinant of one-body, orthonormal

spin-orbitals functions χ_i such that the wave function is expressed as:

$$\psi = \frac{1}{\sqrt{N_e!}} \begin{vmatrix} \chi_1(1) & \chi_2(1) & \cdots & \chi_\nu(1) \\ \chi_1(2) & \chi_2(2) & \cdots & \chi_\nu(2) \\ \vdots & \vdots & \vdots & \vdots \\ \chi_1(N_e) & \chi_2(N_e) & \cdots & \chi_\nu(N_e) \end{vmatrix} \tag{2.12}$$

These spin-orbitals functions should be orthonormal such that $\langle \chi_i | \chi_j \rangle = \delta_{ij}$.
With E_0 the ground state energy of the system, we know from the variationnal principle that $E_0 \leq E[\psi_e]$, with $E[\psi]$ a functional of the trial function ψ.

The eigenvalues of the electronic wave equation can then be derived (see Reference [210] for the detailed calculation):

$$\begin{aligned} E[\psi] &= \langle \psi | H_e | \psi \rangle \\ &= \sum_{\lambda}^{\nu} \langle \chi_\lambda(i) | h_i | \chi_\lambda(i) \rangle + \frac{1}{2} \sum_{\lambda,\mu}^{\nu} \Big[\langle \chi_\lambda(i)\chi_\mu(j) | V_{ij} | \chi_\lambda(i)\chi_\mu(j) \rangle \\ &- \langle \chi_\lambda(i)\chi_\mu(j) | V_{ij} | \chi_\mu(i)\chi_\lambda(j) \rangle \Big] \end{aligned} \tag{2.13}$$

From this last equation, we define two terms. The first one is the *Coulomb term*, denoted $J_{\lambda\mu}$. It represents the mean potential created by the other electrons of the system.

$$J_{\lambda\mu} = \langle \chi_\lambda \chi_\mu | V_{ij} | \chi_\lambda \chi_\mu \rangle = J_{\mu\lambda} \tag{2.14}$$

The second term is called the *exchange term* $K_{\lambda\mu}$. It arises from the antisymmetry of the wave function. Indeed, it corresponds to a matrix element of the V_{ij} between the states $\chi_\lambda(i)\chi_\mu(j)$ and $\chi_\mu(i)\chi_\lambda(j)$.

$$K_{\lambda\mu} = \langle \chi_\lambda(i)\chi_\mu(j) | V_{ji} | \chi_\mu(i)\chi_\lambda(j) \rangle = K_{\mu\lambda} \tag{2.15}$$

As a consequence, $E[\psi]$ can be written more simply with the subsequent definition of $I_\lambda = \langle \chi_\lambda(i) | h_i | \chi_\lambda(i) \rangle$:

$$E[\psi] = \sum_{\lambda} I_\lambda + \frac{1}{2} \sum_{\lambda} \sum_{\mu} \left(J_{\lambda\mu} - K_{\lambda\mu} \right) \tag{2.16}$$

From this point, the next step is to apply the variational principle and find the ψ that minimizes this functional. This condition can be expressed as the seeking of a stationary $E[\psi]$ under small variations $\delta\psi$. These latters are constrained to the orthonormality condition, which implies that

the variational condition should be:

$$\delta E - \sum_{\lambda,\mu} \delta c_{\lambda,\mu} \delta \langle \chi_\mu | \chi_\lambda \rangle = 0 \tag{2.17}$$

For particular $c_{i,j}$ coefficients, called *Lagrange multipliers* and being essentially the energies E_λ of the orbitals, this equation is verified for any small $\delta\psi$, such that the variational principle is reformulated as $\delta E - \sum_\lambda \delta E_\lambda \delta \langle \chi_\lambda | \chi_\lambda \rangle = 0$

Using Equation 2.16 and skipping a few steps [210], we find that it is possible to define the full Hartree-Fock potential V_{HF} as in Equation 2.18, with $V_\mu^J(i)$ and $V_\mu^K(i)$ a Coulomb and an exchange operator respectively, deriving from the aforementioned terms of same name from Equations 2.14 and 2.15.

$$V_{HF}(i) = -\sum_n V_{i,n} + \sum_\mu \left[V_\mu^J(i) - V_\mu^K(i) \right] \tag{2.18}$$

$$\Rightarrow \boxed{\left[T_i + V_{HF} \right] \chi_\lambda(i) = E_\lambda \ \chi_\lambda(i)} \tag{2.19}$$

However, Hartree-Fock equations such as Equation 2.19 are not really eigenvalues equations. An iteration process should be used to solve them, starting from approximate $\{\chi^{(1)}\}$ that give a corresponding $V_{HF}^{(1)}$. The HF equations are then solved to obtain new $\{\chi^{(2)}\}$ and so on until the difference between $V_{HF}^{(n)}$ and $V_{HF}^{(n-1)}$ are identical (within the desired approximation). This iteration method is known as the *self-consistent field* (SCF) method. In practice, a convenient basis set for the $\{\chi_\lambda\}$ is Slater orbitals, taking the form $\chi_{nlm} = N r^{n-1} e^{-\alpha r} Y_{lm}(\theta, \phi)$, which is the form commonly used to describe the molecular orbitals in chemistry.

This HF Hamiltonian $h_{HF} = T_i + V_{HF}$ can be seen as an energy operator acting on the state χ_λ of an electron. First, we note that $V_\lambda^J(i)\chi_\lambda(i) = V_\lambda^K(i)\chi_\lambda(i)$, as the HF model is based in the independent particle model. Therefore, no self-energy contributes to the HF potential. The density matrix $\rho_\lambda(i,j)$ and the spinless density matrix $\rho_\lambda(\boldsymbol{r}_i, \boldsymbol{r}_j)$ are defined following Equation 2.20 as:

$$\begin{aligned} \rho_\lambda(i,j) &= \sum_{\mu \neq \lambda} \chi_\mu(i) \chi_\lambda^*(j) \\ \rho_\lambda(\boldsymbol{r}_i, \boldsymbol{r}_j) &= \sum_{\mu \neq \lambda} \chi(\boldsymbol{r}_i) \chi_\mu^*(\boldsymbol{r}_j) \end{aligned} \tag{2.20}$$

Then the probability density of finding an electron at $\boldsymbol{r}$ in an occupied state $\mu \neq \lambda$ is obtained *via*:

$$\rho_\lambda(\boldsymbol{r}_i, \boldsymbol{r}_i) = \sum_{\mu \neq \lambda} |\chi_\mu(\boldsymbol{r})|^2 = \rho_\lambda(\boldsymbol{r}) \tag{2.21}$$

Using the density matrices, V^J and V^K are therefore given as:

$$\begin{aligned} V_\lambda^J(\boldsymbol{r}_i) &= \int \rho_\lambda(\boldsymbol{r}_j) V_{ij} d\boldsymbol{r}_j \\ V_\lambda^K(i)\chi_\lambda(i) &= \int \rho_\lambda(i,j) V_{ij} \chi_\lambda(j) d(j) \end{aligned} \tag{2.22}$$

$$\begin{aligned} h_{HF}(i)\chi_\lambda(i) &= E_\lambda \chi_\lambda(i) \\ \Rightarrow E_\lambda &= I_\lambda + \sum_\mu [J_{\mu\lambda} - K_{\mu\lambda}] \end{aligned} \tag{2.23}$$

In the end, we find that the sum over all λ states, does not give the total energy due to the double counting of mutual interaction energies. The total energy of the system is in fact given by:

$$\boxed{E[\psi] = \sum_\lambda E_\lambda - \langle \psi | H_{ij} | \psi \rangle} \tag{2.24}$$

I.1.4 Electronic density as basic variable

With the Hartree-Fock model, we see the emergence of density matrices, under the form of Slater determinants, to solve the many-body problem.
The original idea of density functional theory (DFT) was formulated by Thomas and Fermi around the same period as the HF model, in 1927 [211, 212]. Rather than finding a multi-electronic wave function that is a solution to the Schrödinger equation, their idea was to consider a functional of the electronic density ρ that would replace it and give rise to a much simpler problem by reducing the number of degrees of freedom. The method suggested by Thomas-Fermi was still lacking some accuracy, especially on the chemical bonding point of view. Hopefully, further improvements have been developed later on as will be presented now.

I.2 Hohenberg-Kohn theorems

In 1964, Hohenberg and Kohn (HK) [213] formulate DFT as an exact theory of a many-body problem. Their idea is to consider the nuclei as an external potential V_{ext} to the electron density $\rho(r)$. As the wave function is expressed as a Slater determinant in this picture, the density is linked to it *via*:

$$\boxed{\rho(\boldsymbol{r}) = \sum_i |\psi_i(\boldsymbol{r})|^2} \tag{2.25}$$

The Hamiltonian of the system is now expressed as:

$$H = T_e + V_{ee} + V_{ext} \tag{2.26}$$

with V_{ext} the effective potential due to the ions. Two important theorems are formulated in the aforecited article, which have been decisive for the future of DFT.

I.2.1 First theorem: uniqueness of the external potential

From Reference [213], "*the external potential is (to within a constant) a unique functional of the electronic density; since, in turn, the external potential fixes the Hamiltonian H, we see that the full many-particle ground state is a unique functional of the electronic density*", which simply means that the electrons determine the nuclei positions, and as a consequence also all the properties defining the system (H, ψ,..). This is illustrated in Figure 2.2.

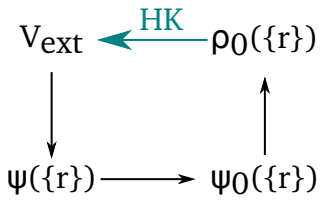

Figure 2.2 – *Schematic summary of the HK theorems. The ground state of the electronic density ρ_0 accounts for a unique V_{ext} (up to a constant). This latter determines all the properties of the system: eigenstates $\psi(\{\boldsymbol{r}\})$, including the ground state $\psi_0(\{\boldsymbol{r}\})$.*

This first theorem is proven by *reductio ad absurdum*: we consider two external potentials $V_{ext,1}$ and $V_{ext,2}$, which differ by more than a constant, with the hypothesis that their associated Hamiltonians H_1 and H_2 applied on their respective ground state wave functions ψ_1 and ψ_2 yield the same ground state density $\rho_0(\mathbf{r})$. Each ground state is supposed to be non-degenerate under the assumptions of Hohenberg and Kohn, and associated with the respective energies denoted E_1 and E_2.

The variational principle implies that:

$$\begin{aligned} E_1 = \langle\psi_1|H_1|\psi_1\rangle &< \langle\psi_2|H_1|\psi_2\rangle \\ &< \langle\psi_2|H_2|\psi_2\rangle + \langle\psi_2|\left[H_1 - H_2\right]|\psi_2\rangle \\ &< E_2 + \int d^3r \left[V_{ext,1} - V_{ext,2}\right]\rho_0(r) \end{aligned} \tag{2.27}$$

The same reasoning applies to E_2, which yields:

$$\begin{aligned} E_2 = \langle\psi_2|H_2|\psi_2\rangle &< \langle\psi_1|H_2|\psi_1\rangle \\ &< E_2 + \int d^3r \left[V_{ext,2} - V_{ext,1}\right]\rho_0(r) \end{aligned} \tag{2.28}$$

The addition of Equations 2.27 and 2.28 results in the contradictory inequality that:

$$E_1 + E_2 < E_2 + E_1 \tag{2.29}$$

Therefore as stated in the theorem, the external potential and all properties of the system are completely and uniquely determined (to within a constant) by the ground state density of the electrons.

I.2.2 Second theorem: Variational principle

The second theorem of Hohenberg and Kohn stems from the variational principle. It states that the functional associated to the total ground state energy is the lowest only if it corresponds to the density of the true ground state of the system.
The first HK theorem indicates that all properties of the system are uniquely determined by the electronic density. Therefore, all properties of the system, V_{ext}, H and even ψ can be considered as functional of $\rho(r)$, such that the total energy functional can be written as:

$$E[\rho] = \underbrace{T[\rho] + E_{ee}[\rho]}_{\text{universal}} + \underbrace{\int d^3r\, V_{ext}(r)\rho(r) + E_{NN}}_{\text{system dependent}} \tag{2.30}$$

The functional $F_{HK}[\rho] = T[\rho] + E_{ee}[\rho]$ is defined as to comprise internal and kinetic energies. Considering a system with ground state density ρ_1 associated with $V_{ext,1}$, the expectation value E_1 of the Hamiltonian H_1 follows the Equation 2.30:

$$E_1 = E[\rho_1] = \langle \psi_1 | H_1 | \psi_1 \rangle \tag{2.31}$$

For any other density ρ_2, associated with is associated to ψ_2 and different from ρ_1, the HK theorem implies that $\psi_2 \neq \psi_1$. As E_1 corresponds to the ground state energy, it follows that the energy $E_2 = \langle \psi_2 | H_1 | \psi_2 \rangle$ associated to this new state is evidently greater than E_1.

I.3 Kohn-Sham ansatz

Unfortunately, the HK theorem does not allow to reduce significantly the degrees of freedom, and the overall problem is still complicated to solve. Kohn and Sham approach [214] allowed a big step forward in the application of DFT. Their idea was to reformulate the problem. Instead of solving the many-body interaction problem, they expressed the ground state energy density of this interacting system of interest ρ^{int} as being equal to another (chosen) one ρ^{nint} in a system of non-interactive particles as depicted in Figure 2.3. Then all the information about interactions and difference in kinetic energy between the interacting and non-interacting systems are enclosed in a

single functional called the *exchange-correlation energy functional* E_{xc} that links the two pictures.

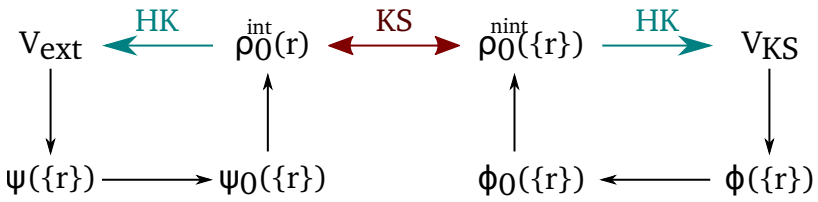

Figure 2.3 – *Schematic summary of the KS ansatz. The electronic density ρ^{nint} of the independent particles problem determines the corresponding external potential V_{KS} by application of HK theorems. Then, the actual electronic density of interest ρ^{int} can be found, thus enabling to completely solve the problem in the interacting picture.*

The Hamiltonian of the non-interacting particles picture H_{KS} can be expressed in a similar way as previously, except that the potential V_{KS} now includes a term of exchange and correlation. The corresponding *Kohn-Sham orbitals* are denoted ϕ_{KS}.

$$H_{KS} = -\frac{\hbar^2}{2m_e}\nabla^2 + V_{KS}(r) \Rightarrow \boxed{H_{KS}\,\phi_{KS} = E_{KS}\,\phi_{KS}} \tag{2.32}$$

The corresponding Kohn-Sham energy of the non-interacting ground state is E_{KS} derived as such:

$$E_{KS}[\rho] = \underbrace{\boxed{T_S[\rho] + \int d^3r\, V_{ext}\rho(r) + E_H[\rho] + E_{NN}}}_{\text{independent particle functional}} + \underbrace{\boxed{E_{xc}[\rho]}}_{\substack{\text{exchange-correlation}\\ \text{functional}}} \tag{2.33}$$

T_S is the Kohn-Sham kinetic energy of the non interacting particles defined as per Equation 2.34:

$$T_S = \sum_i^{N_e} \int d^3r\, \langle\phi_i| \frac{-\hbar^2}{2m_e}\nabla^2 |\phi_i\rangle \tag{2.34}$$

The Hartree energy E_H corresponds to the Coulomb interaction of the electron density with itself such that:

$$E_H[\rho] = \frac{e^2}{2}\int d^3r\, d^3r'\, \frac{\rho(r)\rho'(r')}{|r-r'|} \tag{2.35}$$

E_{xc} includes all the exchange and correlation effects due to the many-body interaction. This term is also a functional and can be expressed more explicitely as in Equation 2.36. The exchange part refers to the interaction between the electrons due to the Pauli principle which compels the wave function to be asymmetric. The correlation part can be defined brutely as how the movement of

an electron will be affected by the presence of other electrons.

$$E_{xc}[\rho] = \int d^3r\ \rho(r)\epsilon_{xc}[\rho(r)] \tag{2.36}$$

Considering the variational expression of Equation 2.33, the two potentials V_{xc} and V_H corresponding respectively to the exchange-correlation and Hartree energies can be defined. The identification of terms with Equation 2.32 yields the following formula for the Kohn-Sham potential V_{KS}:

$$\boxed{V_{KS}(\boldsymbol{r}) = V_{ext}(\boldsymbol{r}) + V_H(\boldsymbol{r}) + V_{xc}(\boldsymbol{r})} \tag{2.37}$$

I.4 Approximations on the exchange-correlation terms

Kohn-Sham approach greatly simplified the application of DFT. What was left after was finding an appropriate exchange-correlation energy functional to completely solve the problem. No exact E_{xc} was determined, yet several approximations have been developed with increasing accuracy. A considerable number of exchange-correlations functionals have been developed: LDA [215], B3LYP [216], PBE [217, 218], HSE06 [219]... with specificities to better describe a phenomenon of interest compared to another one. For instance, chemists are more prone to use B3LYP functional while solid states physicists are more likely to use AM05 functional as it would include surface effects while the first one would be more appropriate for the description of a molecule's physico-chemical properties. Therefore, in this section, only the main families will be described.

I.4.1 Local density approximation (LDA)

The *local density approximation* (LDA) [215] derives from the *local spin density approximation* (LSDA). The difference lies in the fact that LDA deals with unpolarized systems on the contrary to LSDA. The LSDA approximates the exchange-correlation term using homogeneous electron gas (HEG) model, which consists in considering that the positive charges of the nuclei are uniformly distributed in space, therefore so does the electron density. The E_{xc}^{LSDA} can be expressed as such, with $\rho^{\pm}$ denoting the density of spin *up* and *down*:

$$\boxed{E_{xc}^{LSDA}[\rho^+, \rho^-] = \int d^3r\ \rho(r)\epsilon_{xc}^{LSDA}(\rho^+, \rho^-)} \tag{2.38}$$

In the case of LDA, ρ^+ and ρ^- are replaced by setting $\rho^+ = \rho^- = \rho/2$. It is conventional to express ϵ_{xc} as the sum of the exchange and correlation terms such that $\epsilon_{xc}[\rho] = \epsilon_x[\rho] + \epsilon_c[\rho]$.
The first one, ϵ_x, can be derived exactly [220], as it corresponds in fact to the exchange energy

ϵ_x^{HEG} in a simple homogeneous electron gas.

$$\epsilon_x^{LDA} = -\frac{3}{4}\left(\frac{3}{\pi}\right)^{1/3} \int \rho^{4/3}(\boldsymbol{r})d\boldsymbol{r} \tag{2.39}$$

The correlation term ϵ_c on the contrary cannot be derived as easily. For this term, numerical methods such as Monte-Carlo simulations [221, 222] are necessary to get a proper approximate. L(S)DA are not always the best-suited functionals. For metals, whose electronic structure is close to a HEG, it is obviously far better than for other types of solids, especially inhomogeneous ones.

I.4.2 Generalized-Gradient Approximation (GGA)

When the gradient of electronic density cannot be considered negligible, the LDA becomes irrelevant. The *generalized-gradient approximations* (GGA) were developped with the aim of reaching a better accuracy than the LDA, especially for these cases of inhomogeneous solids.
The name GGA regroups several forms of exchange-correlation functionals that have been developed with the same general method, such as the Perdew-Burke-Ernzerhof (PBE) [217, 218] that were developed early and derived in multiple forms (PBEsol [223], RPBE [224],..) or the Armiento-Mattson functional (AM05) [225] which includes some surface effects for instance.
The overall principle is to take into account the inhomogeneities of the gas of electrons of the system by introducing a function F_{xc} that depends on the gradient of density $\nabla\rho$ in the LDA expression.

$$\begin{gathered} E_{xc}^{GGA}[\rho] = \int d^3r\ \rho(r)\epsilon_{xc}\left(\rho, |\nabla\rho|, \right) \\ \boxed{E_{xc}^{GGA}[\rho] = \int d^3r\ \rho(r)\epsilon_{xc}^{HEG}(\rho)F_{xc}\left(\rho, |\nabla\rho|\right)} \end{gathered} \tag{2.40}$$

Although the GGA gives better results than the simple LDA on several aspects such as the correct determination of the ground state in magnetic transition metals, there are still some accuracy lacking. The most obvious one when dealing with semiconductors and insulators is the underevaluation of their bandgaps [226–228].

I.4.3 Meta-GGA and hybrids functionals

To minimize that issue and improve the precision of DFT calculation overall, other forms of functionals have been developed: meta-GGA and hybrid functionals.
Meta-GGA are an extension of the GGA: in addition to the dependency on the electronic density and its gradient, they also consider its Laplacian $\Delta\rho$ or the local kinetic energy [229, 230]. The results for small molecules are quite good with meta-GGA, but for solids it is only a partial success.

On the other hand, hybrid functionals are nowadays a method of choice [219, 231], especially in the chemical community. They are based on two assumptions:

1. The exchange energy E_x is calculated as in the Hartree-Fock model. As discussed in Section I.1.3, this latter is an independent particles approach, therefore all many-body correlations except the ones due to the Pauli principle are discarded.

2. Considering that the LDA/GGA leads to the overestimation of physical quantities, whereas the Hartree-Fock method leads to their underestimation, mixing both in the example form of Equation 2.41 (with a a factor between 0 and 1) should give a better approximation than each one separately.
$$E_{xc} = aE_{xc}^{HF} + (1-a)E_{xc}^{LDA/GGA} \tag{2.41}$$

When parameters are well chosen, the resulting functional improves greatly the accuracy (of the bang gap for instance). The issue is that the calculations are then much longer than when using the other "simple" functionals such as LDA or GGA. It is then a compromise between time and sufficient accuracy.

Density functional theory is a powerful tool to solve a many-body problem. The use of appropriate exchange-correlations functionals enables to describe the system with a high precision. These functionals are multiple, and each one of them has advantages and drawbacks that have to be taken into account depending on the goal of the calculations performed.

II Out-of equilibrium simulations

In order to reproduce the effects induced by a femtosecond laser excitation on our samples, we conducted out-of-equilibrium ab-initio molecular dynamics (AIMD) simulations. This is not an easy task. The first challenge is to generate an initial chalcogenide configuration, amorphous, that is resembling the experimental sample. The overall process will be only briefly reviewed in the Section II.2 as this step was carried out in advance of this thesis work. The second challenge consists in reproducing an experimental out-of equilibrium state with simulations, so obviously a third hidden challenge is to find a way to compare the results from simulations to compare with the experimental ones.

II.1 DFT in practice

II.1.1 Self-consistency loop

In practice, an actual DFT calculation is done iteratively. For example in the case of the VASP code [232–234] used in this thesis, the global scheme is shown in Figure 2.4.

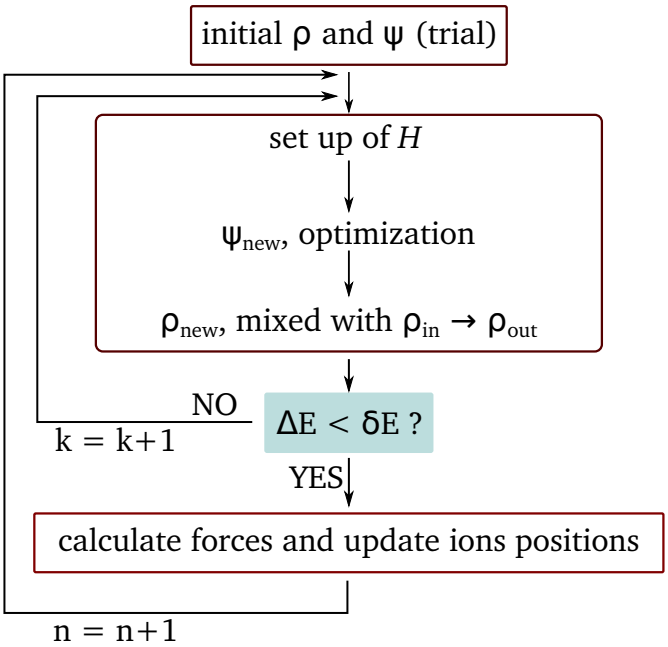

Figure 2.4 – *Schematic representation of DFT in practice. The number of ions iterations steps is denoted by n, the number of electronic steps by k and the difference of energy of the system in the* $k-1$ *and k states by* ΔE*. If* ΔE *is smaller than* δE *(which defines the break condition), then the system is considered to have converged and new properties are calculated. If not, the loop on the electronic part is iterated until the system converges.*

An initial guess for the charge density ρ and the orbitals $\{\psi_n\}$ are assigned to the system. This trial guess is most often consisting of a superposition of atomic charge densities for ρ and random coefficients for the orbitals.
A self-consistency loop for the electrons is then performed using one of the following methods: *blocked Davidson* (DAV) [235], *conjugate gradient* (CG) [236] or *residual minimization* (RMM-DIIS) [237, 238]. The general method is to determine the electronic ground state of the system, which allows to solve the Schrödinger equation and refine the wave function. Then the new density is computed as $\rho = \sum_n f_n|\psi_n|^2$, and refined. The corresponding free energy E of the system (such that $H\psi = E\psi$) is computed and compared to the energy of the system in its trial state. If this ΔE is lesser than a break up condition δE, the system is considered to be convergent and the whole system is resolved. Typically, for the molecular dynamics (MD) trajectories done in this thesis, $\delta E = 10^{-4}$ eV was used while for optical properties calculations as well as density of states, it is refined to 10^{-7} eV. Another MD time step is applied, $n = n + 1$, and the electronic

loop is restarted (k set to zero again). If the system has not converged, *i.e.* $\Delta E \geq \delta E$, then the final charge densities and wave functions at this k iteration step are used as initial trials and the electronic loop is iterated $k = k + 1$ until the break up condition is satisfied.

II.1.2 Pseudo-potentials: frozen core theory

The theory behind pseudo-potentials stems from the striking difference between valence and core electrons. It is a fact that these latter are strongly binded to the nucleus and do not participate in any external chemical bonding. This consideration along with the fact that interactions between core and valence electrons imply difficulties in the calculation (such as rapid oscillations of the wave functions near the ion cores that require a refinement of the method used) lead to the development of pseudo-potentials.

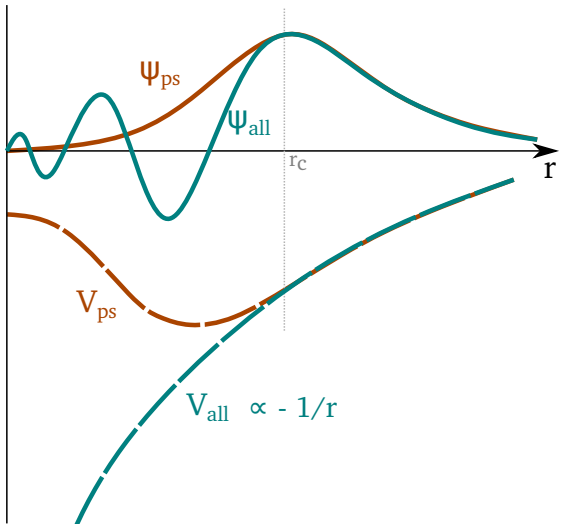

Figure 2.5 – *Schematic representation of the pseudo-potential V_{ps} and pseudo-wave function ψ_{ps} compared to the full potential and wave function V_{all} and ψ_{all} respectively. The radius at which the pseudo-approximation match with the full case is denoted by r_c. Adapted from [239].*

This simplification consists in replacing the exact potential with an effective potential that is still exact towards the valency region, but smoother close to the ion cores as represented in Figure 2.5. The core electrons are considered as part of this frozen core along with the nucleus. The variable r_c, corresponds to the radius at which the pseudo-potential matches exactly the real potential. This variable leads to the definition of the corresponding *cut-off energy* E_{cut}, limiting the plane-wave basis in DFT calculations.

The calculation using pseudo potentials only deals with the valence electrons, which greatly simplifies the problem by reducing considerably the number of variables. Of course, this approximate smoothing needs to be as precise as possible. Two methods of choice are the most used nowadays:

the *norm-conserving* [240] and the *ultrasoft* [241] pseudo-potentials.
For this work projector-augmented waves (PAW) pseudo-potentials were used [242, 243]. It is related to the ultrasoft pseudo-potentials, but are expected to give more accurate results as the full wave functions are reconstructed.

II.2 Generation of the initial amorphous state

As discussed briefly in Chapter 1, the structure of the amorphous phase of the phase-change memory materials has been debated a lot, and simulations, which could have helped getting a better understanding, were not especially the obvious way, in particular for the as-deposited phase, due to the limited computer capabilities. In the case of this work, all the experiments have been performed on the as-deposited phase, which is complicated to reproduce *via* simulations (yet not impossible as shown by Akola *et al.* [112]). In simulations, the melt-quenched method (consisting in heating the material above the melting temperature, then quenching it rapidly enough to prevent crystallisation) is still the easiest.[1]

II.2.1 Amorphous Germanium Telluride

The generation of the *a*-GeTe initial configuration was a two-step process [113].
As previously stated in Chapter 1, as-deposited (AD) amorphous phase of GeTe contains a large amount of Ge atoms in tetrahedra sites compared to the melt-quenched (MQ) one. The samples that were irradiated during the experiments of this thesis were made of as-deposited GeTe, however the usual method to simulate an amorphous phase is the melt-quench method. The issue raised here is the following: one of the main goals in performing the simulations here is to compare the properties obtained with the experimental measurements. However, using the MQ method directly on a GeTe cell would give a wrong ratio of tetrahedra/octahedra (compared to the experimental samples). As discussed in Chapter 1, Section II.2), this difference in local environment leads to differences in properties, preventing an accurate comparison with an experimental AD sample.

STEP 1: In order to obtain a MQ configuration with the closest structure to the experimental sample, the first step consisted in generating a MQ cell, with Te alloyed with an element other than Ge, which would naturally tends to be in tetrahedral environments, even when generated with the MQ method. The Si-Te alloy is such a compound, in which the Si atoms are in a very large amount in tetrahedral environments [113].

For this first step, the melt-quenching of a 216-atoms SiTe alloys was performed using the second

[1]The generation of all initial amorphous phases were performed before-hand of this thesis by J.-Y. Raty from CESAM-Liège University and the detailed process explained here can also be found in the References [47, 113].

generation Car-Parinello scheme [244–246], with a stochastic Langevin thermostat (canonical ensemble). The QUICKSTEP code [247] implemented in the CP2K [246] package was used, such that the basis set for the orbitals was a mix of Gaussian and plane waves (double/triple zeta plus polarisation quality for the Kohn-Sham orbitals in the Gaussian basis and a 300 Ry cut-off for the plane-waves), with GGA-PBE functionals [217, 218]. Scalar-relativistic Goedecker-Teter-Hutter pseudopotentials were used [248]. Calculation was done at the Γ point.[2]
SiTe cell was heated up to 3000 K for 30 ps with a time-step of 2 fs, cooled-down to the melting temperature and then equilibrated during 30 ps. Afterwards, the system was quenched to 300 K in 90 ps and equilibrated again during 30 ps at this temperature. A subsequent quenching to 0 K was performed, followed by a relaxation.

STEP 2: At this point the Si atoms were substituted with Ge atoms. The simulation cells were further annealed at 300/450 K, then quenched again to 0 K and forced to the experimental density of GeTe of 0.0334 $Å^{-3}$.
For this step, van der Waals corrections were added using VdW-DF2 functional [249] for a better accuracy [116] and the PWSCF (plane wave self-consistent field) code from the Quantum Expresso package [250] was used. Perdew-Zunger norm-conserving pseudo-potentials [215] were used with a 34 Ry cutoff energy. Time steps of 3.84 fs with Berendsen thermostat and a relaxation time of 2.7 ps were applied.

Several GeTe cells were generated with this two steps process [113], giving proportions of tetrahedral Ge between 70% to 100%. The configuration whose structure was the most accurate compared the experimental one (structure factor/pair distribution function, concept defined in Section III.3) was chosen to conduct this subsequent thesis work (shown in Figure 2.6).

II.2.2 Ge-Se glasses

$Ge_{72}Se_{168}$ (GS), $Ge_{55}Se_{137}Sb_{48}$ (GSS) and $Ge_{55}Se_{127}Sb_{46}N_{12}$ (GSSN) glasses were obtained using the VASP code [232–234] with GGA-PBE exchange-correlation functionals [217, 218] and PAW pseudo-potentials [242, 243]. A melt-quenched process was also used here: each 240-atoms cell was heated up to 3000 K, equilibrated for 30 ps, then cooled down to 1000 K for 30 ps, and finally quenched to 300 K in 100 ps. A Nosé-Hoover thermostat and time step of 1 fs (GSSN) and 3 fs (GS, GSS) were used for the MD trajectories. The density of the cell were constrained to the experimental ones: 0.0324 $Å^{-3}$ for GS , 0.0344 $Å^{-3}$ for GSS and 0.0361 $Å^{-3}$ for GSSN. The three initial states are shown in Figure 2.6.

[2]The concept of the Γ point used for amorphous states in simulations is explicited in Appendix A

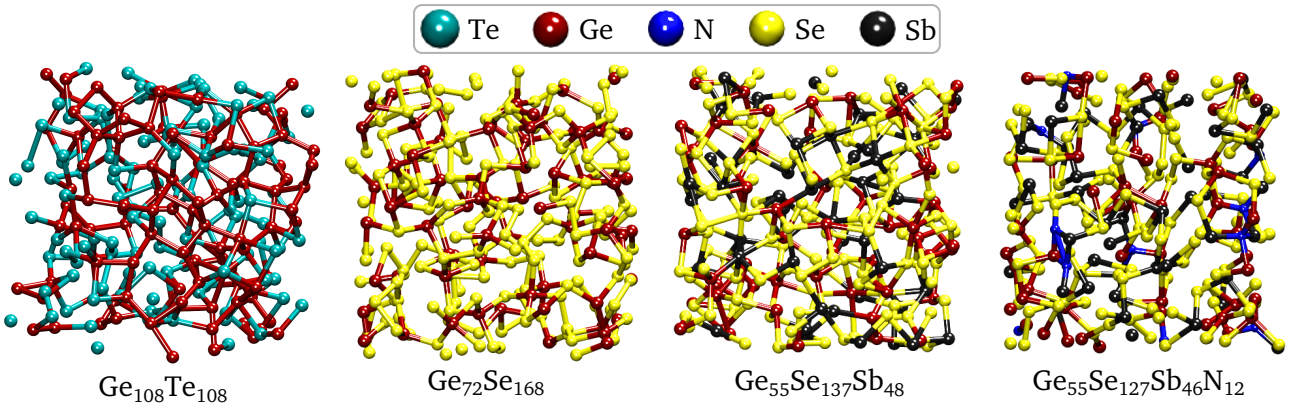

Figure 2.6 – *Simulated configurations of the four chalcogenides in their non-excited states.*

II.3 Modeling a laser excitation

The next step once the initial configurations are generated was to be able to reproduce the excitation induced by a fs-laser.

II.3.1 Transitions induced by femtosecond laser

The excitation of a semiconductor with an ultrashort laser ($\lesssim 10^{-12}$ s) results in transitions that consist in several simultaneous and crossed phenomena (see Chapter 1). The energy is not directly absorbed by the ions: the carriers (electrons/holes) from the valence band (VB) are the ones that absorb the incoming energy (or at least part of it) and get promoted to the conduction band (CB). After some time (on the picosecond timescale), the system thermalizes *via* electron-phonon interaction. However in the meantime, the lattice is still cold whereas electrons are highly excited, resulting in an out-of-equilibrium situation.

One of the methods of choice to reproduce this kind of transition's triggering with simulations nowadays is the two-temperature model [59] evoked in Chapter 1, Section I.1. While it is well-suited for metals, its application to semiconductors can be tricky due to the fact that some of the required parameters, such as the electron-phonon coupling, have never been measured for our systems of interest in out-of-equilibrium conditions.
Another popular technique is to promote a given amount of electrons from the valence band to the conduction band [251–253], following the idea photo-absorption induced by fs pulses. As will be detailed right after, this latter method is the one used here.

II.3.2 Out-of-equilibrium simulations

The excitation induced by our 30-fs laser pump was reproduced in simulations by applying a Fermi-Dirac distribution to the electrons [254], explicited in Equation 2.42 with ϵ the energy, μ

the chemical potential and σ the smearing of the distribution. This latter can in fact be assimilated to the electronic temperature T_e such that $\boxed{\sigma \sim T_e}$. This process of excitation, depicted in the Figure 2.7 depopulates the top of the valence band to populated the bottom of the valence band.

$$f\left(\frac{\epsilon-\mu}{\sigma}\right) = \frac{1}{1+e^{\frac{\epsilon-\mu}{\sigma}}} \tag{2.42}$$

This distribution was forced on the electron for a given pair of ionic and electronic temperatures (T_i and T_e respectively) that are fixed during the whole corresponding MD trajectory, and we let the system equilibrate with those given parameters during 30 to 40 ps of molecular dynamics (MD). These MD trajectories were simulated using the VASP code [232–234], with GGA-PBE functionals [217,218], PAW pseudo-potentials [242,243], in the canonical ensemble (NVT) with a Nosé thermostat. Calculations were done at the Γ point. The specific parameters for each material are specified in the following Table 2.1. By convention, the ionic lattice temperature is given in K while the electronic temperature is in eV.

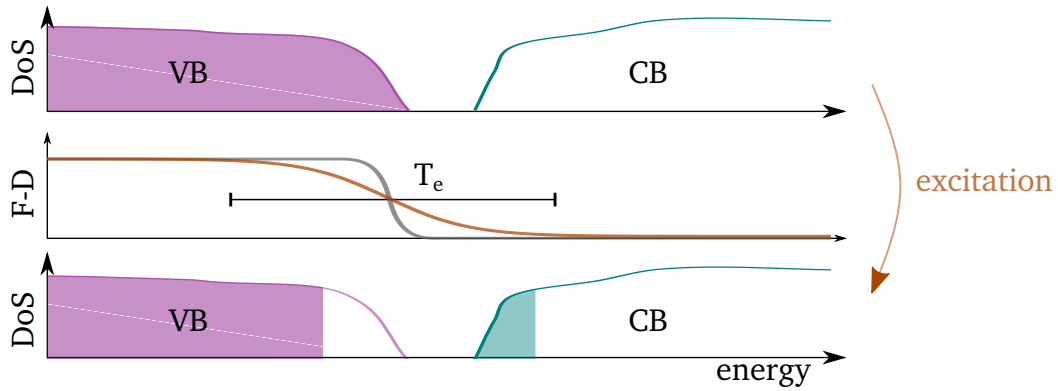

Figure 2.7 – *Schematic representation of the evolution of the density of states under simulated excitation. At first, the valence band (VB) is completely filled with electrons while the conduction band (CB) is completely empty. The electronic distribution can be modeled by a Fermi-Dirac function (F-D) with a sharp step. The excitation is then applied via the widening of the F-D distribution, such that a certain proportion of the VB is depopulated and transferred to the VB.*

II.4 Comparison with the experiments

An important point was to find a way to compare the information obtained *via* simulations with those extracted from experimental measurements. The solution here was to consider the short times after excitation. As the electron-lattice coupling is estimated to be about 1 ∼ 5 ps [45,51] from measurements done in similar phase-change materials, it seems relevant to compare the dielectric function (which is expected to have an ultrafast response [45,60]) obtained experimentally for pump-probe delays lesser than 800 fs with simulations at 300 K.
As the lattice should still be cold, any measurement variation should not be due to thermal effects,

Material	nb of pairs	T_e range	T_i range	E_{cut}	MD time step
GeTe	48	0.001 - 1.0 eV	300 - 1100 K	175 eV	3 fs
GS	6	0.001 - 1.2 eV	300 - 1200 K	212 eV	3 fs
GSS	6	0.001 - 1.0 eV	300 - 900 K	212 eV	3 fs
GSSN	5	0.001 - 0.9 eV	300 - 1200 K	400 eV	1 fs

Table 2.1 – *Parameters used for the out-of-equilibrium simulations: overall number of (T_e, T_i) pairs, ranges of electronic and ionic temperature, cut-off energies for the plane waves and time step for the molecular dynamics trajectories.*

but to electronic contribution. Therefore, finding a simulation (T_e, T_i = 300 K) that matches this variation should give the electronic temperature T_e that corresponds to the laser excitation.

Practically, in order to prevent or at least to diminish the GGA miscalculation of the bandgap, relative variation of the dielectric function was compared instead of absolute quantities:

$$\left.\frac{\Delta\varepsilon^{SIMU}}{\varepsilon_0^{SIMU}} \overset{T_e?}{\longleftrightarrow} \frac{\Delta\varepsilon^{EXP}}{\varepsilon_0^{EXP}}\right|_{t<800fs} \tag{2.43}$$

More precisely,

$$\begin{cases} \Delta\varepsilon^{SIMU} = \varepsilon_0^{SIMU} - \varepsilon^{SIMU}(T_e, T_i = 300K) & \text{with } \varepsilon_0^{SIMU} = \varepsilon^{SIMU}(T_e = 0.001eV, T_i = 300K) \\ \Delta\varepsilon^{EXP} = \varepsilon_0^{EXP} - \varepsilon^{EXP}(t) & \text{with } \varepsilon_0^{EXP} = \varepsilon^{EXP}(t \leq 0) \end{cases}$$

Equation 2.44 highlights the main interest of the approach which is to find the most appropriate electronic temperature T_e that enables to link experiments and simulations:

$$\left.\frac{\varepsilon_0^{SIMU} - \varepsilon^{SIMU}(T_e, 300K)}{\varepsilon_0^{SIMU}} \overset{T_e?}{\longleftrightarrow} \frac{\varepsilon_0^{EXP} - \varepsilon^{EXP}(t)}{\varepsilon_0^{EXP}}\right|_{t<800fs} \tag{2.44}$$

III Structural analysis

Ab initio simulations produce a considerable amount of outputs. In Chapter 1, we have seen that one consensual point regarding the excitation/transition of chalcogenides is the local scale on which it happens. Therefore, it is of primary importance to understand the structure of the simulated configurations, both on an atomic and electronic point of view. Several tools are helpful, such as the pair distribution function or the density of states. The different methods used to obtain the results of the following Chapter 4 and 5 are described hereafter.

III.1 Dielectric function

For each equilibrated configuration, the corresponding *frequency dependant dielectric function* $\varepsilon(\omega)$ of the cell can be calculated using again the V.A.S.P. code.

The number of bands for the calculation needs to be increased compared to the self-consistent calculation of MD trajectory. This is due to the method used. Each component of the dielectric function tensor is obtained first by calculation of the imaginary part via a sum on the valence and conduction band states [255]:

$$\varepsilon^{i}_{\alpha,\beta}(\omega) = \frac{4\pi^2 e^2}{\Omega} \lim_{q\to 0} \frac{1}{q^2} \sum_{c,v,\boldsymbol{k}} 2w_{\boldsymbol{k}} \delta(\varepsilon_{c,\boldsymbol{k}} - \varepsilon_{v,\boldsymbol{k}} - \omega) \times \langle u_{c\boldsymbol{k}+\boldsymbol{e}_\alpha q} | u_{v\boldsymbol{k}} \rangle \langle u_{v\boldsymbol{k}} | u_{c\boldsymbol{k}+\boldsymbol{e}_\beta q} \rangle \tag{2.45}$$

Where the different parameters denote: Ω the volume of the primitive cell, c and v conduction and valence bands respectively, α and β the cartesian components, e_α the unit vectors for the α direction, $w_{\boldsymbol{k}}$ the weight of the corresponding k-point, ω the frequency and $|u_{n\boldsymbol{k}}\rangle$ the cell periodic part of the orbitals at the k-point.
The real part of the dielectric function is retrieved thanks to the Kramers-Kronig transformation, with P the principal value [255]:

$$\varepsilon^{r}_{\alpha,\beta}(\omega) = 1 + \frac{2}{\pi} P \int_0^\infty \frac{\varepsilon^{i}_{\alpha,\beta}(\omega')\omega'}{\omega'^2 - \omega^2} d\omega' \tag{2.46}$$

All our materials being isotropic, the dielectric function is averaged on the x, y, z directions and using N=4 different configurations to improve the statistical precision on the calculation.

$$\varepsilon = \langle \varepsilon_x + \varepsilon_y + \varepsilon_z \rangle_{[t_1,t_2,..t_N]} \tag{2.47}$$

III.2 Density of states

The *density of states* (DOS) was calculated with a grid of 2×2×2 k-points using VASP with the same aforementioned functionals. The weighted histogram of the resulting Kohn-Sham eigenvalues for all k-points allows to retrieve the corresponding DOS. As we used the GGA-PBE, an underestimated bandgap is expected. Hybrid functionals could have improved this issue, but as we computed a lot of (T_e, T_i) pairs, a qualitative rather than quantitative analysis was preferred here.

III.3 Pair distribution function

The *pair distribution function* (PDF), also denoted $g(r)$, gives an indication on the degree of structuration and bond lengths in a material. The function $g_{AB}(r)$ corresponds to the probability to find an atom of type B at a distance r of an atom of type A. The PDF was calculated using the R.I.N.G.S code [256] according to the formula 2.48, with N the number of particles in the cell, V the volume of the cell and $\boldsymbol{r}$ the positions of the atoms.

$$\begin{aligned} g(r) &= \frac{V}{N^2} \sum_{i}^{N} \sum_{j}^{N} \langle \delta \left(\boldsymbol{r} + |\boldsymbol{r}_j - \boldsymbol{r}_i| \right) \rangle \\ g_{A,B}(r) &= \frac{V}{N_A\, N_B} \sum_{i}^{N_A} \sum_{j}^{N_B} \langle \delta \left(\boldsymbol{r} + |\boldsymbol{r}_j - \boldsymbol{r}_i| \right) \rangle \end{aligned} \tag{2.48}$$

As schematically represented in Figure 2.8, the position of the main peak of the distribution corresponds to the most probable bond length r_{max} for a certain type of bonding. We use the position of the first minimum of the total PDF, r_{cut}, to determine the first-neighbouring shell limit.

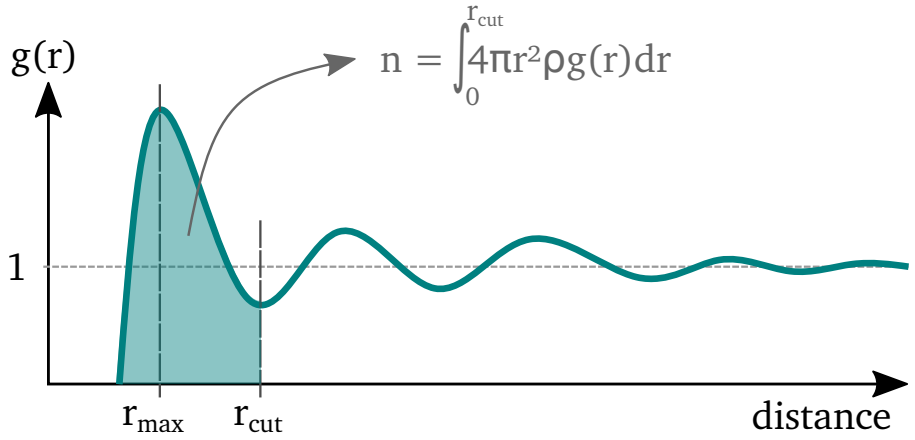

Figure 2.8 – *Schematic pair distribution function* $g(r)$.

III.4 Coordination numbers

The *coordination number* (CN) of each atom can be determined from the PDF. The integration of the PDF up to the cut-off radius r_{cut} (colored area in Figure 2.8) gives the number of atoms in this first neighbouring shell, *i.e.* its number of closest neighbours. As it is computed for a specific type of bond $A-B$, the CN of a given species A is obtained as followed:

$$n_A = \sum_{B} n_{A-B} \tag{2.49}$$

$$n_{A-B} = \int_0^{r_{cut}} \rho g_{AB}(r) 4\pi r^2 dr \tag{2.50}$$

III.5 Angular distribution

As we saw in Chapter 1, the local structure of the atoms is very important in chalcogenides. However, it is not sufficient to compute the bond lengths and the coordination numbers. An efficient way to complement these two types of data is the *distribution of angles*.

As represented in Figure 2.9, the distribution of angles requires first to know the averaged number of neighbours for a given species, *i.e.* first of all, the pair distribution function is used to determine a cut-off radius r_{cut}. This specific radius characterizes the first neighbouring shell of an atom. The mean number of neighbours within this radius, N_v, is then calculated. Only the N_v closest neighbours will be taken into account in the following calculation of the distribution of angles. For each atom of a given species, we consider the $N_v(N_v - 1)/2$ angles that exist between the N_v neighbours. A normalized histogram for each type of atoms is then built over the whole cell. The local maxima of the distribution correspond to the most probable angles for a given species.

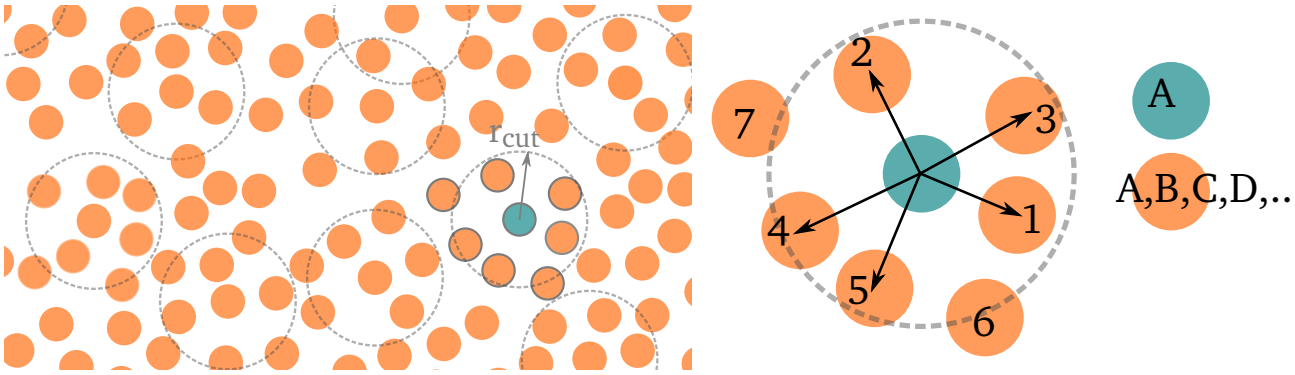

Figure 2.9 – *Schematic representation of the angles calculation. Determined from the pair distribution function, r_{cut} allows to determine the coordination number n of a certain species (in blue), which represents the mean number of neighbours of this species in the simulation box. Then the n closest neighbours of each atom of this given species are considered and all the angles of this configuration are calculated.*
For instance, we consider here the species A. Let's hypothesize that the $g(r)$ gave $n = 5$. On the right, on atom of species A in blue is given as an example. Its 5 closest neighbours are then considered and all the angles that constitute this local environment are calculated (1A2, 1A3, 1A4, 1A5, 2A3, 2A4, 2A5, 3A4, 3A5, 4A5).

III.6 Angular-limited three-body correlation (ALTBC)

Phase-change materials are subject to the Peierls distortion (see Section II.1), consisting in an alternation of aligned short and long bonds. Though this phenomena was observed only in the crystalline phase at first, its reentrance in the liquid phase was shown with the help of *angular-limited three-body correlation* (ALTBC) [72, 131, 257].

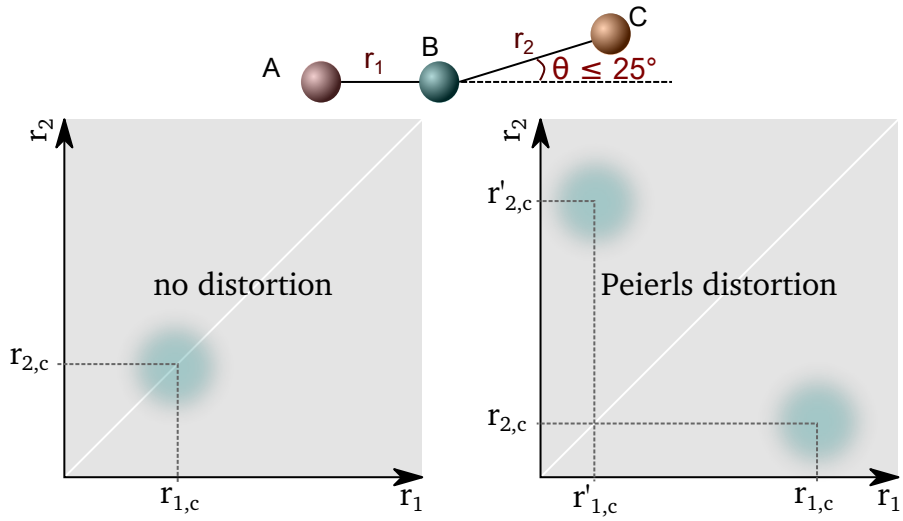

Figure 2.10 – *Top: Representation of two successives bonds between the atoms A, B and C. For an ALTBC calculation, the angle θ limits which (r_1, r_2) pairs are taken into account. Bottom: example of two ALTBC maps. On the left, a situation without Peierls distortion with a peak located on the diagonal. On the right, the Peierls distortion induces an alternation of short and long bonds that shows in the form of two maxima located off the diagonal.*

Considering two successive bonds r_1 and r_2 as in Figure 2.10 between the atoms A, B, and C, the correlation between r_1 and r_2 is calculated only if they are almost close to alignment. This latter condition is satisfied by limiting the cone angle θ to be $\lesssim 25$ °for r_1 and r_2 to be taken into account in the calculation.
The correlation map of r_1 *vs* r_2 reflects the degree of distortion of the structure: if the maximum is off the diagonal, the material possesses a certain degree of distortion while if it is located on it, we expect none.

III.7 Mean square displacement

The *mean square displacement* (MSD) basically gives information about diffusion of the atoms as a function of time. Analyzing the behaviour of this diffusion as a function of temperature reveals interesting properties about the material considered. Indeed, thermal heating implies an increase of kinetic energy, which shows in the MSD curve as will be briefly explained hereafter.
Here, the MSD of the atoms in the cell is calculated using the R.I.N.G.S code [256]. The MSD is

defined as follows, with $\boldsymbol{r_{cm}}$ the position of the center of mass of the cell, A being the species of interest:

$$MSD_A(t) = \left\langle |r_i(t) - r_i(t=0) - [r_{cm}(t) - r_{cm}(t=0)]|^2 \right\rangle_{N_A} \tag{2.51}$$

The calculation is averaged over the N_A atoms of species A in the cell, however that is not quite enough to get a good statistics as our cells contains "only" 240 atoms at maximum.
To circumvent this issue, the Markovian nature of the molecular dynamics trajectory is considered here. Each step being independent of the previous one, the trajectory can be split into n_k sub-trajectories of duration t_k. The MSD is then obtained by varying t_k between 0 and the full trajectory duration $n_k t_k$, yielding the following numerical formula:

$$MSD_A(t_k) = \left\langle \frac{1}{n-k+1} \sum_{j}^{n-k} \left(x_{j+k} - x_j\right)^2 \right\rangle_{N_A} \tag{2.52}$$

The valuable information here is how this MSD evolves with time. Three types of behaviour are encountered (see Figure 2.11). In all cases, for very short times, the MSD has a *ballistic* behaviour. Then depending on the system's temperature T, the rest of the MSD will adopt a different behaviour.

- In a solid, the atom will not move much, the MSD saturates and is trapped in a *caged* behaviour. Indeed, the kinetic energy of the atoms is not sufficient to be in a diffusive regime. If the temperature of the atoms is raised slightly, the system may escape of this regime to get into a *diffusive* regime.
- In the case of a liquid, the temperature is high enough to prevent the caged behaviour, leading to the diffusive regime almost immediately after the ballistic one.

The diffusive regime is characterized by a linear relationship between the MSD and the time t. The diffusion coefficient D links the both of them, with the Equation 2.53, with d the number of dimensions of the system.

$$D = \lim_{t\to\infty} \frac{1}{2d\ t} MSD(t) \overset{3D}{\Rightarrow} D = \lim_{t\to\infty} \frac{1}{6t} MSD(t) \tag{2.53}$$

III.8 Vibrational density of states

The *vibrational density of states* (VDOS) gives the phonon density of states. This information is often analyzed in the case of non-thermal transitions, as this latter induces a bond hardening in metals and softening in semiconductors [86, 88, 259–261] The calculation can be done in two ways: considering the mass-weighted sum of *velocity spectral density* or by the Fourier transform of

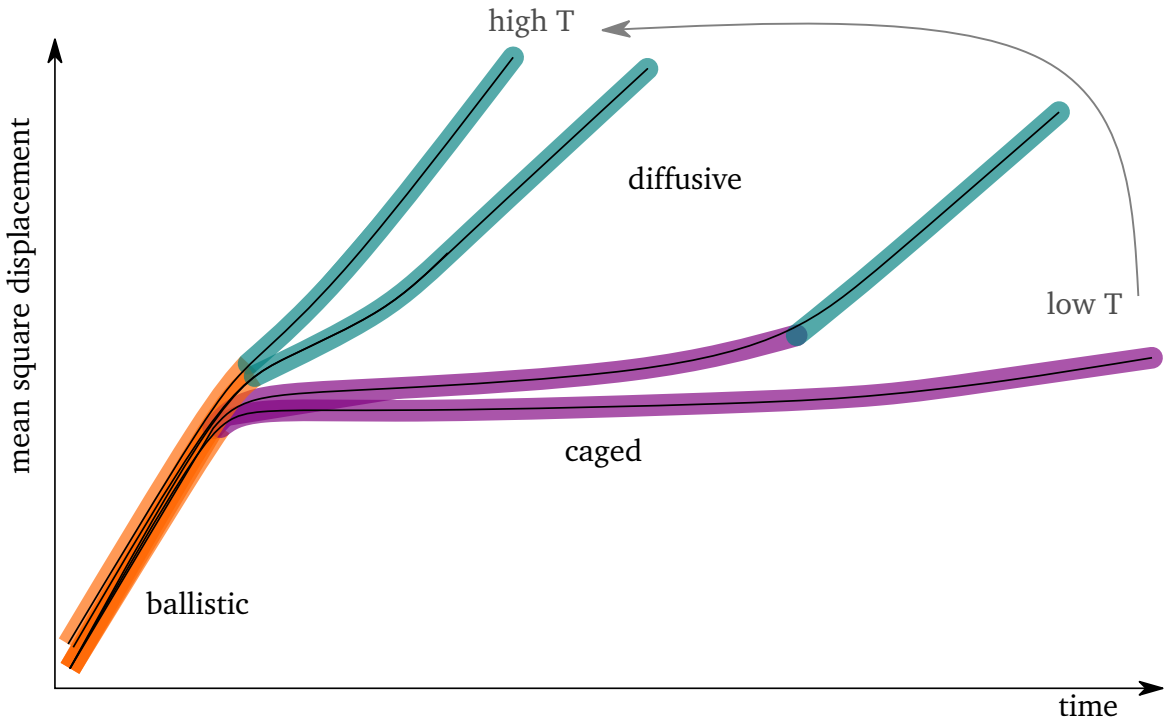

Figure 2.11 – *Schematic representation of the three different behaviours that can be adopted by a MSD, adapted from Reference [258]. At short times, the MSD is ballistic in all cases. Then, if the temperature is sufficient, it adopts a diffusive character on the long term or a caged one if the temperature is low.*

the *velocity autocorrelation function* [262]. It is the second method, implemented in the *nMOLDYN* code that was used in this thesis [263].

$$VDOS(n\,\Delta\nu) = \sum_{\alpha} \omega_{\alpha}\,\frac{1}{3}\,\langle \boldsymbol{v}_{\alpha}(t_0)\cdot\boldsymbol{v}_{\alpha}(t_0+t)\rangle \tag{2.54}$$

With $n = 0, \ldots N_t - 1$, N_t the total number of time steps, $\Delta\nu = 1/2N_t\Delta t$ the frequency, and ω the radial frequency. The VDOS spectra were normalized to unity.

CHAPTER 3

FREQUENCY-DOMAIN INTERFEROMETRY

As seen in the state of the art in Chapter 1, the response of chalcogenide phase change memory materials and glasses to voltage or laser pulses occurs on a very short timescale. For instance, Waldecker *et al.* [45] as well as Miller *et al.* [60] measured an ultrafast change in dielectric properties on a sub-picosecond timescale after femtosecond (fs) laser pulses excitation. Therefore, we need a technique that will enable to follow the effects of a fs-laser irradiation with an adequate temporal resolution: on the order of the femtosecond. Chalcogenides are particularly well-suited for optical techniques as they exhibit a contrast of resistivity of several orders of magnitude between their crystalline and amorphous phases.

Frequency-domain interferometry (FDI) is a technique that was developed by Geindre *et al.* in 1994 [264]. With the initial intent of plasma expansion diagnosis, it was used in the same purpose in numerous studies [65, 265–267]. It is indeed a powerful tool, which gives access to some of the characteristics of plasma propagation, such as its velocity, from the measurement of the phase shift induced by excitation. The development of the *time and space resolved interferometry* (TASRI) method even enabled to have a deeper analysis, with not only temporal, but also spatial information [268]. While most FDI studies rely on the use of a monochromatic laser beam, TASRI exploits the properties of linear chirped pulse. As frequency can be encoded with time on the CCD camera, more information can be obtained from a single acquisition.

But FDI is not limited to plasma-related studies. As it will be presented in this chapter, FDI is an optical technique that allows us, not only to get information with a sub-picosecond timescale on the material's response, but also enables a time-resolved analysis of the nature of the surface and of the dielectric properties, thanks to both the measurement of phase and reflectivity variations. The first section of this chapter will explain the principle of FDI. Then, the second part will show

how to retrieve the surface dynamics and dielectric properties from a typical spectrum. Finally, the third section will detail the experimental set-up used for this thesis work.

I Frequency-domain interferometry principle

The frequency-domain interferometry technique belongs to the broad family of the pump-probe experiments. Usually, these kinds of experiments consist in triggering a process by impingement of a first laser pulse, called the *pump* ; then a second laser pulse of low energy, the *probe*, is used to determine the resulting effects of excitation on the material's properties. As the delay between the pump and the probe is varied, the movie of the material's evolution is obtained. As far as the FDI technique is concerned, the aim is the same, but the implementation is slightly different: it is not only one, but two probe pulses that are used. These two probe pulses have a fixed delay δt and only the delay Δt between the pump and the second probe is varied. The interference of the two probe pulses is analyzed and the reflectivity can be deduced from the generated pattern.

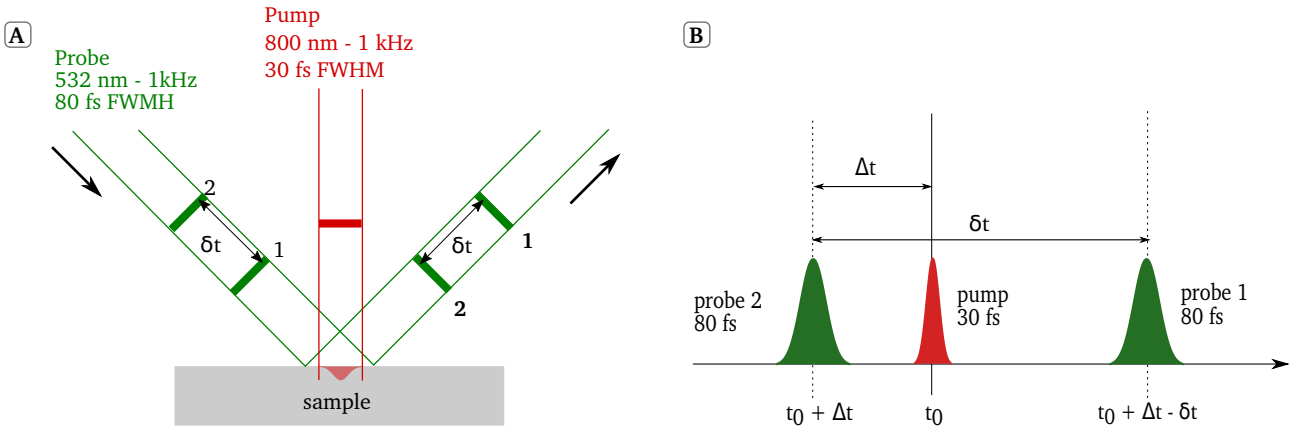

Figure 3.1 – *Spatial scheme of the FDI principle with the pump and probe characteristics used in this study (A). Temporal scheme of the FDI (B). The (fixed) delay between the two probe pulses is denoted by δt while the delay between the pump and the second probe is denoted by Δt.*

A spatial and a temporal schemes of the FDI technique are presented in Figure 3.1. A first probe pulse with a wavelength of 532 nm, 80 fs duration FWHM is reflected onto the pristine material. Then a pump pulse at 800 nm, with a duration of 26 fs deposits energy. Finally, the second probe pulse is reflected, but this time on the excited sample, with a delay $\delta t = 8.7$ ps after the first one. Afterwards, the interference pattern of the two probe pulses is collected and analyzed in order to deduce information about the excited material's surface dynamics and dielectric properties. The acquisition of interference pattern with a varying delay Δt after the pump excitation allows to follow the evolution of the sample's properties. The following subsections will detail how to retrieve these properties from the interferogram of each delay.

I.1 Interferogram

We consider the general case of two pulses, identical apart from their temporal component: they are separated by a delay δt. $E_1(r,t)$ and $E_2(r,t)$, the electric fields of the first and second pulse respectively, are defined as per the Equations 3.1, with E_0 the amplitude of the laser, ω_0 its central radial frequency, $\vec{k}$ its wavevector and ϕ_0 the absolute phase of the pulse. Each electric field is the modulation of a plane wave with a gaussian enveloppe. The resulting electric field $E(r,t)$ of the two probe pulses is simply equal to the sum of E_1 and E_2.

$$\begin{cases} E_1(r,t) = E_0(t)e^{-i\left(\omega_0 t - \vec{k}\cdot\vec{r} + \phi_0\right)} \\ E_2(r,t) = E_0(t-\delta t)e^{-i\left(\omega_0 (t-\delta t) - \vec{k}\cdot\vec{r} + \phi_0\right)} \end{cases} \tag{3.1}$$

When reflected on a material, the electric field is modified due to its specific reflectivity. We consider $R = r \cdot e^{i\phi}$ the reflectivity of the sample, with the indexes 1 and 2 corresponding to the state of the sample when the first and the second probe pulses are reflected respectively. At the entrance slit of the spectrometer, the resulting electric field $E'(r,t)$ can be expressed as such:

$$E'(r,t) = R_1 \cdot E_1(r,t) + R_2 \cdot E_2(r,t) \tag{3.2}$$

It should be noted that even though the temporal dependency of R has not been highlighted here, it is implicit. It is actually the aim of time-resolved FDI to measure this evolution after a triggering process.

The spectrometer comprises a diffraction grating, which stretches temporally both pulses and enable their interference. Indeed, a grating is an array of slits spaced by a distance a, characteristic of a given grating. When the light interacts with the grating, each slit will diffract the incoming beam, causing destructive or constructive interferences. In fact, in order to have constructive interferences, the incident and resulting diffracting beam must follow the condition 3.3, with θ_i the angle of incident on the grating, θ_m the angle of deviation for the diffraction order m and λ the wavelength of the light.

$$a\,(sin\ \theta_m - sin\ \theta_i) = m\lambda \tag{3.3}$$

As the spatial components are identical for both pulses, and independent from their temporal counterparts, we only consider the temporal component of the electric fields in the following calculation. The signal collected on the CCD camera is the spectral intensity $I(\omega)$ whose expression is related to the Fourier transform of the electric field $\tilde{E}'(\omega)$ as follows:

$$\tilde{I}(\omega) = \left|\tilde{E}'(\omega)\right|^2 \tag{3.4}$$

The Fourier transforms are defined as follows:

$$\begin{aligned} \tilde{A}(\omega) &= \int_{-\infty}^{+\infty} A(t) e^{i\omega t} dt \\ A(t) &= \frac{1}{2\pi} \int_{-\infty}^{+\infty} \tilde{A}(\omega) e^{-i\omega t} d\omega \end{aligned} \tag{3.5}$$

Using these conventions, the Fourier transform of $E'(t)$, is given by:

$$\tilde{E'}(\omega) = \left[R_1 + R_2 e^{-i\omega\delta t} \right] \tilde{E_0}\left(\omega + \omega_0\right) e^{i\phi_0} \tag{3.6}$$

The signal on the camera is then simply deduced from the following steps of calculation, with the definition of $\tilde{I_0}\left(\omega + \omega_0\right) = \left|\tilde{E_0}(\omega + \omega_0)\right|^2$ and the relative phase shift $\Delta\phi = \phi_2 - \phi_1$:

$$\begin{aligned} \tilde{I}(\omega) &= \tilde{E'}(\omega)\tilde{E'^*}(\omega) \\ &= \left|\tilde{E_0}(\omega + \omega_0)\right|^2 [r_1^2 + r_1 r_2 e^{i(\phi_1 - \phi_2)} e^{i\omega\delta t} + r_1 r_2 e^{i(\phi_2 - \phi_1)} e^{-i\omega\delta t} + r_2^2] \\ &= \tilde{I_0}\left(\omega + \omega_0\right) [r_1^2 + r_1 r_2 e^{-i\Delta\phi} e^{i\omega\delta t} + r_1 r_2 e^{i\Delta\phi} e^{-i\omega\delta t} + r_2^2] \\ \boxed{\tilde{I}(\omega) &= \tilde{I_0}\left(\omega + \omega_0\right) \left[r_1^2 + r_2^2 + 2 r_1 r_2 cos\left(\omega\delta t - \Delta\phi\right)\right]} \end{aligned} \tag{3.7}$$

This boxed expression shows the mathematical origin of the interference we observe: the spectrum results from a gaussian centered on -ω_0 modulated by a cosinus. The interfringe is $2\pi/\delta t$; it depends explicitly on the delay between the two pulses.

To analyze the implications of this equation, we consider now our FDI experiment. For each pump-probe delay, we acquire two spectra: a *reference* spectrum and a *pump* spectrum.

Reference case: In a *reference* case, the pump is off. The material will be still in its initial (pristine) state, of amplitude reflectivity R_i, when both probe pulses will be reflected. Therefore $R_1 = R_2 = R_i$. The corresponding spectral intensity I_{ref} collected on the CCD camera is given by the Equation 3.8: the relative phase shift $\Delta\phi$ cancels out and the reflectivity modulus becomes a factor of amplitude.
As can be seen on the simulated spectrum in Figure 3.2 (left), the fringes are straight.

$$\tilde{I}_{ref}(\omega) = 2 r_i^2 \cdot \tilde{I_0}\left(\omega + \omega_0\right) \left[1 + cos\left(\omega\delta t\right)\right] \tag{3.8}$$

Pump case: Now we allow the pump to deposit energy in the sample between the two probe pulses reflections, this is a *pump* case. The material is in the pristine state when the first probe pulse is reflected, so $R_1 = R_i$, but that is not the case for the second probe. As the material as been

excited in the meantime, its reflectivity has changed. We declare R_x the amplitude reflectivity of the excited sample when the second probe pulse is reflected upon it. The Equation 3.9 gives the spectral intensity in the pump-on case with the updated indices.

$$\tilde{I}_{pump}(\omega) = \tilde{I}_0(\omega + \omega_0)\left[r_i^2 + r_x^2 + 2r_i r_x cos(\omega\delta t - \Delta\phi)\right] \tag{3.9}$$

This time, we see in Figure 3.2 (right) that this aspect is totally different from the reference case. If we analyze the impact of each term separately, the phase shift $\Delta\phi = \phi_x - \phi_i \neq 0$ induces a shift of the fringes and the variation of reflectivity modulus implies a decrease in visibility.

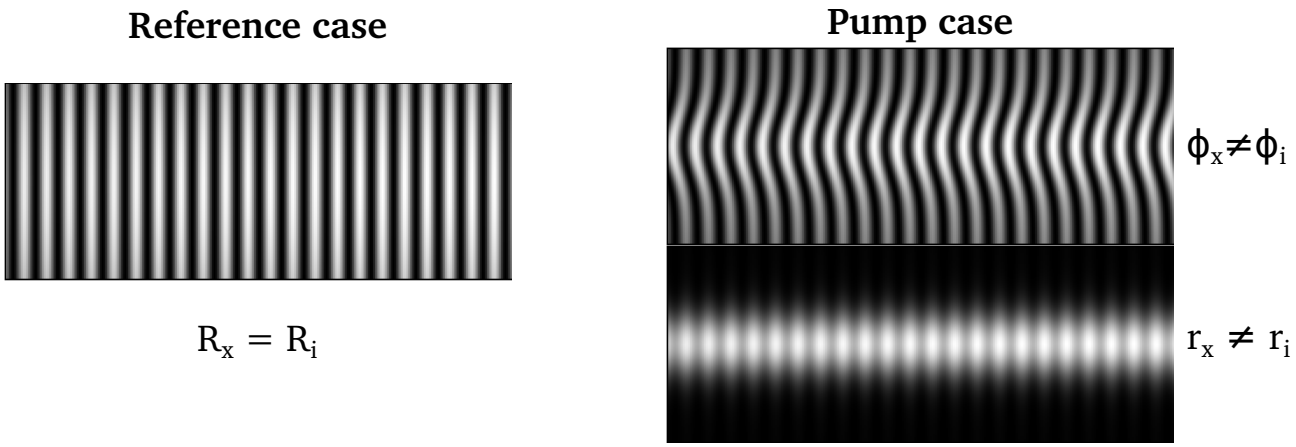

Figure 3.2 – *Simulated interference spectra. On the left side: a reference case, where the amplitude reflectivity is not modified between the reflection of both pulses. This case is characterized by straight fringes with great visibility. On the right side: a pump case. The amplitude reflectivity encountered by the second pulse is not the same as the first one. If we decompose the effect from the modulus and phase, we see that a phase shift induces a shift of the fringes while the modification of modulus implies a decrease in visibility.*

	Reference case	*Pump* case
Reflectivity	$r_1 = r_2 = r_i$	$r_1 = r_i$ $\neq$ $r_2 = r_x$
Phase	$\phi_1 = \phi_2 = \phi_i$	$\phi_1 = \phi_i$ $\neq$ $\phi_2 = \phi_x$

Table 3.1 – *Overview of the reflectivity and phase parameters for the pump and reference cases. The index i corresponds to the initial state of the material while x denotes an excited state.*

I.2 Relative phase and modulus of R

The reflectivities involved in the Equations 3.8 and 3.9 cannot be extracted directly from the raw reference and pump spectra. The images are treated using filters and Fourier transforms to retrieve them.

The first step is to Fourier transform the spectral intensity $\tilde{I}(\omega)$ of each pulse to get $I(t)$. As in the first part of the previous subsection, we consider the general case first, which gives the following expression:

$$I(t) = I_0(t)\left[r_2^2 + r_1^2\right]\underbrace{\boxed{e^{-i\omega_0 t}}}_{t=0 \text{ peak}} + I_0(t+\delta t)r_1 r_2 e^{-i\Delta\phi}\underbrace{\boxed{e^{-i\omega_0(t+\delta t)}}}_{t=-\delta t \text{ peak}} + I_0(t-\delta t)r_1 r_2 e^{i\Delta\phi}\underbrace{\boxed{e^{-i\omega_0(t-\delta t)}}}_{t=+\delta t \text{ peak}} \tag{3.10}$$

This signal contains one dirac peak centered on $t = 0$, which will not give information about the phase shift as $\Delta\phi = \phi_2 - \phi_1 = 0$ for this term. On the contrary, the two other terms: two symmetrical gaussians centered on $t = +\delta t$ and $-\delta t$, contain the information in duplicate.
A gaussian filter that keeps only the positive frequencies of the signal is applied on the signal. Following the previous reasoning, keeping the positive or negative ones gives the same results, as long as the terms are correctly identified with Equation 3.10 (otherwise the sign of $\Delta\phi$ might be incorretly determined). The resulting Fourier transform of filtered intensity $\tilde{I}^F(\omega)$ is expressed as such:

$$\boxed{\tilde{I}^F(\omega) = r_1 r_2 e^{i\Delta\phi} e^{-i\omega\delta t} I_0\left(\omega + \omega_0\right)} \tag{3.11}$$

The Equation 3.12 regroups the two expression adapted to the reference and pump cases that we encounter in our experiment.

$$\begin{cases} \tilde{I}^F_{ref}(\omega) = r_i^2 e^{-i\omega\delta t} I_0\left(\omega + \omega_0\right) \\ \tilde{I}^F_{pump}(\omega) = r_i r_x e^{i\Delta\phi} e^{-i\omega\delta t} I_0\left(\omega + \omega_0\right) \end{cases} \tag{3.12}$$

The relative variation of reflectivity $\Delta R = \Delta r e^{i\Delta\phi}$ of one pulse compared to the other is extracted by comparing those two expressions. The only condition is then to acquire a reference and a pump measurement for a same pump-probe delay Δt.

$$\Delta R = \frac{\tilde{I}^F_{pump}}{\tilde{I}^F_{ref}} \Rightarrow \boxed{\Delta R = \frac{r_x}{r_i} e^{i(\phi_x - \phi_i)}} \tag{3.13}$$

I.3 Retrieving the absolute reflectivities

We have deduced ΔR the variation of amplitude reflectivity. Yet, we seek the absolute amplitude reflectivity of the excited material R_x. In order to do that, there is no other choice than to resort

to ellipsometry measurement done on the pristine material right after its elaboration at the LETI facility in Grenoble. This measurement gives the dielectric function of the initial state, from which the reflectivity R_i can be computed.
As $\Delta R = R_x/R_i$, we deduce $R_x = R_i \cdot \Delta R$, from which the modulus and phase are identified as follows:

$$\boxed{\begin{aligned} r_x &= r_i \cdot \Delta r \\ \phi_x &= \phi_i + \Delta\phi \end{aligned}} \tag{3.14}$$

Though we will see later on that it is not always as straightforward..
For the rest of this manuscript, we will refer to the value measured by FDI as $R = re^{i\phi}$ instead of $\Delta R = \Delta r e^{i\Delta\phi}$ for a lighter writing.

II Surface dynamics & dielectric properties

Up to now, the relative change of reflectivity R has been deduced from the ratio of $\tilde{I}_{pump}$ and $\tilde{I}_{ref}$. From this, the aim is now to analyze the behaviour of the interface air/material as well as the nature of the sample's surface and its dielectric properties. There is one requirement, conditioned by the process used to go further into the material's properties analysis: the S and P polarizations spectra must be simultaneously measured.

II.1 Derivation of the Fresnel equations

The process of analysis of our FDI measurements relies on the use of the Fresnel equations. These latter define the reflection and the transmission of an electromagnetic (EM) wave at an interface between two media of different optical indexes. Both media should be non-magnetic, isotrope and uniform. The S and P polarization are defined from the orientation of the electric field of the EM wave. The Figure 3.3 illustrates those two situations, for a laser incoming on this interface between the media 1 and 2, of complex optical index $N_1 = n_1 + i\,\kappa_1$ and $N_2 = n_2 + i\,\kappa_2$ respectively. The electric fields are denoted by $\vec{E}$, the magnetic fields by $\vec{H} = \vec{B}/\mu$ and the angles with the normal to the interface by θ . The indexes characterize the incident (i), reflected (r) and transmitted (t) parts.

$$\begin{cases} \vec{E_{i,r,t}} = \vec{E}_{0i,r,t} e^{-i\left(\omega t - \vec{k_{i,r,t}}\cdot\vec{r}\right)} \\ \vec{H_{i,r,t}} = \vec{H}_{0i,r,t} e^{-i\left(\omega t - \vec{k_{i,r,t}}\cdot\vec{r}\right)} \end{cases} \tag{3.15}$$

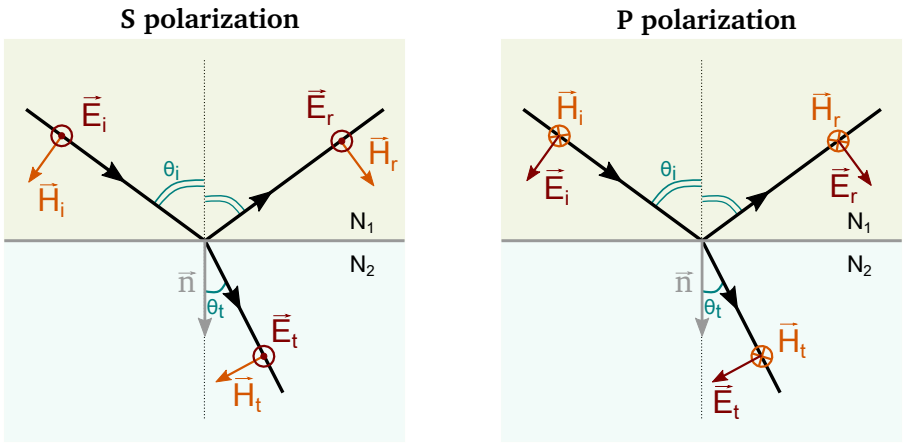

Figure 3.3 – *Scheme representing the a laser at the interface of two media of different refractive index $N = n + i\kappa$, depending on the incident polarisation of the electric field. The electric field is denoted by $\vec{E}$ and the magnetic field by $\vec{H}$. The subscript i corresponds to the incident wave, r to the reflected one, and t to the transmitted one. The normal to the interface from medium 1 to 2 is denoted by $\vec{n}$.*

The Maxwell's equations [269] result in a continuity condition for the electric and magnetic fields between the two media. With $\vec{n}$ the normal vector from medium 1 to medium 2, we find that:

$$\begin{cases} \vec{n} \wedge \left[\vec{E}_t - \left(\vec{E}_i + \vec{E}_r\right)\right] = 0 \\ \vec{n} \wedge \left[\vec{H}_t - \left(\vec{H}_i + \vec{H}_r\right)\right] = 0 \end{cases} \tag{3.16}$$

The Equations 3.16 imply the equality of the tangential components of $\vec{E}$ and $\vec{H}$ on both sides of the interface. The reflectivities R_S and R_P, respectively for the S and P polarizations, are defined as $R_S = E_r^S/E_i^S$ and $R_P = E_r^P/E_i^P$. In a similar manner, the transmissivities are defined as $T = E_t/E_i$.

II.1.1 *S* polarization:

The S polarization, also called TE for *Transverse Electric*, is depicted on the left side of Figure 3.3. In this configuration, the electric field is polarized perpendicularly to the plane of incidence. The continuity Equations 3.16 become:

$$\begin{cases} E_{0,i} + E_{0,r} = E_{0,t} \\ H_{0,i}cos(\theta_i) - H_{0,r}cos(\theta_r) = H_{0,t}cos(\theta_t) \end{cases} \tag{3.17}$$

As the incident and reflected beams are in the same medium, Snell-Descartes law gives $N_1 sin\theta_r = N_1 sin\theta_i$, which results in $\theta_r = \theta_i$. Moreover, as this work concerns only semiconductors, we can use the approximation that $\mu_i \sim \mu_r \sim \mu_t \sim \mu_0$, with μ_0 the vacuum permeability. Then, as

$\vec{H} = N\sqrt{\frac{\varepsilon_0}{\mu_0}}\vec{E}$, with ε_0 the vacuum permittivity, we deduce the following steps:

$$\begin{aligned} N_1\left[E_{0,i}cos\theta_i - E_{0,r}cos\theta_r\right] &= N_2\left[E_{0,i} + E_{0,r}\right]cos\theta_t \\ \Rightarrow E_{0,i}\left[N_1cos\theta_i - N_2cos\theta_t\right] &= E_{0,r}\left[N_2cos\theta_t + N_1cos\theta_r\right] \end{aligned} \tag{3.18}$$

Snell-Descartes law applied for the incident and transmitted beam gives the expression for $cos\theta_t = \sqrt{1 - \frac{N_1}{N_2}sin^2\theta_i}$. The reflectivity $R_S = E_{0,r}/E_{0,i}$ is then deduced to be:

$$R_S = \frac{N_1cos\theta_i - N_2\sqrt{1 - \left(\frac{N_1}{N_2}\right)^2 sin^2\theta_i}}{N_1cos\theta_i + N_2\sqrt{1 - \left(\frac{N_1}{N_2}\right)^2 sin^2\theta_i}} \tag{3.19}$$

II.1.2 *P* polarization:

The *P* polarization, also called *TM* for *Transverse Magnetic*, is depicted on the right side of the Figure 3.3. In this configuration, the magnetic field is polarized perpendicularly to the interface. The continuity Equations 3.16 become:

$$\begin{cases} \left[E_{0,i} - E_{0,r}\right]cos\theta_i = E_{0,t}cos\theta_t \\ N_1\left[E_{0,i} + E_0, r\right] = N_2E_{0,t} \end{cases} \tag{3.20}$$

Similarly to the *S* polarization, we separate the $E_{0,i}$ terms and $E_{0,r}$ ones to get the expression for R_P:

$$R_P = \frac{N_2cos\theta_i - N_1\sqrt{1 - \left(\frac{N_1}{N_2}\right)^2 sin^2\theta_i}}{N_2cos\theta_i + N_1\sqrt{1 - \left(\frac{N_1}{N_2}\right)^2 sin^2\theta_i}} \tag{3.21}$$

II.1.3 Fresnel equations in our experiment

In our experiment, the medium 1 is either air or vacuum, implying $N_1 = 1$ and medium 2 is the chalcogenide's sample, whose index N_2 will now on be called N for practical reasons. The Fresnel

equations in the two polarisations become:

$$\boxed{\begin{aligned} R_S &= \frac{cos\theta_i - N\sqrt{1-\frac{1}{N^2}sin^2\theta_i}}{cos\theta_i + N\sqrt{1-\frac{1}{N^2}sin^2\theta_i}} \\ R_P &= \frac{Ncos\theta_i - \sqrt{1-\frac{1}{N^2}sin^2\theta_i}}{Ncos\theta_i + \sqrt{1-\frac{1}{N^2}sin^2\theta_i}} \end{aligned}} \tag{3.22}$$

II.2 Surface dynamics

Though R_S and R_P have now been derived, the material's properties, the surface dynamics for example, cannot be determined using the formulas as such. A specific angle of reflection $\theta_i = 45°$ for the incident probe beam leads to a relationship between the amplitude reflectivities $R = re^{i\phi}$ of the S and P polarizations that will facilitate further considerations:

$$R_S^2 = R_P \qquad \Rightarrow \begin{cases} r_S^2 = r_P \\ 2\phi_S = \phi_P \end{cases} \tag{3.23}$$

In fact, this equation is only true when the interface between the air and the material is steep, *i.e.* if there is the step in the index of both media, taking place on a bigger scale than the wavelength of the laser. If the equation does not hold on, we find ourselves in some other regimes that can be characterized based on the introduction of two parameters [65], β_r and β_ϕ, defined as follows:

$$\boxed{\begin{aligned} \beta_r &= \frac{r_P}{r_S^2} \\ \beta_\phi &= 2\phi_S - \phi_P \end{aligned}} \tag{3.24}$$

From these two parameters' values, we divide the possible cases encountered into three categories [65].

II.2.1 $\beta_r = 1$, $\beta_\phi = 0$: Fresnel regime

In this first case, we find back the Fresnel canonical case for which the hypotheses are valid. The Equation 3.23 still describes accurately the situation at the interface. As showed in the Equation 3.25, the reflectivity and phase variations r and ϕ measured in this case correspond to the Fourier regime (denoted by the index F).
The parameter $\beta_r = 1$ means that the interface air/material is still sharp, implying that the sample is either in a solid or a liquid state. The additional fact that $\beta_\phi = 0$ leads to the expectation of a

solid case, as a transition towards a liquid phase would most certainly induce a change of volume due to the different density. It is therefore an isochoric case.

$$\begin{matrix} \beta_r = 1 \\ \beta_\phi = 0 \end{matrix} \Rightarrow \begin{matrix} r = r_F \\ \phi = \phi_F \end{matrix} \tag{3.25}$$

II.2.2 $\beta_r = 1$, $\beta_\phi \neq 0$: surface in movement

This second case depicts a situation where the interface is still sharp, but moving. Either the sample is still solid or undergoes a transition through a liquid phase, but in all cases, the variation of its density induces a shrinkage or an expansion.
This displacement can be retrieved by considering the optical path difference between the second probe and the first probe. Indeed, while the first probe is reflected on the material in its pristine state, the second probe is reflected on the interface after it has moved by a distance d.

Due to the surface displacement d, what we measure now are $r = r_F$, but $\phi = \phi_F + \delta\phi(d)$ for S and P polarizations, $\delta\phi$ being a phase difference between the two pulses, resulting from the displacement of the surface. $\delta\phi$ does not depend on the laser polarisation, only on d, implying that we find:

$$\begin{cases} r_P = r_S^2 \\ \phi_P = \phi_{P,F} + \delta\phi(d) \\ \phi_S = \phi_{S,F} + \delta\phi(d) \end{cases} \tag{3.26}$$

The phase shift $\delta\phi$ is therefore determined by the Equation 3.27 as being equal to the parameter β_ϕ.

$$\boxed{\delta\phi(d) = 2\phi_S - \phi_P = \beta_\phi} \tag{3.27}$$

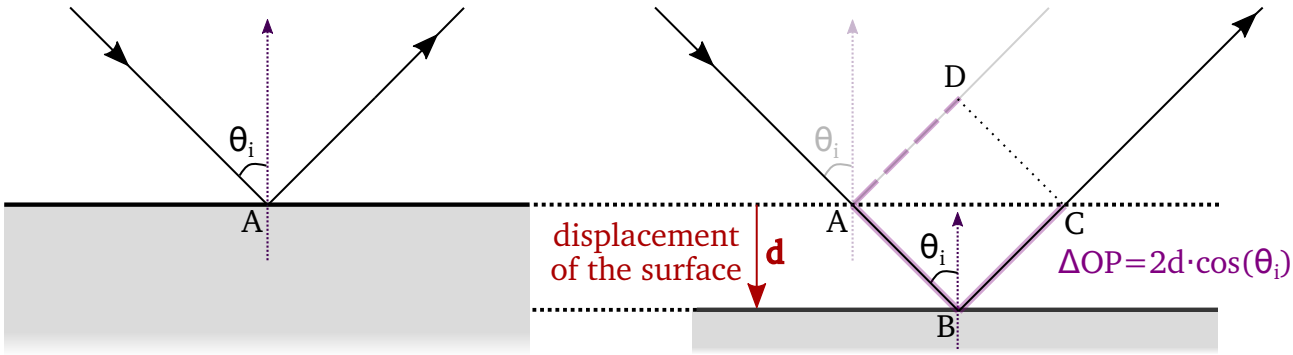

Figure 3.4 – *From the optical path difference ΔOP expressed in terms of d, we are able to retrieve the phase difference between the first probe, reflected on the material in its initial position, and the second probe, reflected on the material which has undergone a shrinkage or expansion by d.*

Now, in order to determine the displacement d of the interface, we consider the optical path difference ΔOP from one pulse to the other. The Figure 3.4 depicts the case of an interface which moves by a distance d. The convention chosen assumes that positive d means an expansion of the sample. The phase difference $\delta\phi$ resulting from the displacement of the interface can be expressed in terms of ΔOP, corresponding on the Figure 3.4 to:

$$\Delta OP = N_{air}\left(\overline{AB} + \overline{BC} - \overline{AD}\right) = 2dcos\theta_i \tag{3.28}$$

Using this expression, d is retrieved by using the Equation 3.27 [65]:

$$\begin{aligned} \delta\phi(d) &= 2\pi\frac{\Delta OP}{\lambda_0} = \beta_\phi \\ \Rightarrow &\boxed{d = \frac{\lambda}{4\pi cos\theta_i}\beta_\phi} \end{aligned} \tag{3.29}$$

II.2.3 $\beta_r \neq 1$: gas expansion

When matter is excited above a certain intensity threshold, it can loose its cohesion as the sum of the ionic and electronic pressures will exceed the cohesion pressure and a gas develops. Instead of a steep interface with a step of optical index between the air and the sample, there is now a smooth gradient of optical index, implying that the Fresnel equations are not valid anymore. Two scenarios are then possible:

1. Plasma expansion: $\beta_r < 1$, $\beta_\phi > 0$
   As the laser impinges the sample, the energy is absorbed mostly by the electrons inducing a rise of the electronic pressure P_e and temperature T_e. If P_e surpasses the cohesion pressure P_c, the electrons will "detach" themselves from the surface and charged ions will also be able to move freely, resulting in a plasma expansion.
   The phase shift and change of amplitude felt by the second probe reflected on the plasma depends on several coupled processes: in the case of an over-dense plasma, *i.e.* if the free electron density n_e exceeds the critical density n_{cr}($n_{cr} = 2.08 \times 10^{21}$ cm^{-3} for $\lambda = 532$ nm, the probing wavelength in our experiments) the material exhibits a mirror-like behaviour and the probe is reflected on it. Still, in addition to that, the probe beam can penetrate further the material if the penetration length defined as $\delta = \frac{\lambda}{2\pi Im(N)}$ is larger than the front of plasma critical density. Due to the plasma, it implies that the beam is modified by a non-uniform dielectric function ε. Finally, the resonant absorption of the P polarization contributes to the modification of the probe beam.
   All these contributions can be taken into account by resolving the Helmholtz equations for the S and P polarizations [270].

2. Neutral gas expansion: $\beta_r > 1$
   For a condensed state at T = 0 K, the total pressure of the system, which is the sum of the ionic P_i, electronic P_e and cohesion P_c pressures is zero. However, if $P_e + P_i$ becomes greater than $|P_c|$, but the temperature reached by excitation is not high enough to stay in a plasma state, the electrons and the ions will recombine giving rise to a neutral gas [65]. In that case, we expect β_r to be greater than 1.

With the pump laser intensities that we are using in our experiment, we do not expect to reach this last regime of $\beta_r \neq 1$.

II.3 Dielectric properties

FDI also enables to retrieve the dielectric properties of the sample studied. As for the surface dynamics, the Fresnel equations are the key to unlock the access to the dielectric function $\varepsilon = \varepsilon_r + i\varepsilon_i$ of our excited chalcogenide sample. With this sign convention, $\varepsilon_i > 0$ corresponds to absorption (see Appendix B).

II.3.1 In Fresnel validity regime

In the regime where $\beta_r = 1$ and $\beta_\phi = 0$, the dielectric function can be easily derived from the Fresnel Equations 3.22. Those Equations express the reflectivities R as a function of N, the complex optical index of the sample, that will be the link to the dielectric function. Indeed, $N^2 = \varepsilon$, and by considering the S and P polarizations, we find that:

$$N^2 = \frac{1 - R_S}{1 + R_S} \frac{1 + R_P}{1 - R_P} \tag{3.30}$$

The electric field's convention $E = E_0 e^{-i(\omega t - \vec{k}\cdot\vec{r})}$ constrains the complex refractive index to be such as $N = n + i\kappa$, for $n, \kappa > 0$ (see Appendix B). The real and imaginary parts of ε are identified with those of N to deduce the following expressions:

$$\boxed{\begin{aligned} \varepsilon_r &= n^2 - \kappa^2 = Re\left(\frac{1 - R_S}{1 + R_S} \frac{1 + R_P}{1 - R_P}\right) \\ \varepsilon_i &= 2n\kappa = Im\left(\frac{1 - R_S}{1 + R_S} \frac{1 + R_P}{1 - R_P}\right) \end{aligned}} \tag{3.31}$$

In practice, due to the fact that we measure R_S and R_P as a relative variation from one probe pulse to the other, ε found with the Formula 3.31 corresponds also to a relative variation. The absolute values for ε_r and ε_i are obtained by replacing $R \longrightarrow R \cdot R_i$ in the previous equation, R_i being the reflectivity of the pristine material deduced from ellipsometry measurement.

II.3.2 Steep interface moving regime

In the previous subsection II.2.2, the amplitude reflectivities measured in the case of a moving interface were linked to the Fresnel case equations as:

$$\begin{cases} r_P = r_S^2 \\ \phi_S = \phi_{S,F} + \beta_\phi \\ \phi_P = \phi_{P,F} + \beta_\phi \end{cases} \tag{3.32}$$

As a consequence, it is still possible to use the Equation 3.31, by replacing the reflectivity R from FDI measurement with $R \longrightarrow R \cdot R_i e^{-i\beta_\phi}$ to take into account the phase shift induced by the displacement of the interface.

II.3.3 Plasma or gas expansion regime

In the cases of plasma and neutral gas development, the dielectric properties cannot be retrieved as easily as previously. In the case of the plasma expansion for example, the dielectric function is now dependant on the position, and is therefore also dependent on the temperature and hydrodynamics of the system. As these cases will not be encountered in this work, they will not be detailed further.

III FDI in practice: experimental set-up

III.1 Experimental set-up

The experimental set-up we used to perform frequency-domain interferometry (FDI) is depicted in Figure 3.5. The incoming beam from the Aurore beamline [271], delivers gaussian pulses with an energy of 10 mJ, a repetition rate of 1 kHz and a central wavelength of 800 nm. The Figure 3.6 shows a typical 3ω autocorrelation trace of the laser measured by a SEQUOIA system (Amplitude Technologies). The peaks at -24 ps and 12 ps are replicas from the apparatus. The background level is appreciated by the feature at -44 ps measured while shutting off the beam. The pedestal observed in the ± 10 ps time window results from the scattering light induced by the grating of the stretcher in the chirped pulse amplification (CPA) [272]. The baseline at 10^{-7} corresponds to the amplified spontaneous emission (ASE), which amounts for about 1.5% of the femtosecond pulse energy. This autocorrelation signal shows without doubt that the laser beam has a sufficient contrast to prevent any pre-heating of samples during experiments.

At the entrance of the experimental room, the laser beam is first split in two by a beam splitter (BS in Figure 3.5) between the probe (70%) and the pump (30%) arm. The full width at half maximum (FWHM) pulse duration of the incoming pulses being about 320 ps at the entrance of the

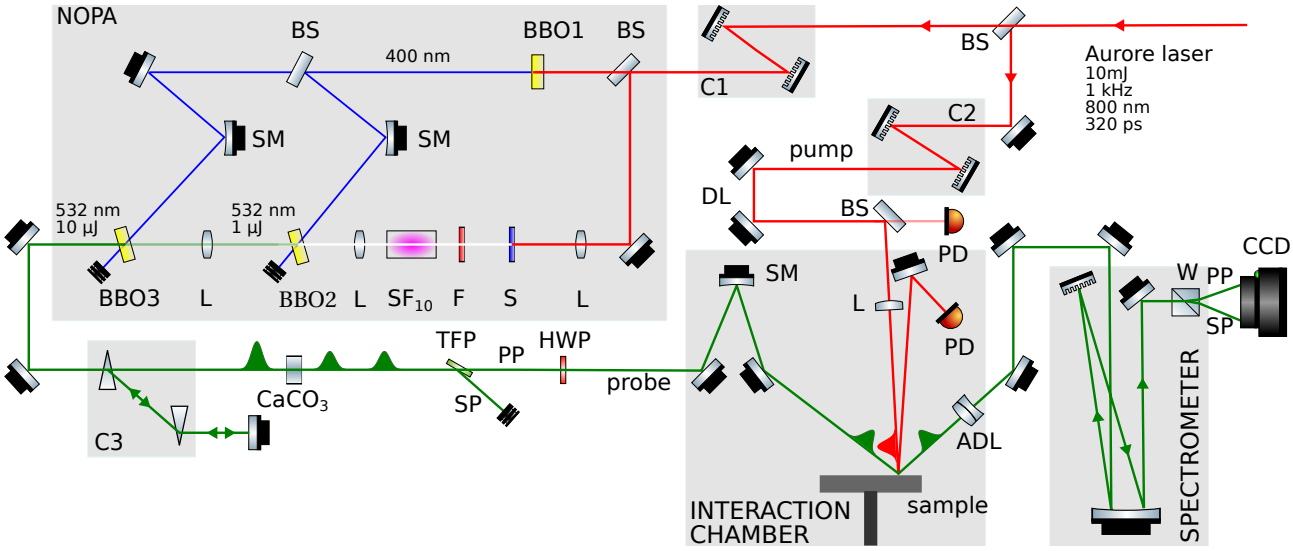

Figure 3.5 – *Experimental set-up.*
BS: beam splitter - C1 & C2: gratings compressor for the probe and pump arm respectively - BBO1 & BBO2 & BBO3: Beta-Barium-Borate crystals for the frequency doubling, first stage amplification and second stage amplification respectively - SM: spherical mirrors - L: lens - S: sapphire plate - F: 800-nm Notch-filter - SF_{10}: heavy-flint glass - C3: prism compressor - $CaCO_3$: calcite crystal - TFP: thin film polarizer - PP: P polarized beam - SP: S polarized beam - HWP: zero order half wave plate - PD: photodiode - ADL: achromatic doublet lens - DL: delay line - W: Wollaston prism.

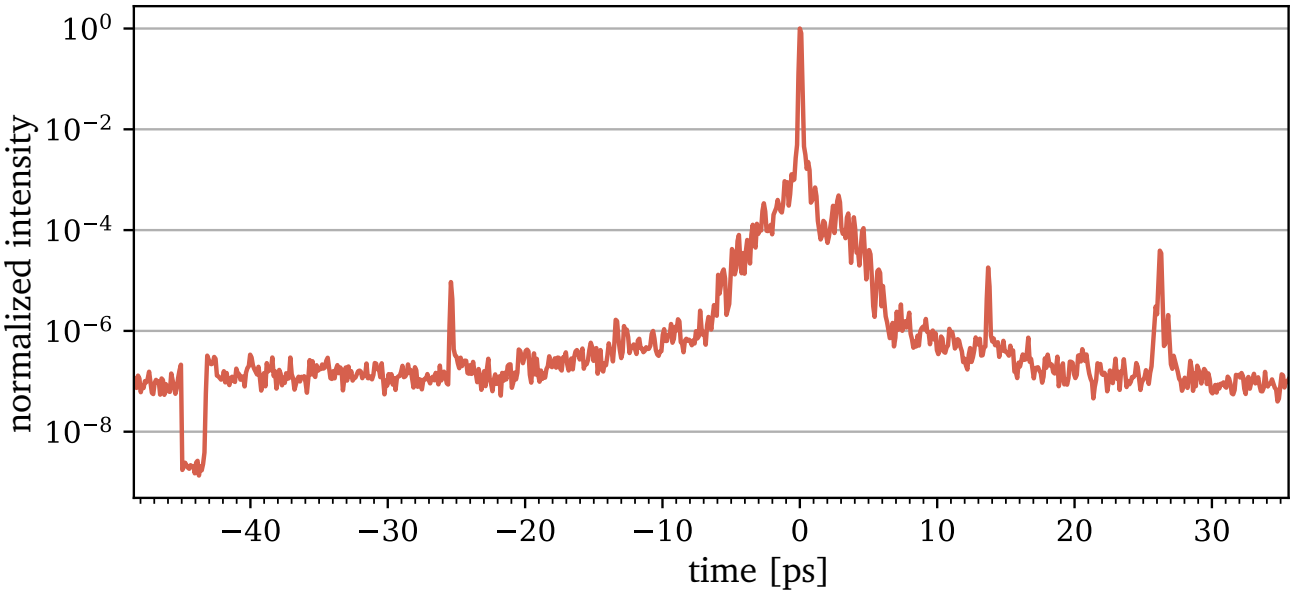

Figure 3.6 – *Third-order autocorrelator trace of the Aurore laser beam before it is propagated to be distributed to the experimental room, from [271].*

experimental room due to the propagation on a long distance of the laser, they are re-compressed thanks to gratings compressors (C1 and C2) to reach down to 26 fs FWHM duration.

III.1.1 Pump arm

After being recompressed by the C2 compressor, a delay line on the optical path of the pump beam allows to vary its delay Δt with respect to the probe beam. The pump is focused on the target with an angle of 10° by a 200 mm plano-convex lens down to a spot size of ~50 µm FWHM.

III.1.2 NOPA

After the C1 compressor, a *non-collinear optical parametric amplifier* (NOPA) [273] tunes the probe's wavelength to 532 nm. This NOPA is build on a two-stages amplification scheme. The 800 nm probe beam is split in two with a 95/5 ratio (95% going to the NOPA's pump arm and 5% to the signal one). The amplification relies on the fulfillment of the phase-matching condition for each stage. This condition, ruled by the Equation 3.33, implies the momentum and energy conservations between the pump, the signal and the idler beams, with wavevectors $\vec{k_p}$, $\vec{k_s}$ and $\vec{k_i}$ respectively. The non-collinear configuration facilitates the phase-matching condition and helps discard the pump easily after each amplification.

$$\hbar\vec{k_p} = \hbar\vec{k_s} + \hbar\vec{k_i} \tag{3.33}$$

The generation of a white light continuum by self-phase modulation in a 3 mm thick sapphire crystal (S) for the 1^{st} stage amplification allows to tune the NOPA in the range of wavelength from 380 nm up to 680 nm. For practical reason, we chose to run it at 532 nm (choice made before running the *ab initio* simulations). At this point, the energy of the amplified 532 nm probe pulse reaches about 10 µJ. This resulting pulse is then filtered spatially by a 2.5 mm diameter diaphragm and then re-compressed in a double-pass SF_2 prisms compressor (C3) in order to compensate the chirp induced by the path through numerous optical components.

III.1.3 Two pulses generation and interaction with the target

The FDI technique requires the use of two probe pulses that are identical before reflection on the sample. In our set-up, it is a 15 mm thick calcite ($CaCO_3$) monocrystal mounted on the optical path of the probe arm that generates those pulses. As calcite is a birefringent material, its ordinary refractive index $n_o = 1.66$ is different from its extraordinary one $n_e = 1.49$. Therefore, as the polarization of the incoming laser beam is not on either of these two specific axis, the pulse will propagate with different velocities, giving rise to two different pulses with orthogonal polarizations, delayed by $\Delta t = d|n_e - n_o| = 8.66$ ps at 532 nm, with d the crystal's thickness.

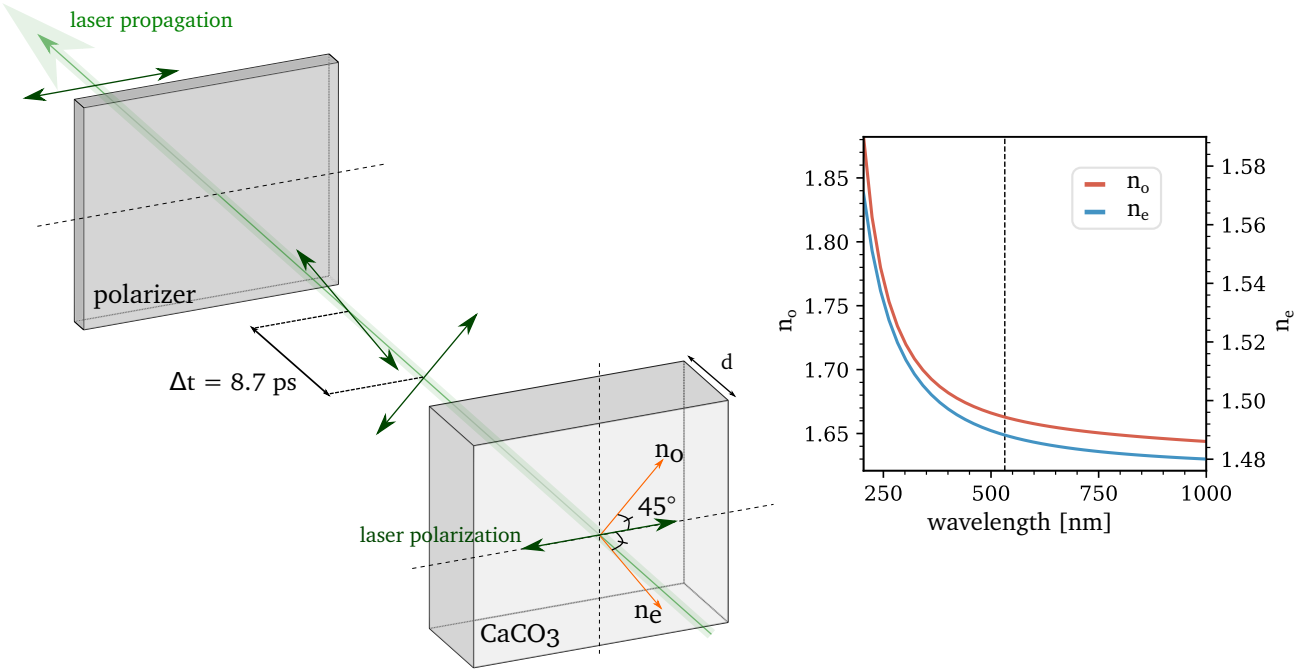

Figure 3.7 – *Evolution of the laser polarization as it goes through the calcite crystal and the polarizer film (left) - Ordinary n_o and extraordinary n_e refractive indexes of calcite as a function of wavelength (right), data from [274].*

A schematic view of the laser's path through calcite is represented in Figure 3.7 as well as the ordinary and extraordinary refractive indexes (n_o and n_e) as function of wavelength.
Following Heisenberg uncertainty principle, $\Delta E \Delta t \geq \hbar/2$, a large wavelength bandwidth is required to generate femtosecond pulses. However, when passing through an optical component, every frequency ω of the pulse may not propagate at the same speed depending on the dispersion $n(\omega)$ of the refractive index of the material. The velocity of the pulse's envelope is given by the *group velocity* $v_g = 1/(\partial k/\partial\omega)^{-1}$.
To characterize the induced dispersion, the concept of *group velocity dispersion* (GVD) arises. It is the second-order dispersion, defined as:

$$GVD = \frac{\partial}{\partial\omega}\left(\frac{1}{v_g}\right) = \frac{\partial^2 k}{\partial\omega^2} \tag{3.34}$$

In the case of our calcite crystal, the ordinary and extraordinary rays undergo different optical indices n_o and n_e. The dispersion equations for the refractive indices n of the material obeys a Sellmeier equation, in the form of Equation 3.35 [274, 275].

$$n^2 = a_1 + \frac{a_2\lambda^2}{\lambda^2 - a_3} + \frac{a_4\lambda^2}{\lambda^2 - a_5} + \frac{a_6\lambda^2}{\lambda^2 - a_7} \tag{3.35}$$

with $\{a_i\}$ real coefficients.

The GVD at $\lambda = 532$ nm are then deduced for the ordinary and extraordinary directions:

$$GVD = \frac{\lambda^3}{2\pi c}\frac{\partial^2 n}{\partial \lambda^2} \Rightarrow \begin{cases} GVD_o(532\text{ nm}) = 66.504\,\text{fs}^2/\text{mm} \\ GVD_e(532\text{ nm}) = 138.73\,\text{fs}^2/\text{mm} \end{cases} \tag{3.36}$$

Using the GVD, it is possible to retrieve the *group delay dispersion* (GDD) due to the passage through the d =15 mm-thick calcite:

$$GDD = GVD \times d \Rightarrow \begin{cases} GDD_o(532\text{ nm}) = 998\,\text{fs}^2 \\ GDD_e(532\text{ nm}) = 2081\,\text{fs}^2 \end{cases} \tag{3.37}$$

For a gaussian pulse, the resulting stretched pulse has a duration Δt_{str} that can then be expressed as:

$$\Delta t_{str} = \sqrt{\Delta t + \left(\frac{4\ ln2\ GDD}{\Delta t}\right)^2} \tag{3.38}$$

For an initial pulse duration of $\Delta t = 80$ fs, we find a reasonable stretching for each type of ray:

$$\boxed{\begin{array}{l} \Delta t^o_{str}(532\text{ nm}) \sim 87\,\text{fs} \\ \Delta t^e_{str}(532\text{ nm}) \sim 108\,\text{fs} \end{array}} \tag{3.39}$$

After the calcite crystal, a thin film polarizer gets both pulses back in the same polarization by filtering out all but the P one. The intensities of the S and P polarizations on the sample are then finely tuned thanks to a zero order half wave plate to balance the intensities on the CCD camera. Finally, the probe beam is focused with an incident angle of 45° onto the material by a 500 mm focal length mirror followed by a 0.5 mm pinhole that homogenizes the probe spot intensity.

The experiments are performed in the non-reversible regime, requiring the refreshment of the sample between each pump-on case. This is achieved by mounting the sample onto a specific rotating holder of speed 120 RPM, represented in the Figure 3.9. The tricky part here is having the surface of the sample always in the same plane with an accuracy of less than 10 µm. Indeed, any sample movement bigger than this would result in a misalignment of the following imagery. This is dealt with by the help of three picomotors assembled onto the sample's holder while monitoring the surface thanks to a laser displacement detector (Keyence LKG500 with 2 µm of resolution). The target flatness is checked both *via* rotation and translation. An example of these measurements, shown in Figure 3.8 reveals that the target is flat within 5 µm in translation and 9 µm within rotation.

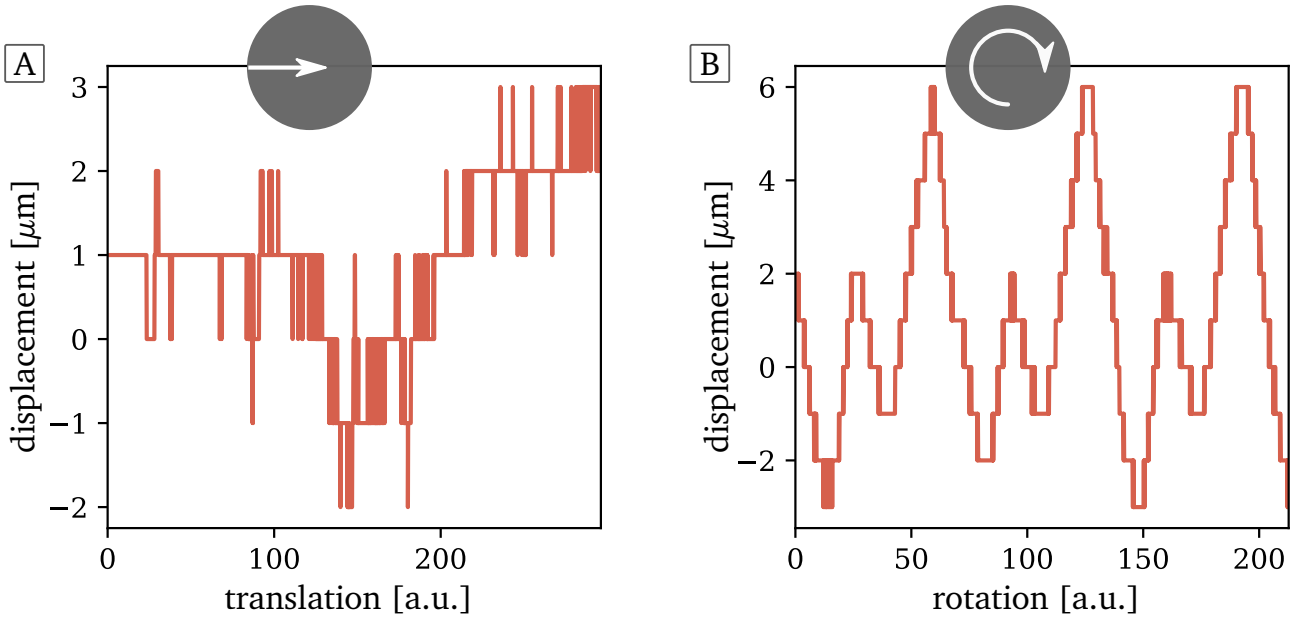

Figure 3.8 – *Translational (A) and rotational flatness of the target (B).*

The depth of field, which defines the length of which the focus on the sample is sharp, is characterized in the case of the (gaussian) probe by the Rayleigh length z_R. It is calculated thanks to the waist length w_0 and the wavelength of the laser λ with the Equation 3.40.

$$z_R = \frac{\pi w_0^2}{\lambda} \tag{3.40}$$

As the laser beam is "cut" by a ⊘ 0.5 mm pinhole right before being focused onto the sample, we estimate the waist of the laser on the target as equal to that on the focusing lens, so $w_0 \sim 0.25$ mm. Using this waist value gives a Rayleigh length of $z_R \sim 0.37$ mm, which is thankfully far greater than the derivation of the target from the perfect flatness.

III.1.4 Spectrum imaging

The interaction point is imaged on the entrance slit of a spectrometer by a 200 mm focal length achromatic doublet lens. This spectrometer is build in a Fastie-Ebert configuration: the 200 µm entrance slit is placed at the focal distance (1 m) of a spherical mirror which reflects the probe beam onto a 1200 l/mm grating blazed at 532 nm. This stretching of the two probe pulses gives them a sufficient overlap to interfere. The 1st order is diffracted back to the spherical mirror, sending the slit image onto the back-illuminated CCD camera (Princeton Instruments Pixis 1024 eXcelon, 16-bit cooled camera with 13 µm pixels sizes). Right before the CCD detector, a Wollaston prism (W) separates spatially the S and P polarizations. Each spectrum acquired is in fact the accumulation of 1000 laser shots (1 s acquisition).

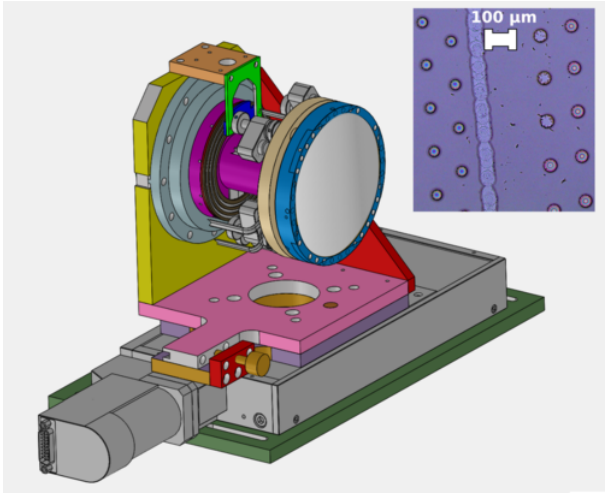

Figure 3.9 – *Sample rotating holder. The sample is mounted on the blue holder. The picomotors located at the rear allow to tune the flatness of the target. An example of an irradiated sample observed with phase-contrast microscopy is shown in the top right inset.*

III.2 Beamline characterization

III.2.1 Probe characterization

The NOPA is a fine-tuning work of both temporal and spatial components. To get the most effective amplification, *i.e.* with the maximum amplification along with the shortest pulse duration, the spectrum, energy, and spatial overlapping are checked during the alignment of the laser.
The spectrum, shown in Figure 3.10A is measured thanks to an Acton 500i spectrometer including a mirror with focal length $f = 500$ mm and a 300 l/mm grating blazed at 500 nm. This measurement is a diagnosis for the NOPA. Indeed, the spectral distribution does not only allow us to check if the central wavelength is the right one, it also defines the minimum pulse duration Δt that is reachable considering the spectral broadening of the pulse. The FWHM width of the distribution $\Delta\lambda$ is linked to Δt via the Fourier inequality [276] $\Delta\nu\Delta t \geq K$, with K a factor depending on the pulse's shape ($K = 0.441$ for a gaussian shaped pulse [276]) and $\Delta\nu$ the FWHM frequency. As $\nu = c/\lambda_0$ (with c the speed of light and λ_0 the central wavelength of the laser), the FWHM duration is retrieved from the spectrum thanks to the Equation 3.41 to be 37.26 fs ± 0.08 fs.

$$\Delta t = \frac{0.441}{\Delta\lambda}\frac{\lambda_0^2}{c} \tag{3.41}$$

The important point is that this value only represents the minimum pulse duration that could be reached, *i.e.* in an ideal case. The actual duration's measurement is based on the utilization of a homemade wavefront-splitting autocorrelator based on second-harmonic generation (SHG) in a 60 µm thick BBO crystal. A gaussian fit of this autocorrelation signal, represented on Figure 3.10, gives a real pulse duration value of 72 fs ± 2 fs FWMH.

The difference between those two values is explained by the refraction through multiple optical components as well as the imperfect overlapping of the pump and signal beams during the two amplifications. Chirp and third-order non linear effects are introduced and result in a frequency-dependent spectral phase. The prism compressor and the diaphragm are not sufficient to compensate those negative effects which manifest by a pulse duration longer than in the ideal case.

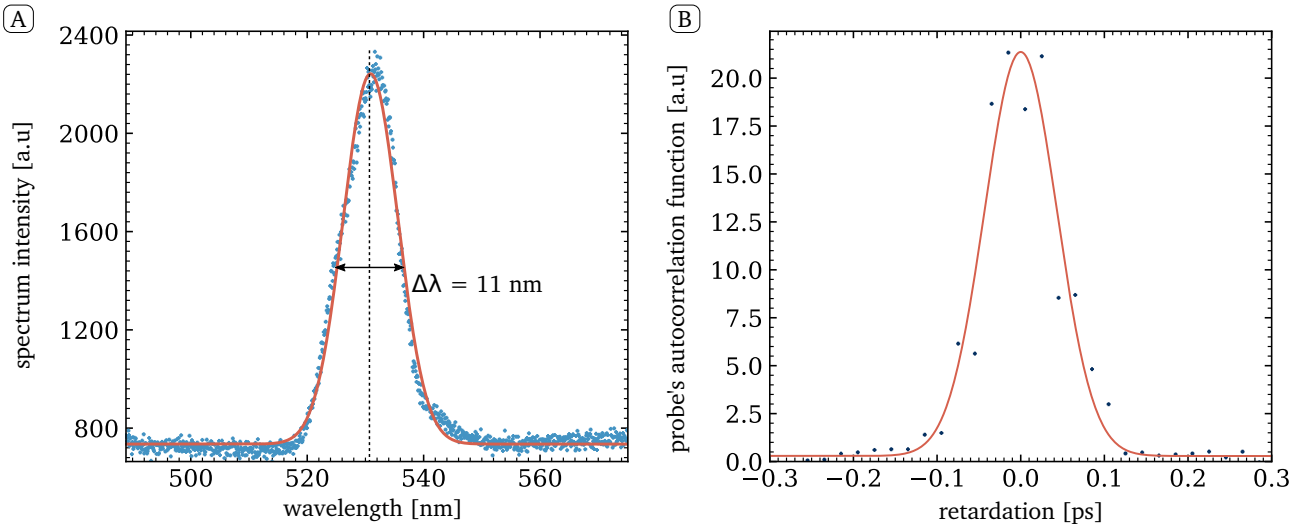

Figure 3.10 – *Spectrum of the probe (A). Autocorrelation function of the probe vs the retardation induced by the translation stage (B). A gaussian fitting is applied on both traces (red solid lines)*

III.2.2 Pump characterization

The *pump fluence* is determined thanks to incident energy measurement and a calibration consisting in imaging its spot via a 12 bit CCD camera. First, the camera needs to be calibrated. In order to do that, we place a tip or a razor blade on the intersection point of the pump and the probe, such that the pump will be calibrated on the position it will occupy during the experiments. The tip must therefore be placed in the same plane as the target face.
Then, the image of the tip is collected, as shown in Figure 3.11. We move the tip of a known distance d and acquire a second image in that second position. Then we identify a same feature in both images, and the longitudinal distance Δx that separates that feature in both images gives the relationship pixel-real distance as Δx [pix] = d [µm]. We usually find that 1 pix = 0.29 ± 0.01 µm.

Once that the calibration has been done, an image of the pump (without the tip) is acquired. The size is then determined by two gaussian fits of the spot intensity profile in the x and y directions in order to retrieve the standard deviations σ_x and σ_y. This double fitting checks the symmetry of the pump beam. Using the formula 3.42, the fluence is computed with E the incident energy, T

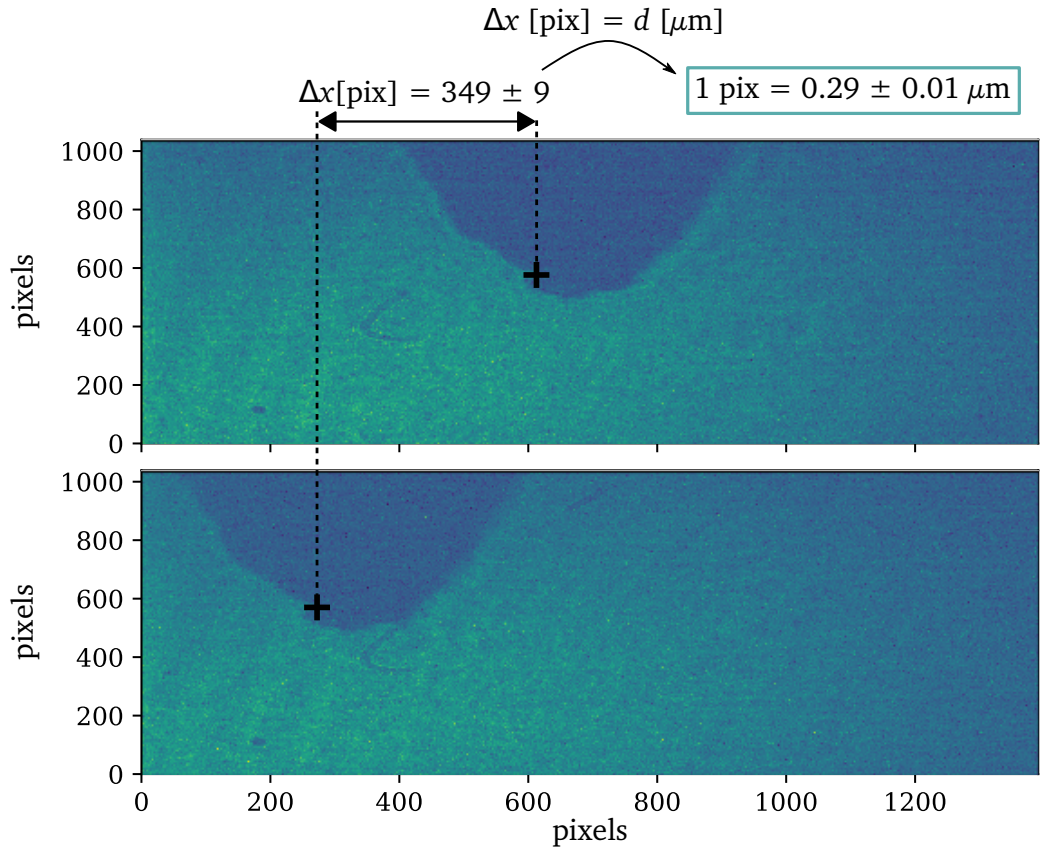

Figure 3.11 – *Calibration of pixels-real distance.*

the transmission of the line, and A=0.86 the Airy factor.

$$F = \frac{E}{2\pi\sigma_x\sigma_y} T \cdot A \tag{3.42}$$

From the curve chosen as example in Figure 3.12, we find $\sigma_x = 28.5 \pm 0.2\,\mu m$ and $\sigma_y = 28.4 \pm 0.2\,\mu m$: the pump spot is almost a perfect gaussian. The pump intensity is limited by using a pinhole, whose diameter constrains the maximum energy E_{max} attainable. In the example given here, a 2 mm pinhole was used, resulting in a the maximum energy $E_{max} = 2.5\,\mu J$, which corresponds to a maximum fluence is $F_{max} = 30\,mJ/cm^2$.

The *pump duration* is measured right before it enters the interaction chamber by reflecting it towards a 2ω autocorrelator. The pump duration is measured to be 25 to 30 fs FWHM.

III.2.3 Pump-probe zero delay determination

The pump-probe zero delay is obviously very important in a pump-probe experiment in order to have a good precision on the dynamics timescale. As stated in Chapter 1, as the samples we analyze are chalcogenides, they demonstrate a huge change in reflectivity very fast under

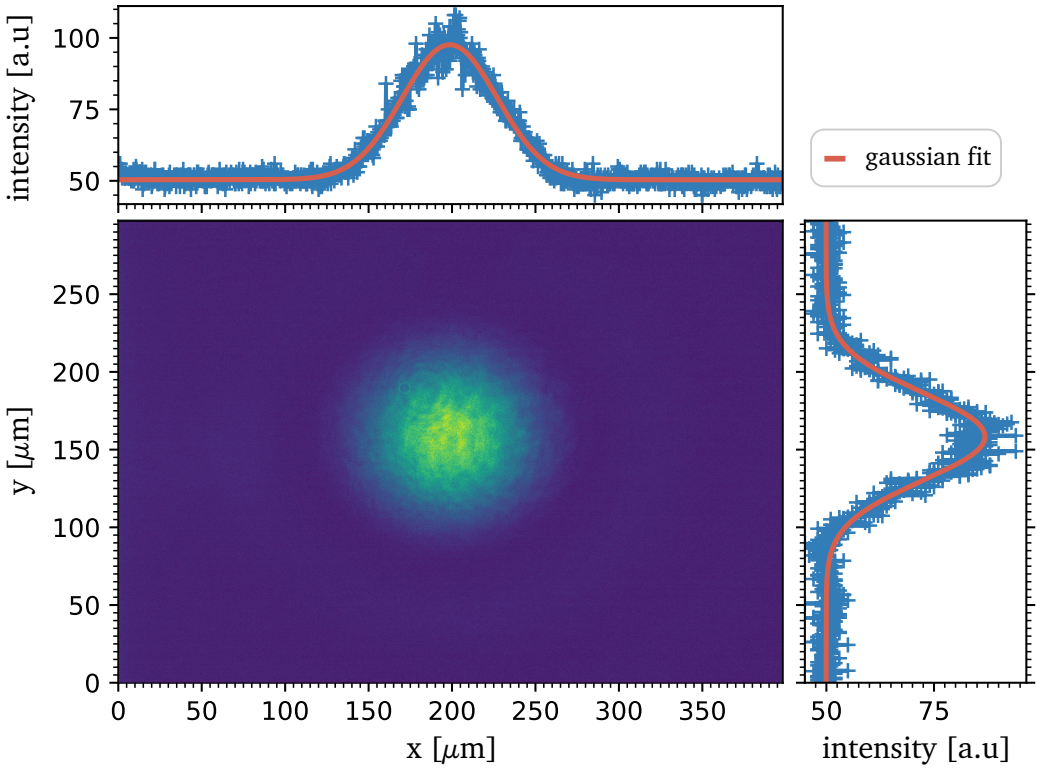

Figure 3.12 – *Pump spot for a 2 mm pinhole. The gaussian fits of the x and y spatial profiles allow to characterize the pump pulse and retrieve the fluence from the energy measured upstream.*

excitation. This property is used here to synchronize the pump and the probe arm. First, the calcite crystal slow axis (n_o) is aligned with the laser polarization in order to generate only the second probe pulse. The time $t = 0$ is defined as the moment when the probe is reflected on the sample. To synchronize the pump and probe, *i.e.* to find $\Delta t = 0$, it requires to find the position x_0 on the pump delay line that corresponds to this condition.

The pump delay line is moved backward and forward via a translation stage down to a 10 µm precision (with care about the hysteresis of the stage). A camera collecting a probe leak downstream in the set-up allows to see if the pump impinges the sample before or after the probe is reflected. During this process, the probe shutter is left open continuously. As we move the position of the delay line forward and backward, in terms of spatial position, the pump temporal position is also modified as the total length of its optical path is varied. We consider two cases, illustrated in the Figure 3.13: first, the delay line is shortened, with a corresponding position on the delay line x_1; and second, if the delay line is lengthened, the position will be denoted as x_2. It follows that:

$$x_2 > x_0 > x_1 \tag{3.43}$$

From this, the shift of delay induced by the variation of optical path is deduced (with c the light velocity):

$$\frac{2(x_2 - x_0)}{c} > 0 > \frac{2(x_1 - x_0)}{c} \Rightarrow \boxed{\Delta t_2 > 0 > \Delta t_1} \tag{3.44}$$

1. When the delay line is shortened compared to the position of the zero delay, the pump is early compared to the probe. Therefore, the probe will be reflected on the excited sample, we see a clear change of reflectivity induced by the pump.

2. On the contrary, if we increase the optical path, the probe will be reflected first, and then the pump will impinge the material. The probe just gives us an image of the material in its initial state (no change).

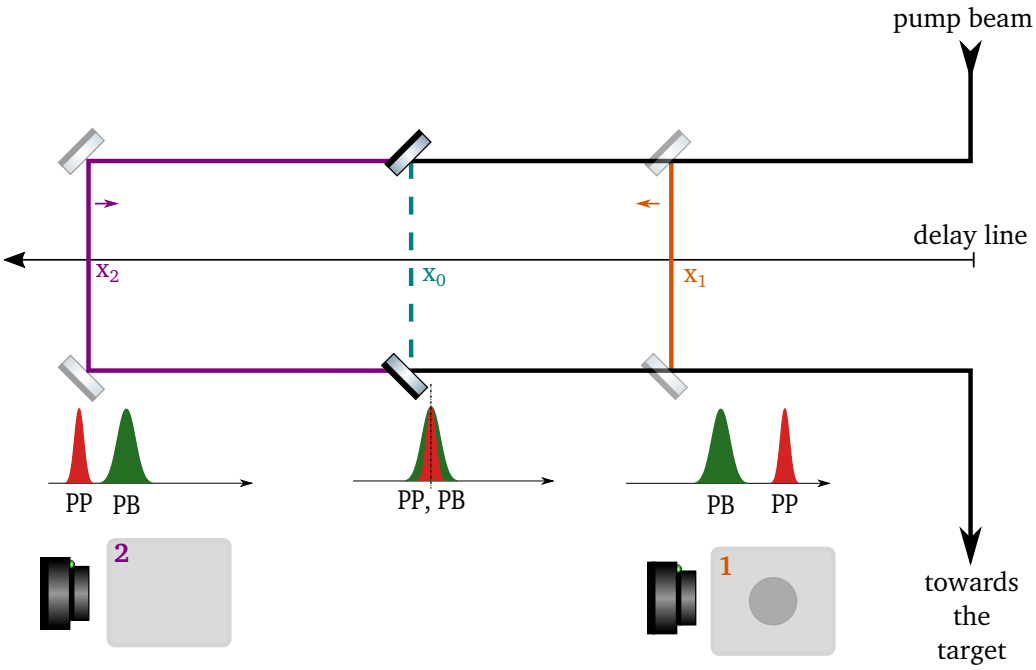

Figure 3.13 – *Schematic representation of the zero delay determination. PP: pump, PB: probe.*

The idea is then to refine the inequality 3.43, such that $x_1 \longrightarrow x_1 + \delta x$ and $x_2 \longrightarrow x_2 - \delta x$, with δx a spatial increment, until we reach the optimal precision of the translation stage. The delay line allows a 30 fs precision thanks to the OWIS P90 delay line controller. However, as the method used here depends intrinsically on the probe duration, it is this latter that determine the uncertainty on the zero delay determination. The probe duration spans from 80 to 100 fs, and so does the accuracy on $t = 0$.

CHAPTER 4

DYNAMICS OF AMORPHOUS GERMANIUM TELLURIDE THIN FILM UNDER EXCITATION

GeTe is a prototypical phase-change memory (PCM) material. Photo-excitation of this latter family of materials has been shown to lead to large variations of optical properties in very short times after excitation [9]. Typically Callan *et al.* [62] measured an ultrafast response in 200 fs after irradiation by a 50 fs laser pulse. The rapidity of the transitions undergone by GeTe and other PCMs has triggered an interest in the possible non-thermal character of this switching, though it is still questioned.

From these observations, studying the photo-excitation of thin films of amorphous GeTe (*a*-GeTe) with an optical technique should be pertinent. With the aim at observing utra-fast dynamics in those films with a sub-100 fs resolution, and a spatial resolution on the nanometer scale, pump-probe experiment with frequency-domain interferometry (FDI) seems an appropriate idea. In previous studies, the final state was seen to be depending on several parameters, the intensity of excitation among others. The fluence was therefore varied here to reproduce a panel of different excitation intensities. While the initial state is known (though the precise structure is still debated [32–36]), it is more difficult to predict what is going to be the final state and the transient states from one phase to the other. Among other parameters, the cooling rate is crucial for these states.

Although FDI retrieves precise information on the surface dynamics as well as on the dielectric properties, on itself this technique is not sufficient to fully understand the structural changes of excited GeTe: what are the changes on the atomic scale? What is the nature of the excited state?

To answer this kind of questions, *ab initio* molecular dynamics (AIMD) simulations are tools of choice. Thanks to the structural analysis of well-chosen configurations (pair distribution function, distributions of angles, mean square displacement, ...), it is possible to track down the evolution of experimentally excited GeTe as will be detailed in Section II fo this chapter.

Brief reminder of the structure of *a*-GeTe:

As presented in Chapter 1, *a*-GeTe is characterized by Ge atoms both in octahedral and tetrahedral sites [277–279]. These two types of sites are found to be quite distorted: the angles are not exactly 90° and 110° respectively . The as-deposited (AD) and melt-quenched (MQ) phases display slightly different properties due to their local differences: the AD phase comprises a majority of tetrahedral units (between 80% and 100%) while the MQ has a 1:3 proportion of tetrahedral *vs* octahedral sites [112].
In both cases, Te atoms are found with a coordination number of 2 and angles close to 90°. No Te-Te bonds are found in the first neighbouring shell while Ge-Te and Ge-Ge bonds lengths are estimated to be about 2.628 Å and 2.473 Å respectively by EXAFS measurements [92].

I Experimental results of the excitation of amorphous GeTe

I.1 *a*-GeTe sample and static optical characterization

Amorphous GeTe (*a*-GeTe) is our material of interest in this chapter. Thin films of *a*-GeTe were deposited *via* a *physical vapor deposition* (PVD) method, namely *magnetron sputtering* by P. Noé's team at the CEA LETI, Grenoble. A schematic representation of this technique is represented in Figure 4.1. Basically, a *wafer* is placed on an anode in a vacuum chamber containing a neutral gas (Ar in most cases). A *target* made of the species needed for the final material is placed on the cathode. A plasma is triggered by applying a RF or DC voltage, so the gas is now positively charged. Attracted by the negatively charged target, the ionized gas move towards the target. The magnetic field generated by the arrays of magnets (*S* and *P* poles) of the magnetron cathode accelerates the gas which collide with high kinetic energy with the atoms from the target. Those are then ejected and deposited on the wafer.

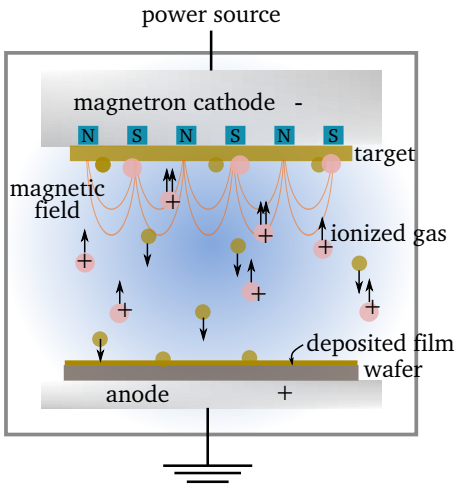

Figure 4.1 – *Magnetron sputtering.*

The thickness of deposited material is determined by the duration of the sputtering. A prior calibration is required as the speed of deposition is, among other parameters, species-dependent.

This is done by measuring the thickness of layer deposited for a given period of time by *x-ray reflectivity* (XRR) [280]. For example with a given set of parameters for the power source, etc...5 nm of GeTe are deposited in 26.5 s while 3 nm of Carbon would take 131 s.
In our case, the wafer was a 1 mm thick undoped Prime CZ Si (100) substrate and the target made of stoichiometric GeTe. A thin film of 500-nm thick GeTe is obtained in the aforementioned *as-deposited* amorphous phase (see Figure 4.4). Chalcogenide being highly subject to oxidation [281,282], half of the samples were capped *in situ* by a 10-nm SiN layer, which is transparent to the pump and probe wavelengths used. In any case, all experiments were conducted in vacuum environment (10^{-2} mbar).

All static characterizations were conducted by P. Noé's team at CEA LETI right after the films deposition. The refractive indexes $N = n + i\kappa$ of *a*-GeTe and SiN, represented in Figure 4.2, are obtained from ellipsometry measurements[1]. The method consists in measuring the change of polarization of a laser after reflection on the sample of interest with an angle close to Brewster. The ratio of r_S and r_P (see Chapter 3 for the S/P polarization explanation) gives the complex reflectance ratio. From these measurement, the fitting with a model, such as the Cody-Lorentz [284] or the Tauc-Lorentz [285], is needed to retrieve the optical constants. Fitting the experimental data with the chosen model determines the uncertainty on the refractive index. For n, a precision of 10^{-2} is a good approximation: the interface roughness is neglected, and presence of the capping layer has be taken into account. For κ, it is more complicated to estimate, the only sure thing is that the ellipsometer cannot detect under 10^{-4}. At the wavelength probed, the fitting gives $\varepsilon^{cold}_{a\text{-}GeTe}(532\text{ nm}) = 12.66 + 14.93\ i$.

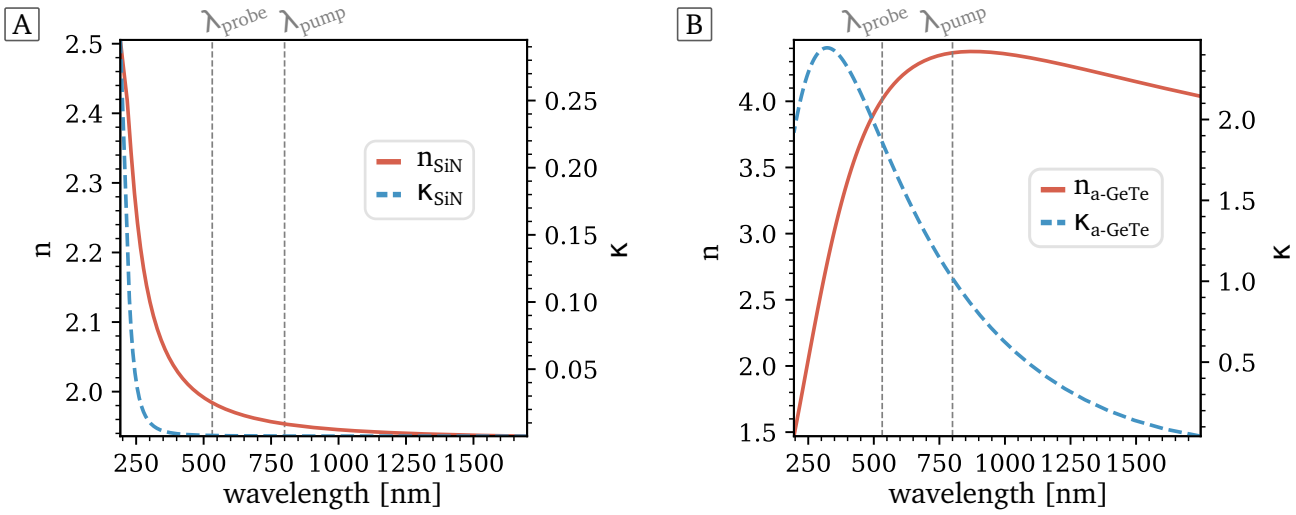

Figure 4.2 – *Refractive index $N = n + i\kappa$ from ellipsometry measurement for SiN (A) and a-GeTe (B).*

[1] 1.6 nm step between 200 and 1000 nm then 3.4 step above. These ellipsometry measurements were done *via* a M-2000 J. A. Woollam ellipsometer at the angles of incidence 55°, 65°and 75°. Intrinsic software was used to fit the measurements and obtain n and κ. [283]

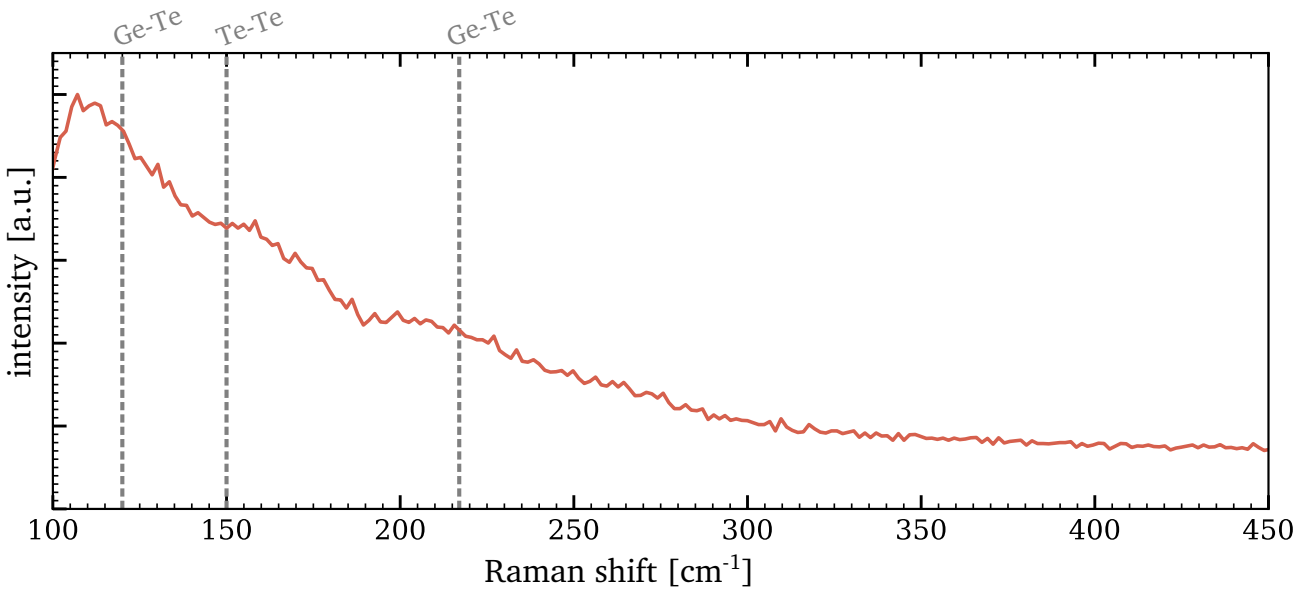

Figure 4.3 – *Raman spectrum of the a-GeTe thin film [283].*

The process of a semiconductor's excitation with ultrashort lasers is intimately linked to its band structure, and therefore to its optical band gap. This latter is commonly deduced in semiconductors by using the Tauc formula [66, 286–290] (see Appendix C). Using the refractive index measured by ellipsometry, we find a band gap $E_g(GeTe) = 0.80 \pm 0.01$ eV, in adequation with literature [291, 292].

In addition to the ellipsometry measurements, Raman spectra were also collected using a Micro-Raman Renishaw InVia reflex with confocal microscope instrument, with $\lambda_{laser} = 532$ nm and an adapted intensity to prevent any modification during the measurements [283]. The analysis of the spectrum, shown in Figure 4.3, reveals that the main mode is around 120 cm^{-1} and corresponds to Ge-Te bonds in tetrahedral $GeTe_{4/2}$ [27]. A second peak due to these vibrations is also seen at 217 cm^{-1}, but of much lesser importance. These Raman peaks are very broadened due to the multiple local environment that are present in the material: tetrahedral $GeGeTe_3$ as well as distorted octahedral $GeTe_6$ environments contribute to the two aforementioned peaks [293, 294]. Such broad distributions of bonds also lead to large phonon modes. At 150 cm^{-1}, Te-Te contribution could be identified [295], unexpected for the Ge/Te ratio of our samples, but probably due to the film's deposition technique [140].

I.2 Surface dynamics

The next step after this static characterization is to study the time-resolved response to excitation. Frequency-domain interferometry (FDI) experiments were conducted on thin films of the obtained *a*-GeTe (see Figure 4.4) A pump beam characterized by 30 fs duration FWHM pulses and a central

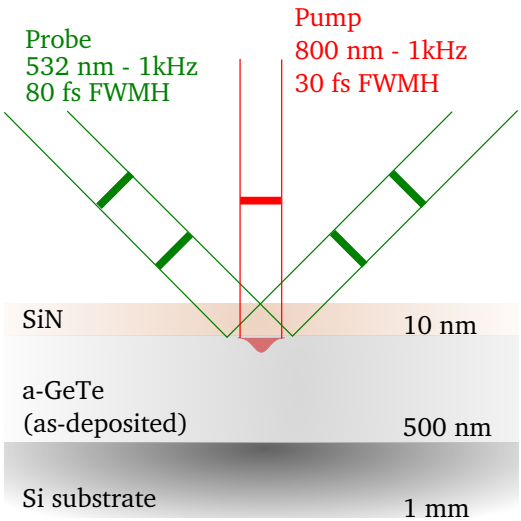

Figure 4.4 – *Representation of the FDI experiment on a-GeTe.*

wavelength of 800 nm and a probe beam of 80 fs duration FWHM pulses with a central wavelength of 532 nm was used, as indicated in Figure 4.4. More details about the experimental parameters and set-up can be found in Chapter 3 [271]. Eight pump fluences from 16 ± 2 mJ/cm^2 to 80 ± 2 mJ/cm^2 on both capped and uncapped samples of *a*-GeTe were applied, and the responses of these samples were studied for 8.7 ps after photo-excitation.
As explained in Chapter 3, FDI allows to retrieve both the surface dynamics and dielectric properties thanks to its measurement of the change of reflectivity amplitude r and phase ϕ.

I.2.1 Nature of the interface

The nature of the interface is determined *via* the parameter β_r, linked to the variation of r measured (see Chapter 3, Equation 3.24). The Figure 4.5 represents the scattering plot of β_r, retrieved from FDI measurement as a function of the pump-probe delay.
The β_r parameter shows no significant variation during the whole experiment for all impinging fluences. As explained in Chapter 3, since its value stays close to 1, it implies that the surface of GeTe is still steep. This has two consequences. First, revealing the nature of the surface: the sample is either solid or liquid during the whole experiment. But it is also a pre-requisite to the further use of the Fresnel equations to deduce the dielectric function using Equations 3.31.

I.2.2 Propagation of a liquefaction front

In Figure 4.6 the displacement is represented as a function of the pump-probe delay. It is calculated thanks to the measured phase shifts in S and P polarizations applied to Equation 3.29. Below 1 ps, no clear displacement can be observed.
Starting from 1 ps, the response differs depending on the intensity of excitation. Fluences $F \geq 26$

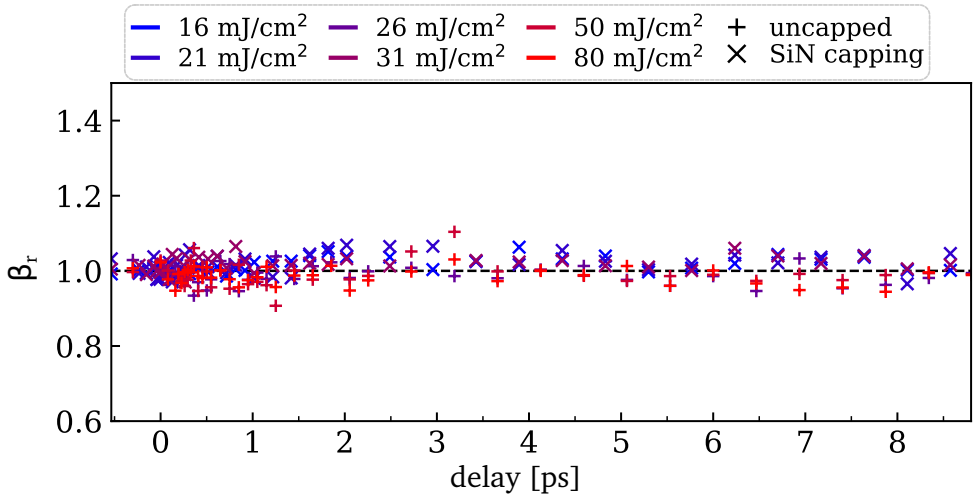

Figure 4.5 – *Evolution of the β_r parameter as a function of pump-probe delay [296].*

mJ/cm^2 show an interesting behaviour: there is an increasing negative displacement, up to ~4 nm at $t = 8.7$ ps for the highest fluence. As it was previously checked through the β_r parameter, the interface is effectively still sharp. Therefore, this displacement indicates an actual shrinkage of the material, not just a lack of matter due to a gas or a plasma. This picosecond timescale is seemingly corresponding to the beginning of thermal effects, as the electron-phonon constant is of the same order [45, 51, 297]. The maximal velocity of shrinkage is found to be 460 m/s, *i.e.* about 20% of the sound velocity in typical chalcogenides such as Se or $Ge_xSb_ySe_z$ with $v_s \sim 2\times 10^3$ m/s [298], which is therefore non negligibly fast, but still reasonable.

Still, the question is whether this shrinkage is the proof of an excited solid state or of a liquid phase with higher density. Though surprising, an anomalous melting with a higher density was previously observed for other GeTe compounds [122, 128]. Therefore, both hypotheses are plausible. To deal with this issue, we consider the volume of excited material. It is limited by the optical penetration depth δ of the pump, determined *via* the following Equation 4.1, with λ the wavelength of the laser and κ the extinction coefficient of GeTe for the given laser wavelength.

$$\delta = \frac{\lambda}{4\pi\kappa(\lambda)} \tag{4.1}$$

For our GeTe sample, the penetration depth is estimated to be $\delta = 125 \pm 15$ nm for an irradiation with central wavelength 800 nm, in adequation with the study of Gu *et al.* [197]. As the shrinkage measured is proportional to the total melted/excited volume ratio and increases with time, it cannot be due to an excited phase.

It is more likely the development of a liquid phase that we detect. As represented schematically in Figure 4.7, the pump irradiation leads to the excitation of a thin layer of material. At first, its

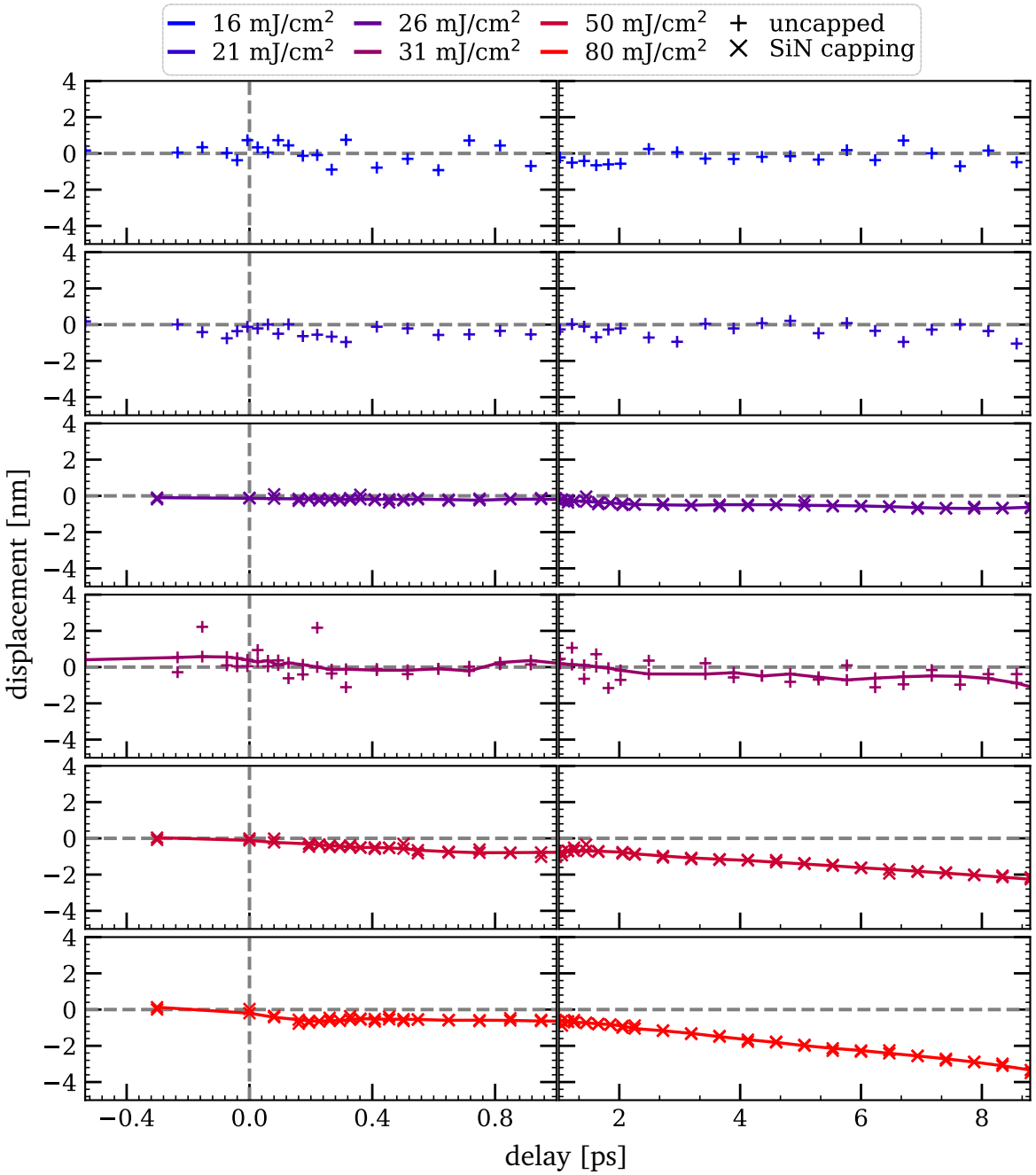

Figure 4.6 – *Displacement of a-GeTe interface as a function of fluence and pump-probe delay. Adapted timescales are used for the short and long times, as the dynamics does not take place on the same scale [296]. Solid lines are guides to the eyes.*

thickness is limited by the penetration depth determined previously. The lattice heats under the influence of electron-phonon scattering, and a part of the excited phase becomes liquid when the melting temperature of GeTe is reached. This liquid phase is characterized by a larger density than that of the initial amorphous phase. As a consequence, as the volume of melted layer increases due to thermal transport, after 1 ps, the shrinkage becomes large enough to be detected. The phenomenon goes on with the propagation of the liquefaction front, inducing the continuous

displacement of the interface that is found *via* FDI measurements.

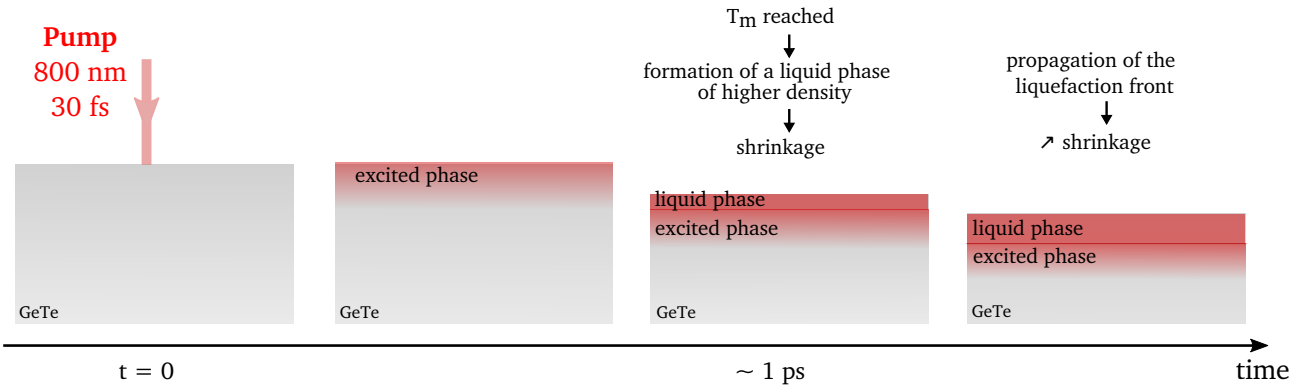

Figure 4.7 – *Schematic representation of the liquid front propagation in GeTe.*

I.2.3 A transition towards another state

This theory of a liquid forming is partly backed up by post-experiment *phase-contrast microscopy* images. This technique is an optical microscopy technique which basically transforms the phase shift induced by the sample on a laser that is sent through the sample into a variation of brightness in the images (~ enhancement of the contrast) [299]. One of these images is shown in Figure 4.8, for a spot resulting from an irradiation fluence of 25 mJ/cm^2. The presence of fingerprints pattern is clearly visible. We have shown, by studying this phenomenon in more details (see Reference [48]), that these wrinkles are the signature of a liquid phase. Indeed, they result from the stress resistance of the SiN layer which is more rigid than the melted chalcogenide layer. Basically, when the chalcogenide melts, the internal stress of the SiN layer relaxes slightly within the irradiated area. As this latter is delimited by the rigid borders of the non-irradiated region, the only direction of relaxation possible is the vertical one. By cooling down, wrinkles appear, with a frequency that is dependent on the laser intensity and thickness of the SiN layer.
With the parameters of our experiments, wrinkles are only observable for the fluences that were identified as those characterized by a shrinkage. As a consequence, it seems fair to expect that the shrinkage measured by FDI is the proof a liquid phase developing.

The phase-contrast microscopy images do not only give information about the presence of a liquid phase. The first striking observation in Figure 4.8 is the fact that the irradiated spots (area 2 in Figure 4.8) do not have the same refractive index as the surrounding material (area 1). Basically, they are not of the same color. This means that the final state (relaxed state) of the GeTe thin film has been changed compared to the pristine (initial as-deposited) state. The material has effectively undergone a transition. The question is: towards which state?

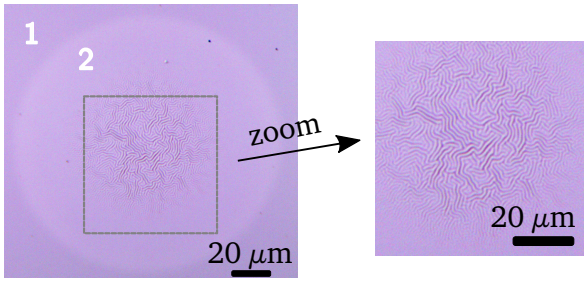

Figure 4.8 – *Post-experiment phase-contrast microscopy image of a spot irradiated with a fluence of 25 mJ/cm*^{2}.

While a lot of studies on PCMs have been (and still are) conducted with the aim of reproducing the same phenomena as in memory devices, this is not especially the case here. Here, we do not especially seeking parameters to perform reversible transitions between the crystalline and amorphous states [2]. It is the process of excitation that we are interested in. The final state could have happened to be the crystal one. However, as we observe an irradiated area by means of *high-angle annular dark-field scanning transmission electron microscopy* (STEM-HAADF [300]), shown in Figure 4.9A, no sign of any structuration that would evidence the formation of crystalline pattern, nor segregation of Ge, is detected. Nano-beam electron diffraction was performed on two chosen spots of the previous slice: (1) in the irradiated area, and (2) closer to the bottom of the GeTe layer, expected to have not been impacted by the laser. Figure 4.9B clearly shows no difference between the two spots. Moreover, they are both characterized by the absence of diffraction pattern.

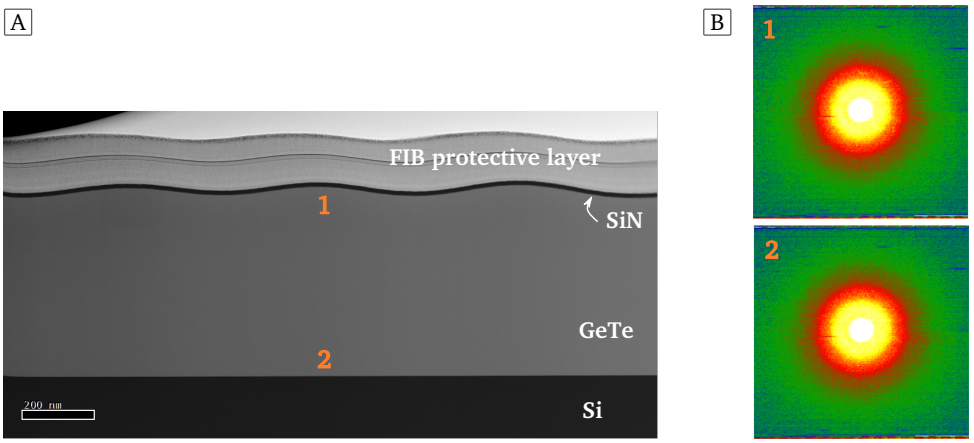

Figure 4.9 – *(A) Post-experiment HAADF-STEM performed on a slice of GeTe irradiated by 30 mJ/cm*^{2}. *This slice was previously prepared by focused ion beam technique (FIB). (B) Corresponding nano-beam electron diffraction of the two points 1 and 2 identified on the subplot A [48]. The point 2 being on a far greater distance to the interface than the penetration depth, it is a reference of the pristine material.*

[2]The repetition rate of the probe and the pump being 1 kHz, a rotating target holder was used to avoid any issue of irreversible transition and/or energy accumulation (as described in Chapter 3, Figure 3.9).

From all these observations, we deduce that the transition is occurring towards an amorphous state, yet different from the initial one.

I.3 Dielectric properties

The shrinkage of *a*-GeTe implies that its structure should have also changed after the photo-excitation. And that makes the dielectric function a good observable to detect such variation. Indeed, it accounts for both the electronic and structure contributions. The evolution of the dielectric function's real ε_r and imaginary ε_i parts with time are represented in Figures 4.10 and 4.11. These two responses are very different.

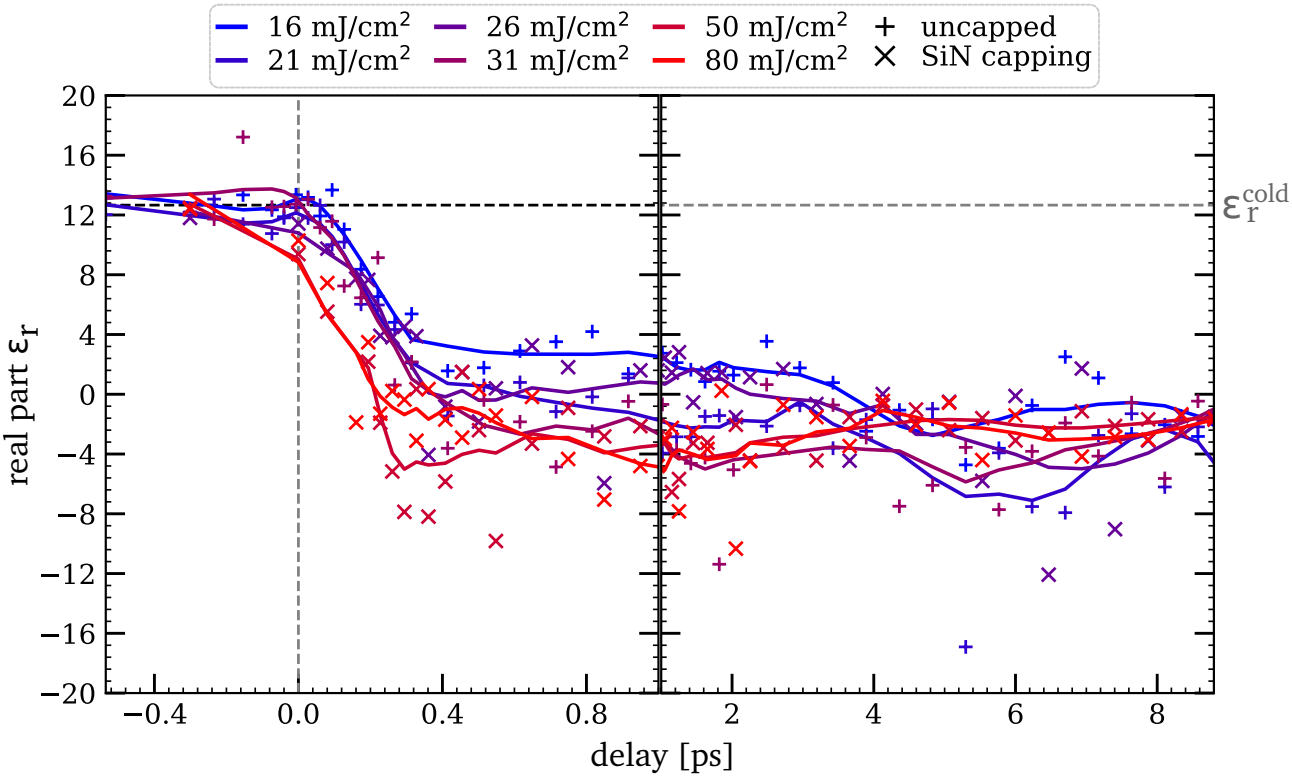

Figure 4.10 – *Real part of the dielectric function of a-GeTe obtained from time-resolved FDI measurements [296]. Solid lines are guides to the eyes.*

The real part of the dielectric function shows an ultrafast decrease as soon as the pump irradiates the *a*-GeTe sample, and reaches a saturation regime in about 300 fs. From an initial value of ε_r^{cold} = 12.66, represented by horizontal dashed line in Figure 4.10, it transitions to a value of ε_r = -1 ± 2. The variation of pump fluence has here no effect on ε_r, and the timescale on which it happens is also completely different from the one that was characteristic of the surface dynamics observed previously.

On such a short timescale, it cannot be thermal effect that are responsible from the variation

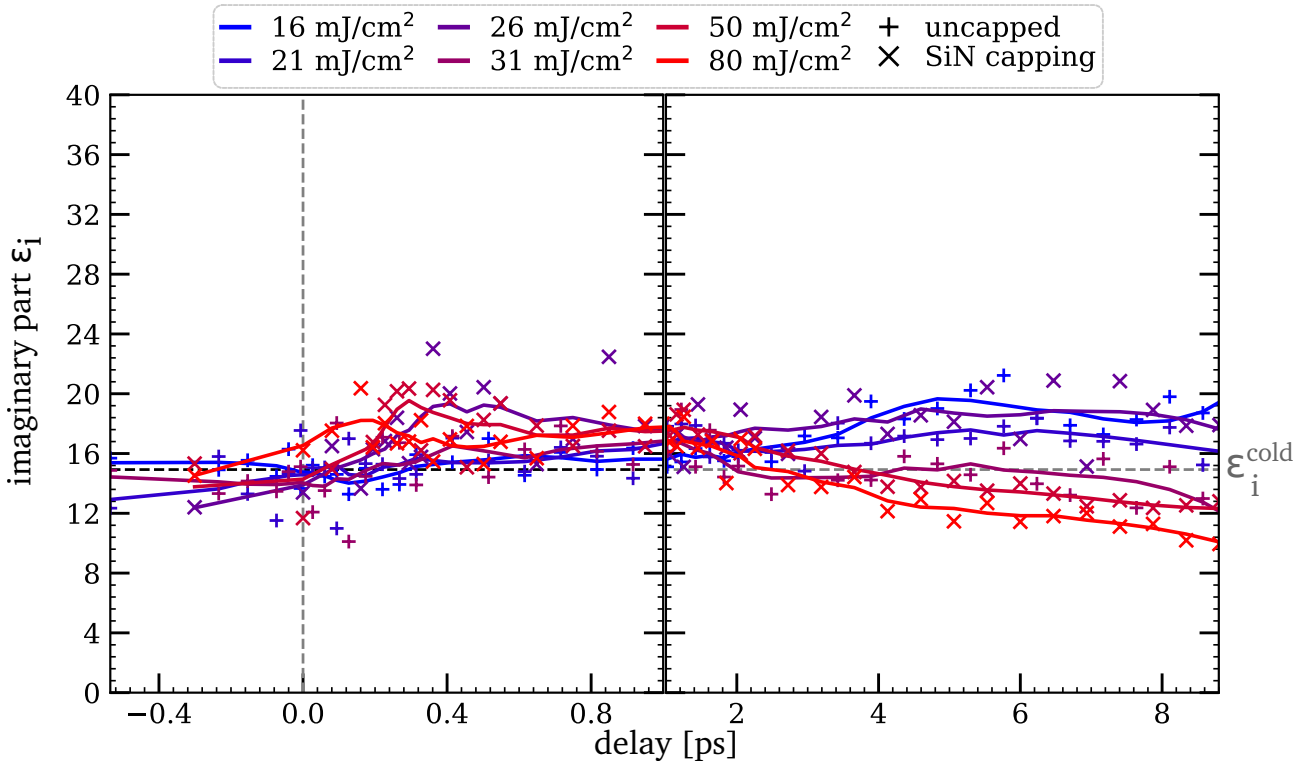

Figure 4.11 – *Imaginary part of the dielectric function of a-GeTe obtained from time-resolved FDI measurements [296]. Solid lines are guides to the eyes.*

measured. Indeed, the electron-phonon coupling is estimated to be about the picosecond [45,297], and from the evolution of the surface dynamics, it seems fair to estimate it is also the case here.

The evolution of the imaginary part of the dielectric function with time is very different from its counterpart ε_r. On the short times, ε_i does not vary much. However, after 1 or 2 ps, the impinging fluence separates the response into two categories:

- for low fluences ≤ 26 mJ/cm^2: ε_i increases
- for higher fluences ≥ 31 mJ/cm^2: ε_i decreases

Overall, though this variation of ε_i can be measured, it is really negligible compared to that of the real part and there is no clear explanation behind this fluence dependency.

Conclusion of the experiments on *a*-GeTe

Thin films of 500 nm of *a*-GeTe alloy were pumped at 800 nm by a 30-fs laser. This photo-excitation triggers a transition towards another amorphous phase which has different optical properties from the pristine one.

We decipher two types of transition. A non-thermal one, which occurs on a very short timescale of hundreds of femtoseconds for all fluences, and a thermal one, only for high fluences, happening on a longer timescale and resulting in the shrinkage of the material. This latter is due to the development of a liquid phase of higher density. Even without the presence of wrinkles, we could still see a change of color in phase-contrast microscopy images, evidencing that a phase change occurs in all cases, regardless of the development of the liquid phase.

II *Ab initio* molecular dynamics simulations of *a*-GeTe

FDI and other post-experiment analyzes cannot tell exactly what is the mechanism at play even though we detect a transition. Simulations are still the method of choice to do that. Unfortunately, it is not possible to separate clearly the electronic and atomic contributions from the optical response measured *via* FDI. A deeper understanding of the structural changes can be obtained *via* simulations, provided that it resembles the experimental scenario. In our case, it means that we need to simulate out-of-equilibrium states to reproduce the transient states encountered due to femtosecond laser excitation.

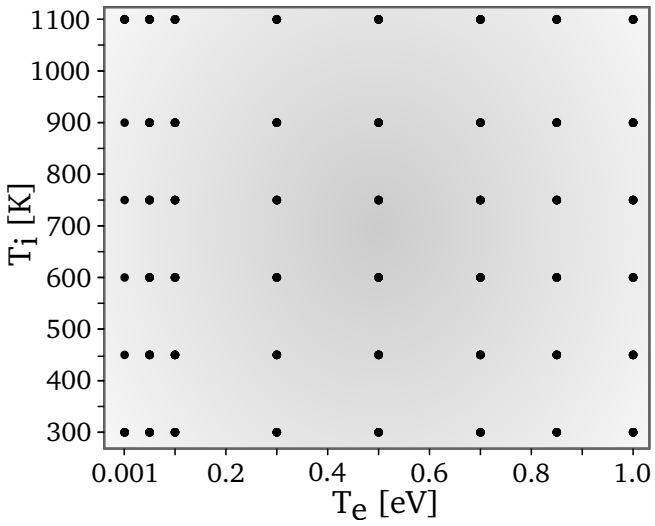

Figure 4.12 – *Each black dot correspond to a simulated T_e-T_i pair for GeTe.*

All the procedure and parameters for the generation of the initial amorphous state and its further excitation with *ab initio* molecular dynamics (AIMD) are detailed in Chapter 2, Section II. Basically, reproducing the photo-excitation of a fs laser was done here by changing the width of the electron distribution such that we obtained an overall range of electronic temperatures T_e from 0.001 eV, the non-excited state, up to 1 eV (11600 K), an highly excited state. It was clear from the experiments that GeTe melts for the high fluences, so the ionic temperature T_i was also varied between 300 K, room temperature, up to a lattice temperature above the melting point (T_m =

998 K [121]) such that $T_{i,max}$ = 1100 K. These (T_e - T_i) parameters are shown by black dots in Figure 4.12.

II.1 Structural analysis of the non-excited *a*-GeTe

The non-excited *a*-GeTe configuration is calculated with T_e = 0.001 eV and T_i = 300 K. The analysis of its structure is detailed hereafter.

Pair distribution function

The pair distribution (PDF) of *a*-GeTe, Figure 4.13, is consistent with previous studies [69, 83, 92, 98, 114–118, 177, 301]. Except for the Te-Te partial PDF, they all exhibit one pronounced peak and then a flatness with only a few periodic little bumps characteristics of the loss the long range order in amorphous states. The first neighbouring shell is characterized by the presence of homopolar Ge-Ge bonds as well as Ge-Te bonds and a very tiny proportion of Te-Te bonds, as seen by the small peak at 2.86 Å. The position of the first sharp peak of the total PDF, r_{GeTe}, represents the average bonding length in the material. Here it is estimated to 2.66 Å. This is slightly smaller than in some other DFT studies such as in Akola *et al.* [98], where it as found to be 2.78 Å.

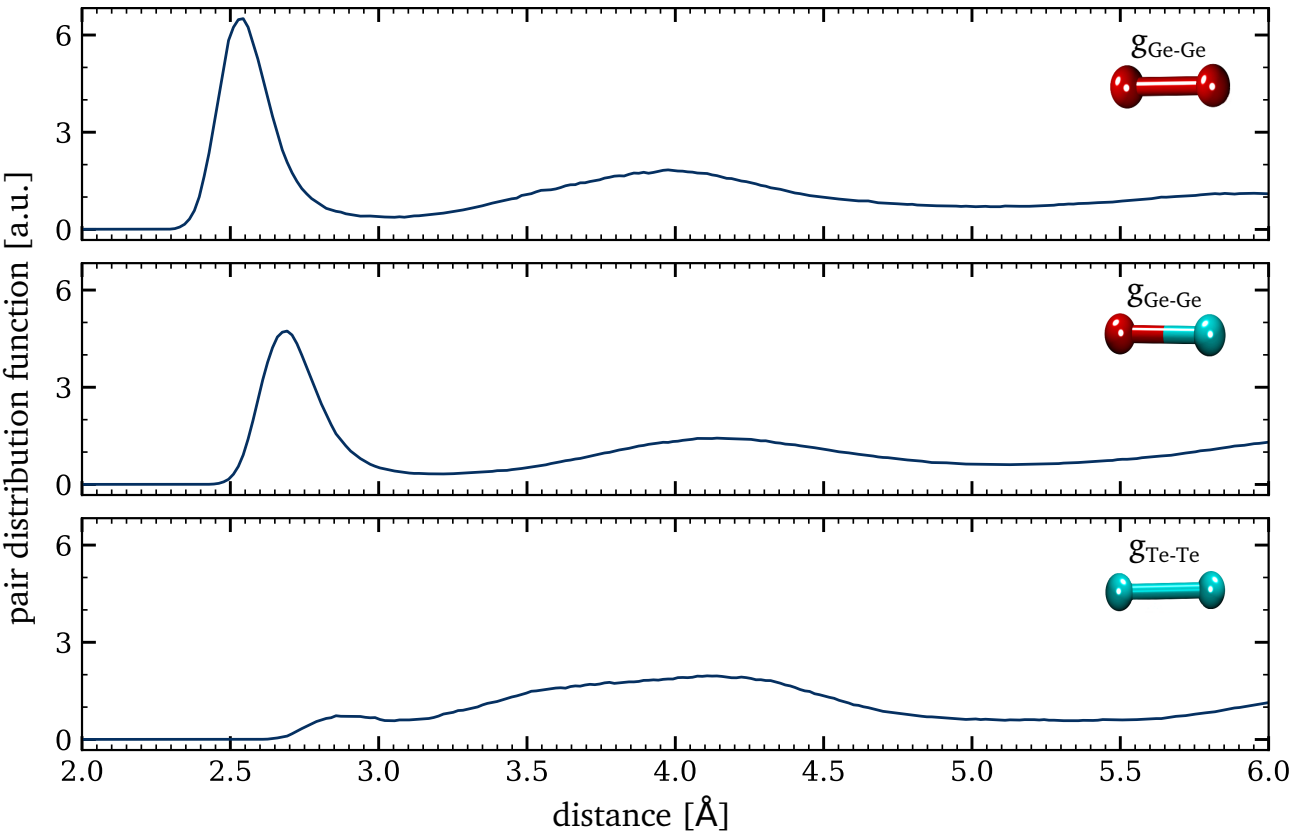

Figure 4.13 – *Pair distribution function of simulated a-GeTe.*

Overall, the bond lengths obtained for this initial state with the analysis of the partial PDF are in good agreement with previous DFT studies, but a bit further from the experimental measurements, as presented in Table 4.1.

Bond type	This study	Exp. literature	Simu. literature
Ge-Ge	2.54 Å	2.47-2.48 Å [92, 114, 117]	2.45-2.60 Å [69, 98, 116, 117]
Ge-Te	2.69 Å	2.60-2.65 Å [92, 114, 117]	2.60 - 2.78 Å [69, 83, 98, 115, 116, 118]
Te-Te	2.86 Å		2.86 Å [98]

Table 4.1 – *Comparison of the bonds lengths determined for the simulated non-excited state of a-GeTe with literature (experiments and simulations).*

Angular distribution

The distribution of angles around Ge and Te atoms are rather well defined, as seen in Figure 4.14. As expected, Ge atoms are found with angles ~104°, close to the 110° of ideal tetrahedral sites. The coordination number (~ the number of neighbours, see Chapter 2) of Ge, n_{Ge}, being 4.15, the great majority of the Ge atoms in this initial state seems to be in tetrahedral local environments. The distribution of angles for the Te atoms is less smooth, but still display a peak centered at 95°, in close agreement with the expected 90°. The coordination number n_{Te} equals 2.36, which is in adequation with previous studies, and does not allow us to define a specific type of environment.

Tetrahedra

Angles and number of coordination are consistent with a (distorted) tetrahedral environment for the Ge atoms. In order to check if Ge atoms are actually in tetrahedral sites or if it is just a lucky coincidence, the percentage of Ge atom in tetrahedral environment has been calculated. Several methods are possible: consideration of the orbitals (also known as C6 method), counting the tetrahedra by considering the angles and number of neighbours (which might be quite a handful given the distorted environment),... Here we consider the order parameter. The quantity d_4 is defined as the distance of an atom Ge to its fourth closest neighbour and d_0 the average of three closest ones [113,279]. The ratio d_4/d_0 reveals the local order of the atom of interest. Based on the ranges given in Reference [113], if this ratio d_4/d_0 is comprised between 1.0 and 1.1, it is a tetrahedral site.

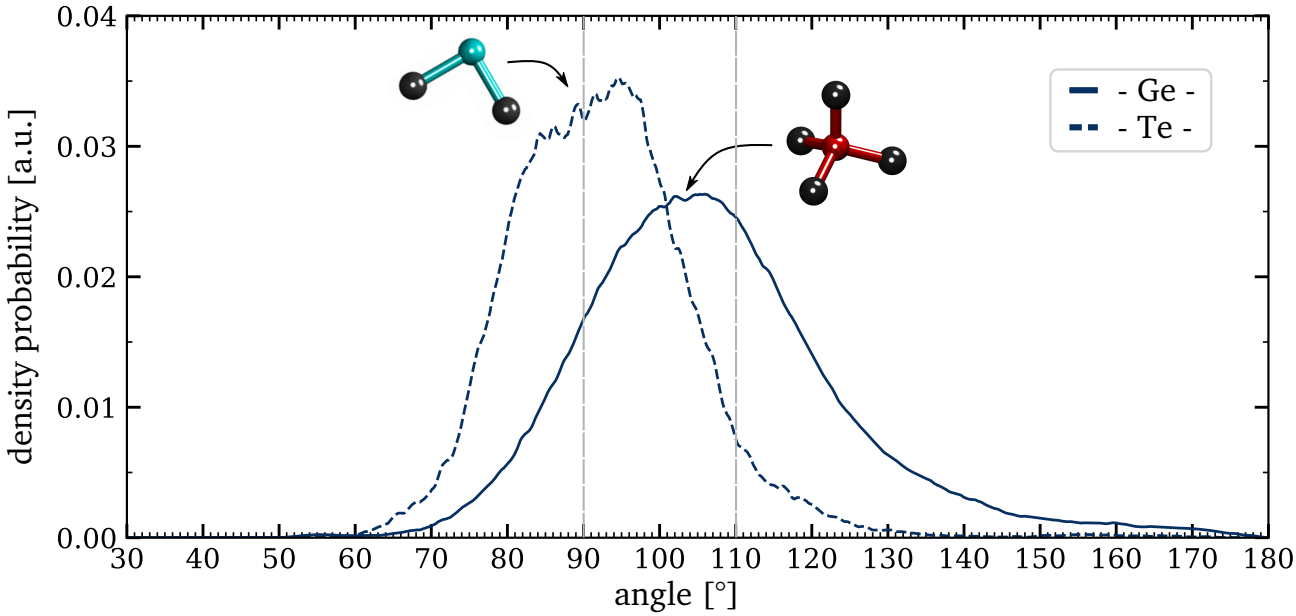

Figure 4.14 – *Angular distribution of simulated non-excited a-GeTe. The vertical dashed lines correspond to ideal angles in tetrahedral (110°) and octahedral (90°) configurations (all types of bonds considered).*

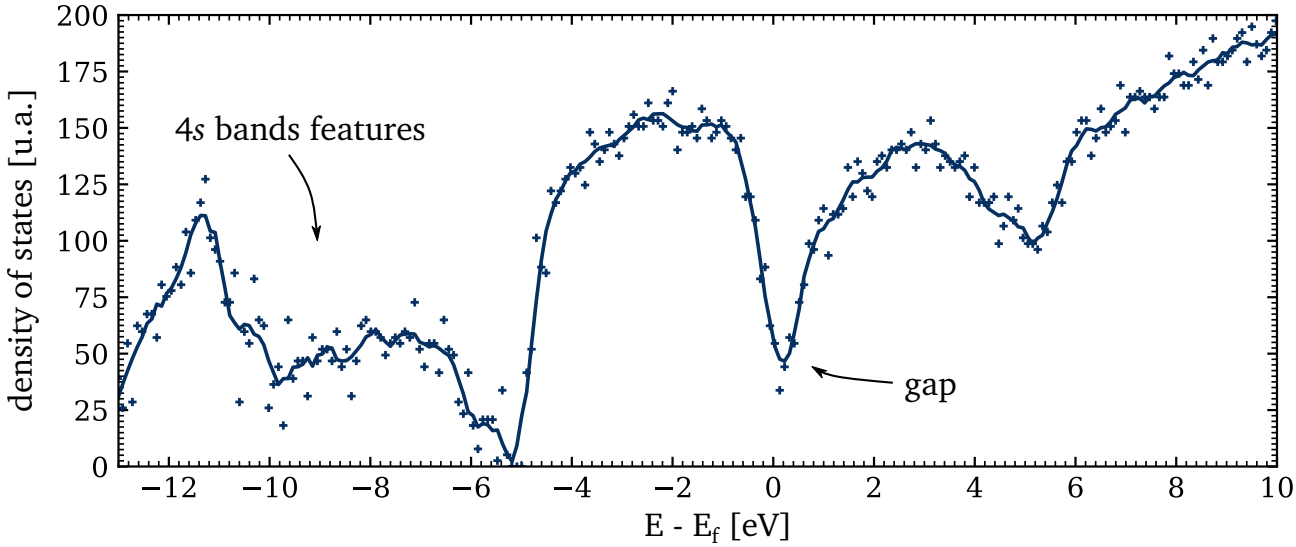

Figure 4.15 – *Density of states of non excited a-GeTe. The Fermi energy E_f corresponds the valence band maximum, determined by VASP. Solid lines are guides to the eyes.*

We find that in the non excited state, the simulated *a*-GeTe possesses 80% Ge atoms that are in tetrahedral sites. Only 5% of Ge are determined in octahedral sites with a coordination number of 5 or 6.
Although the method to generate the cell was the melt-quench one, choosing the cell that best fitted the as-deposited (AD) *a*-GeTe's structure proves to be relevant: we find, as expected for an AD GeTe, a prevalence of the tetrahedral sites over the octahedral ones.

Density of states

A large number of tetrahedra implies a large number of homopolar Ge-Ge bonds [113]. These bonds are known to form localized defect states in the bandgap of GeTe, which hinders the correct estimation of the bandgap. GeTe, whose optical band gap is quite small by nature (estimated to be ~ 0.8 eV [291, 292]), and the use of GGA functionals (known to underestimate the optical band gaps in semiconductors) explains why the density of states of the pristine material in Figure 4.15 is gapless.

II.2 Link with the experiment

The challenge to compare the results of simulation with experiments, is to find the correct electronic temperature that could reproduce the photo-excitation by the 30-fs pump. As explained in Chapter 2, Section II.4, this is done by considering the relative variations of the dielectric function for the shortest times.

Analysis of the surface dynamics revealed thermal effects starting from about 1 ps. Therefore, only times before 0.8 ps will be considered for this comparison. This ascertains that the lattice is still cold ($T_i \sim 300$ K), such that any variation that is measured cannot be due to lattice thermal effects, but only the electronic contribution.
As ε_i^{EXP} does not show variation on the timescale considered, it is the real part of the dielectric functions ε_r^{EXP} and ε_r^{SIMU} that will be compared.
The relative variation of ε_r is computed for the simulations with $T_i = 300$ K and all T_e, and the experiments for $t < 0.8$ ps. It is interesting to note that for simulation, we have a clear dependency of ε_r^{SIMU} with the intensity of excitation (represented by the parameter T_e). In experiments, it was not the case, the variation of ε_r^{EXP} was independent of the impinging fluence (Figure 4.10).

This comparison of $\Delta\varepsilon^{SIMU}/\varepsilon_0^{SIMU}$ and $\Delta\varepsilon^{EXP}/\varepsilon_0^{EXP}$ shown in Figure 4.16 reveals that in order to reproduce the experimental variation, the best fit is the application of an electronic temperature of $\boxed{T_e \sim 0.5 \text{ eV}}$. The adequation is not optimal for all fluences, yet from all our simulation, this value of T_e is the closest one for all cases.

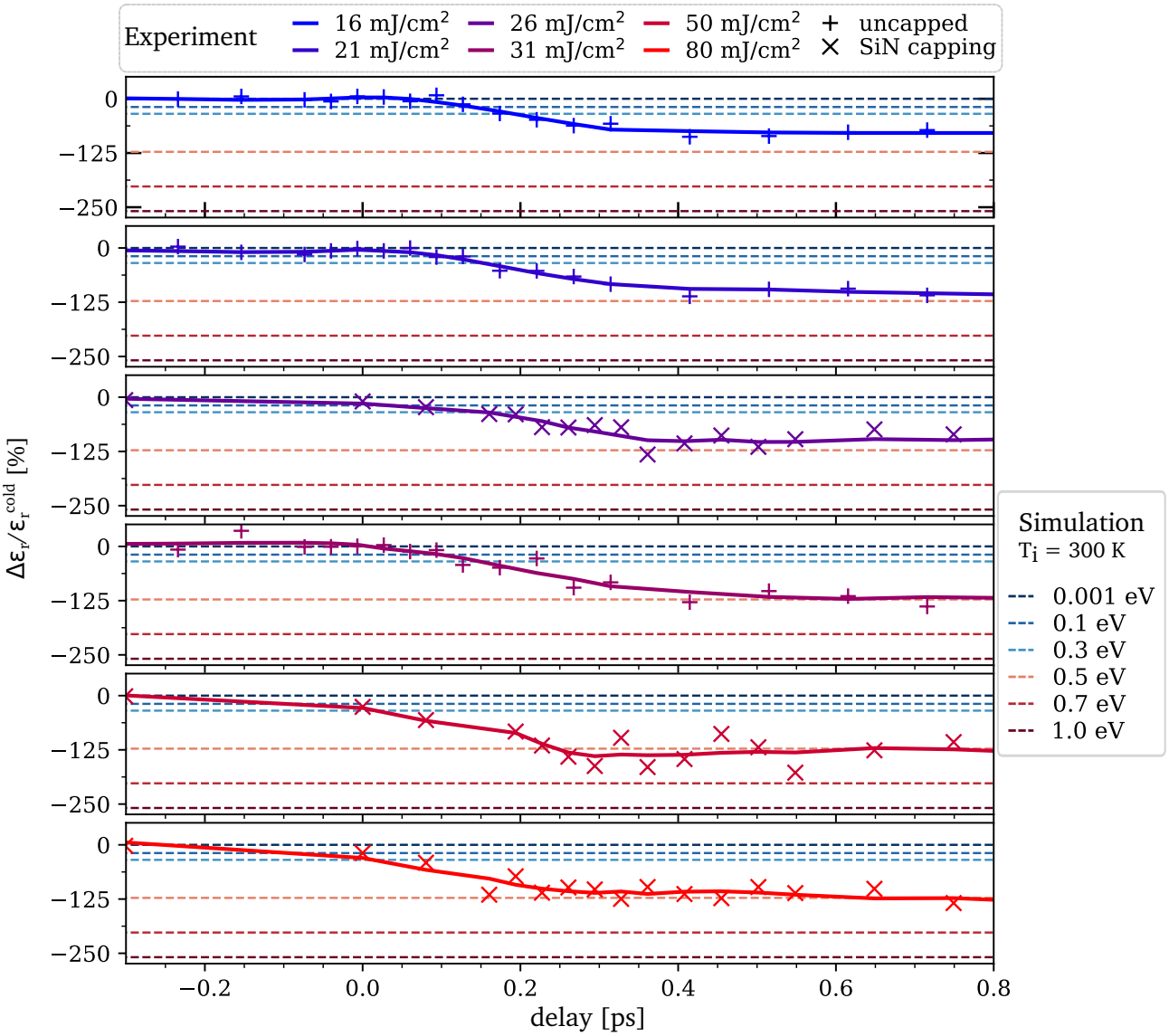

Figure 4.16 – *Comparison of the relative variation of dielectric function from simulations and experiments [296]. Solid lines are guides to the eyes.*

From the determination of this value of T_e, five cases, represented in Figure 4.17, are chosen to study the evolution that is expected of GeTe after the photo-excitation, following the overall processes detailed in Chapter 1, Section I.1:

A. T_e = 0.001 eV, T_i = 300 K - non excited case or "cold" material. This configuration represents the pristine *a*-GeTe. Its structure has been described in the Section II.1.

B. T_e = 0.5 eV, T_i = 300 K: out of equilibrium state. The application of electronic excitation reproducing the laser irradiation triggers an out-of equilibrium state as only the electrons absorb energy from the laser. The corresponding T_e was determined right before.

C. T_e = 0.3 eV, T_i = 600 K: out of equilibrium state. After some time, the electron and the

lattice start exchanging energy, thus leading to the heating of the lattice (and a cooling of the electrons).

D. T_e = 0.1 eV, T_i = 900 K: supercooled liquid. Electrons and phonon continue their coupling, the lattice heats. This case is right under the melting point T_m = 998 K [121].

E. T_e = 0.1 eV, T_i = 1100 K: equilibrium liquid state. To reproduce the liquid state observed experimentally, we simulate a liquid configuration, which is at equilibrium ($T_e \sim T_i$) above the melting temperature.

The cases *A*, *B* and *E* are guesses made from the information extracted during the experiments: initial state, passage through a liquid state...However, for the *C* and *D* configurations, the parameters are chosen arbitrarily, intermediate between the *B* and *E* ones.

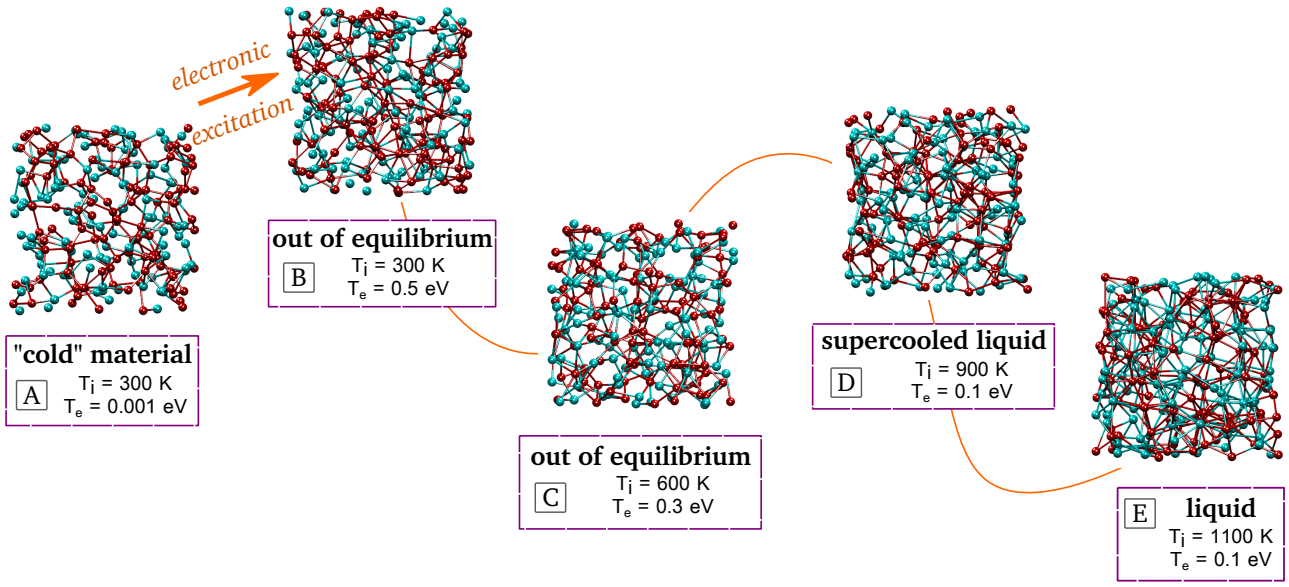

Figure 4.17 – *Five configurations chosen to reproduce the evolution of photo-excited a-GeTe.*

II.3 Structural variation induced by excitation

To understand the local changes triggered by the excitation, the structure of the five chosen case was analyzed.

II.3.1 Electronic properties

Density of states

The DOS, shown in Figure 4.18, does not exhibit drastic changes with the excitation.

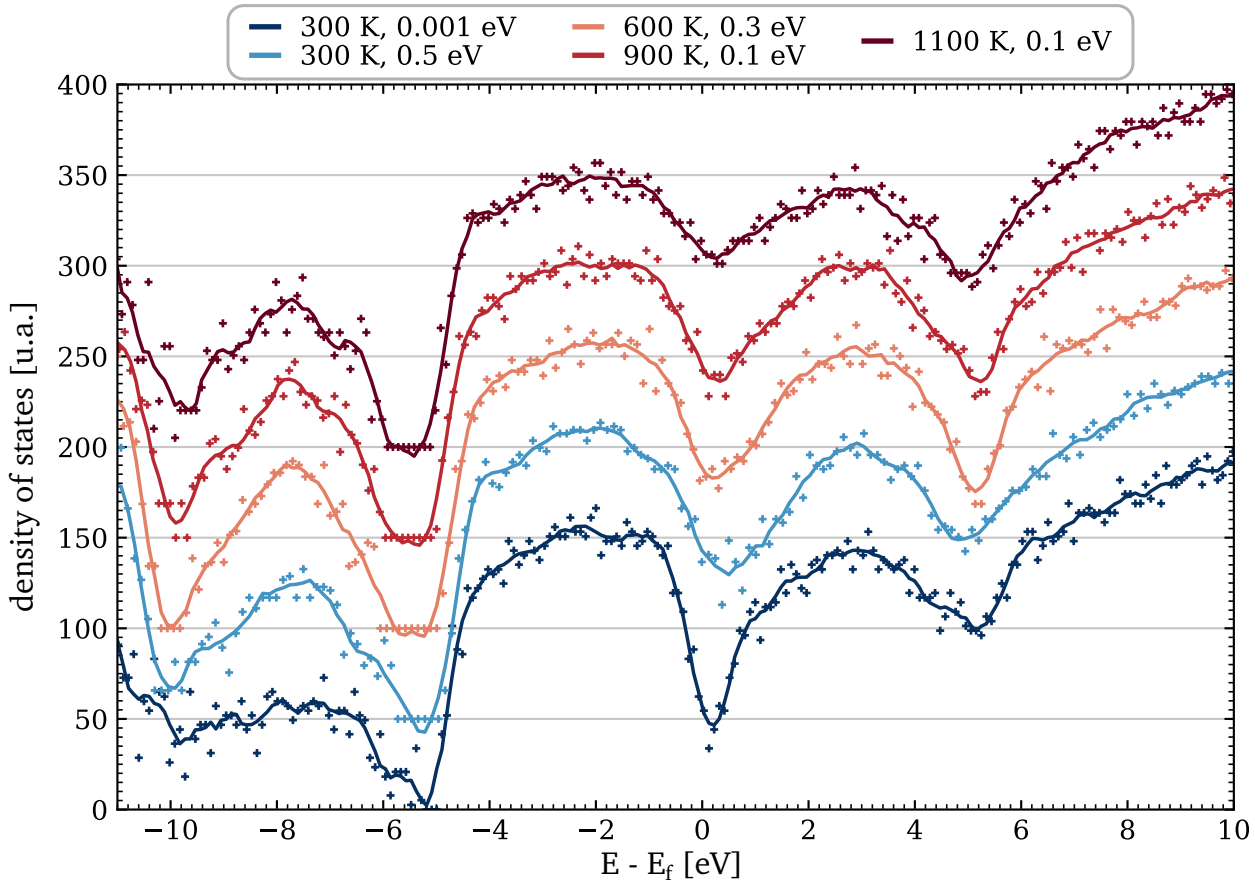

Figure 4.18 – *Density of states for all five cases of GeTe considered [296]. Solid lines are guides to the eyes.*

The main change is at $E - E_f = 0$, where the pseudo-band gap, which was already not much open, closes even more. It leads to a more metallic material, which is an phenomenon similar to non-thermal effects in covalent materials [302].

Dielectric function

The simulated dielectric function *vs* wavelength is represented in Figure 4.19. The vertical dashed line highlights the probe wavelength (532 nm). For the imaginary part, there is a clear lack of sensitivity for wavelengths under 650 nm. The real part, ε_r decreases under photo-excitation and further relaxation.

II.3.2 A shift of local environment

Pair distribution function

The first striking observation of the PDF, represented in Figure 4.20 is the similarity of the excited and liquid states. The excitation leads to a shift away from the initial state resulting in a lengthe-

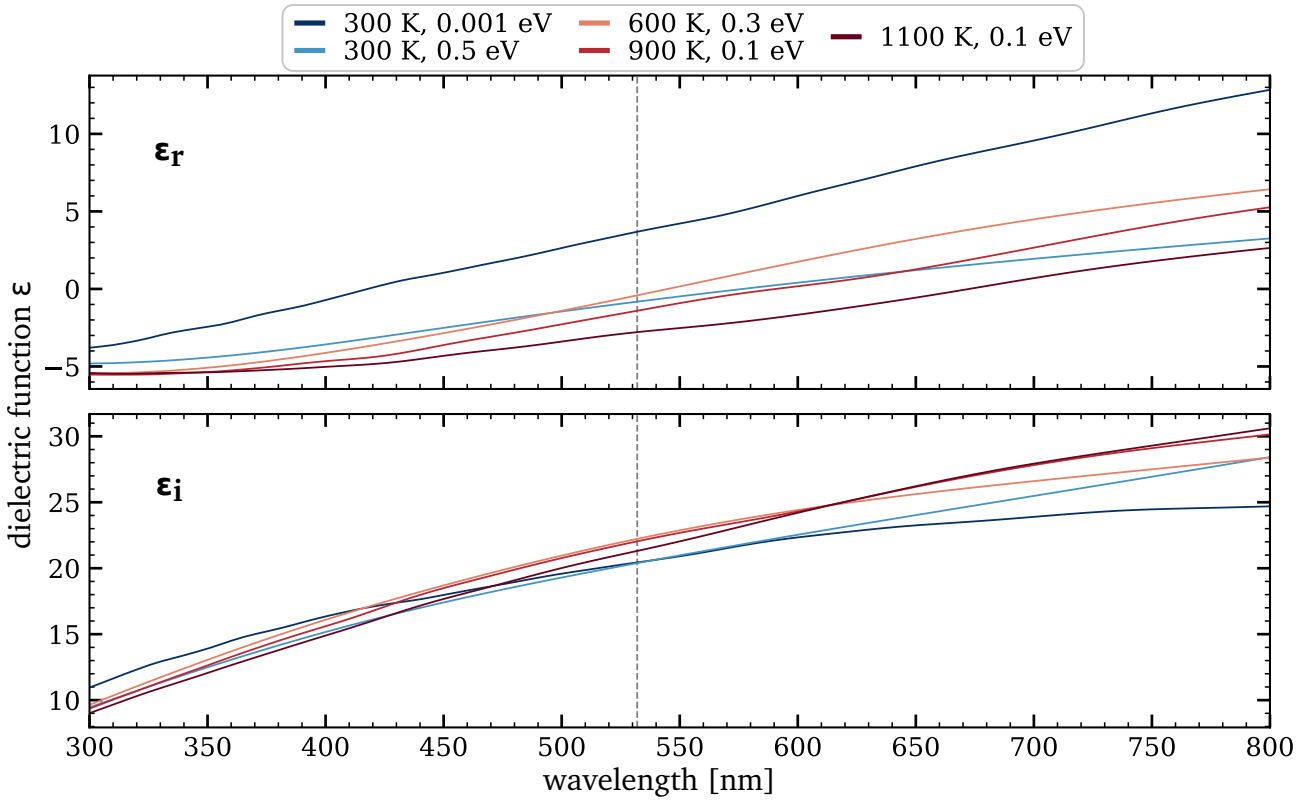

Figure 4.19 – *Dielectric function as a function of wavelength for the five cases characteristic of the evolution of photo-excitation of a-GeTe. The vertical dashed line recalls the experimental probing wavelength* $\lambda_{probe} = 532$ *nm.*

T_i [K]	T_e [eV]	$r_{\text{Ge-Ge}}$ [Å]	$r_{\text{Ge-Te}}$ [Å]	$r_{\text{Te-Te}}$ [Å]	r_{GeTe} [Å]
300 K	0.001 eV	2.54	2.69	2.86	2.66
300 K	0.5 eV	2.66	2.79		2.79
600 K	0.3 eV	2.69	2.81		2.81
900 K	0.1 eV	2.69	2.81		2.79
1100 K	0.1 eV	2.69	2.81		2.81

Table 4.2 – *Bond lengths determined from the position of the first peak of the PDF distribution (uncertainty on the peak position between 0.01 Å for sharp peaks and 0.05 Å for broad, not very intense peaks).*

ning of all types of bonds, explicited in the Table 4.2. As the lattice heats, the bonds lengthen a bit more, but the position of the peak does not change after that. Only the distribution flattens, such that liquid GeTe is characterized by much loosely defined neighbours. This seems in contradiction with the experimental shrinkage observed, but in the simulations, the overall cell actually tends to shrink too (see Appendix C).

The bond lengths values determined from the PDF are not agreeing as much as the pristine state with literature: XRD measurements and DFT simulations of liquid GeTe (965 K and 1032 K) lead to a value of 2.57 Å for the Ge-Ge bonds [69] while we find 2.69 Å, and 2.74 Å compared to 2.81 Å for Ge-Te bonds. Another DFT simulation of the liquid state at 1073 K results in an average bond length r_{GeTe} of 2.72 Å, quite far below the 2.79-2.81 Å determined here.
As the bonds lengths are not determined adequately using GGA functionals in DFT calculations, this discrepancy with the experimental values was expected. It is also understandable that the other DFT calculations are not so close. As it was stated previously, in most cases the simulations of *a*-GeTe are done in order to resemble to the melt-quenched experimental case, while we chose a configuration closer to the structure of an as-deposited phase. Some properties of the initial state might persist in the liquid state.

Characteristic angles

The angles surrounding each species are important to determine the changes of local environment that might have occurred. The Figure 4.21 reveals that the Ge (left) and Te (right) atoms undergo very different changes under excitation.
The distribution of angles around Te is characterized by a thermal broadening, but the mean peak is still at the same position of 95° in average. The situation is really different for Ge. As soon as *a*-GeTe is excited, the distribution shifts towards lower values of angles, determined to be 94°. While there is also here a thermal broadening, this shift holds at least until we reach the liquid state. This value of angle for a liquid state is in agreement with previous studies [69, 81, 303].
Similarly to the pair distribution function, the high resemblance between the out of equilibrium and liquid states is striking. Apart from the effects of thermal agitation, the characteristics values are the same.

Coordination numbers

From the analysis of the angle distributions, it is fairly expected that the Ge atoms see a change of their local environment. The coordination numbers listed in Table 4.3 show an increase up to 5-6 (7 for the liquid state). With this angle value of 94° and coordination numbers of 5-6, the logical conclusion is that Ge atoms are shifting towards octahedral sites. The Te atoms' coordination

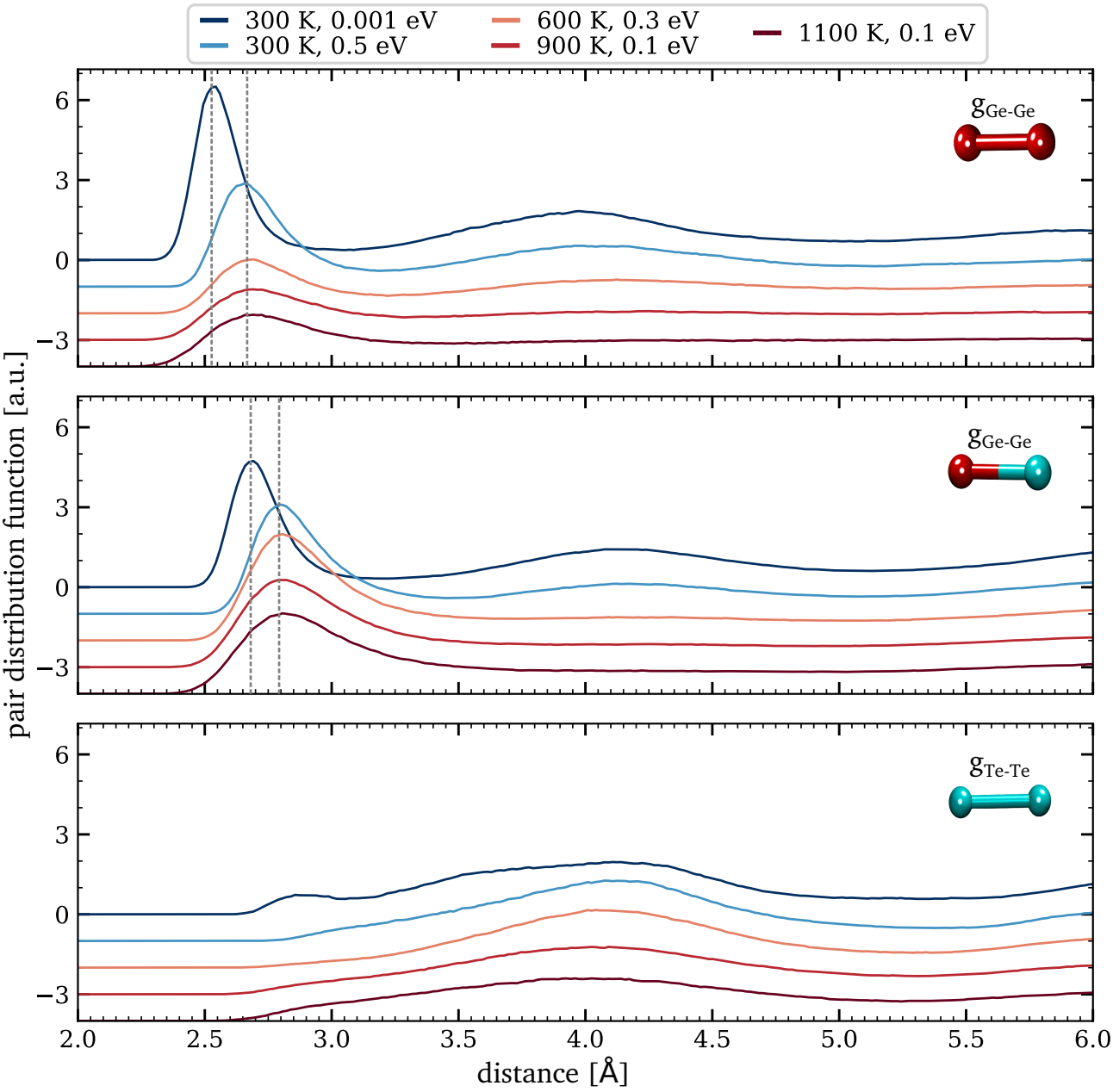

Figure 4.20 – *Pair distribution function of the simulated a-GeTe [296]. Vertical dotted lines correspond to the maximum peak positions.*

number also increases yet the configuration remains octahedral.

A non-thermal transition

The excitation results quite immediately in an out of equilibrium state which is fairly similar to the liquid state in terms of bonding properties. The key question is whether this out-of-equilibrium state is a liquid in the thermal sense or still an amorphous state (non-thermal liquid).
Investigating this idea, the mean square displacement (MSD) was calculated for each case and

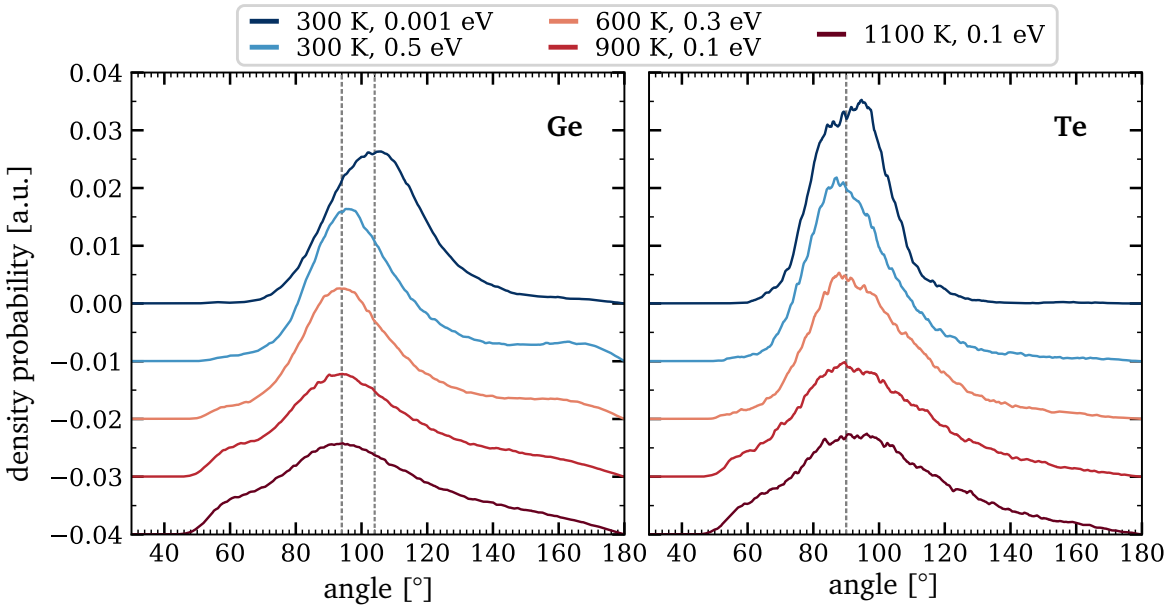

Figure 4.21 – *Angular distribution of simulated out of equilibrium a-GeTe [296]. Vertical dotted lines correspond to the maximum peak positions.*

T_i [K]	T_e [eV]	n_{Ge}	n_{Te}	r_{cut} [Å]
300 K	0.001 eV	4.15	2.36	3.10
300 K	0.5 eV	5.25	3.42	3.35
600 K	0.3 eV	4.88	3.69	3.33
900 K	0.1 eV	5.41	4.08	3.40
1100 K	0.1 eV	7.06	6.16	3.73

Table 4.3 – *Coordinations numbers n with the corresponding cut-off radius r_{cut} used. The precision on n is ± 0.01-0.03.*

represented in Figure 4.22. A clear difference is observed for T_i = 300 K and T_i > 300 K. To characterize this difference, the diffusion coefficients were calculated from the slope of the MSD *vs* MD time (detailed formula and explanation in Chapter 2). The diffusion coefficients D deduced from MSD fitting using Equation 2.53 are listed in the Table 4.4. When T_i > 300 K, GeTe is identified as a liquid state. The value of D reaches then 30 to 200 times the value of the initial state $D_{init} \sim 3.2\times10^{-7}$ cm^2/s, in the same order of magnitude as values that can be found in the literature for the liquid state [98]. For the special case of T_i= 300 K, T_e = 0.5 eV, though there is an increase of the slope of the MSD compared to the initial state (which shows in the values of D), it is ambiguous whether the material should still be considered as an amorphous (solid) state or a very viscous supercooled liquid state.

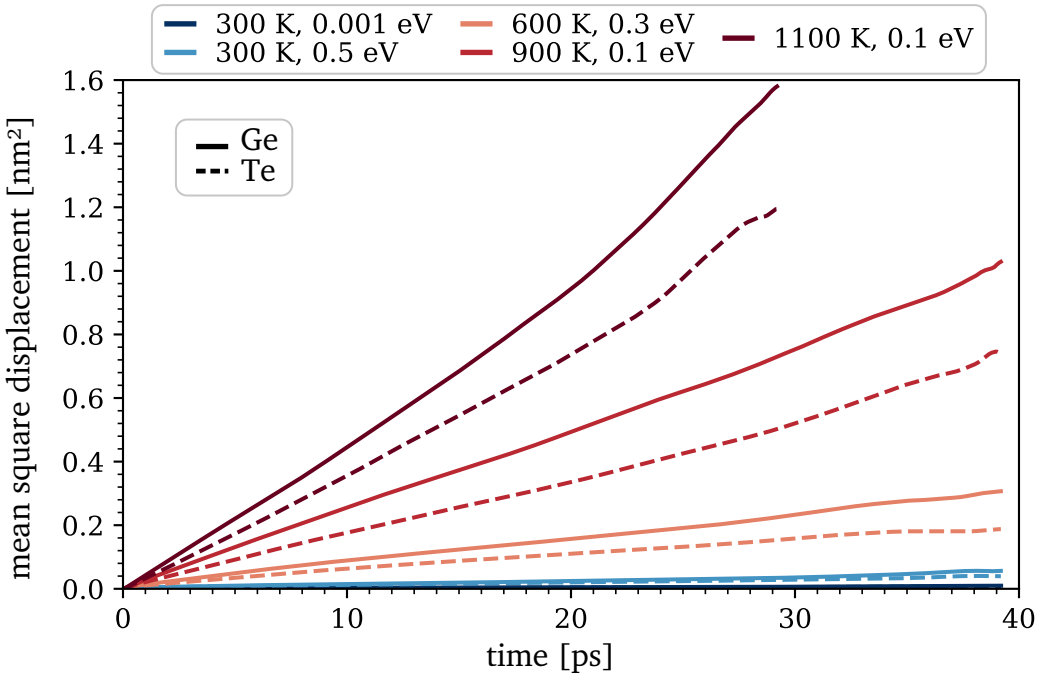

Figure 4.22 – *Mean square displacement of a-GeTe.*

T_i [K]	T_e [eV]	D_{Ge} [cm^2/s]	D_{Te} [cm^2/s]
300 K	0.001 eV	0.0035×10^{-4}	0.0030×10^{-4}
300 K	0.5 eV	0.0198×10^{-4}	0.0158×10^{-4}
600 K	0.3 eV	0.1294×10^{-4}	0.0890×10^{-4}
900 K	0.1 eV	0.4155×10^{-4}	0.2855×10^{-4}
1100 K	0.1 eV	0.7698×10^{-4}	0.6072×10^{-4}

Table 4.4 – *Diffusion coefficients D extracted from the MSD.*

Vibrational density of states

In out-of-equilibrium states, the phonon density of states, also known as the vibrational density of states (VDOS) has been seen to undergo a softening under excitation [86,260], which means that the bonds are weaker under excitation. The VDOS is represented in Figure 4.23. The total VDOS in the initial state is dominated by the Ge contribution for the high frequencies, and a balanced contribution for low frequencies. When *a*-GeTe is excited, the VDOS of the Te atoms does not change much (which is consistent with our prior analyzes of the PDF and distribution of angles), whereas the VDOS of the Ge atoms is shifted towards lower frequencies, resulting in a softening of the Ge phonon modes. This latter observation seems consistent with the loosened neighbours effect that could be seen in the pair distribution function.

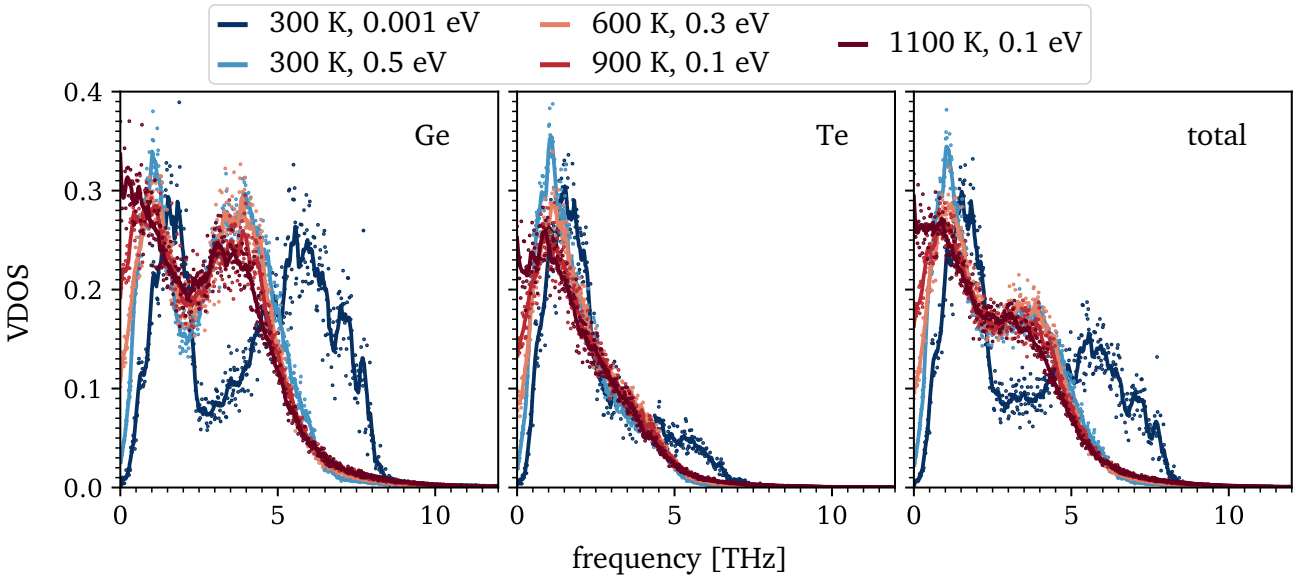

Figure 4.23 – *Vibrational density of states (VDOS) of a-GeTe out of equilibrium states. Solid lines are guides to the eyes. [296]*

II.3.3 A re-entrance of Peierls distortion ?

The switching of the Ge atoms brings out an interrogation: in the crystal phase, Ge atoms in octahedral environment phases are characterized by an alternation of short and long bonds, a phenomenon called Peierls distortion (see Chapter 1, Section II.1.2). Here, considering the out of equilibrium states, do the Ge atoms (now also in octahedral sites) also end up in this type of distorted local environment? This is especially interesting given the fact that several studies evidenced the re-entrance of a Peierls distortion in the liquid phase.
To answer this question, the angular-limited three-body correlation (ALTBC) map of the configuration was calculated. We will focus on the Te-Ge-Te type of bonds as it has been shown that the alternation of species is favored by the Peierls distortion [81, 131]. The maps for other types of bonds can be found in Appendix C, Section IV.

As explained in the Chapter 2, the ALTBC correlates the distance of two successive almost aligned bonds. Restraining the angle to a deviation of 25° from the ideal aligned configuration (consisting in an angle of 180° between the two bonds) implies that all the Ge in tetrahedral sites will not contribute to the calculation of the ALTBC. This is why the initial *a*-GeTe, whose ALTBC is in Figure 4.24A, exhibits only a small reminescence of Peierls distortion with a maximum correlation being off-diagonal with (r_1 = 2.9 Å, r_2 = 3.1 Å).

The excitation of this pristine state implies a change of correlation pattern: from a kind of "boomerang" pattern, it becomes triangular, with an harmonisation of the bond lengths in the

out-of-equilibrium state (Figure 4.24B). Then further heating leads to a kind of cross-pattern (Figure 4.24C and D), with a maximum located at (2.9, 2.9 Å). Therefore, we cannot conclude as in the previous studies. In our case, the liquid state does not exhibit a Peierls distortion, but harmonized successive bonds. Still, it is noticeable that there is a clear increase of the aligned bonds proportion, given the fact that the maximum correlation intensifies when exciting and transitioning to the liquid phase.

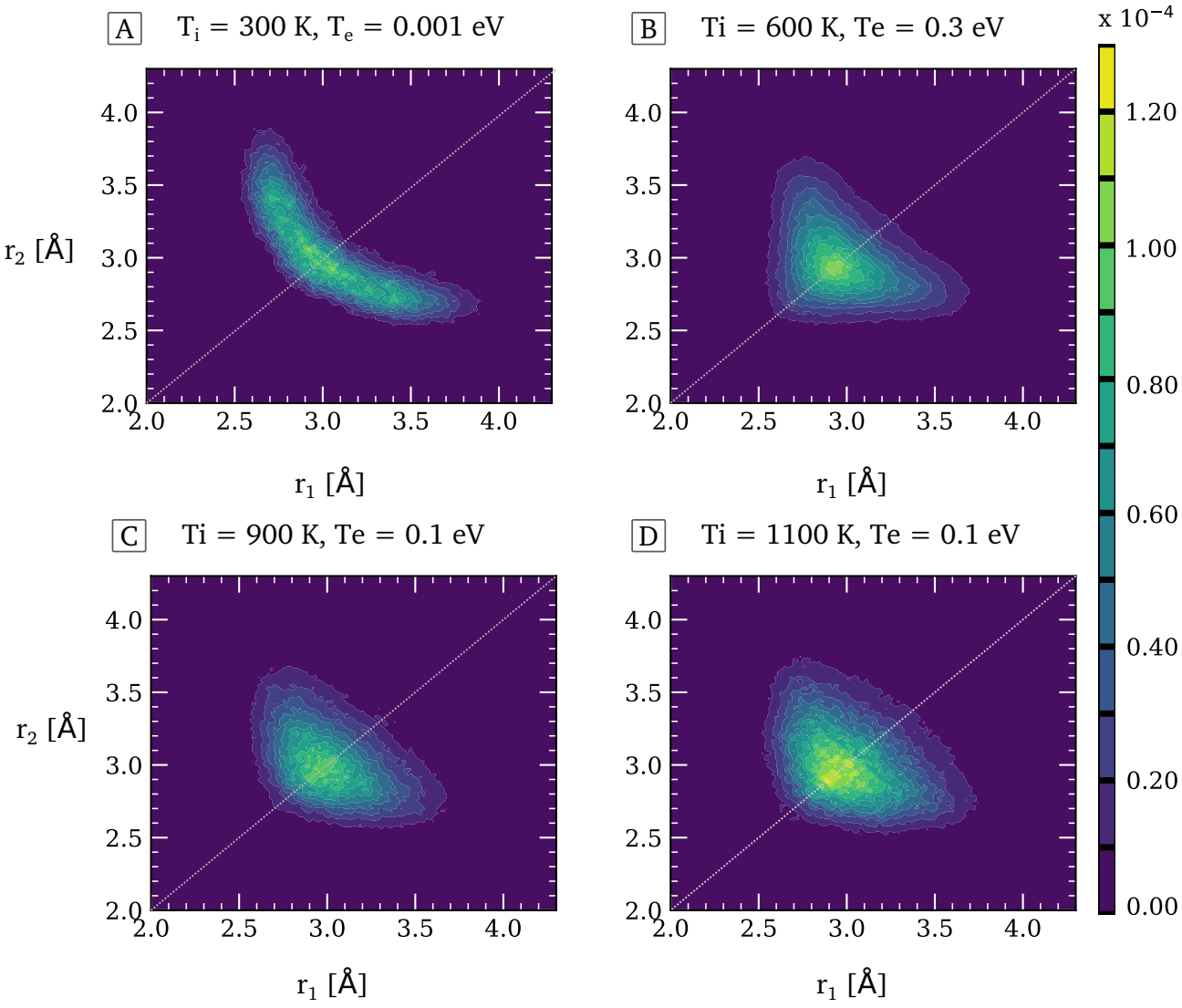

Figure 4.24 – *Angular-limited three-body correlation (ALTBC) of simulated a-GeTe. The intensity of the correlation between the two successives bonds r_1 and r_2 identifies the most probable bond lengths for those two when their angle is limited to 180°± 25° [296]. Only the alternating bonds Te-Ge-Te are considered here.*

Conclusion on investigation of the excitation of *a*-GeTe

The excitation of *a*-GeTe was investigated using femtosecond-laser techniques. A 30-fs pump with 800 nm central wavelength triggered an ultrafast phase transition towards another amorphous state, whose properties are quite different from the pristine state.
Indeed, probing the first picoseconds after excitation with frequency-domain interferometry revealed a non-thermal transition occurring in $\sim$ 300 fs, detected through the dielectric function and leading to a more metallic state.
Another transition, thermal this time, is seen on a longer timescale: after about 1 ps, the development of a liquid phase leads to the shrinkage of the material. After about 8.7 ps post-excitation, we measured up to 4 nm of shrinkage: a non negligible variation of volume!

A deeper understanding of the excitation of *a*-GeTe was possible thanks to out-of-equilibrium AIMD simulations. Once that configurations that reflected best the excitation and relaxation states of the material were determined, the analysis of their structure revealed that the excitation of *a*-GeTe results in a non-thermal transition.
This is evidenced by most of the structural quantities computed: VDOS, pair distribution functions, angles,... all showing that the out of equilibrium states are very similar to the liquid state. Only thermal agitation disturbs slightly the distributions.

The overall scenario of *a*-GeTe excitation follows: at the beginning, the initial state of amorphous GeTe is full of Ge atoms in tetrahedral sites. When the pump impinges the sample, the excitation triggers a change of local environment of the Ge atoms towards octahedral sites. In less than 300 fs, this non-thermal switching is completed and results in an out-of-quilibrium state whose structure and properties can be identified as those of the liquid phase of GeTe.
With the electron-phonon coupling, the lattice heats and reaches the melting temperature T_m. Although the local structure does not change much now, the propagation of the liquid phase with a higher density leads to the continuous shrinkage of the material.

CHAPTER 5

DYNAMICS OF CHALCOGENIDE GLASSES THIN FILMS UNDER EXCITATION

Chalcogenide glasses are mostly studied for their applications in the domain of optics and optronics thanks to their properties of non linearity and transparency in the infrared domain [12]. Still, they are not limited to this domain. For example, the ovonic threshold switching (OTS) phenomenon, which consists in the switching between two amorphous states of contrasted resistivity under application of an electrical or light pulse, lead to their use as selectors in memory devices such as in the Xpoint cross-bar architecture present in the phase-change random access memory (PC-RAM) technology.

In Chapter 4, it was shown that a short light pulse irradiation can trigger a non-thermal transition in amorphous GeTe. Although there is a difference in the definition of an amorphous state and a glassy state (see Reference [14] and Introduction of this thesis), both types of phases are disordered ones. It is intriguing to see how differently chalcogenide glasses would response to a fs laser pumping compared to GeTe. Indeed, this latter belongs to the other aforementioned sub-category of chalcogenide: the phase-change memory materials (PCM). Though the threshold switching phenomenon does not express itself in the same way for PCM and OTS materials, we expect that light triggering will also induce an ultrafast response in the chalcogenide glasses studied here.

The protocol was similar to the one used for *a*-GeTe described in Chapter 4: the photo-excitation of three chalcogenide glasses ($Ge_{31}Se_{69}$, $Ge_{23}Se_{57}Sb_{20}$ and $Ge_{23}Se_{53}Sb_{19}N_5$) by a fs laser pump was investigated using frequency-domain interferometry (FDI). The surface nature and dynamics as well as the dielectric properties were retrieved from these FDI measurement and are presented

in Section I. In the Section II, *ab initio* molecular dynamics (AIMD) simulations were performed for several out-of-equilibrium excited states in the aim of a deeper understanding of the changes of structure that occurred on the local scale, with the calculation of the pair distribution functions, angles distributions, or proportion of tetrahedra.

Brief reminder of the structure of selenide chalcogenide glasses

Ge-Se glasses are characterized by the presence of a covalent network of tetrahedral $GeSe_4$ units that are either corner-sharing (CS) or edge-sharing (ES) [47, 154] (see Chapter 1, Figure 1.6). Ge-Se bonds as well as homopolar Se-Se bonds are present in the first neighbouring shell, but almost no Ge-Ge bonds.

With the addition of Sb-doping, Se-Sb bonds as well as Sb-Sb and Ge-Sb bonds are formed [47]. Though the first type of bonds has no particular drawbacks, the two latter have the major disadvantage of introducing band gap defects (unwanted in memory devices applications).

The subsequent addition of N dopant solves this issue: Ge-N bonds as well as Sb-N bonds are preferred to Ge-Sb and Sb-Sb bonds [47]. No N-N bonds are detected in the first neighbouring shell in the GSSN compound, and only a small proportion of Se-N bonds are present [156].

Ge-Se compound are characterized by a predominance of tetrahedral Ge [73,154,157], with angles found to be 80° and 100°, corresponding to the edge-sharing and corner-sharing configuration respectively (both illustrated in Chapter 1, Figure 1.7). Sb- and N-doping lead to a more octahedral configuration with angles close to 90° [206].

I Experimental results of the excitation of chalcogenide glasses

I.1 Samples and static optical characterization

These three chalcogenide glasses were not randomly chosen. $Ge_{30}Se_{70}$ is a glass, and was a promising compound as a potential selector element of a memory application. However, its large band gap (E_g^{GS} = 2.2 eV [47]) leads to a threshold voltage V_{th} that is too high and the material is subject to Ge segregation [288], making it unstable for long term applications. The addition of Sb element decreases greatly the band gap (E_g^{GSS} = 1.4 eV [47]) and therefore also V_{th}. Yet, the issue for this second compound is that homopolar Sb-Sb bonds are formed and induce a leakage current I_{OFF} that is too high. A solution is an additional doping of the material with nitrogen, which results in the breaking of the Sb-Sb bonds in favor of Ge-N and Sb-N bonds [23, 47] with

the compromise of a slightly higher gap ($E_g^{GSSN} = 1.8$ eV).

The three selenide compounds studied in this Chapter were prepared at the CEA LETI by P. Noé's team by magnetron sputtering. This method of physical vapor deposition (PVD) was explained in Chapter 4, Section I.1. The difference with GeTe lies in the use of a Se-rich GeSe target instead of a GeTe one. Doping with antimony was done by placing an additionnal Sb target, while N-doping was realized with the introduction of N_2 gas in the sputtering chamber.

In the three cases, a layer of chalcogenide alloy (with or without dopant) of 500 nm is deposited on a 1 mm thick undoped Prime CZ Si (100) substrate. All films were capped *in situ* with a 10 nm layer of SiN in order to prevent oxidation of the chalcogenide [281, 282]. The exact compositions, determined *via wavelength-dispersive x-ray fluorescence* (WDXRF) are $Ge_{31}Se_{69}$ (GS), $Ge_{23}Se_{57}Sb_{20}$ (GSS) and $Ge_{23}Se_{53}Sb_{19}N_5$ (GSSN). Basically, this method consists in irradiating the material and collecting the fluorescence emitted thanks to a dispersive detection system [304]. Characteristic emission lines can be associated to a given element. It is then possible to identify the corresponding element, and its proportion. To lighten the writing and reading, the three glasses will be abbreviated as GS, GSS and GSSN, in the same order as they were presented right before.

The refractive indexes, determined by ellipsometry measurements[1], are shown in Figure 5.1. Though the tendencies are similar, there are some noticeable differences between the three alloys. For example, we can compare the absorption properties of the three glasses at the laser pumping wavelength that will be used in the experiments: $\lambda_{pump} = 800$ nm. The optical properties for the specific cases of pump and probe wavelengths used in the following experiments (800 nm and 532 nm respectively) are listed in Table 5.1.

In the complex refractive index $N = n + i\kappa$, the imaginary term is called the *extinction coefficient*. This latter sizes with the absorption, therefore the more κ increases, the more the absorption of the material increases (see Appendix B).
In the case of our glasses, GS is the one with the smallest absorption at 800 nm, while GSS will most likely be the easiest to photo-excite due to its larger value of κ_{GSS}. Still, if we compare with GeTe, even GSS is expected to respond very differently to a 800 nm photo-excitation as $\kappa_{GeTe} \sim 10\kappa_{GSS}$ at this wavelength. This difference of absorption can also be seen in the optical band gap values, estimated *via* Tauc plot (see Appendix D) to 2.2 ± 0.4 eV for GS, 1.3 ± 0.2 eV for GSS and 1.5 ± 0.2 eV for GSSN (compared to 2.2 eV, 1.4 eV and 1.8 eV [47]).

[1]These ellipsometry measurements were done *via* a M-2000 J. A. Woollam ellipsometer at the angles of incidence 55°, 65°and 75°. Steps of 1.6 nm between 200 and 1000 nm then 3.4 nm above were used. Intrinsic software was used to fit the measurements and obtain n and κ. [283]

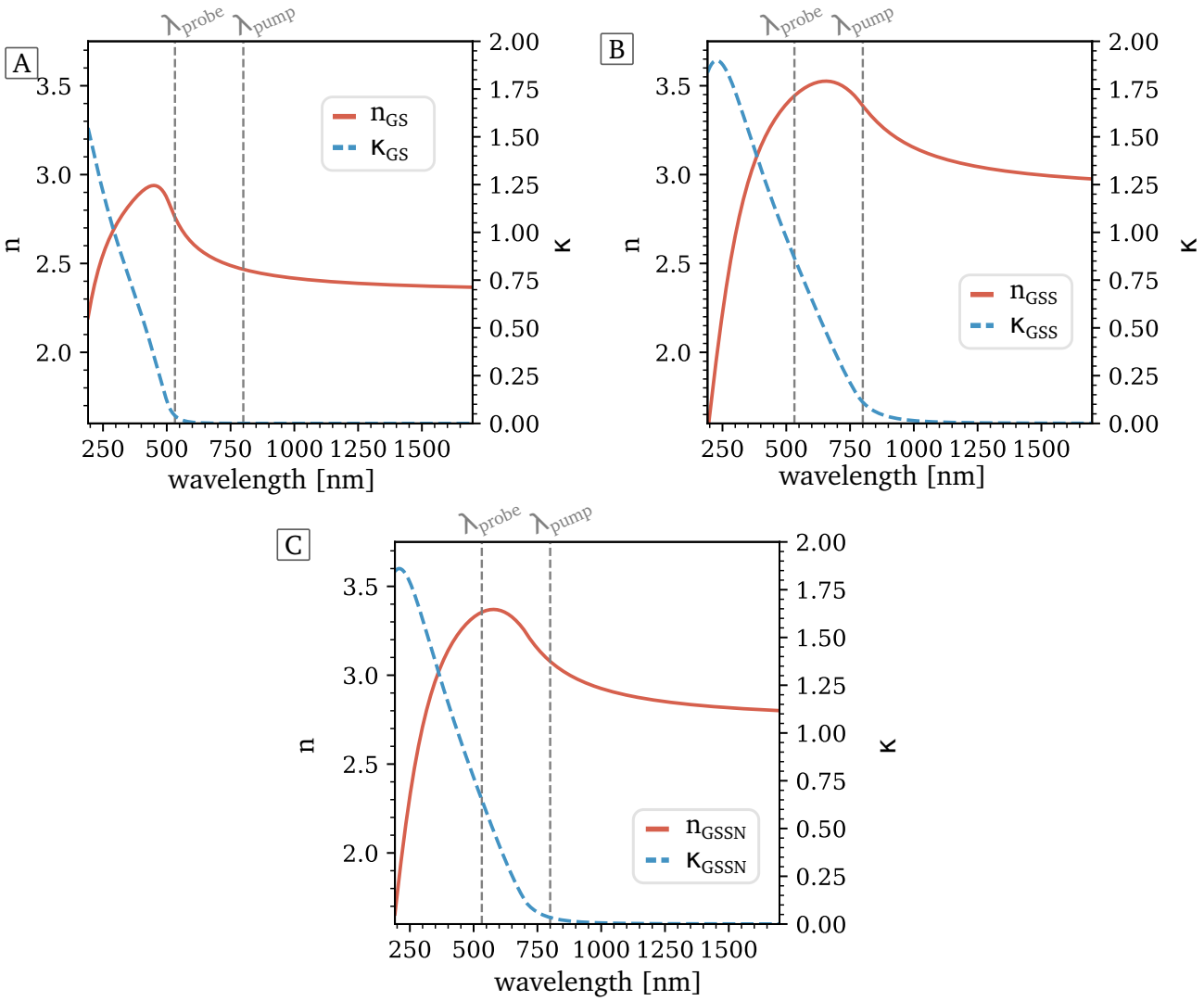

Figure 5.1 – *Refractive indexes $N = n + i\kappa$ of GS (A), GSS (B) and GSSN (C). The pump (800 nm) and probe (532 nm) wavelengths used in the experiments are highlighted with dotted lines.*

Composition		$Ge_{31}Se_{69}$ (GS)	$Ge_{23}Se_{57}Sb_{20}$ (GSS)	$Ge_{23}Se_{53}Sb_{19}N_5$ (GSSN)
532 nm	N^{cold}	2.76 + 0.04 i	3.44 + 0.87 i	3.35 + 0.65 i
2.33 eV	ε^{cold}	7.62 + 0.22 i	11.11 + 5.96 i	10.83 + 4.36 i
800 nm	N^{cold}	2.47 + 10^{-4} i	3.39 + 0.11 i	3.08 + 0.03 i
1.5 eV	ε^{cold}	6.09 + $10^{-3}i$	11.46 + 0.75 i	9.47 + 0.21 i
Band gap		2.2 eV	1.4 eV	1.8 eV

Table 5.1 – *Refractive index and dielectric function of the three chalcogenide glasses in their initial states for the two wavelengths of interest: $\lambda_{pump} = 800$ nm and $\lambda_{probe} = 532$ nm, extracted from static ellipsometry measurements.*

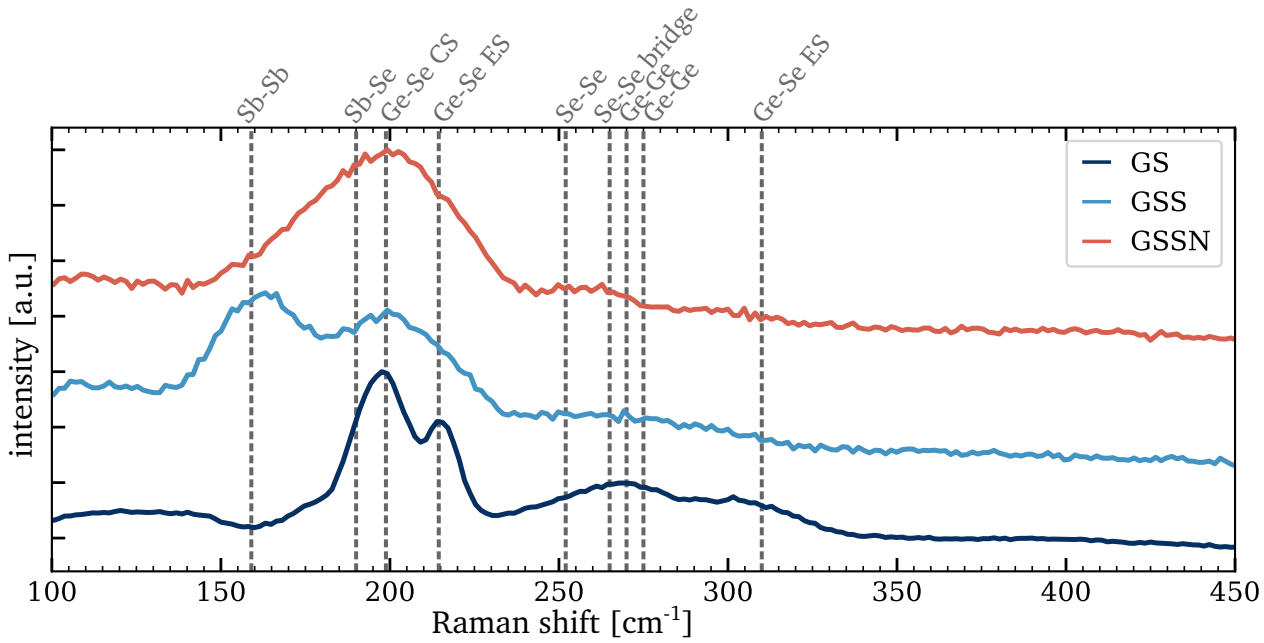

Figure 5.2 – *Raman spectra of the three chalcogenides [23, 66].*

An analysis of the structure *via* the investigation of the Raman modes was subsequently performed. The Raman spectra were collected using a Micro-Raman Renishaw InVia reflex with confocal microscope instrument, with $\lambda_{laser} = 532$ nm and an adapted intensity to prevent any modification during the measurements [23, 66, 283]. The full analyzes of these spectra are available in the references cited right before. Here, we will only briefly recall the main conclusions. The Raman spectra of the three chalcogenides glasses are shown in Figure 5.2. In GS, the predominant phonon modes come from the Ge-Se bonds presents in corner-sharing (CS) and edge-sharing (ES) tetrahedra [305], at 195-200 cm^{-1} and 215 cm^{-1} respectively (with an additional lower contribution to the ES at 310 cm^{-1}). We note the presence of Se-Se "bridges" between the tetrahedral units at 265 cm^{-1}, forming the covalent network described previously [73].
The addition of Sb in Ge-Se compound induces a clear change of structure: for GSS, a large peak emerges in the spectrum at 159 cm^{-1}, corresponding to the formation of homopolar Sb-Sb modes [306, 307]. Ge-Se modes from the CS- and ES- tetrahedra are still found in GSS, but the Sb-Sb modes cited right before are the predominant ones.
Finally, with the additional doping with nitrogen, the Sb-Sb modes quasi completely disappear and the main contribution is back to CS-tetrahedral modes, with a broadening that seems to include also pyramidal $SbSe_{3/2}$ at 190 cm^{-1} [306] and the ES tetrahedra.

Once that the initial state of the material has been characterized statically at the CEA LETI, the samples were brought to the CELIA laboratory to study their response to ultra-short pulses ir-

radiation. The optical investigation was conducted with the same protocol as the one used for *a*-GeTe: a 30 fs FWHM duration laser pump with a central wavelength of 800 nm was used to irradiate the samples. The response of the material was followed as a function of pump-probe delay using frequency-domain interferometry (FDI), with probe pulses of 80 fs FWHM of duration and a central wavelength of 532 nm. The repetition rate of the probe and the pump being 1 kHz, a rotating target holder was used to avoid the issue of irreversible transition and energy accumulation (as described in Chapter 3, Figure 3.9).

The majority of fluences used here are far below the ablation threshold of SiN, determined to be around $F_{th} = 110$ mJ/cm^2 [308]. The hypothesis of non-involvement of this capping layer in the measurement is therefore valid for these cases. However, for the highest fluences (typically above 130 mJ/cm^2), we approach and/or exceed F_{th}, suggesting that we might have to deal with some electronic effects that will disturb the FDI measurements. In fact, we actually see the deliminating of SiN for the highest fluences with phase-contrast microscopy, though we cannot be completely sure when the disturbances from the capping layer will take place exactly in terms of timescale. **As a consequence, although plotted in this Chapter, these questionable cases will not be interpreted (129 and 149 mJ/cm^2 for GSS, 130 and 165 mJ/cm^2 for GS).**

I.2 Surface dynamics

The analysis of FDI measurements allows us to extract the variation of phase and reflectivity from one probe pulse compared to the other one (see Chapter 3). From these variations, information on the surface can be retrieved.
The energy of the pump was varied for each material: six fluences from 47 ± 1 mJ/cm^2 to 165 ± 2 mJ/cm^2 were used on GS, twelve fluences spanning from 34 ± 1 mJ/cm^2 to 149 ± 2 mJ/cm^2 for GSS and five fluences from 44 ± 1 mJ/cm^2 to 100 ± 2 mJ/cm^2 were chosen for GSSN.

I.2.1 Nature of the surface

Thanks to the reflectivity measurements r_S and r_P, the β_r parameter gives an indication on the nature of the sample (see Chapter 3, Section II.2)
The evolution of β_r as a function of the pump-probe delay is represented in Figure 5.3 for all three chalcogenide glasses. All three glasses show the same behaviour during the 8.7 ps probed: β_r keeps a value of 1, implying that there is still a clear index step between the material and the air (all samples being capped by a Si-N layer, it was not necessary to perform the experiment in vacuum conditions). As a consequence, for all fluences and all materials considered, the irradiated sample is either in a solid or a liquid state in the time window probed.

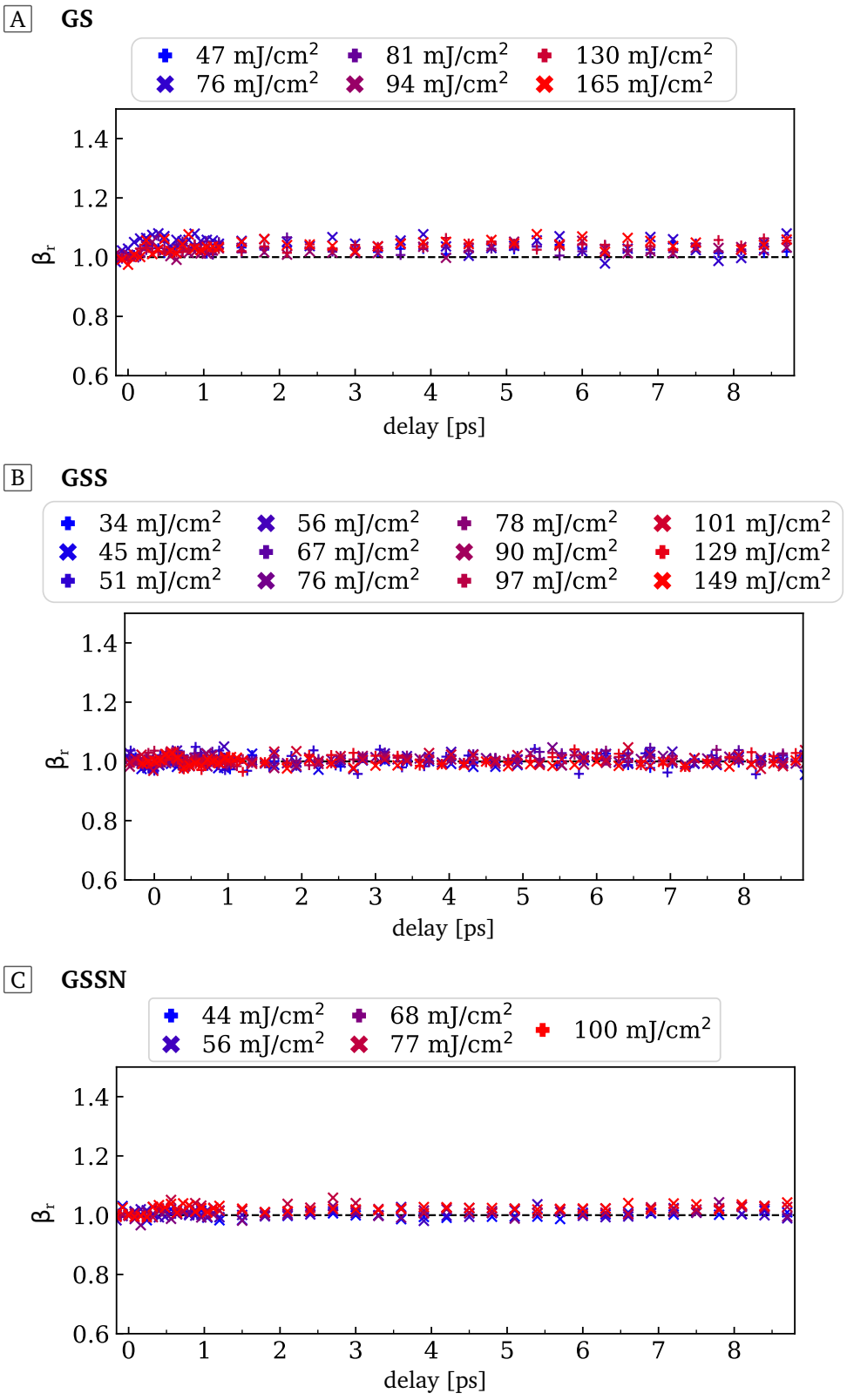

Figure 5.3 – *Evolution of the β_r parameters for GS (A), GSS (B) and GSSN (C). In all three cases, the value is stagnating at 1, implying a sharp interface (solid or liquid) during the whole time window. The difference of symbols only serves as a better differentiation between the successive fluences.*

I.2.2 Displacement of the interface

Knowing that the interface is sharp for all three materials and all fluences applied allows to consider next whether the samples experience any change of volume. To do so, the phase shift measured by the FDI is considered. The β_ϕ parameter defined from it (as per the Equation 3.24), is in turn useful to retrieve the surface displacement d through Equation 3.29.
As can be seen in Figure 5.4, the three glasses demonstrate the same behaviour during the time probed: no motion of the surface is detected.

$Ge_{31}Se_{69}$ (GS)

Similarly to GeTe, it is interesting to observe the sample long after the experiments *via* phase-contrast microscopy [299]. Indeed, it might take longer than the the timescale available with our setup (9 ps) for some effects to be noticeable.
In the case of GS, we detect a change of color in the phase-contrast microscopy images (Figure 5.5) starting from an irradiation fluence of 76 mJ/cm^2. This change of color is evidencing a phase transition in the material. Increasing the fluence leads to the formation of a SiN dome from a fluence of 91 mJ/cm^2. Starting from 94 mJ/cm^2, this dome has popped, quite brutally for the two highest fluences 130 mJ/cm^2 and 165 mJ/cm^2.

The formation of wrinkles pattern is observed for fluences $F \geq 81$ mJ/cm^2. In the case of $F = 91$ mJ/cm^2, they demonstrate a radial behaviour due to the formation of the SiN dome. This effect was previously observed by Bowden *et al.* [309] as a result of a pressure constraint. Once again, these patterns are proof of the melting of the chalcogenide films after the excitation. Indeed, as explained in Chapter 4, they result from the stress resistance of the SiN layer more rigid than the melted chalcogenide layer (see also Reference [48] for more details).

$Ge_{23}Se_{57}Sb_{20}$ (GSS)

For the GSS sample, we note the presence of wrinkles patterns from an irradiation fluence of 45 mJ/cm^2, which evidences the presence of a melted phase at some point (see Figure 5.6). Increasing the pump fluence up to 56 mJ/cm^2 leads to the presence of a brilliant spot at the center of the irradiation spot as well as a pattern more radial. Similarly to GS, these observations are the proof of the formation of a SiN dome.
Reaching 78 mJ/cm^2, this dome that became larger with the rise of fluence, pops due to the excess of surface constraint. We see that the more intense the fluence, the more impressive this breaking seems to be: for 149 mJ/cm^2, we barely see any residual SiN capping on the irradiated area.

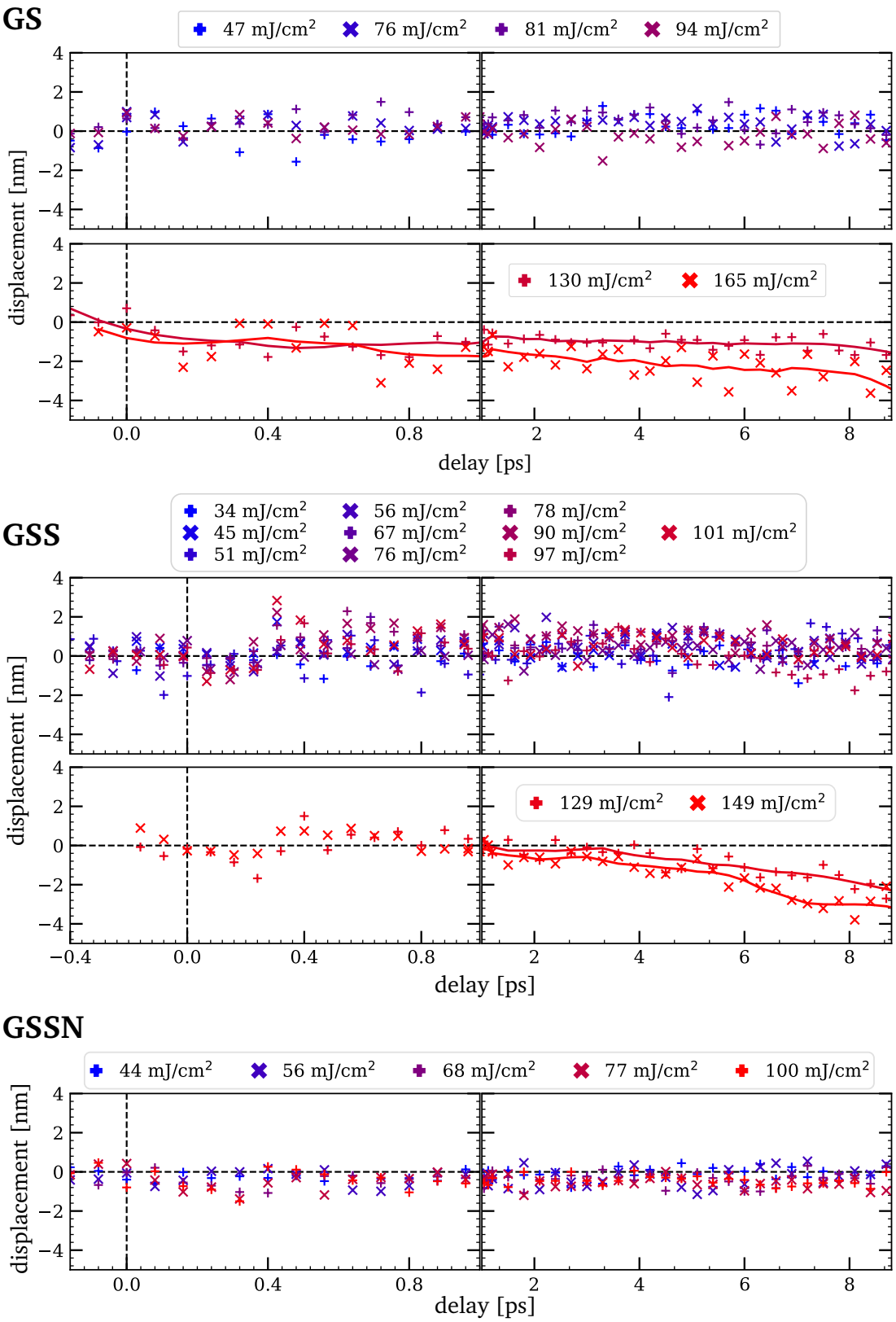

Figure 5.4 – *Displacement of the surface from FDI measurements for all three chalcogenide glasses. Solid lines are guides to the eyes.*

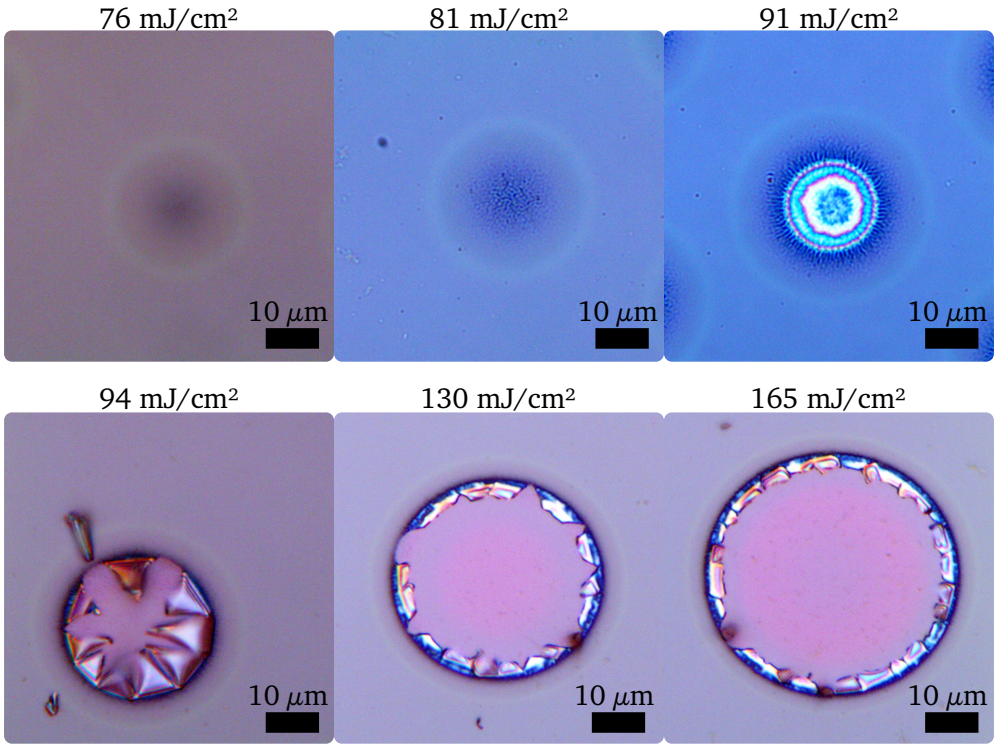

Figure 5.5 – *Phase-contrast microscopy images of GS irradiated spots. Random pattern starts to form for fluences of 68 mJ/cm^2. Then as a fluence of 100 mJ/cm^2 is reached, we notice the formation of a dome and the radial character of the wrinkles.*

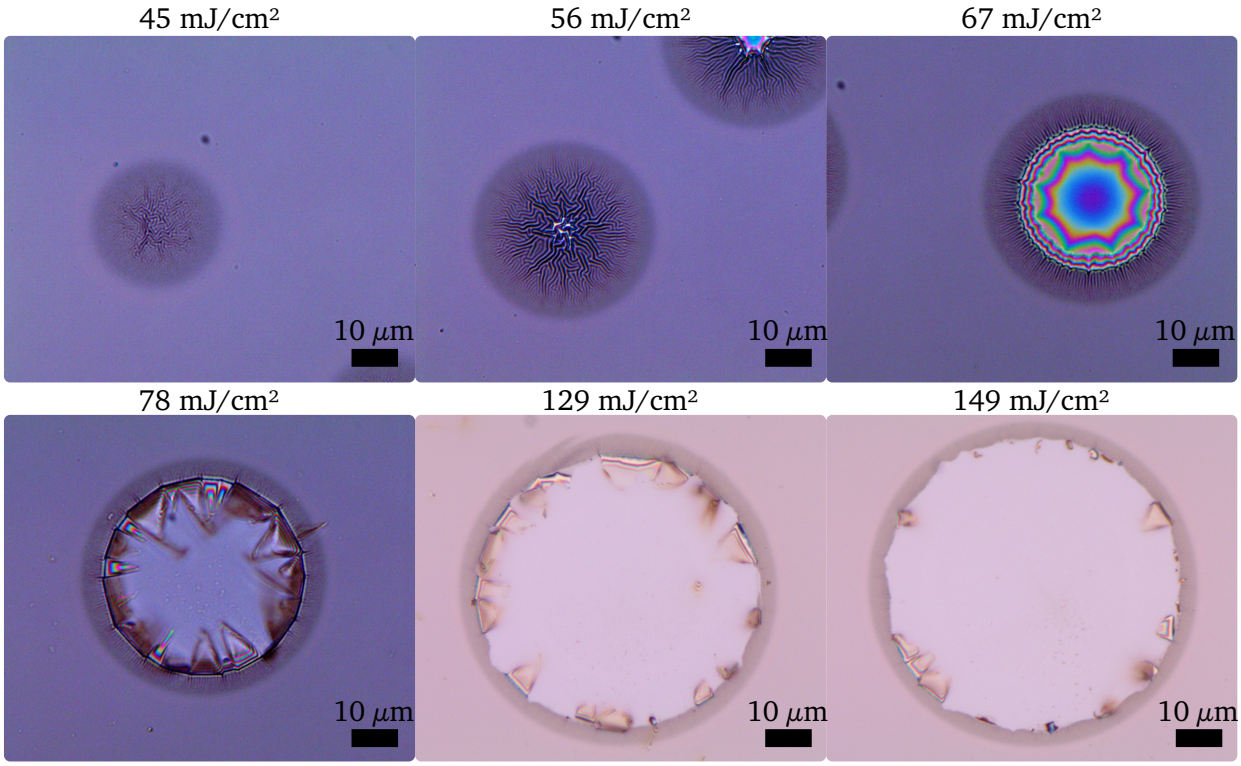

Figure 5.6 – *Phase-contrast microscopy images of GSS irradiated spots.*

$Ge_{23}Se_{53}Sb_{19}N_5$ (GSSN)

The post-experiment phase-contrast microscopy images of GSSN (Figure 5.7) reveal a phase change for fluences $F \geq 56$ mJ/cm^2. As the fluence is increased, above $F \geq 68$ mJ/cm^2, wrinkles can be seen, evidencing the fusion of the material. For the lowest fluence of 45 mJ/cm^2 (not shown here), the irradiation spot cannot be detected with this technique, which could mean either that the material does not transition when irradiated by this intensity, or that the variations induced by the transition are too negligible to be noticed.

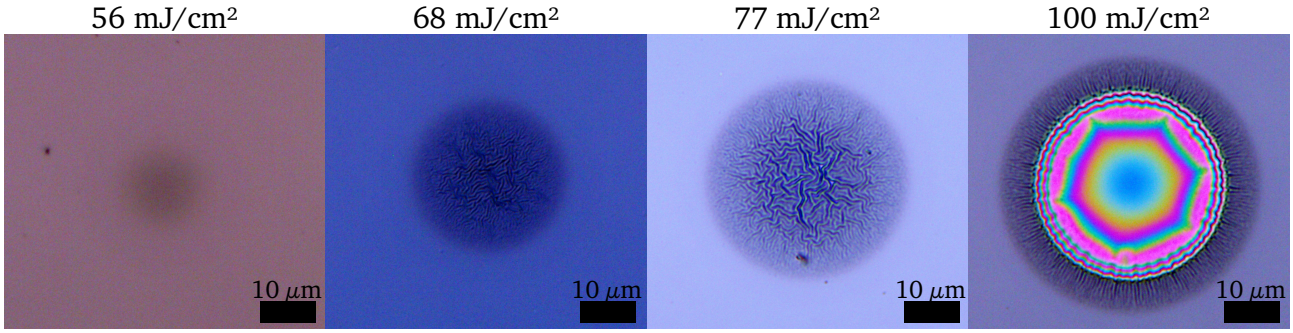

Figure 5.7 – *Phase-contrast microscopy images of GSSN irradiated spots for four pump fluences.*

Increasing even further the intensity of the laser up to 100 mJ/cm^2 results in the formation of an inner disk with different height than the surrounding non-irradiated sample (identified by the colorful pattern). This is expected to be the formation of a SiN dome resulting from thermal effects.

Post-experiment phase contrast microscopy images clearly reveal the existence of a liquid phase while nothing was detected from the FDI measurements. Two hypotheses are then possible: either the melting occurs on a timescale longer than the one available with our set-up, or the liquid phases induce a variation of the samples volume that is too small to be detected with our method.

I.3 Dielectric properties

Although the surface dynamics extracted from FDI measurements show no sign of a phase change, phase-contrast microscopy images revealed in (almost) all cases that a transition has effectively occurred (change of color). Moreover, this transition is done through a liquid state. For GeTe, surface motion and dielectric properties timescales were uncorrelated, it is interesting to see if the same applies here: will the dielectric function reveal some variation?

The dielectric functions $\varepsilon = \varepsilon_r + i\ \varepsilon_i$ of the excited states are retrieved thanks to both the variation of phase and reflectivity in the S and P polarization, as well as the value of the initial state ε^{cold} measured by ellipsometry.

I.3.1 $Ge_{31}Se_{69}$ (GS)

The evolution of the real part of the dielectric function of GS with the fluence intensity (Figure 5.8) is quite interesting. The lowest fluence of irradiation, $F = 47$ mJ/cm^2, leads a continuous increase from $t = 0$ until the 8.7 ps probed. As the fluence is increase, we see that the onset of ε_r's increase is delayed in time: only after 500 fs for 76 mJ/cm^2 and even 1 ps for 81 mJ/cm^2. After that, it is still a rise in ε_r that is measured.
While an incident fluence of 94 mJ/cm^{2}does not trigger right away a variation in ε_r similarly to what was observed previously, it is a drop that we observe when it does, 3 ps after excitation.

The response of the imaginary part ε_i, shown in Figure 5.9, is less peculiar, though the responses can be separated into two sub-categories for the long delays. In all cases, there is an initial increase of ε_i until 450 fs. After this, samples irradiated by fluences strictly lower than 81 mJ/cm^2 are characterized by a continuous drop, almost back to the initial ε_i^{cold} for the lowest case. For fluences $F \geq 81$ mJ/cm^2, a saturation regime is reached right after the initial rise.

Given the short timescale on which the variations in ε_r occur, they are most probably due to electronic effects. A model of the variation of the dielectric function of a material optically excited by a sub-picosecond laser was tried [310]. In fact, the overall variation $\Delta\varepsilon$ such that $\varepsilon^{exc} = \varepsilon^{cold} + \Delta\varepsilon$ is due to several processes occurring due to the excitation, simplified in the following model:

1. As the population of charge carriers in the valence and conduction bands is disturbed by the excitation, this variation induces a contribution to the change in dielectric function. This latter can be estimated using the following expression, with N_v the total valence band density in the non-excited state and N_{e-h} the density of excited electron/hole pairs.

$$\Delta\varepsilon^{pop} = -(\varepsilon^{cold} - 1)\frac{N_{e-h}}{N_v} \tag{5.1}$$

2. The many-body interactions in the excited state induce a renormalization of the band structure. It is usually treated as a rigid shift of the band structure, which shows a shrinking of the band gap by ΔE_g. In the simple version, this contribution is estimated as:

$$\Delta\varepsilon^{bg} = \varepsilon^{cold}(\hbar\omega + \Delta E_g) - \varepsilon^{cold}(\hbar\omega) \tag{5.2}$$

3. The photo-excitation induces free charge carriers, whose response can be approximated using a Drude model (detailed in Appendix B), with ν the collision frequency and ω_p the

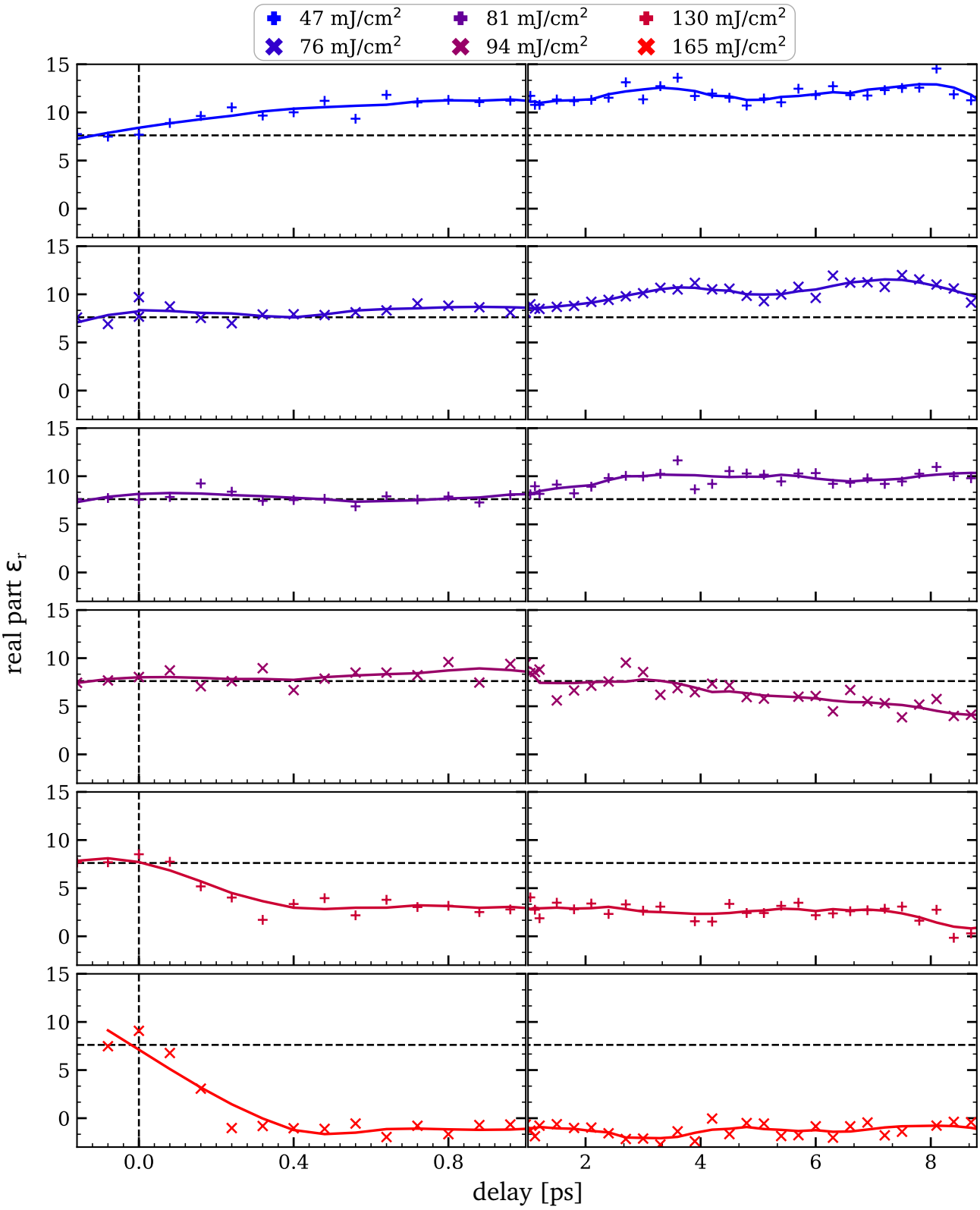

Figure 5.8 – *Real part of the dielectric function as a function of delay for the GS sample. The horizontal dotted lines highlight the value of the initial state* $\varepsilon^{cold}(532\ nm) = 7.62 + 0.22\ i$. *Solid lines are guides to the eyes.*

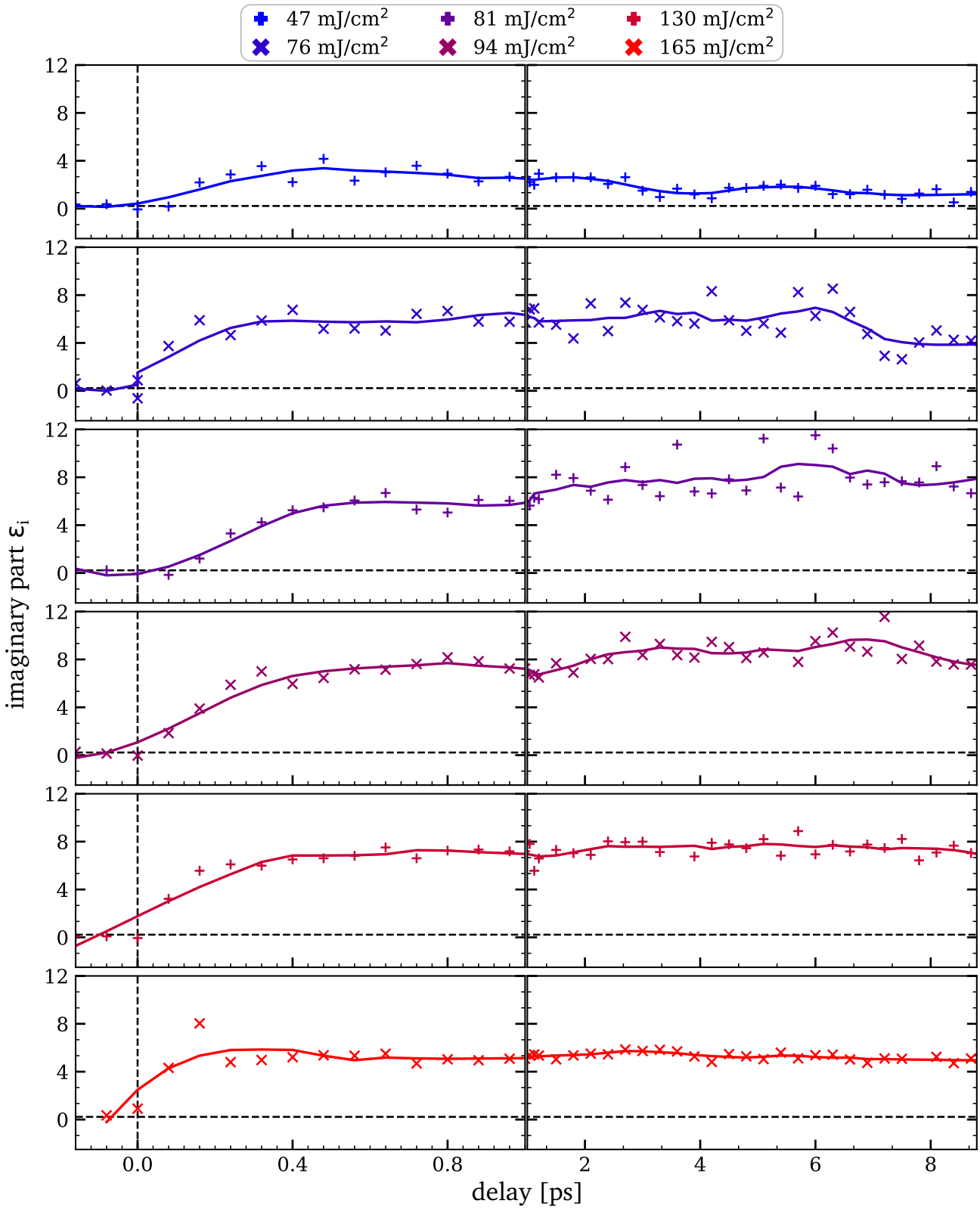

Figure 5.9 – *Imaginary part of the dielectric function as a function of delay for the GS sample. The horizontal dotted line highlights the value in the initial state* $\varepsilon^{cold}(532\ nm) = 7.62 + 0.22\ i$. *Solid lines are guides to the eyes.*

plasma frequency defined as $\omega_p = \frac{N_{e-h}e^2}{m^*\varepsilon_0}$, such that the corresponding contribution is:

$$\Delta\varepsilon^D = -\frac{\omega_p^2}{\omega^2}\frac{1}{1+i\frac{\nu}{\omega}} \tag{5.3}$$

The overall excited dielectric function regroups the contributions stated above, such that the final expression for a probing wavelength of $\lambda = 2\pi c/\omega$ is:

$$\varepsilon(\hbar\omega) = 1 + \left[\varepsilon^{cold}(\hbar\omega + \Delta E_g) - 1\right]\frac{N_V - N_{e-h}}{N_V} - \frac{\omega_p^2}{\omega^2}\frac{1}{1+i\frac{\nu}{\omega}} \tag{5.4}$$

In Figure 5.10, this model described by the Equation 5.4 was applied to estimate the excited dielectric functions of GS as a function of the density of excitation N_{e-h}. The effective mass of the holes m_h^* and of the electrons m_e^* were estimated using mobility measurements from Reference [14] in glassy $GeSe_2$ giving $\mu_e = 0.2$ cm^2.V^{-1}.s^{-1} and $\mu_h = 0.04$ cm^2.V^{-1}.s^{-1}. Using these mobilities, the effective masses are calculated as:

$$\mu = \frac{e}{m^*\nu} \Rightarrow \boxed{m^* = \frac{e}{\mu\nu}} \tag{5.5}$$

The optical effective mass m_{opt}^* is then defined as:

$$(m_{opt}^*)^{-1} = \frac{1}{m_e^*} + \frac{1}{m_h^*} \tag{5.6}$$

The hole effective mass m_h^* is used to estimate the total valence band density N_V using Equation 5.7.

$$N_V = 2\left(2\pi\frac{k_B T m_h^*}{h^2}\right)^{3/2} \tag{5.7}$$

The band gap shrinkage ΔE_g cannot be directly deduced from the FDI experimental measurements. Therefore, we try here varying this shrinkage from the situation of no band gap closure ($\Delta E_g = 0$ eV) to the complete closure of the optical band gap ($\Delta E_g = E_g = 2.2$ eV, determined by Tauc plot, Appendix D [47]). As for the value of $\varepsilon^{cold}(\hbar\omega + \Delta E_g)$, they are deduced from the static ellipsometry measurements (Figure 5.1).

The variation of the dielectric function in both the real part and the imaginary part is almost completely driven by the shrinkage of the band gap. Indeed, the density of excitation does not impact much the form of the curves, while varying ΔE_g shifts greatly the value obtained for the excited dielectric function. The effect of the other parameters are completely negligible compared to it. For the collision frequency ν, a value of 10^{15} s^{-1} is required to observe a curved decrease,

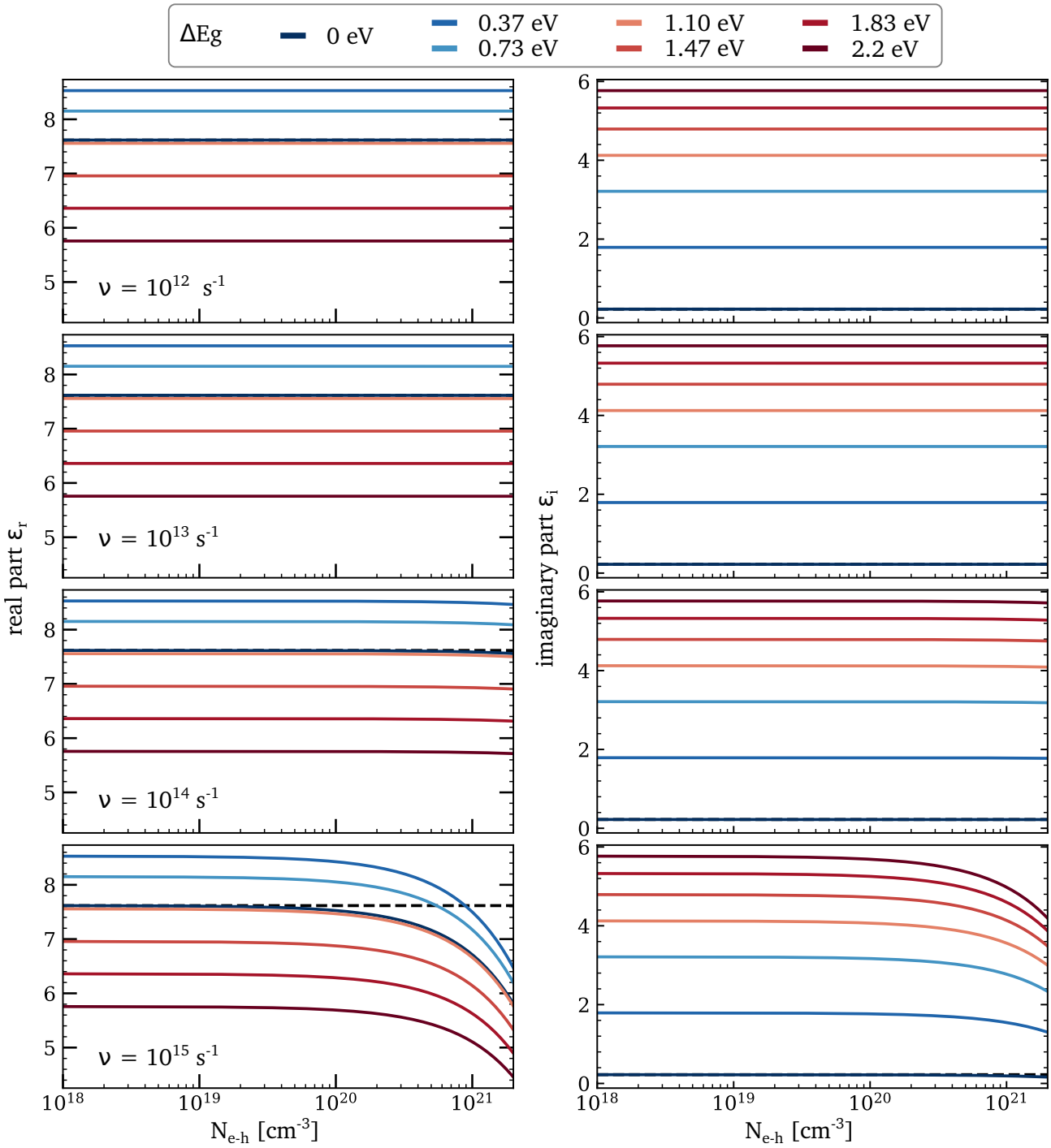

Figure 5.10 – *Excited dielectric function of GS for different collision frequencies ν and different band gap closure ΔE_g, using Equation 5.4. The value for the initial state, $\varepsilon^{cold} = 7.62+0.22\,i$, is represented by a black dotted line in each subplot.*

and only at high density of excitation ($\gtrsim 10^{21}$) cm^{-3}). The effect of the N_{e-h} parameter is even more negligible than that of ν.

While the imaginary part of the dielectric function only shows a basic increase when the band gap closes (still, in adequation with the FDI data), the response of the ε_r is more interesting. The cases $\Delta E_g = 0$ eV (no closure of the band gap) and $\Delta E_g = 1.10$ eV are very similar, with a value of ε_r equal to that of the initial state $\varepsilon_r^{cold} = 7.62$. In between, small shrinkages of the band gap (see $\Delta E_g = 0.37$ eV) induce an increase in ε_r, just as what we observed in the experiments.
As the band gap is closed even more ($\Delta E_g \geq 1.10$ eV), ε_r decreases again and reaches lower values than in the initial state. This is illustrated in Figure 5.11, where ν and N_{e-h} have been chosen arbitrarily as $\nu = 10^{13}$ s^{-1} and $N_{e-h} = 10^{19}$ cm^{-3}. The changes in ε_r are very similar for all N_{e-h} when $\nu \leq 10^{14}$s^{-1}.

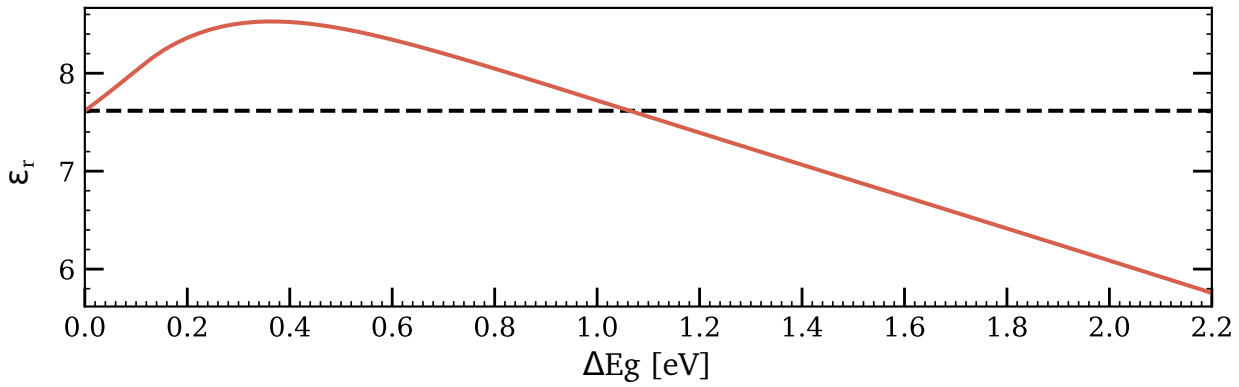

Figure 5.11 – *Evolution of the real part of the dielectric function when the shrinkage of the band gap is varied for* $\nu = 10^{13}$ s^{-1} *and* $N_{e-h} = 10^{19}$ cm^{-3}.

For this specific case, we find that a closure of the band gap by $\Delta E_g = 0.36$ eV induces the maximum increase in ε_r, up to $\varepsilon_r^{max}\left(\Delta E_g\right) = 8.53$. By closing more the band gap, *i.e.* when ΔE_g reaches a value of about 1.07 eV, ε_r takes again the initial state value of $\varepsilon_r^{cold} = 7.62$, and continues to decrease as the band gap is closed further on.

Experimentally, we found a higher increase in ε_r, but the model used here is simplified, and several parameters are only estimated. Nevertheless, we are able to retrieve this rise qualitatively, which gives an idea on its origin.

The conclusion that can be drawn from this model is the importance of the band gap closure. It is the parameter that drives the variation of ε on the short scales. The analytical expression of Equation 5.4 reveals that the role of the band gap parameter ΔE_g is to act as a shift, similarly to a scissor correction [311]. This latter is an empirical method used in DFT simulations to account for

the miscalculation of the band gap. Therefore, the variation of ε_r actually stems directly from the dispersion relation of the dielectric function. This shift of band structure can be interpreted very roughly as looking at the value of ε^{cold}, but at another energy ("$E_{probe} + \Delta E_g$"). Basically, if we look at the dispersion of refractive index from Figure 5.1, we find that for smaller wavelengths than λ_{probe} (corresponding to the shifting energy), κ is monotonous, but n shows a change of curvature. This latter is probably the reason of the peculiar behaviour seen for ε_r. Indeed, the same model applied to GSS and GSSN (see Appendix D, Figures D.3 and D.4) does not imply an increase in ε_r as observed for GS (which thankfully though, is consistent with the experiments), but the dispersion curves of these two material only show monotonous behaviour as we look at smaller λ.

I.3.2 $Ge_{23}Se_{57}Sb_{20}$ (GSS)

In Figure 5.12 representing the evolution of ε_r, a sudden decrease is observed as soon as the pump impinges the material, with a minimal value of ε_r is reached within 400 fs. After that, we note a slight rise until a saturation regime is reached, 3 ps after excitation. While the saturation value is different for $F \leq 78$ mJ/cm^2, spanning from $\varepsilon_r^{sat}(F = 34\ mJ/cm^2) = 9.58$ down to $\varepsilon_r^{sat}(F = 78\ mJ/cm^2) = 1.51$, it is the same for all fluences above that $\varepsilon_r^{sat}(F > 78\ mJ/cm^2) = 0.5$.

The imaginary part of the dielectric function, represented in Figure 5.13, does not show the same kind of plateau, but the fluence dependency is still present. The response to excitation can be categorized in three types:

- $F \leq 56$ mJ/cm^2: a continuous increase is observed starting from the moment of energy deposition until the end of the 8.7 ps probed. The higher the intensity of excitation, the more pronounced the rising slope.

- 56 mJ/cm^2 $\leq F \leq$ 78 mJ/cm^2: ε_i rises, with a higher slope than for lower fluences. In addition, a maximal value is reached for a delay of about 450 fs, followed by a saturation regime that lasts until the end of the time probed.

- $F = 90$ mJ/cm^2: after a large increase in ε_i during 450-500 fs, the response due to this high fluence is characterized by a slight decrease with time.

The increase of ε_i along with the decrease in ε_r for fluences below 90 mJ/cm^2 leads to the conclusion that with excitation, the GSS sample becomes more metallic. However for higher fluences, the conclusion cannot be drawn as straightforwardly.

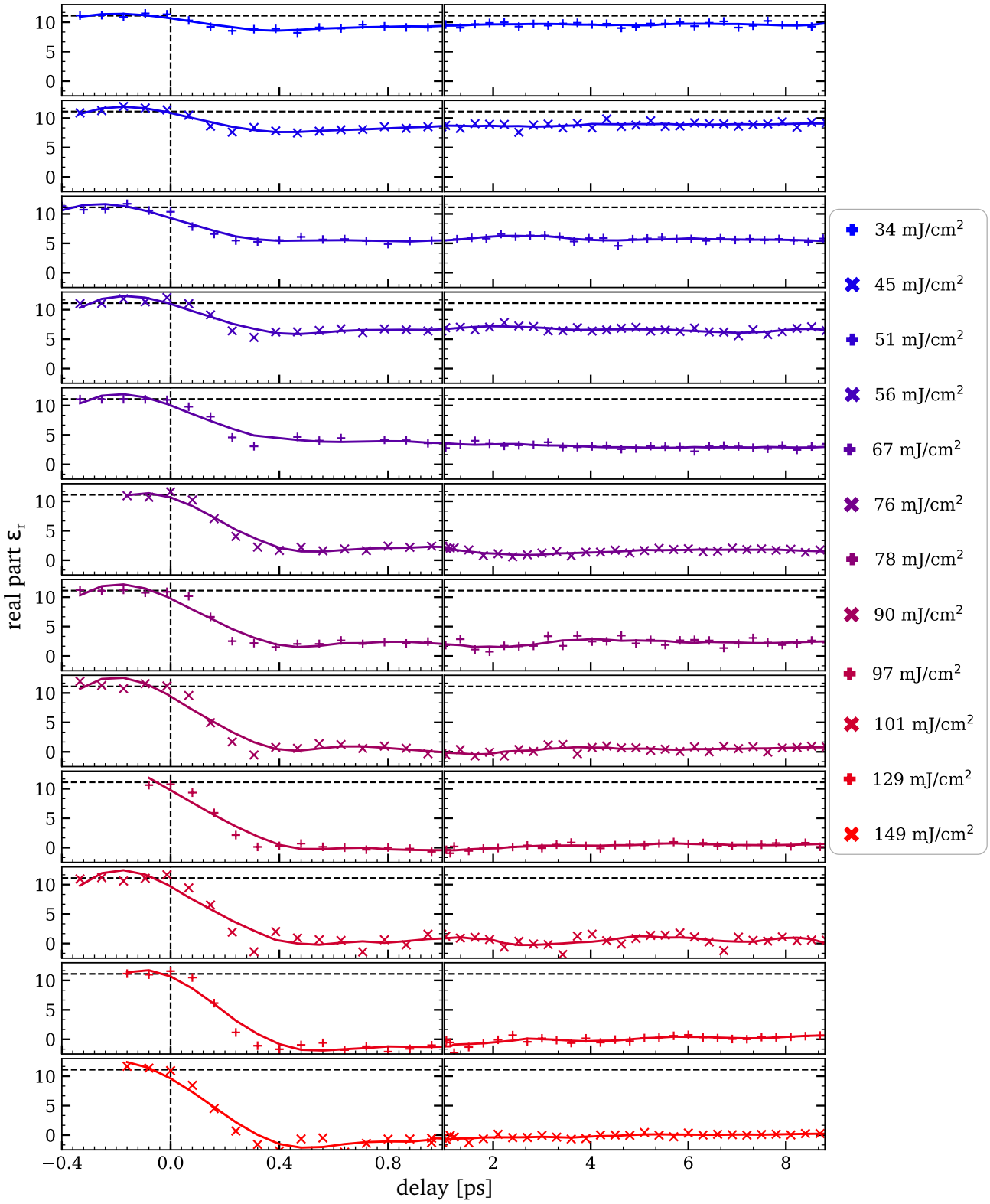

Figure 5.12 – *Real part of the dielectric function as a function of delay for the GSS sample. The horizontal dotted line highlights the value of the initial state* ε^{cold}*(532 nm) = 11.11 + 5.96 i. Solid lines are guides to the eyes.*

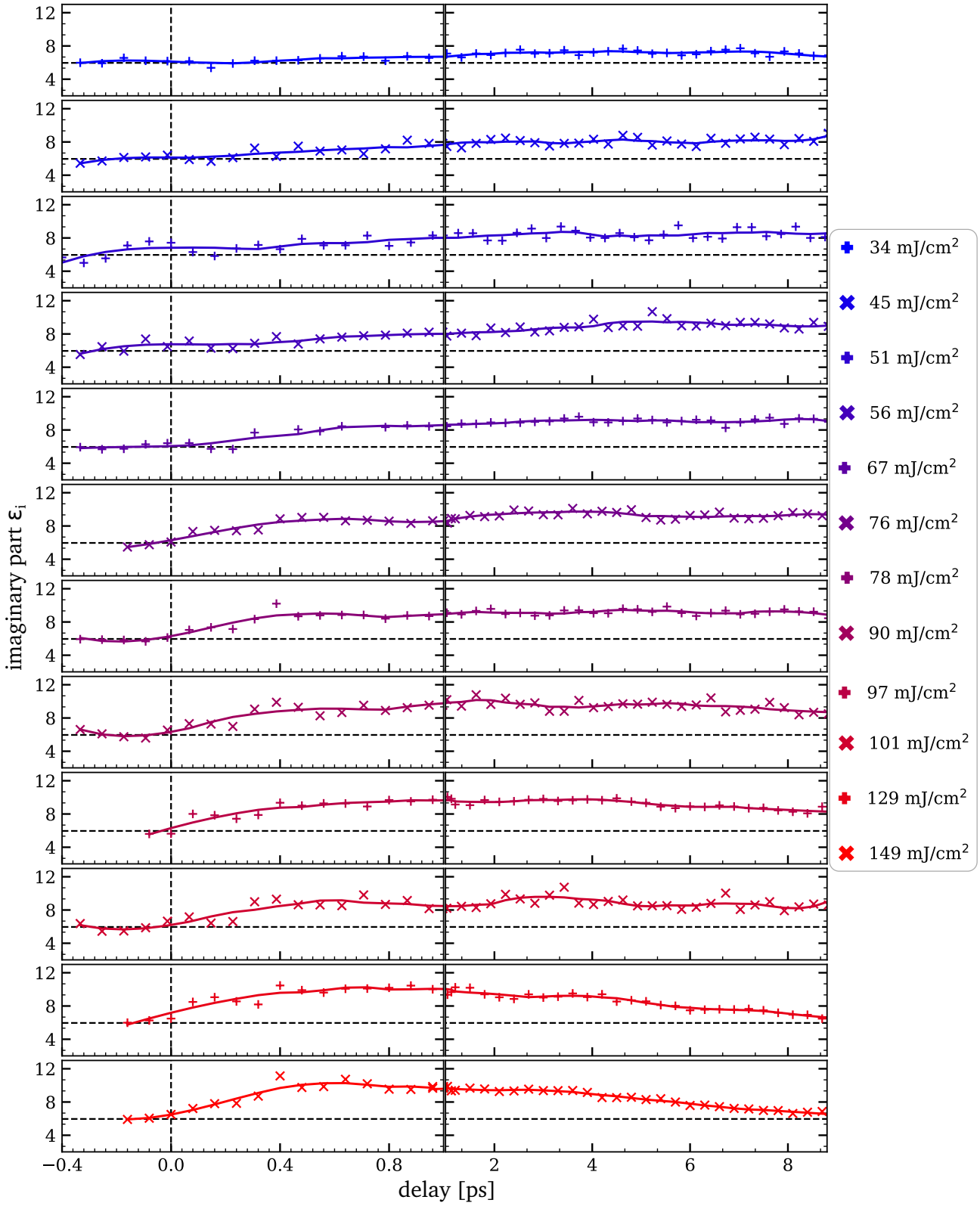

Figure 5.13 – *Imaginary part of the dielectric function as a function of delay for the GSS sample. The horizontal dotted line highlights the value in the initial state $\varepsilon^{cold}(532\ nm) = 11.11 + 5.96i$. Solid lines are guides to the eyes.*

I.3.3 $Ge_{23}Se_{53}Sb_{19}N_5$ (GSSN)

As can be seen in Figure 5.14 for the real part and in Figure 5.15 for the imaginary part, the dielectric function of GSSN compound exhibits the same tendencies for all fluences. Only a variation of amplitude as a function of fluence is really noticeable.

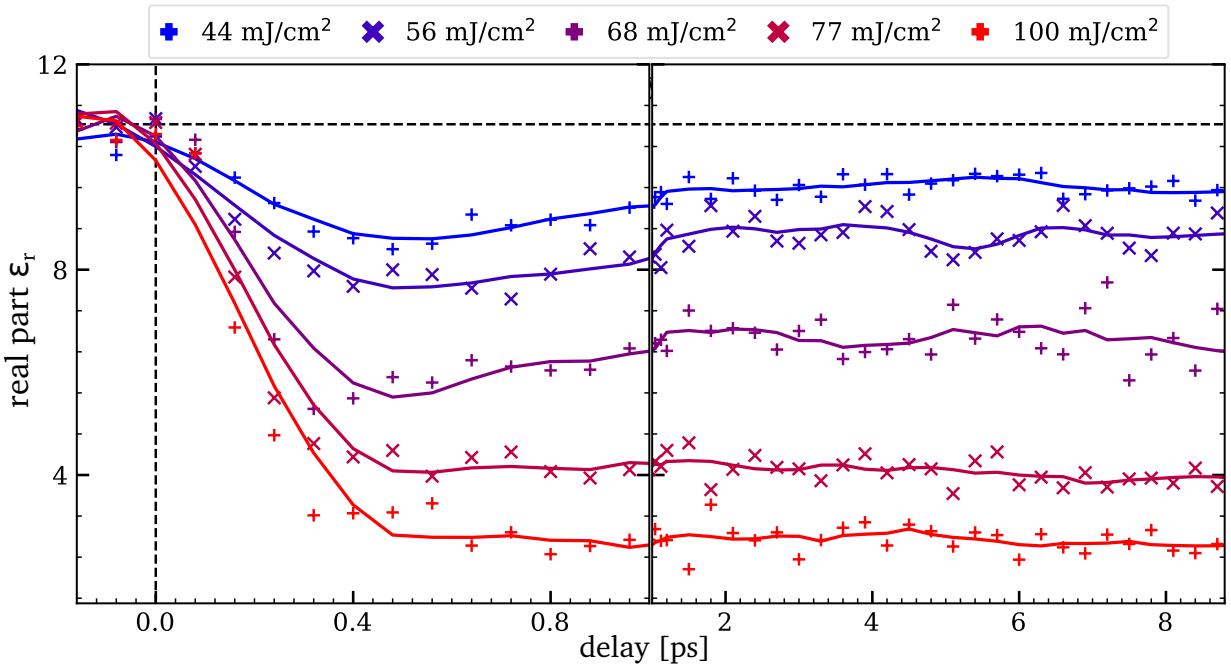

Figure 5.14 – *Real part of the dielectric function as a function of delay for the GSSN sample. The horizontal dotted line highlights the value in the initial state $\varepsilon^{cold}(532\ nm) = 10.83 + 4.36\ i$. Solid lines are guides to the eyes.*

As soon the material is excited, a drop in ε_r is measured. This decrease reaches its maximal value after about 450-500 fs. A slight difference between the fluences below 77 mJ/cm^2 and above can be noted: for the low fluences, the decrease of ε_r is followed by a small rise during about 3 ps until it reaches a saturation regime. For the highest fluences, this first increase does not occur: the material enters the plateau regime as soon as ε_r reaches its minimal value. On the contrary to GeTe, for which the saturation value was roughly identical for all fluences, here the amplitude of the variation measured becomes larger as the intensity of the laser is increased: an irradiation fluence of 44 mJ/cm^2 leads to a decrease by 11 ± 2% of ε_r while a fluence of 100 mJ/cm^2 implies a decrease by 75 ± 3%.

Similarly to the real part, as soon as the energy is deposited by the pump, a variation is measured in ε_i. This latter consists in an increase with time, with an amplitude that is larger as the laser fluence is risen. However, all fluences exhibit the same tendency after that: about 1 ps after excitation, a saturation regime is reached. The final values span from 126 ± 3% (lowest fluence

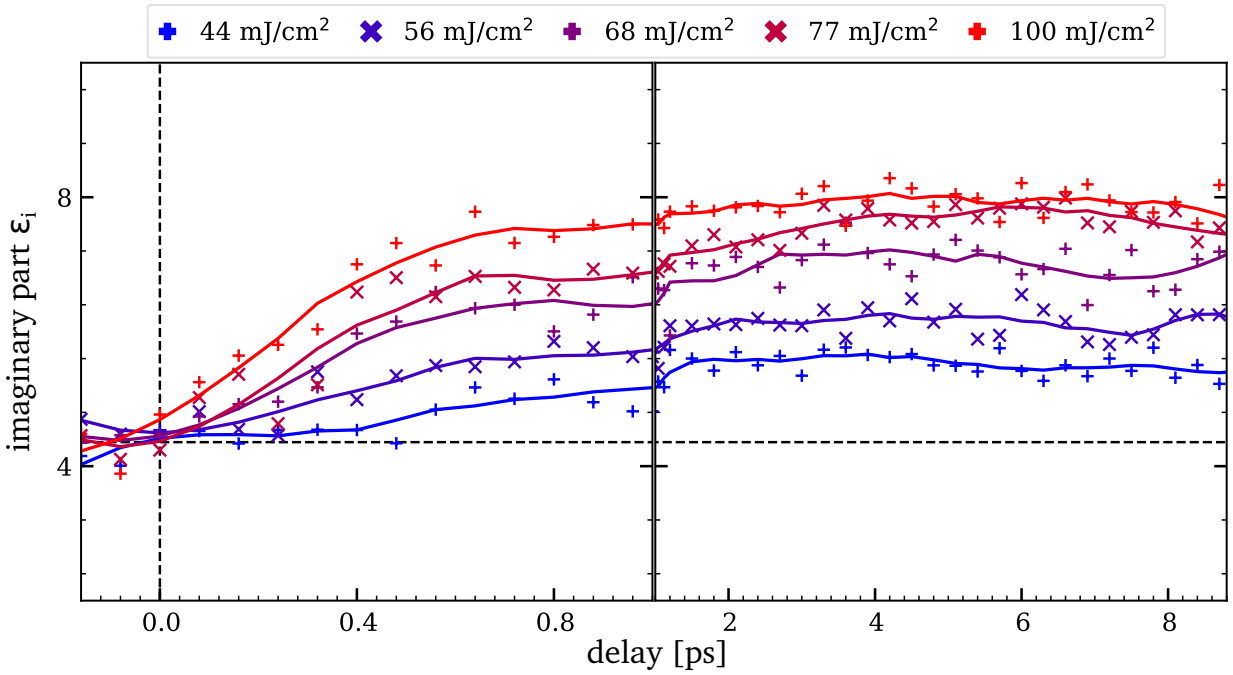

Figure 5.15 – *Imaginary part of the dielectric function as a function of delay for the GSSN sample. The horizontal dotted line highlights the value of the initial state ε^{cold}(532 nm) = 10.83 + 4.36 i. Solid lines are guides to the eyes.*

of 44 mJ/cm^2) up to 180 ± 6% (highest fluence of 100 mJ/cm^2) of ε_i^{cold}.

The decrease of ε_r along with the increase of the imaginary part ε_i suggest that GSSN becomes more metallic as it is excited.

Conclusion of the FDI experiments on the three chalcogenide glasses

The first 9 picoseconds after excitation of 500-nm thick films of $Ge_{31}Se_{69}$ (GS), $Ge_{23}Se_{57}Sb_{20}$ (GSS) and $Ge_{23}Se_{53}Sb_{19}N_5$ (GSSN) were investigated using fs lasers. A pump pulse of 30 fs duration with central wavelength 800 nm was used to trigger the excitation and the response to this photo-excitation was probed using frequency domain interferometry with a probe beam delivering 80 fs pulses with central wavelength 532 nm.

The results are strikingly different from those obtained for GeTe. First, no melting is detected during this time window. For all three chalcogenides, the FDI measurements do not exhibit any change in surface dynamics nor in nature. However, phase-contrast microscopy images clearly indicate a transition for all glasses, with a passage through a molten phase.
As for the dielectric properties, the response to photo-excitation is quite dissimilar for the three, though we can note that in all cases the main variations occur in the time window of 400 - 500 fs after excitation.

The hypothesis of a metallization of all compounds seems to be consistent, with a closure of the band gap reflected in the dielectric functions. *Ab initio* molecular dynamics results will help disentangle these observations and understand what happens on a local scale.

II *Ab initio* molecular dynamics simulations of chalcogenide glasses

To back up the FDI experiments and obtain further information on the excitation of the three selenide chalcogenide compounds, *ab initio* molecular dynamics (AIMD) simulations were conducted. As the band is miscalculated due to the use of GGA functionals [226–228], we know beforehand that the comparison will only be qualitative.

The starting configuration was generated using a melt-quenched method, as detailed in Chapter 2, Section II. Then, several cases were simulated. The same procedure of excitation was used for all glasses (and GeTe) to simulate the experimental out-of-equilibrium states triggered by laser excitation: a Fermi distribution is applied to the electrons. The width of this distribution, assimilated to the electronic temperature T_e, drives the magnitude of the excitation, as explained in Chapter 2, Section II.3.2.

The pristine phase (initial non-excited case) is reproduced by using an ionic temperature T_i = 300 K and an electronic temperature of T_e = 0.001 eV. Then, the electronic temperature was varied from 0.3 eV (non excited case) to 1.2 eV for an ionic temperature of T_i = 300 K to simulated out-of-equilibrium excited states resulting from a fs laser pumping. Moreover, as phase-contrast microscopy images reveal transition through a melted state for most fluences, an additional equilibrium liquid state was simulated with an ionic temperature T_i of either 900 K (GSS) or 1200 K (GS and GSSN). As explained in Chapter 1, Section III.1, it is difficult to choose an ionic temperature to reproduce the liquid state expected experimentally. Indeed, these materials are characterized by several melting temperature and we cannot know exactly how much the lattice heats up during the FDI experiments. Due to this ambiguity, the liquid state lattice temperature was chosen above all incongruent and congruent T_m values.

II.1 Analysis of the non-excited glasses

First, it is important to analyze the structure and properties of the initial (non-excited) states, to understand what we start from. These states correspond to the equilibrated GS, GSS and GSSN AIMD simulations, with T_i = 300 K and T_e = 0.001 eV for GS, GSS and GSSN. The resulting configurations are depicted in Figure 5.16.

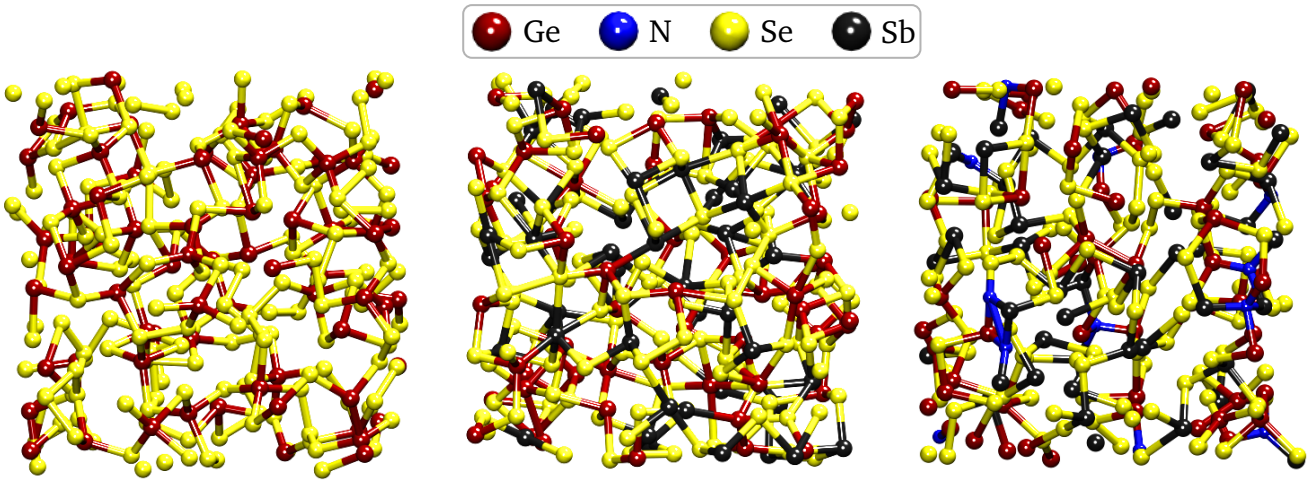

Figure 5.16 – *Non-excited configurations for the three chalcogenide glasses GS (A), GSS (B) and GSSN (C).*

Amount of tetrahedra for the non-excited states of the glasses

Ge-Se glasses are characterized by the presence of numerous Ge atoms in tetrahedral sites (Ge^T) [31, 154, 158]. These tetrahedra demonstrate the peculiarity to be connected *via* an edge (ES: edge-sharing) or *via* a corner (CS: corner-sharing).

The Figure 5.17 shows the proportion of Ge atoms that are at the center of tetrahedral units, denoted Ge^T. These compounds, on the contrary to GeTe, do not exhibit short and long bonds which could hinder the "simple" calculation of tetrahedra, therefore those proportions were calculated using the R.I.N.G.S. code [256].

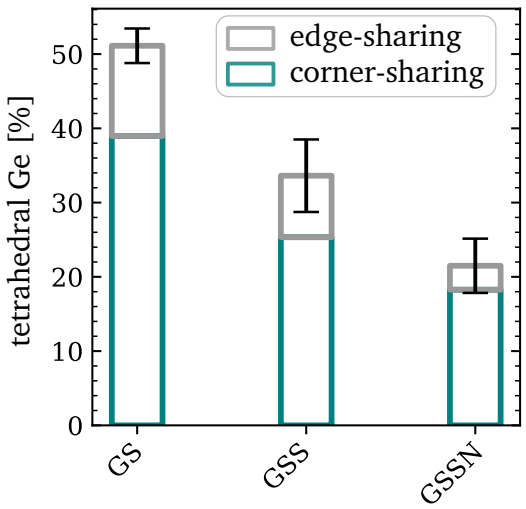

Figure 5.17 – *Percentage of Ge^T in the initial configurations of the three chalcogenide glasses. Errorbars correspond to the total number of tetrahedras in each material.*

GS is effectively constituted of a large number of Ge atoms in tetrahedral local environment with an overall percentage of 52 ± 3% Ge^T. In a previous study a ratio of edge-sharing to corner-sharing tetrahedra of 0.21 was determined by Raman scattering measurements [312]. Here the ES:CS ratio is estimated to 0.32 ± 0.1, in good agreement with another AIMD study conducted by Micoulaut *et al.* [154] who also found ratio of 0.32.

Although the two other compounds derive from GS, the presence of dopant has a non-negligible impact on the structure: from 52 % in GS, the proportion of Ge^T drops to 34 ± 5% for GSS, and even lower for GSSN with only 22 ± 4% Ge^T. Though the total number of tetrahedra drops when Sb dopant is added, the ratio of ES:CS does not change for GSS. However, the additional doping of N implies a drastic reduction of the ES tetrahedra compared to the CS ones, leading to a ratio of 0.17 ± 0.1.

Bond lengths for the non-excited states of the glasses

The partial and total pair distribution functions $g(r)$ of the non-excited states are represented in Figure 5.18. The peak positions give an idea of the corresponding bond lengths with an uncertainty estimated to 0.05 Å. The intensities of the peaks are also important, as the more a peak is intense, the more this type of bond can be found in the material.
We find a good agreement between the first peak positions determined here and in previous studies [31, 47, 73, 80, 89, 154, 158, 159](also listed in Chapter 1, Table 1.2,1.3 and 1.4).

GS is characterized by a majority of Ge-Se bonds, whose lengths is about 2.41 Å. This value is quite large compared to 2.36-2.37 Å found *via* both AIMD and experimental methods for compounds close to this composition. Homopolar Se-Se bonds are found in lower proportion than the Ge-Se ones. The first peak of the Se-Se distribution is located at 2.37 Å, in adequation with literature, giving 2.32 - 2.38 Å. However, this is actually not the main peak of this distribution, which lies in fact in the second neighbouring shell, at 3.93 Å. As far as the Ge-Ge bonds are concerned, the first peak is identified at 2.55 Å (other studies determined this peak between 2.42 and 2.69 Å) but this type of bonds is in fact almost non existant, especially in the first neighbouring shell (evidenced by the flatness of the curve compared to Ge-Se).
The coordination numbers, calculated *via* the integration of a given $g(r)$ up to the first minimum of g_{total} (cut-off in Appendix D, Table D.1), are $n_{Ge} = 3.62$ and $n_{Se} = 2.22$, in adequation with previous studies [47, 154] and consistent with the large proportion of Ge^T found beforehand.

Ge-Ge bonds as well as Se-Se bonds disappear in GSS. The main bonds are now Se-Sb ones, with distances of 2.68 Å. This length is larger than the 2.53 - 2.63 Å determined in the study of Fabian *et al.* [73]. Ge-Se is the second main type of bonds in GSS. The length of Ge-Se has

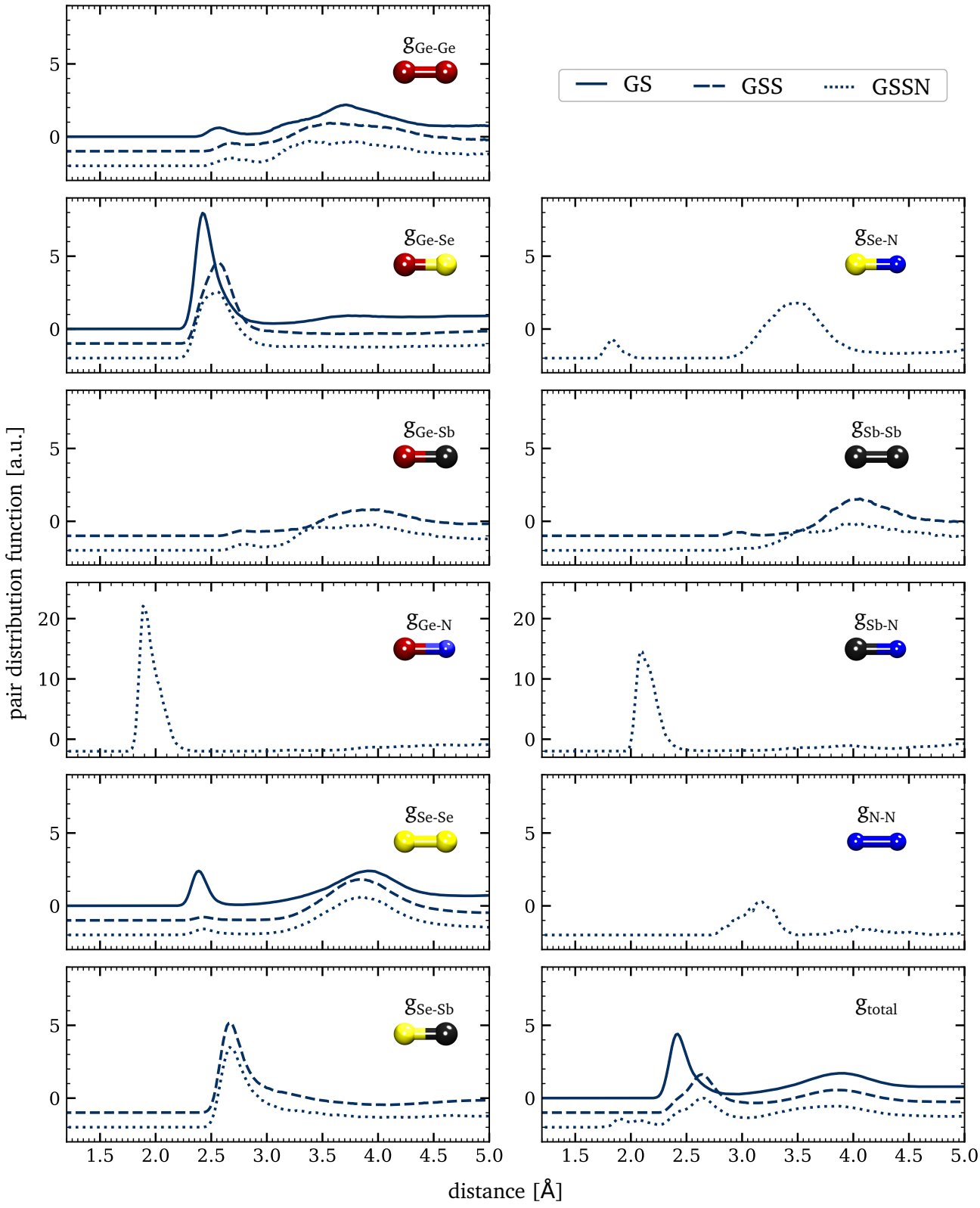

Figure 5.18 – *Pair distribution functions of the initial states of the three chalcogenide glasses (vertically shifted by -1 and -2 for GSS and GSSN respectively). The y scales of the partial g_{Ge-N} and g_{Sb-N} have been adapted for more clarity.*

increased compared to those in GS, with a value of 2.68 Å. For this bond, the value is quite far from literature, with 2.54 Å compared to 2.35 - 2.39 Å. As expected, we note a non-negligible proportion of Sb-Sb, and Ge-Sb to a lesser extent, that have formed in the second neighbouring shell. The coordination number of Ge remains close to that of GS with a value of $n_{Ge} = 3.80$, but Se increases slightly its number of neighbours, with $n_{Se} = 2.75$. The coordination number of Sb is determined to be $n_{Sb} = 3.69$ (cut-off in Appendix D, Table D.2).

The introduction of Nitrogen dopant changes drastically the proportions of bonds. The Sb atoms will preferentially bond with N atoms, forming very short bonds (at 2.10 Å, consistent with XAS study [47]), in a very large proportion rather than Sb-Sb or Ge-Sb bonds. Ge-Se as well as Se-Sb bonds are still present with partial pair distribution functions very similar to the ones of GSS compound (bond lengths of 2.55 Å and 2.42 Å). N-N bonds are found in a non-negligible amount in the second neighbouring shell at 3.17 Å. The coordination number are similar to those in GSS, with $n_{Ge} = 3.72$, $n_{Se} = 2.65$, $n_{Sb} = 3.53$ and $n_N = 3.35$ (cut-off in Appendix D, Table D.3).

Characteristic angles for the non-excited states of the glasses

The number of tetrahedra calculated previously showed discrepancy between the three glasses. Therefore, the distribution of angles should confirm that the local environment of the Ge atoms change with the addition of doping elements. Then what is the final configuration adopted? The Figure 5.19 shows the distribution of angles around each type of atoms for the non-excited configurations of the three chalcogenide glasses.

In GS, the Ge atoms are characterized by an asymmetric distribution with a maximum at 108°, consistent with the large presence of tetrahedra calculated before as well as the coordination number n_{Ge} close to 4. The asymmetric broadening towards lower angles might be the proof of existence of a small amount of defective octahedral configuration giving angles close to 90°. This kind of shouldering of the distribution was also seen in the study of Raty *et al.* [206]
For Se, there are clearly two different contributions. The majority of angles peaks at 101° but we identify a bump peak at 82°. These two features are characteristic of edge-sharing (~80°) and corner-sharing (~100°) tetrahedra, corresponding to Ge-Se-Ge bonds [31, 154].

With the introduction of Sb, the Ge angular distribution becomes more symmetric with a shift of the main peak towards 94°. The same goes for Se atoms, whose distribution also shifts to lower values of angles of 93°. As the main bonds were determined to be the Se-Sb type, it explains the tendency to form octahedral sites [47]. The Sb atoms are found in octahedral environment, with two local maxima at 89° and 167° (corresponding to the aligned bonds of octahedral sites). Fabian *et al.* [73] found a predominance of tetrahedral angles in several compositions of N-doped

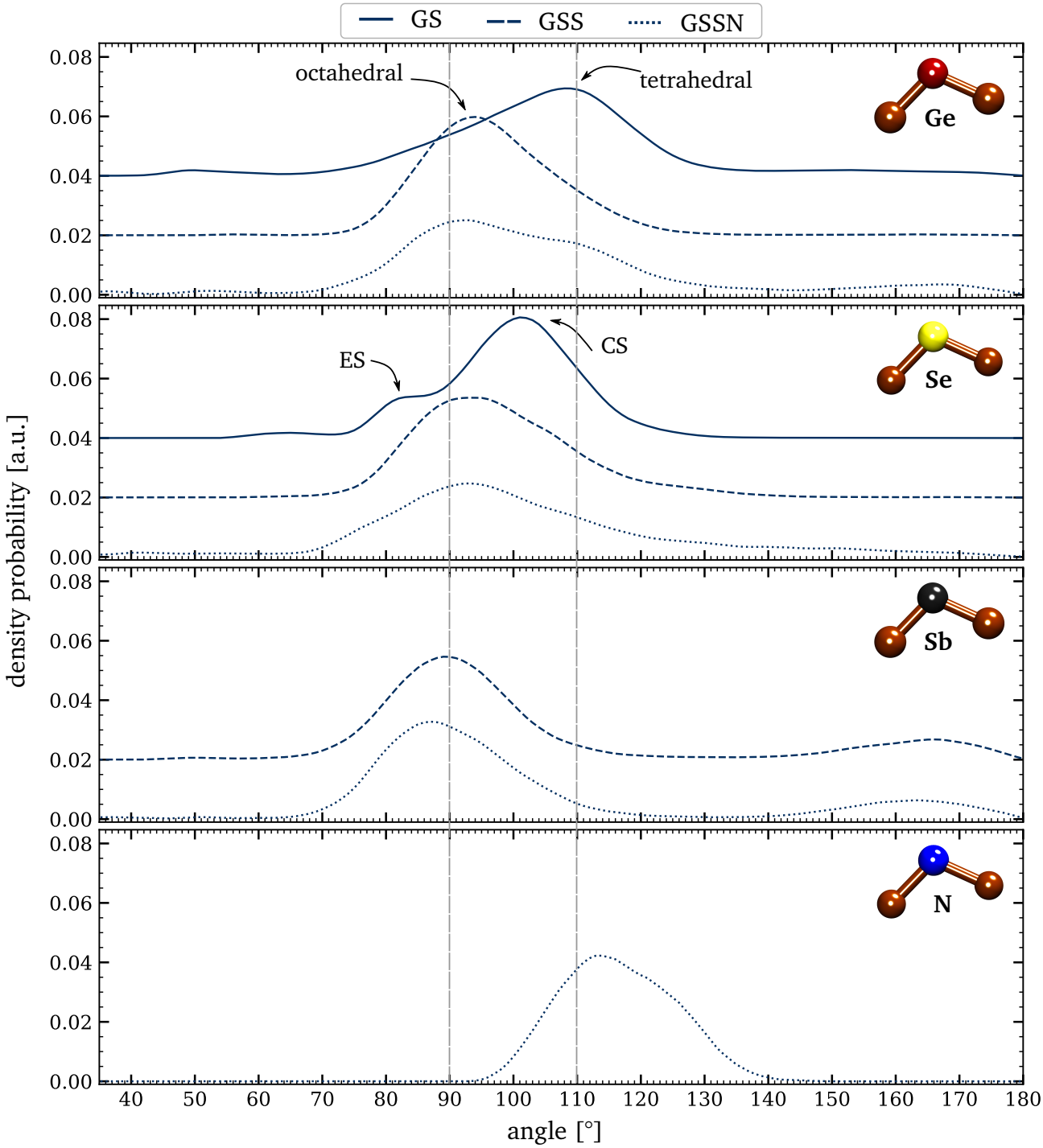

Figure 5.19 – *Distributions of angles for the three glasses in their non excited state, from simulations (vertically shifted by +0.02 and +0.04 for GSS and GS respectively).*

Ge-Se. The discrepancy might be due to the method of simulations. They used Reverse Monte Carlo simulations, giving them a lower coordination compared to what we find here. It ensues that calculated bonding angles reflect this difference.

GSSN is characterized by Sb and Se angular distributions that resemble those of GSS. These two types of atoms are found with angles of 87° and 93°/164° respectively, characteristic of octahedral configurations. For Ge, the main peak is split up between a contribution at 93° and one at 110°. We also see the emergence of a peak around 168°. While the angles of 93° and 168° are once again characteristic of octahedral environments, the peak at 110° must correspond to the tetrahedra reminescence determined beforehand. The angular distribution of the N atoms shows only on peak, at 118°. Their small proportion as well as this value does not allow to conclude further on a specific type of local environment.

Alloy	Atom	Local structure	Angle [°]	*n*
GS	Ge	TD OH	108 90	3.62
	Se	TD - ES TD - CS	82 101	2.22
GSS	Ge	OH TD	94 110 ?	3.80
	Se	OH	93	2.75
	Sb	OH OH	89 167	3.69
GSSN	Ge	OH OH TD	93 168 110	3.72
	Se	OH OH	93 164	2.65
	Sb	OH	87	3.53
	N		118	3.35

Table 5.2 – *Summary of the properties of the non excited glasses from simulations (OH : octahedral, TD : tetrahedral, ES : edge-sharing, CS : corner-sharing).*

The Table 5.2 summarizes the structural analysis of the non-excited configurations: in GS, both Ge and Se atoms are contributing in great majority to tetrahedral units. The broadening of the angle distribution around 90° might indicate a small proportion of Ge atoms in (defective) octahedral units. With the addition of Sb and N, the structure undergoes a large variation : in GSS and GSSN, all atoms are found in octahedral local environment, except for a small proportion of Ge atoms that show a reminescence of tetrahedra in GSSN, in good agreement with previous studies [206].

Density of states for the non-excited states of the three glasses

The density of states (DOS) of the non-excited states of GS, GSS and GSSN are represented in Figure 5.20. The DOS of the three glasses are very similar. As we are interested in the photo-excitation of these materials, what interests us is the DOS around the band gap. The limitation in using GGA functionals appears clearly here, with gaps that are wrongly calculated. Experimentally, the band gaps of the three glasses have been measured to be about 2.2 eV for GS, 1.4 eV for GSS and 1.8 eV for GSSN [47], and with AIMD simulations, Micoulaut *et al.* [154] found a gap of 1.55 and 1.61 eV for $GeSe_3$ and $GeSe_2$ respectively. Here they are estimated about 1.30 eV (GS), 1.34 eV (GSS) and 1.33 eV (GSSN), strangely close to each other, yet all underestimated compared to the true values. This issue prevents an accurate comparison of the absolute optical properties.

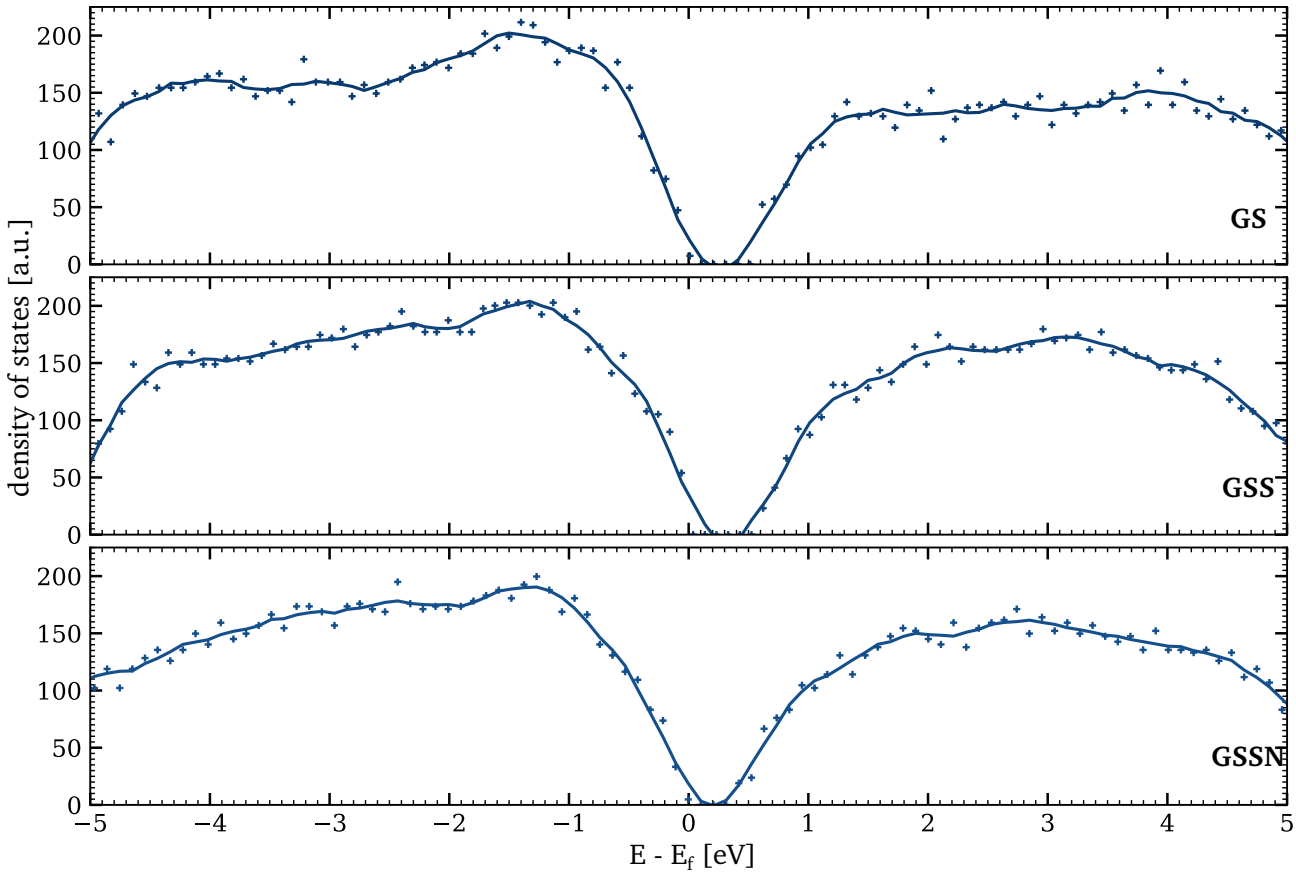

Figure 5.20 – *Density of states of the non excited states of GS (top), GSS (middle) and GSSN (bottom) from AIMD simulations. The Fermi energy E_f corresponds the valence band maximum, determined by VASP.*

II.2 Link with the experiments

To understand the structural changes resulting from a photo-excitation, we tried to link the experimental and simulation results. As stated right before, the calculation of the optical properties will be wronged by the underestimation of the band gap. As a consequence, the same strategy that was used for GeTe was tried here: instead of comparing absolute physical quantities, relative variations were compared.
With the hypothesis that at short times after excitation (roughly below 1 ps) the electron-phonon coupling is negligible, the dielectric function ε obtained experimentally should only reflects variations due to the electronic contributions. Therefore, the comparison of these experimental values with the ones simulated for a "cold" lattice (ionic temperature of T_i = 300 K) under different intensity of excitation (*via* the variation of the electronic temperature T_e) should identify which T_e can reproduce the effects of a fs laser excitation.

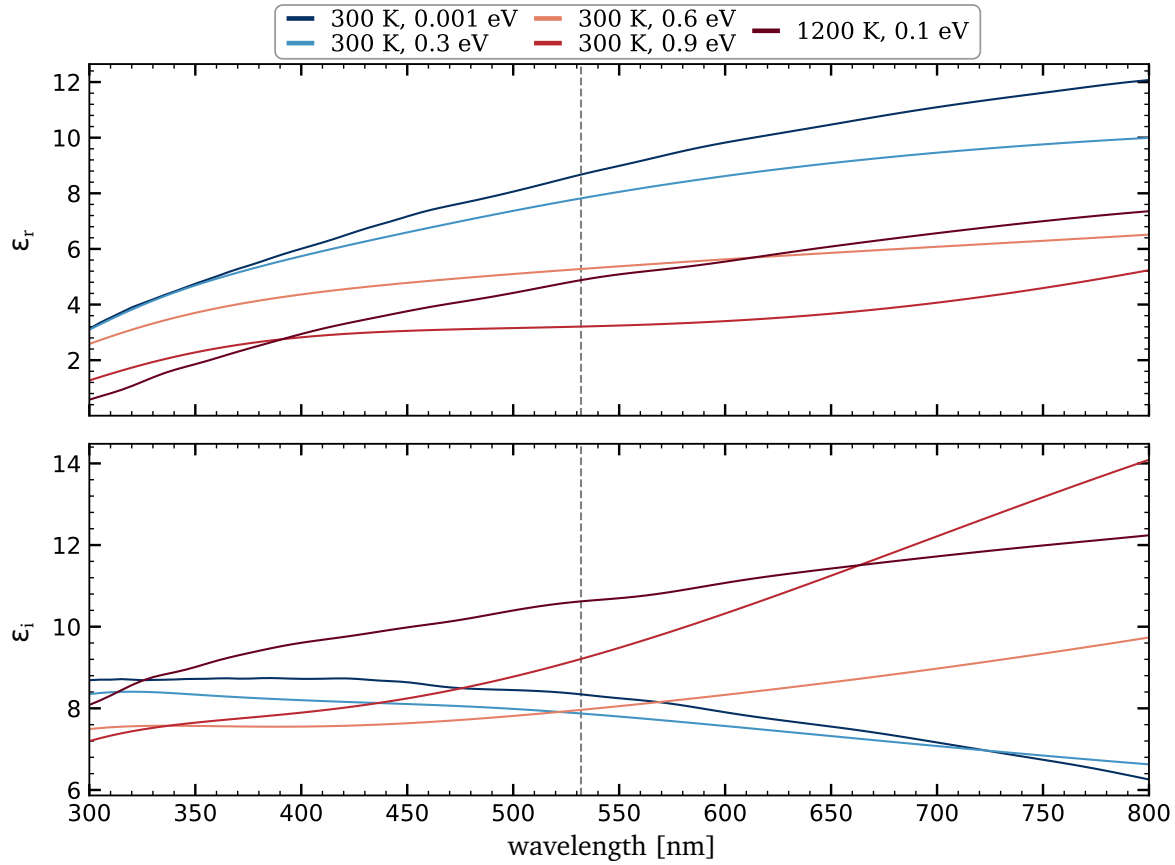

Figure 5.21 – *Dielectric function vs wavelength for the GS sample from simulations. The vertical dotted line correspond the probing wavelength of 532 nm.*

$Ge_{31}Se_{69}$ (GS)

The Figure 5.21 shows the dielectric function as a function of wavelength for GS compound, for all five pairs of (T_e, T_i) that were simulated. In this Section, only the evolution at 532 nm for the cold lattice (T_i = 300 K) interests us. The real part of the dielectric function ε_r decreases

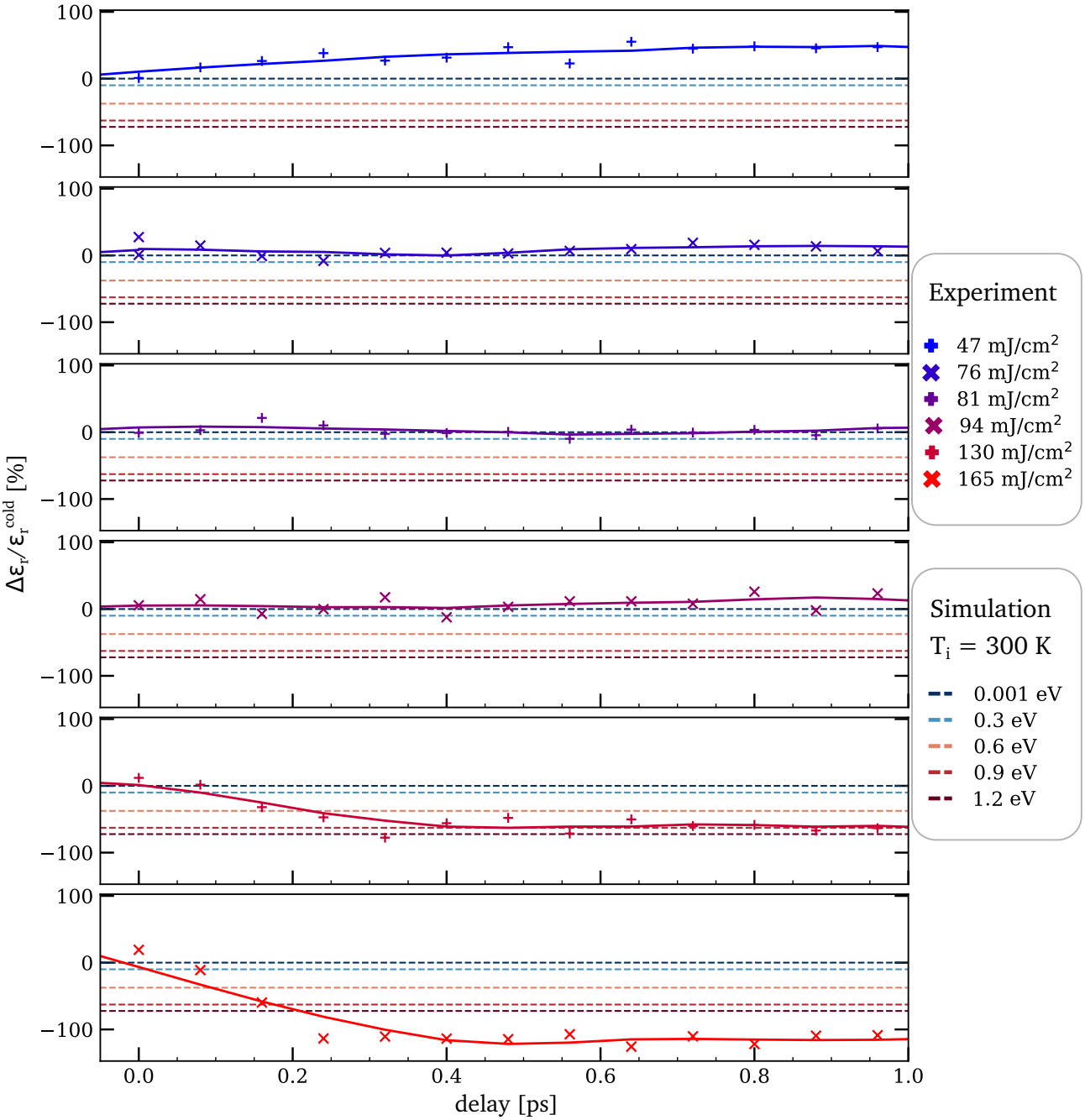

Figure 5.22 – *Relative variation of the real part of the dielectric function for the GS sample. Only the early times after excitation are considered for the experiments (solid lines) in order to have a "cold" lattice. For simulations (horizontal dotted lines), the values correspond to T_i = 300 K and different electronic temperatures.*

as the excitation is raised. However it is not as straightforward for the imaginary part ε_i. The wavelength of 532 nm is at the crossing of the curves. Actually, if we compare the experimental relative variation of the imaginary part $\Delta\varepsilon_i^{EXP}/\varepsilon_{i,cold}^{EXP}$, we obtain $\Delta\varepsilon_i^{EXP}/\varepsilon_{i,cold}^{EXP} \sim 3000\%$, while the simulations only give a maximum variation of 10%.

This observation lead us to only compare the real part of the dielectric function, as represented in Figure 5.22. The evolution of the dielectric function obtained *via* simulation and experiments is completely different. While the experimental one shows an increase, with simulations the dielectric function of the excited state is only seen to be decreasing. Therefore there is no electronic temperature that can be assimilated to these fluences. We note that the values obtained with simulations tends to saturate when T_e is increase very high. This is due to the volume constraint of DFT calculation. As observed in Appendix D, Figure D.1, this condition is complicated to respect for $T_e = 1.2$ eV.

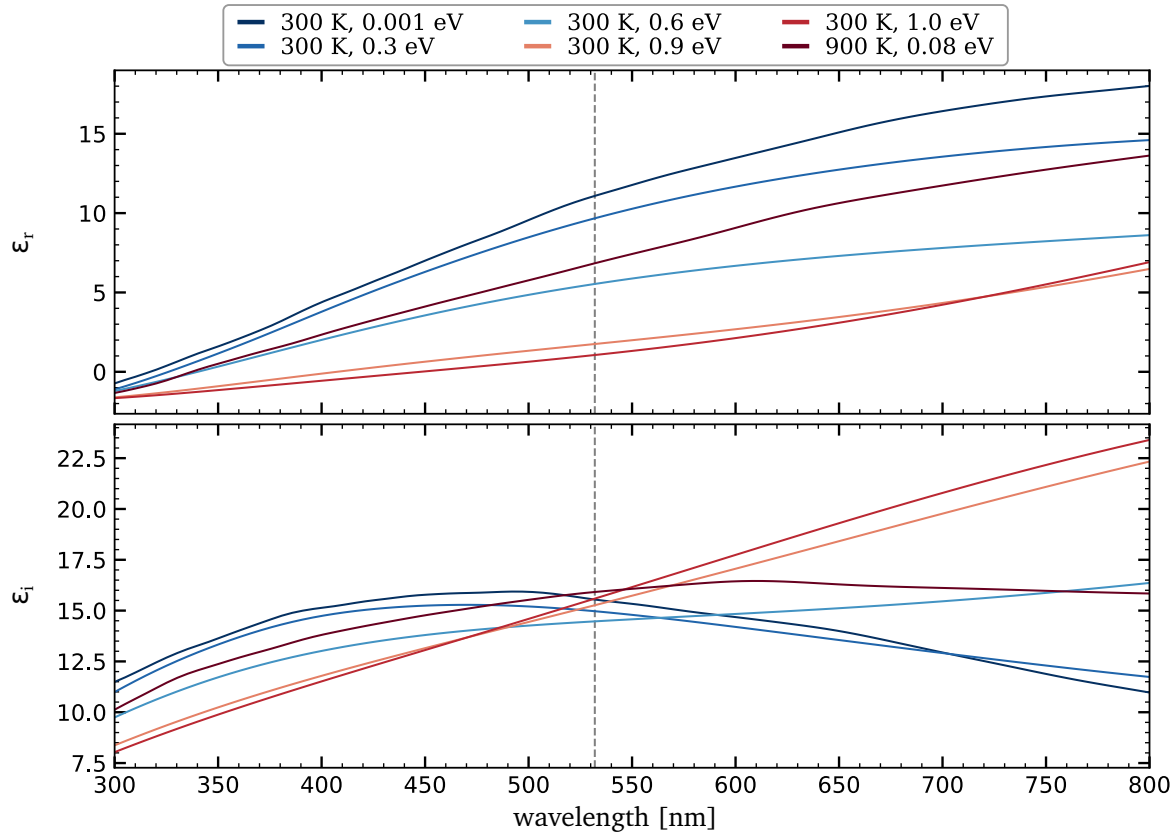

Figure 5.23 – *Dielectric function vs wavelength for the GSS sample from simulations. The vertical dotted line correspond the probing wavelength of 532 nm.*

$Ge_{23}Se_{57}Sb_{20}$(GSS)

The Figure 5.23 shows the simulated dielectric functions *vs* wavelength in the case of the GSS compound. At the probing wavelength of 532 nm, the rise of electronic temperature while keeping

the ionic temperature T_i at room temperature induces a decrease in ε_r.

The variation in ε_i from simulations is again completely negligible compared to the one measured in experiment. As a consequence, only the real part will be used.

The relative variation $\Delta\varepsilon_r/\varepsilon_r^{cold}$ found in experiments and simulations is depicted in Figure 5.24. The identification is easier than for GS sample. Five different regimes can be identified.

- For the lowest fluences, 34 and 45 mJ/cm^2, the application of an electronic temperature of $T_e \sim 0.3$ eV enables to reproduce the laser excitation.
- Fluences slightly higher, between 51 and 67 mJ/cm^2 can be approached using $T_e \sim 0.6$ eV.
- For fluences of 76 and 78 mJ/cm^2, the excitation corresponds to $T_e \sim 0.9$ eV.
- $F = 90$ mJ/cm^2 seems to be equivalent to an electronic temperature of $T_e \sim 1.0$ eV. Similarly to GS, we note the saturation of the dielectric value, which results again from the volume constraint (see Figure D.2 in the Appendix D), so this $T_e = 1.0$ eV case should be interpreted carefully.

$Ge_{23}Se_{53}Sb_{19}N_5$ (GSSN)

The same reasoning applies for GSSN, for which the probing wavelength of 532 nm is again corresponding to a node of the ε_i curves *vs* wavelength (see Figure 5.25). It leads to a variation in simulation very small compared to that obtained in the experiments. As for the real part, ε_r decreases when excitation intensifies, in agreement with the tendency observed in the experiments.

The electronic temperatures reproducing the experimental excited configurations are identified through the comparison of $\Delta\varepsilon_r/\varepsilon_r^{cold}$ in Figure 5.26:

- For the lowest fluences of 44 and 56 mJ/cm^2, the corresponding electronic temperature seems to be $T_e \sim 0.3$ eV.
- In the case of intermediate fluences, we expect $T_e \sim 0.6$ eV.

This attempt to identify the simulations and experiments is not as conclusive as we could have hoped for. Chalcogenide glasses have a non-negligible band gap compared to GeTe. The miscalculation of this latter in the simulations prevents a correct comparison. Indeed, the larger the band gap, the more difficult it is to compare experiments and simulations. For the GS compound, no T_e matched the experimental data, while for GSS and GSSN it seemed to work in some cases.

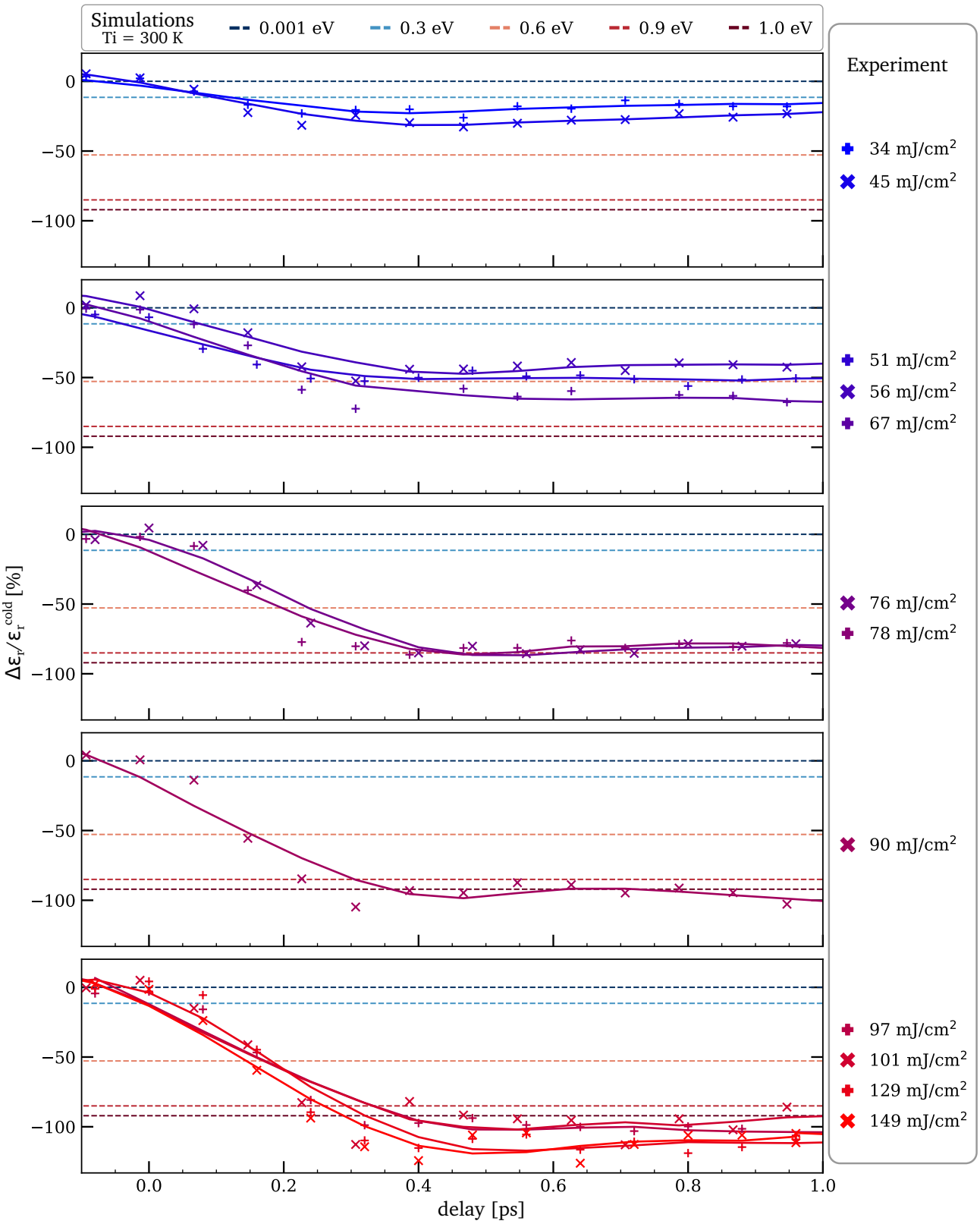

Figure 5.24 – *Relative variation of the real part of the dielectric function for the GSS sample. Only the early times after excitation are considered for the experiments (solid lines) in order to have a "cold" lattice. For simulations (horizontal dotted lines), the values correspond to T_i = 300 K and different electronic temperatures.*

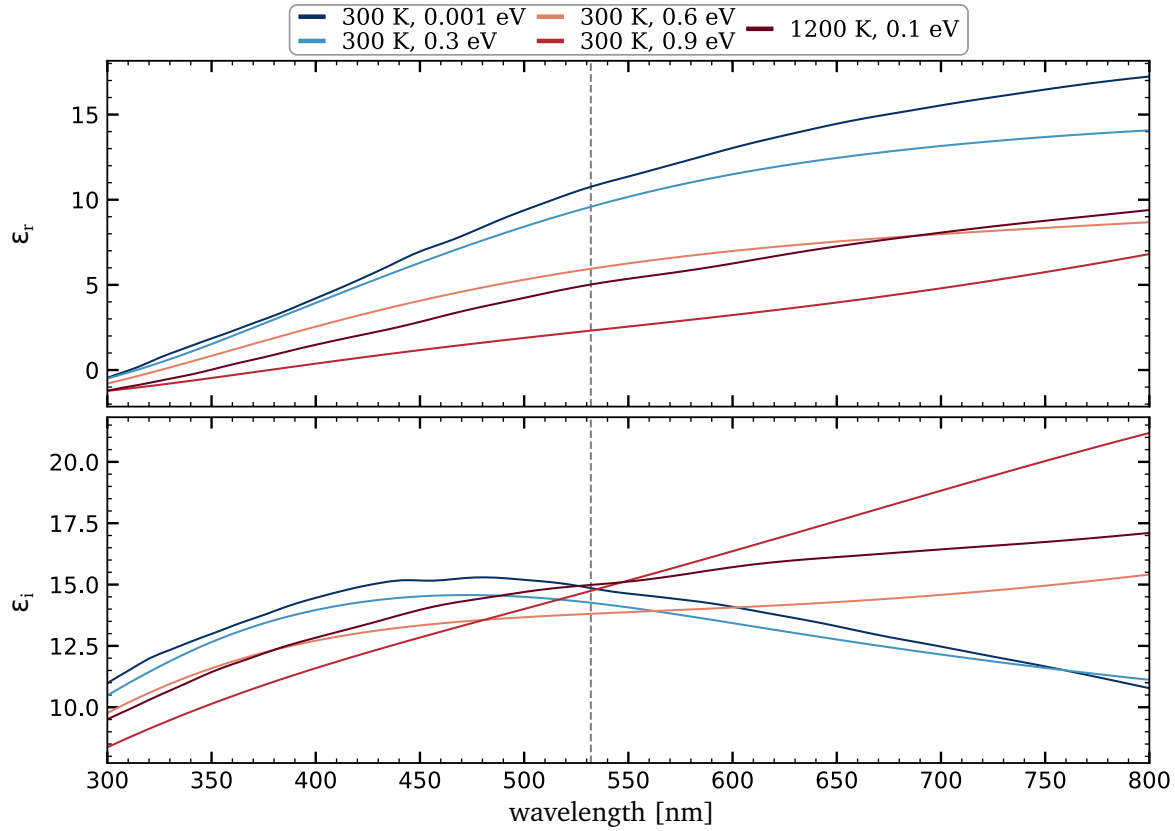

Figure 5.25 – *Dielectric function vs wavelength for the GSSN sample from simulations. The vertical dotted line correspond the probing wavelength of 532 nm.*

II.3 Structural analysis of out-of-equilibrium states

Even though the experiments - simulations comparison cannot be done accurately, it is interesting to investigate the effects of excitation anyways. The densities of states (DoS), pair distribution functions, distributions of angles, number of coordination as well as mean squared displacement were therefore calculated and will be presented in this section.

II.3.1 $Ge_{31}Se_{69}$ (GS)

Density of states of GS

The DoS of the simulated out-of-equilibrium states of GS are shown in Figure 5.27. The excitation leads to a closure of the gap. One remarkable thing is that the liquid state is very different from the out-of-equilibrium states, on the contrary to what we found for GeTe.

A Tauc model could not retrieve the band gap due to the wrongly calculated properties (the gap is estimated about 0.08 eV (GSSN) and 1.51 (GS) and 0.3 (GSS), irrelevant values compared to the experimental ones).

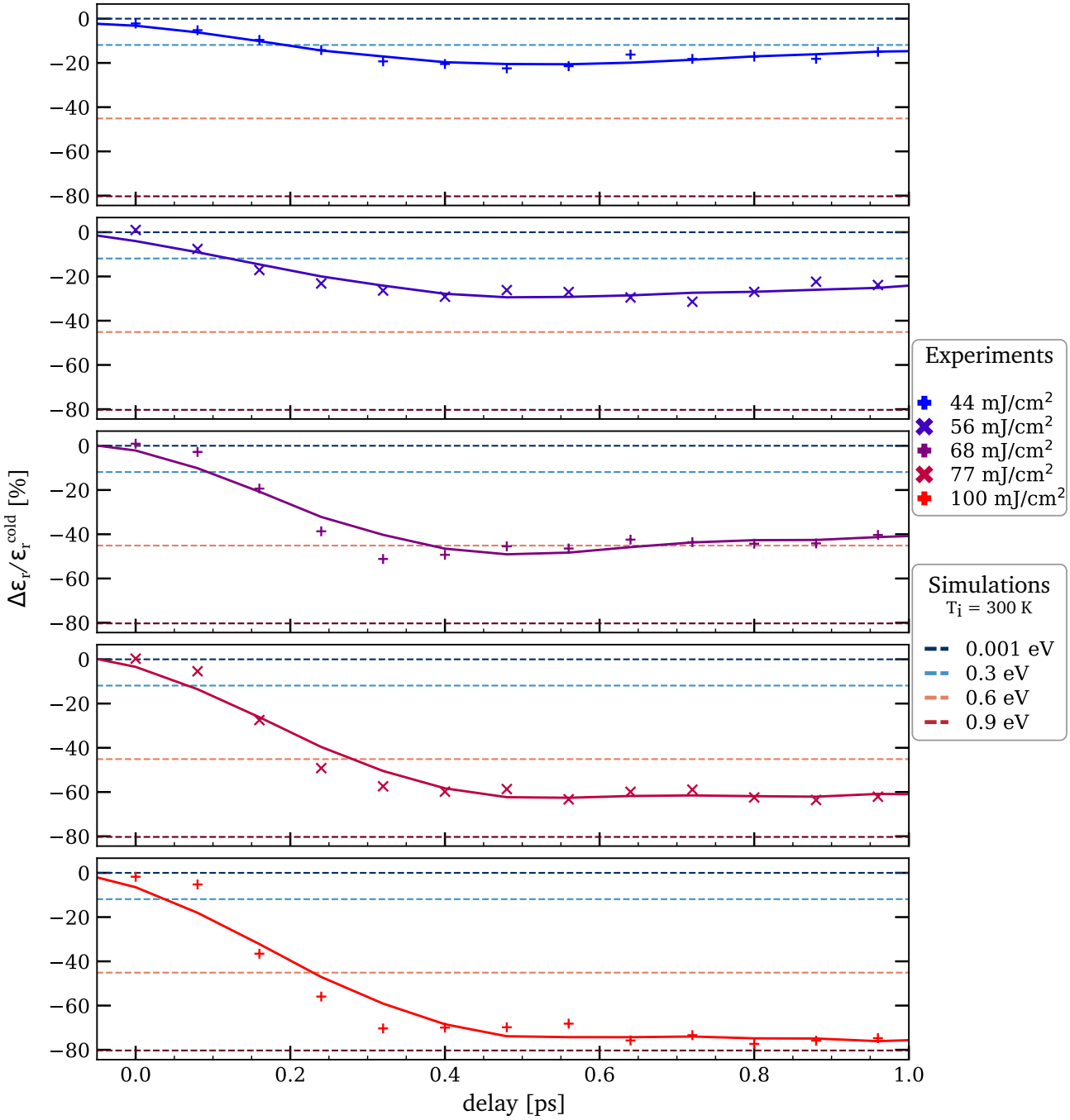

Figure 5.26 – *Relative variation of the real part of the dielectric function for the GSSN sample. Only the early times after excitation are considered for the experiments (solid lines) in order to have a "cold" lattice. For simulations (horizontal dotted lines), the values correspond to T_i = 300 K and different electronic temperatures.*

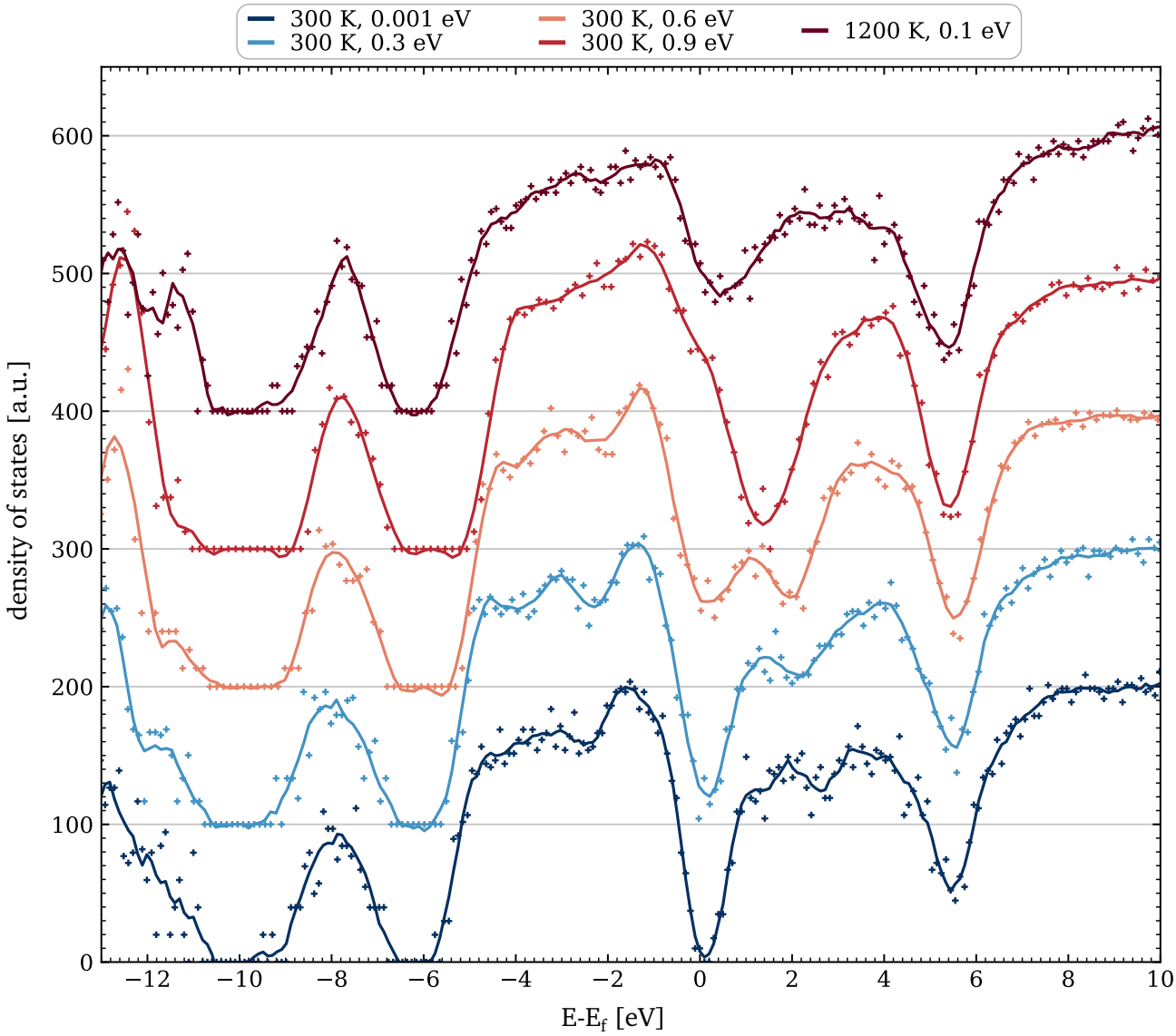

Figure 5.27 – *Density of states of the GS sample from simulations for different (T_i - T_e) pairs (each case is vertically shifted by +200 compared to the previous one).*

Pair distribution function of GS

The partial and total pair distribution functions of GS are shown in Figure 5.28. The evolution of the main peaks positions are represented as a radar chart in Figure 5.29. Overall the bonds tends to lengthen upon increasing excitation.

The out-of-equilibrium states are characterized by the concomitant disappearance of the Se-Se along with the Ge-Ge ones in the first neighbouring shell. The first peak position, determined to be r_{Ge-Ge} = 2.55 Å in the non-excited case, slowly shifts towards higher values with this disappearance. Se-Se bonds length is more stable, yet we still notice a lengthening under high excitation.

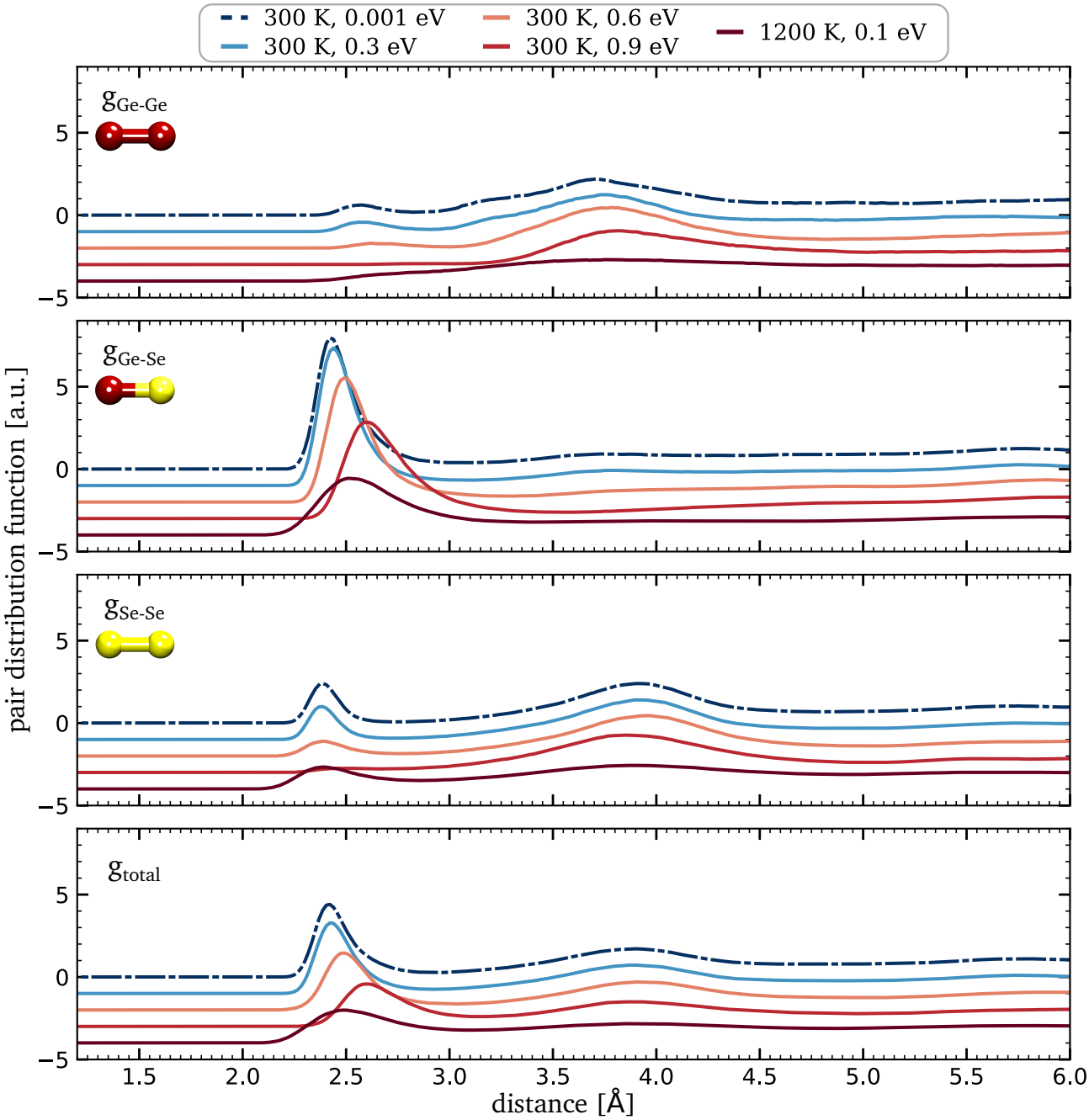

Figure 5.28 – *Partial and total pair distribution functions of the GS sample from simulations (shift by -1 for each case compared to the previous one).*

In the 2^{nd} shell, the amount of Ge-Ge bonds is quite stable, except when the material melts. In this case, the pair distribution function of Ge-Ge shows no distinctive peak.

For an excitation of T_e = 0.3 eV, the Ge-Se bonds are more predominant than in the non-excited case. However, this tendency does not last with the increase of excitation. Moreover, a clear lengthening of the bonds from 2.41 to 2.60 Å is observed. These Ge-Se bonds dominate completely the total pair distribution function in the first shell.

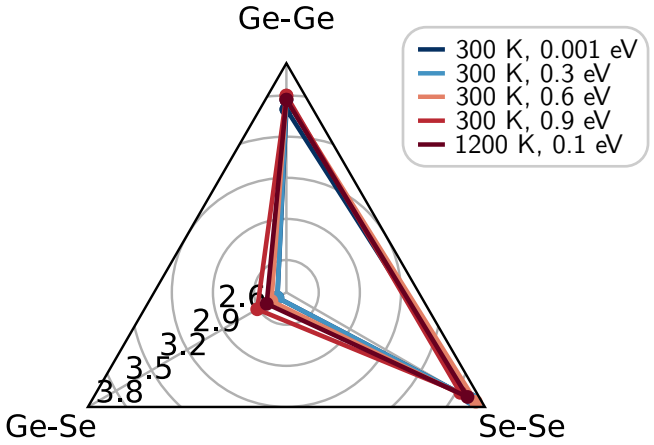

Figure 5.29 – *Radar chart of the main bond peaks distance extracted from the $g(r)$ of GS in Å.*

The liquid state is less structured than all the others. For the Ge-Se bonds, its features are resembling those of the intermediate case 0.6 eV. However, the Se-Se distribution is characterized by a non-negligible peak in the first shell, more similar to the non-excited case, yet without the same long distance structuration.

Local environment of GS

The Figure 5.30 represents the coordination numbers calculated from the partial pair distribution functions of the GS sample.

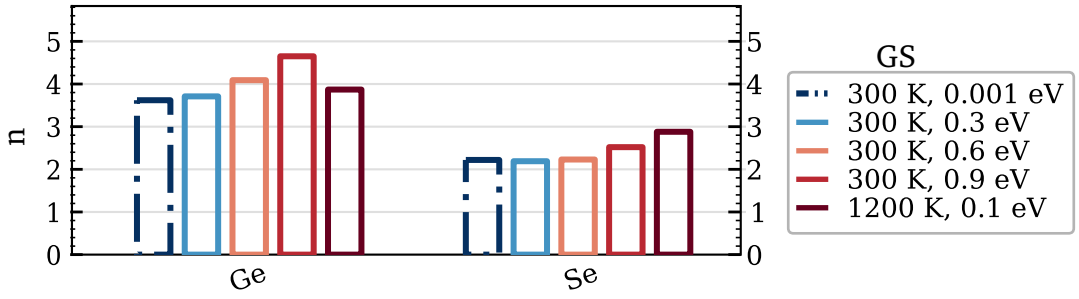

Figure 5.30 – *Coordination numbers of GS (cut-offs in Appendix D, Table D.1).*

The coordination numbers of the Ge and Se atoms are not behaving in the same way upon excitation. Increasing the intensity of excitation leads to a clear increase in coordination number of Ge from $n_{Ge}^{cold} = 3.62$ up to a value of 4.65 for $T_e = 0.9$ eV. For Se, it is quite stable around $n_{Se} = 2.22$, except for the highest excitation of $T_e = 0.9$ eV for which a slight increase up to 2.52 is calculated. The liquid state is different from all out-of-equilibrium states with an intermediate CN for Ge: $n_{Ge}^{liq} = 3.87$, but the highest calculated of all simulated states for Se: $n_{Se}^{liq} = 2.88$.

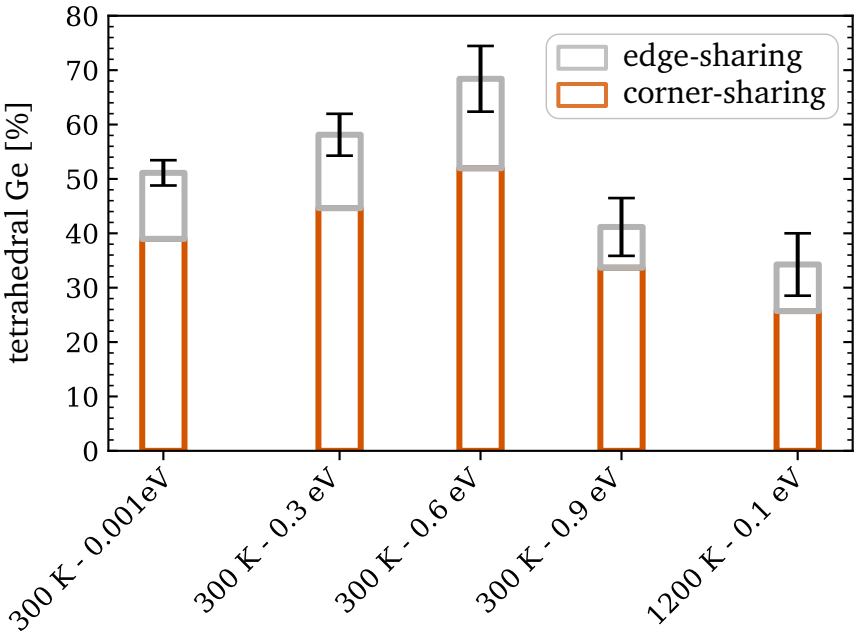

Figure 5.31 – *Evolution of the proportion of tetrahedral Ge atoms (Ge^T) in GS.*

These coordination numbers compared to the amount of tetrahedral Ge for each configuration (Figure 5.31) and to the distribution of angles (Figure 5.32) gives an idea of the evolution of the local environments of each type of atom.

The distributions of angles of the out-of-equilibrium states resulting from an excitation of $T_e = 0.3$ and 0.6 eV are very similar to the non-excited state:

- For the Ge-centered angles, we find an assymetric distribution, with a main peak about 100°, corresponding to tetrahedral units. This observation is consistent with the coordination number determined previously. An increase of the Ge^T with excitation can be noted.
- The distribution of angles around Se is characteristic of the Ge-Se-Ge bonds found in edge- and corner-sharing tetrahedra.

If the excitation is increased higher than $T_e = 0.6$ eV, the resulting structure changes greatly: an electronic temperature of $T_e = 0.9$ eV gives in an out-of-equilibrium state that is completely different from the previous ones. The Ge as well as the Se atoms shift towards octahedral environments with angles of 94° and 91° respectively. This is confirmed by the clear decreased in Ge^T: from 70% for an excitation of $T_e = 0.6$ eV, it drops down to about 40% for $T_e = 0.9$ eV.

The configuration of the liquid state is not very clear: the distribution of angles is greatly flattened, though the main peak seems to be about 101° for Ge and 99° for Se, similar to the non-excited state values. The percentage of Ge^T is the lowest of all, but is still non-negligible as 32% of the Ge

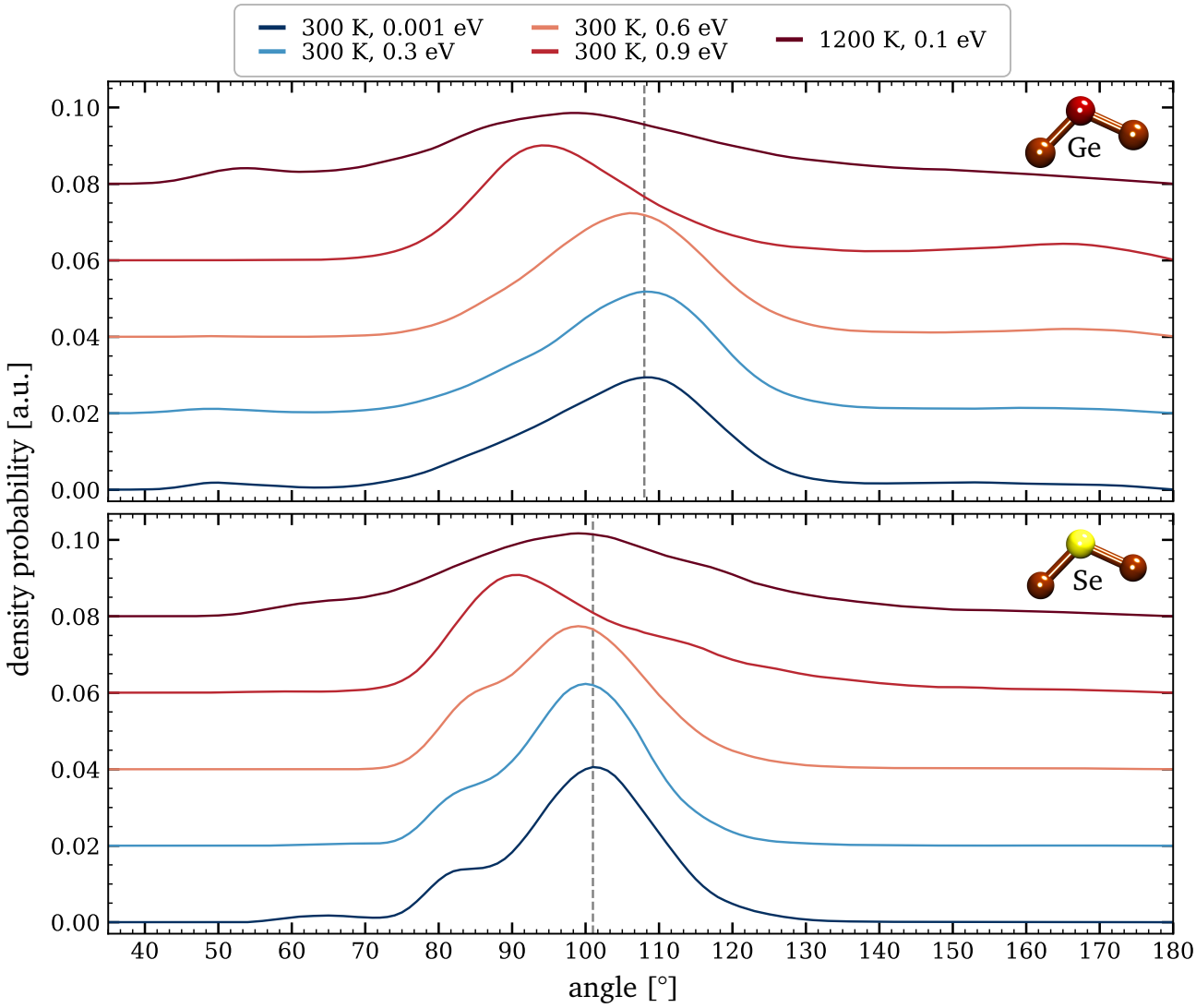

Figure 5.32 – *Distribution of angles of the simulated out-of-equilibrium states of GS. The gray dotted lines correspond to the maximum peak position in the initial state.*

atoms are found in tetrahedral sites.

From the evolution of the number of tetrahedra, of the coordination numbers and of the angles, we can hypothesize that a low excitation tends to form more Ge-Se bonds in tetrahedra configurations by breaking the Se-Se and Ge-Ge bonds. If the excitation is higher than $T_e = 0.6$ eV, all these latter bonds have been broken. Therefore, the system breaks now the Ge-Se bonds from the tetrahedra sites to rise the number of coordination and adopt octahedral configurations.

Mean squared displacement of GS

The mean squared displacement (MSD) of GS, represented in Figure 5.33 confirms the difference between the out-of-equilibrium and liquid states. Non-excited states as well as low-excited cases

are characterized by very small diffusion coefficients: $D_{Ge} \sim 1{\times}10^{-6}$ cm^2/s and $D_{Se} \sim 2{\times}10^{-6}$ cm^2/s. Even for the configuration resulting from the highest excitation, the value of D is small: we find $D(T_e = 0.9eV) \sim$ 5-6 $\times\ 10^{-6}$ cm^2/s. The liquid state shows a clear discrepancy from the other states, with a diffusion coefficient 10 times larger: $D_{Ge}^{liq} \sim 8{\times}\ 10^{-5}$ cm^2/s and $D_{Se}^{liq} \sim 10^{-4}$ cm^2/s. In terms of orders of magnitude, it is comparable to the value determined by Yildirim *et al.* [157]: $D = 4{\times}10^{-5}$ cm^2/s, though there is a ratio of 2 between both. All diffusion coefficients calculated are listed in the Table D.4, Appendix D.

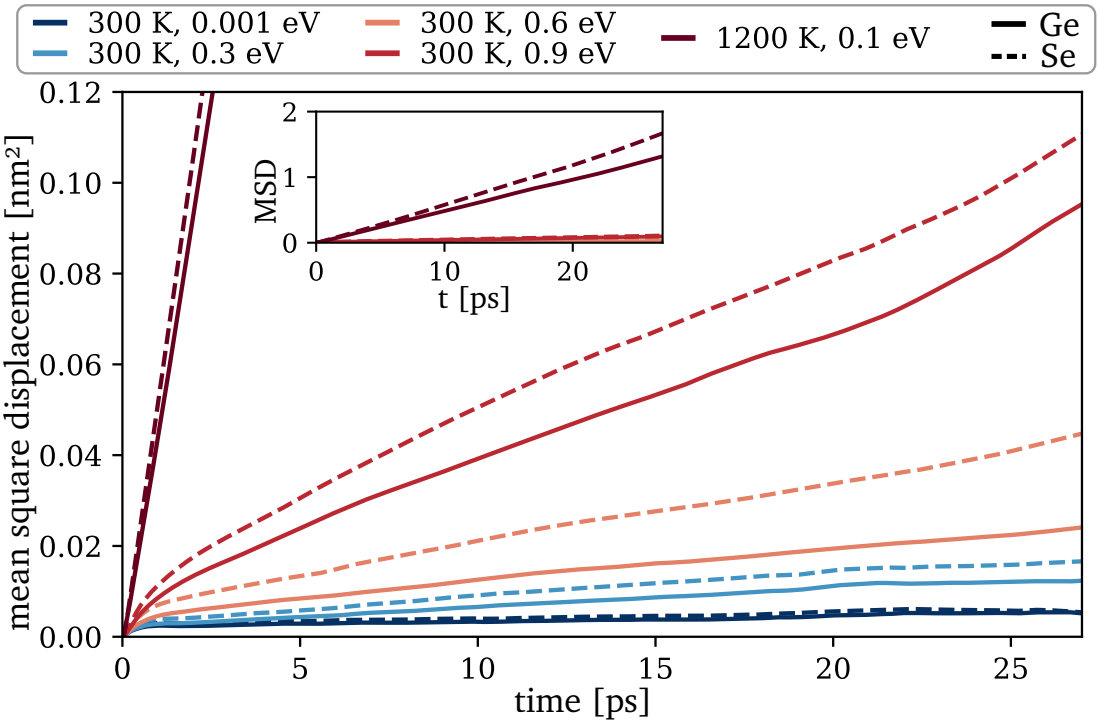

Figure 5.33 – *Mean squared displacement of the atoms as a function of the simulations time steps for the GS alloy.*

II.3.2 $Ge_{23}Se_{57}Sb_{20}$ (GSS)

Density of states of GSS

The density of states of GSS is represented in Figure 5.34. What interests us is the energy window around the Fermi energy. The main feature that appears in the DOS is the closure of the band gap upon excitation. The more the material is excited, the more the gap closes. The liquid state's main features are similar to the low excited states.

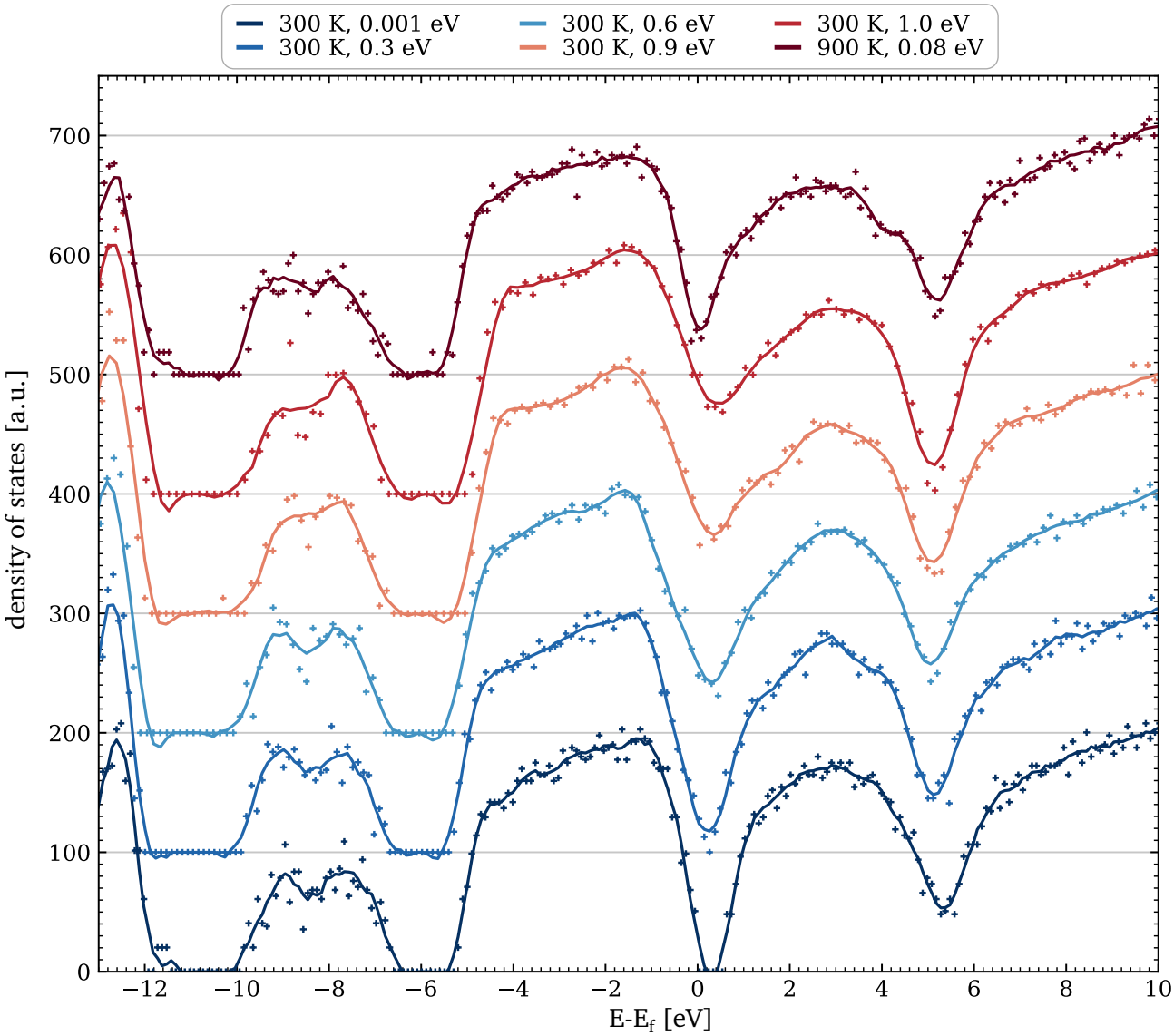

Figure 5.34 – *Density of states for the GSS alloy from simulations (each case vertically shifted by +100 from the previous one).*

Pair distribution function of GSS

The Figure 5.35 shows the partial and total distribution functions (PDF) of the GSS compound. Similarly to GS, the liquid state features are similar to the non/low-excited states rather the highly excited ones for the main types of bonds of GSS: Ge-Se, Se-Sb, Sb-Sb and total PDF. The positions of the main peaks of each distribution are represented as a radar chart in Figure 5.36.

A lengthening of the main types of bonds, Ge-Se and Se-Sb is seen upon increased excitation. Both of these bonds are only present in the first neighbouring shell.
Ge-Ge as well as Ge-Sb bonds are present in a negligible amount in the first neighbouring shell. With excitation, the peaks of these distributions smoothly shift to higher distances. Their amount

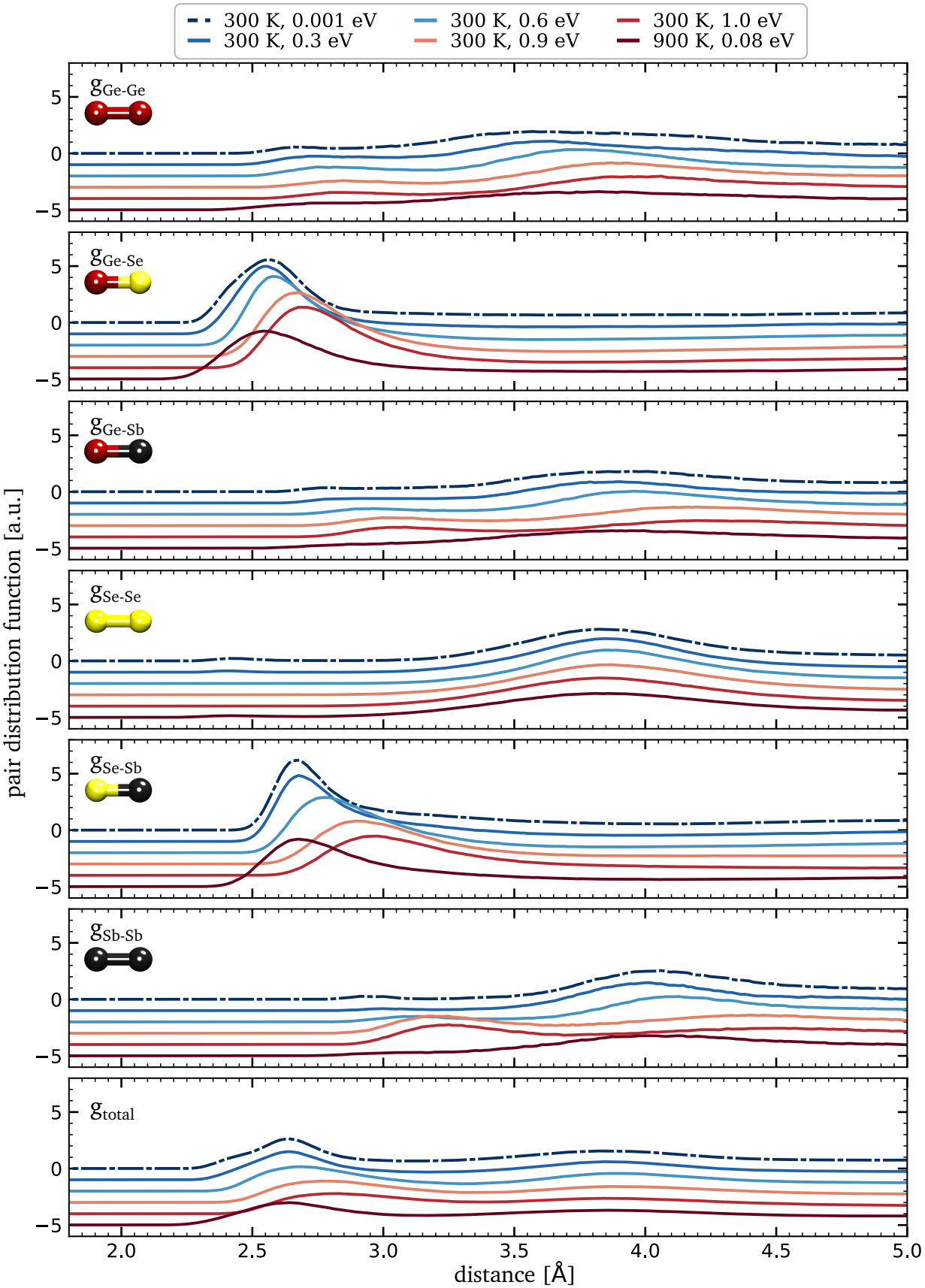

Figure 5.35 – *Partial and total pair distribution functions (PDF) of GSS (cumulative shift by -1 in each case).*

is slightly larger in the second shell. The same lengthening is observed upon excitation.
The curve of the liquid state for both types of bond is rather flat, implying that their amount is completely negligible for these states.

For low excitation ($T_e \leq 0.6$ eV), Sb-Sb bonds are detected in a very small (negligible) amount in the first sphere of coordination with a length of $r_{Sb-Sb} \sim 2.95$ Å. The main peaks of this distribution are located is the second neighbouring shell, corresponding to bond lengths of 4 Å.
However, the response to a higher excitation is interesting: the second shell peak flattens while being slightly shifted towards higher distances. However, at the outer border of the first neighbouring shell around 3.2 Å, a peak appears with a high contribution to the g_{Sb-Sb} partial distribution function. This mechanism is interpreted as a shortening of the Sb-Sb bonds.

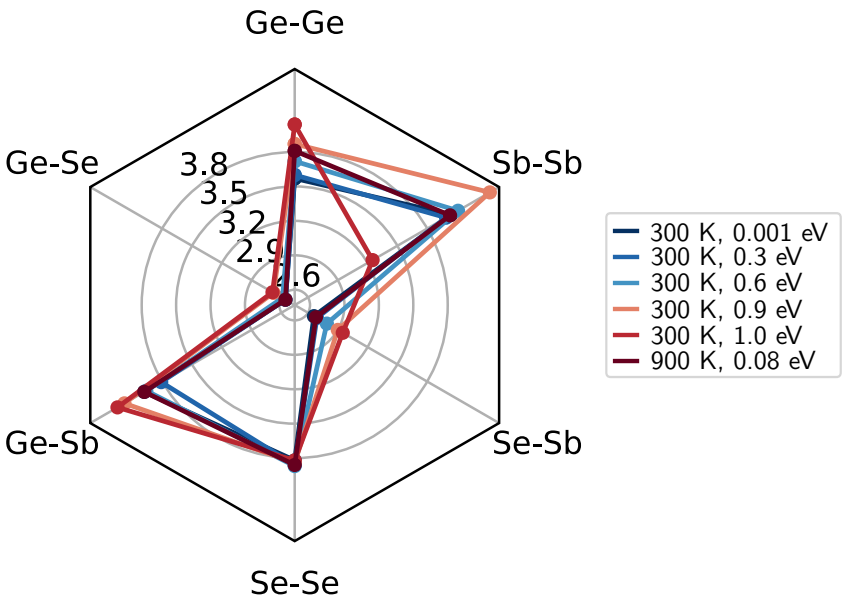

Figure 5.36 – *Radar chart of the main bond peaks distance extracted from the $g(r)$ of the simulated out-of-equilibrium states of GSS, in Å.*

The Figure 5.37 represents the coordination numbers calculated from the partial pair distribution functions of the GSS sample. With the increase of excitation intensity, n increases towards 5-6 for Ge, 5 for Sb and 4 for Se. To interpret these variations, it is necessary to analyze also the distributions of angles as well as the proportion of Ge^T.

The distribution of angles around each species is represented in Figure 5.39. Upon low excitation, $T_e \leq 0.6$ eV, the distributions of angles do not change much. In the case of Ge and Se, the main peak amplitude slightly increases. The maximum stays at about 93°, meaning that octahedral-like configurations are favored. This is also observed for Sb, with a maximum of the distribution staying at 89°. However, we also notice the flattening of the peak at 165° upon excitation.

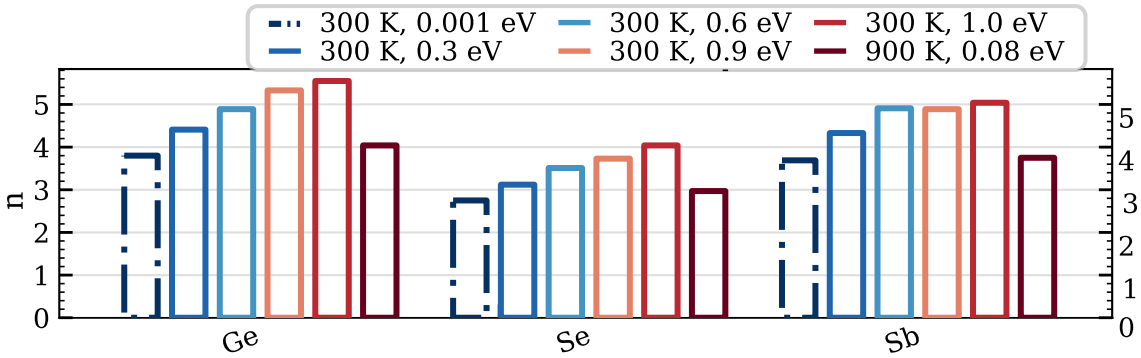

Figure 5.37 – *Coordination numbers of the out-of equilibrium states of GSS (cut-offs in Appendix D, Table D.2).*

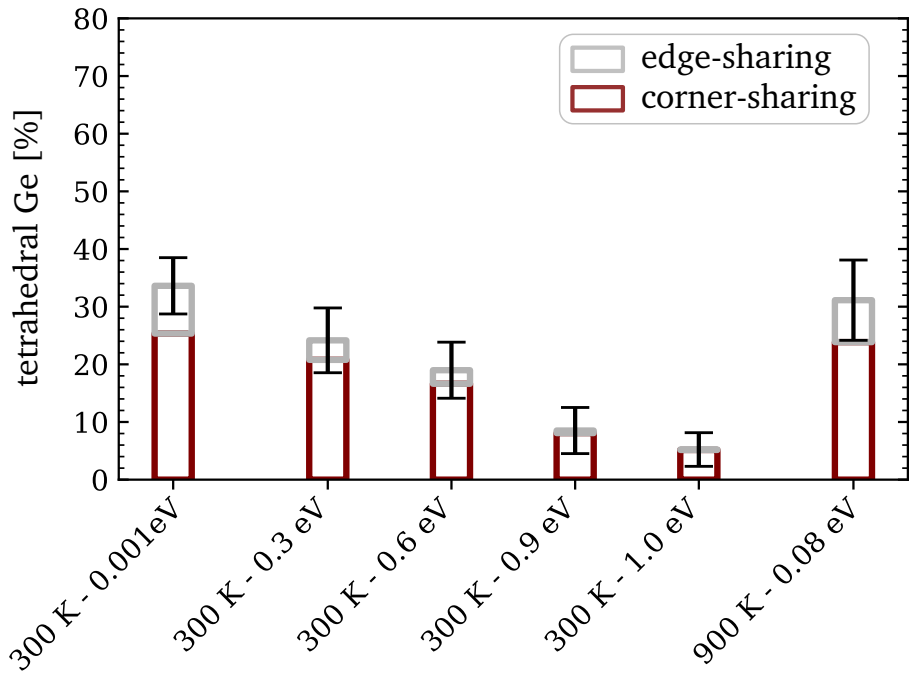

Figure 5.38 – *Evolution of the proportion of tetrahedral Ge atoms (Ge^T) in GSS.*

For higher excitations, the corresponding out-of-equilibrium states are characterized by smaller Ge and Sb angles: the main peak positions are found to be 93° and 84° respectively. Se atoms are not affected by this variation, but similarly to the other species, we still observe a broadening of the distributions.

In GS, 80° was a particular value of angles, corresponding to edge-sharing tetrahedra. However, if we analyze the proportion of tetrahedral Ge in this compound as a function of excitation, shown in Figure 5.38, the obvious conclusion is that the shift of angles does not correspond to the emergence of tetrahedral units. Indeed, the amount of tetrahedra, which was at 32% in the non-excited

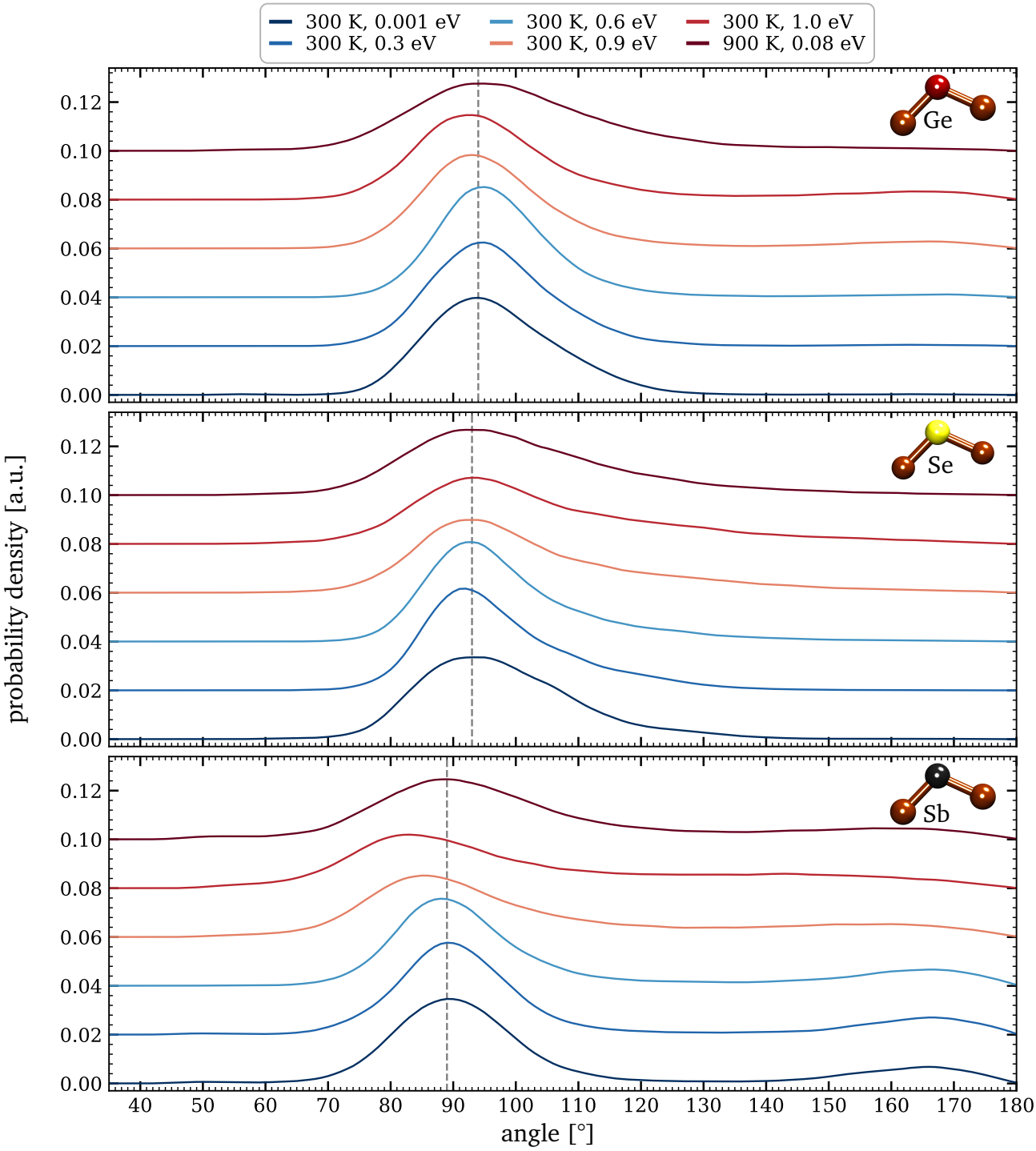

Figure 5.39 – *Distribution of angles of the simulated out-of-equilibrium states of GSS. The gray dotted lines correspond to the maximum peak position in the initial state.*

state, drops with the excitation. It reaches its minimal value of 6% for the highest excitation of T_e = 1.0 eV with almost no edge-sharing tetrahedral detected. It is more likely a distortion of the octahedral local environment due to the high excitation, which is consistent with the coordination numbers about 5-6 calculated for Ge and Sb in those two cases.
Here the Se-Sb bonds cannot be broken as easily it was the case for Ge-Ge/Se-Se in GS. Hence, the material does not form more tetrahedra, but rather breaks directly the Ge-Se bonds from the tetrahedra sites to "reinforce" the octahedral configurations. This is why we observe a continuous decrease in the number of tetrahedral units.

The liquid state is very similar to the non-excited state: the main peak positions of each type of atom are the same, only thermal broadening really discriminates the both of them. The amount of tetrahedra is also very similar.

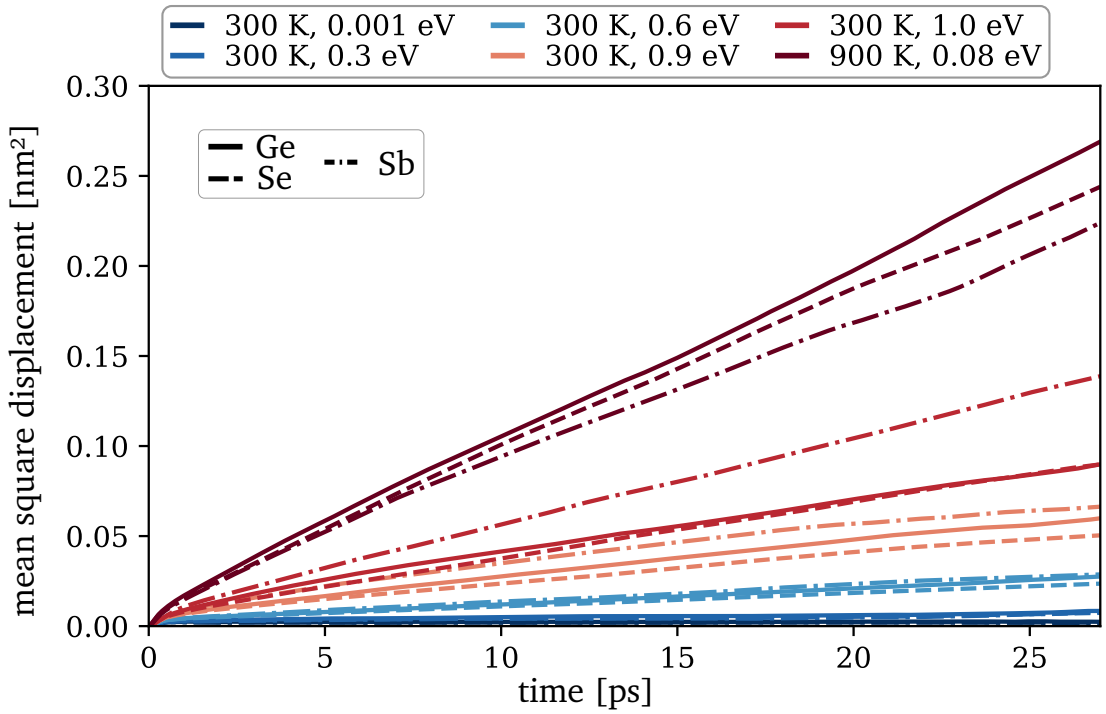

Figure 5.40 – *Mean squared displacement of the simulated out-of-equilibrium states of GSS. The initial and low excitation curves are in caged states, while higher excitations lead to diffusive regimes and the increase of the slope (and therefore of D).*

Mean squared displacement of GSS

The mean squared displacement of GSS, represented in Figure 5.40, does not exhibit a pronounced gap between the liquid and out-of-equilibrium/non-excited states such as in the case of GS. It

is interesting to note that the MSD of the Sb atoms, which has the highest slope for $T_i = 300$ K, becomes the one with the lowest slope in the liquid state. As it is directed linked to the diffusion coefficient D, this tendency is also seen in the values of D_{Sb} which go from 0.3×10^{-6} cm^2/s up to 1.4×10^{-5} cm^2/s, whereas for Ge for example, the diffusion coefficient increases from $D_{Ge} = 0.5 \times10^{-6}$ cm^2/s up to 1.7×10^{-5} cm^2/s. If we compare the values of the liquid states of GSS and GS, we find that D^{liq}_{GSS} is almost 5 times smaller than D^{liq}_{GS}. The ionic temperatures chosen for both are not the same, it is true, but this discrepancy is very large. Stokes-Einstein relation states that the coefficient diffusion is inversely proportional to the viscosity η such that:

$$D = \frac{k_B T}{6\pi\eta r} \tag{5.8}$$

with r the radius of the particles considered and T the temperature. Therefore, in the case of GSS, the viscosity of the liquid state is very high, resulting in a state that behaves almost like a solid in terms of atomic diffusion.

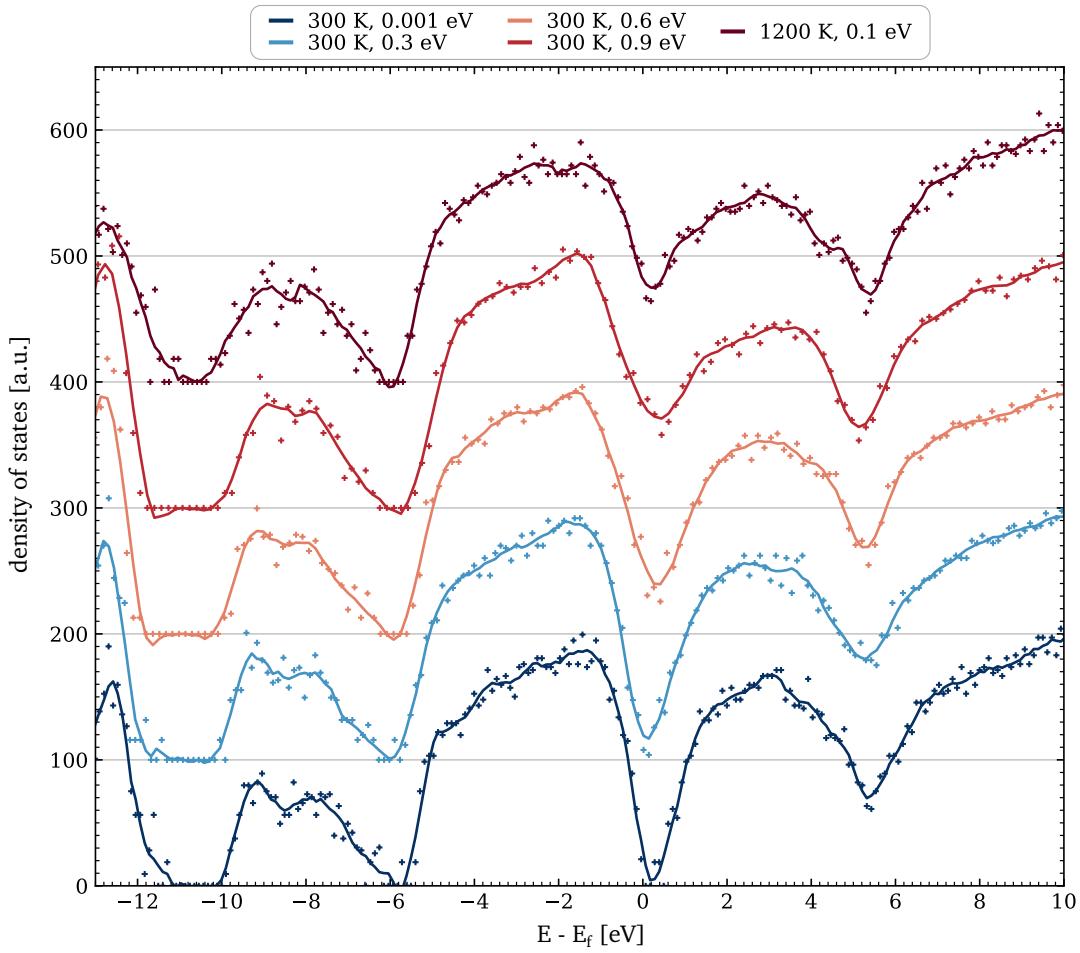

Figure 5.41 – *Density of states for the GSSN simulated states (each case vertically shifted by +100 from the previous one).*

II.3.3 $Ge_{23}Se_{53}Sb_{19}N_5$ (GSSN)

Density of states of GSSN

The density of states of GSSN is represented in Figure 5.41. It is very similar for the out-of-equilibrium, liquid and non-excited states. We notice a closure of the band gap upon excitation, with the same noticeable dependency: the more intense the excitation, the more the gap closes. Outside that close-up on the band gap, all cases show the same features, with slight differences, but nothing as striking.

Pair distribution function of GSSN

The Figure 5.42 shows the partial and total pair distribution functions of GSSN alloy from simulations. The main peaks positions were reported in a radar chart in Figure 5.43.

Similarly to the non-excited material, the highest proportion of bonds is for Ge-N and Sb-N types for the excited and liquid states. The out-of-equilibrium states are characterized by the sharpening of Ge-Ge and N-N peaks. In the first case, the Ge-Ge bonds in the first neighbouring shell lengthens slightly upon excitation while those in the second one are stable in amount and length.

A shortening of the N-N bonds is observed. The melting induces a large shift of the main peaks down to even shorter N-N distances.

Se-Se bonds disappear from the 1^{st} shell upon excitation, but their amount is similar for the liquid and the non-excited cases. In the second neighbouring shell, they are very stable, both in length and amount. Only when the GSSN melts, the distribution flattens in this 2^{nd} shell, but the peak position is still very close to that of the other states.

It is interesting to note that both Ge-Se and Ge-Sb, the two major bonds not involving N, demonstrate a similar variation upon excitation and in the liquid phase. The out-of-equilibrium states are characterized by an increasing interatomic distance. But this trend is completely broken by the liquid phase: in this state, both Ge-Se and Ge-Sb bonds are shorter than in the non-excited case.
The coordination numbers extracted from the $g(r)$ are represented in Figure 5.44. The Ge and Se atoms see their number of neighbours increase with the excitation intensity, but it is more complicated in the case of Sb. The coordination number of N does not change much, though we note a slight decrease.
While the amount of Ge^T in GSSN is stable upon excitation (Figure 5.45), the Ge atoms tend to adopt a more octahedral type of configuration, as can be seen in Figure 5.46. The 110° peak in

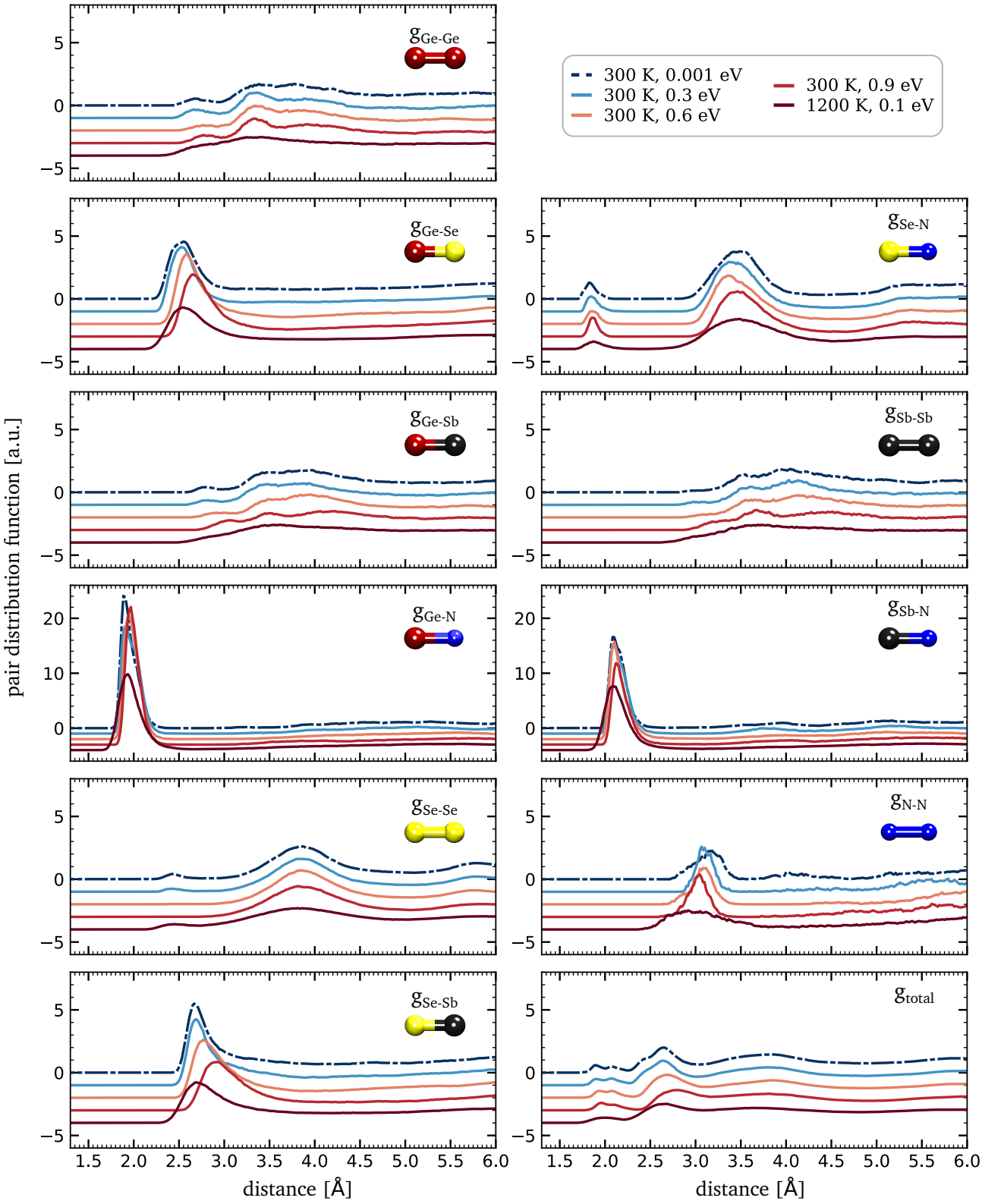

Figure 5.42 – *Partial and total pair distribution functions of GSSN. (Cumulative shift by -1 in each case. The y scales of the partial g_{Ge-N} and g_{Sb-N} have been adapted for more clarity).*

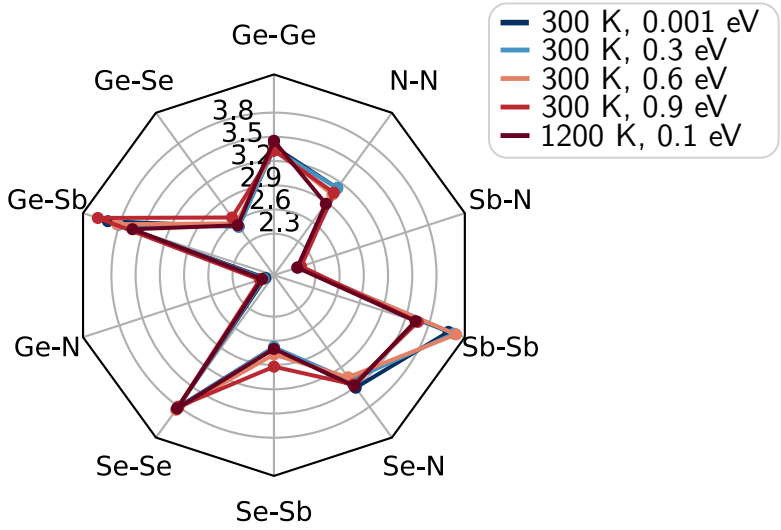

Figure 5.43 – *Radar chart of the g(r) main peaks positions for the simulated out-of-equilibrium states of GSSN, in Å.*

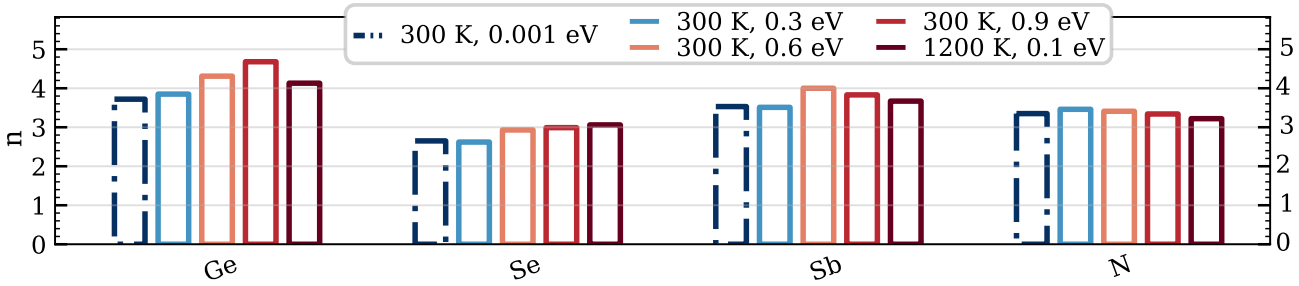

Figure 5.44 – *Coordination numbers of the simulated out-of-equilibrium states of GSSN (cut-offs in Appendix D, Table D.3).*

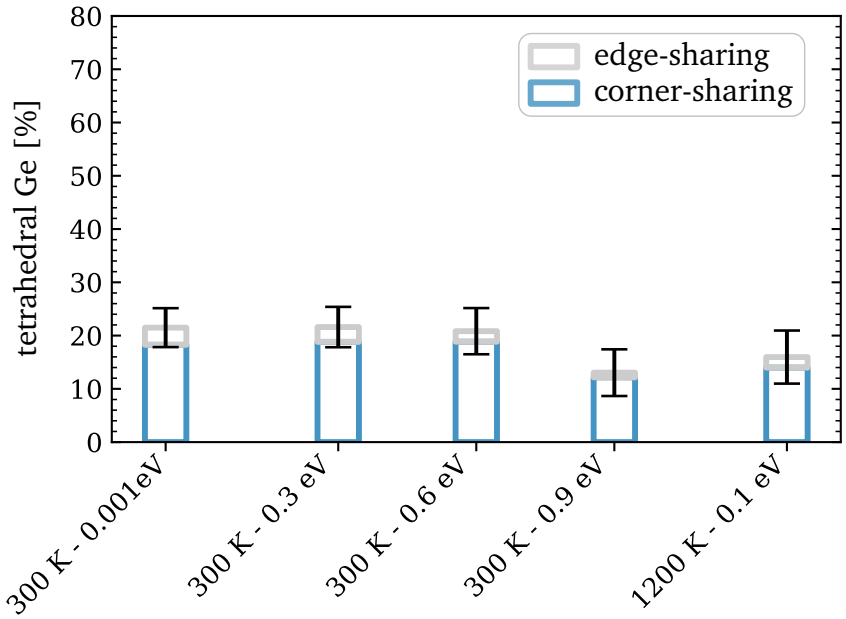

Figure 5.45 – *Evolution of the proportion of tetrahedral Ge atoms (Ge^T) in GSSN.*

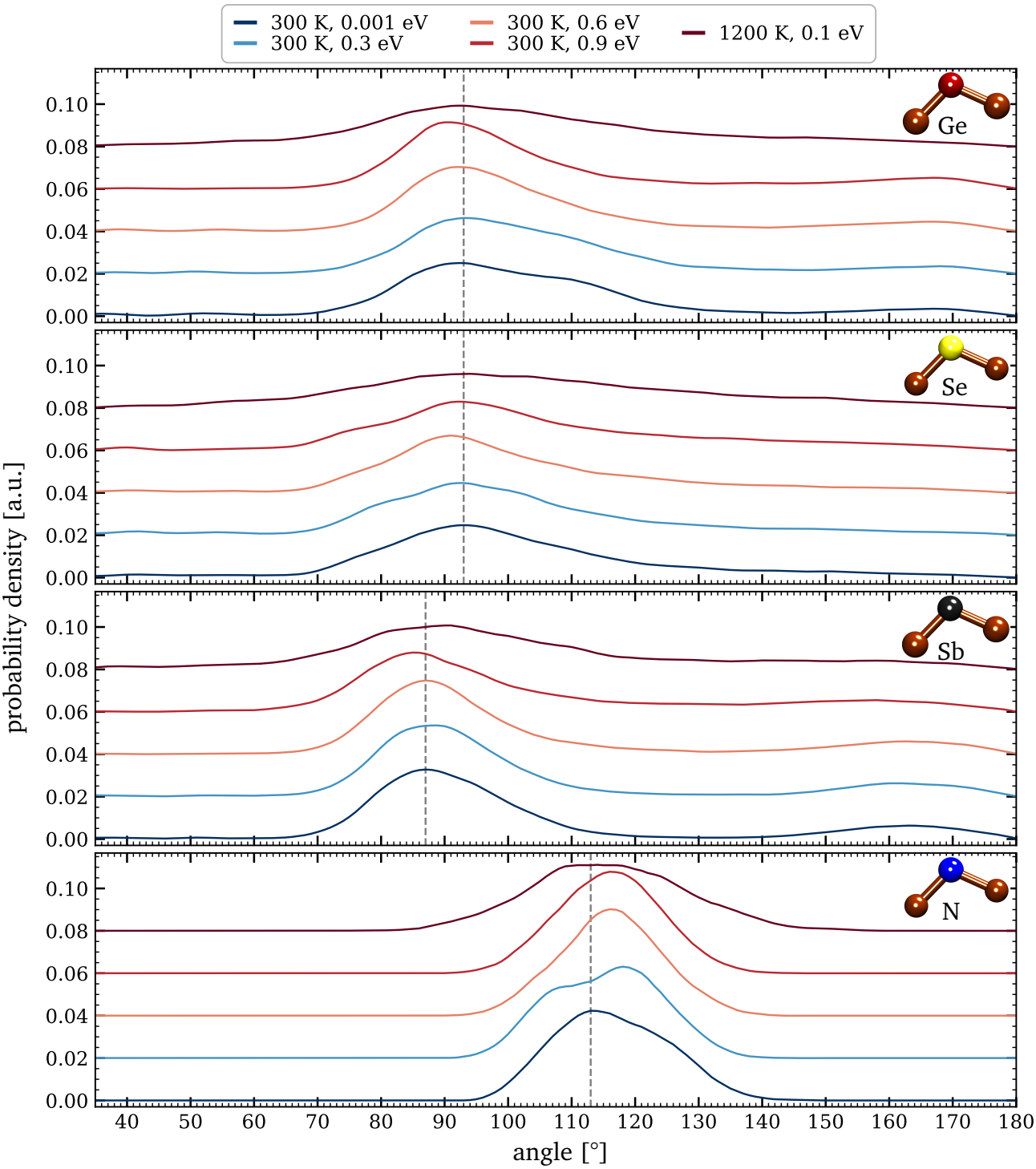

Figure 5.46 – *Distribution of angles of the simulated out-of-equilibrium states of GSSN. The gray dotted lines correspond to the maximum peak position in the initial state.*

the non-excited case disappears with high excitation. Only when the excitation is chosen as high as $T_e = 0.9$ eV, the number of tetrahedral Ge drops from 21% down to 12%, with the concomitant the slight shift of the angle distribution towards a maximum peak position at 91°, even more characteristic of octahedral angles.

In the case of Se and Sb atoms, the distributions peak at the same value for the non-excited and all excited states, corresponding to octahedral configurations.

The N atoms undergo the most striking transition: the initial distribution that peaks at 113° splits into two contributions upon application of $T_e = 0.3$ eV: one at 107° and one at 118°. If the excitation is stronger than that, it is not a splitting but a shift of the distribution that is observed, towards angles of 116°. Due to the small proportion of N atoms, it is hard to interprete this behaviour.

In the liquid state, the distribution of all types of atoms are greatly broadened due to thermal agitation, yet the characteristic angles are the same as in the non-excited state.

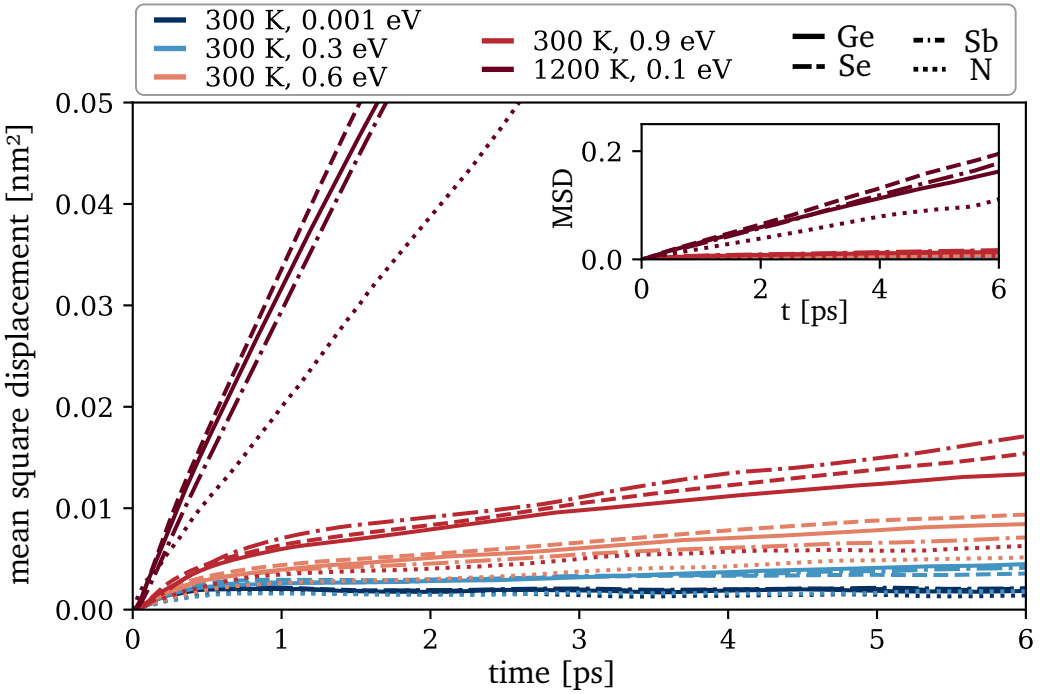

Figure 5.47 – *Mean squared displacement of the simulated states of GSSN.*

Mean squared displacement of GSSN

Finally, the mean squared displacement of each species in the GSSN compound was computed and is represented in Figure 5.47. Similarly to GS, a clear difference can be seen between the

liquid state and the other out-of-equilibrium states. The initial and out-of-equilibrium states are found with diffusion coefficient about 2-5×10^{-6} cm^2/s while this value is multiplied by 9, giving $D \sim$ 3-5 10^{-5} cm^2/s in the liquid state. This latter is therefore characterized by a large discrepancy in terms of diffusion compared to the other states. It is clearly not a very viscous phase.

Conclusion on the investigation of the excitation of chalcogenide glasses

The excitation of three chalcogenide glasses: $Ge_{31}Se_{69}$ (GS), $Ge_{23}Se_{57}Sb_{20}$ (GSS) and $Ge_{23}Se_{53}Sb_{19}N_5$ (GSSN), was investigated in the sub-picosecond regime. First, each thin film was irradiated by a 30-fs laser pump with central wavelength of 800 nm.
This photo-excitation induces a transition towards another supposedly disordered state[2] *via* a melted phase. This is evidenced by the presence of fingerprint structures observed post-experiment by means of phase-contrast microscopy. The first 9 picoseconds after excitation were probed *via* frequency domain interferometry with a probe at 532 nm with pulses of 80 fs. On the contrary to GeTe, this liquid state is not detected by our FDI measurements. Two hypotheses can explain this fact: either the electron-phonon coupling takes longer such that this melting occurs after the 9 ps probed, or the liquid phase does not induce a change of volume/too small to be detected by FDI.

In this 9 ps time window, an ultrafast dynamics is observed within 500 fs, with the sudden variations of the dielectric functions in all three materials. The transition is not over at this point: after the maximal variation has been reached around 400-500 fs, changes in both the real part and the imaginary part are measured. For all three glasses, the experimental results show a metallization upon excitation.

Out-of-equilibrium *ab initio* molecular dynamics simulations were performed in order to have a better understanding of the changes that might take place on a local scale. As these glasses have a non-negligible gap, between 1.4 and 2.2 eV, the miscalculation of the gap induces some troubles in the comparison of optical properties with the experiments (especially in the case of GS, which possesses the largest gap). Nonetheless, the structural analysis of the out-of-equilibrium excited states simulated was very informative. Ge, Se and Sb atoms tend to get into (defective) octahedral environment upon excitation in GSS and GSSN in adequation with Raty *et al.* [206]. For GS, this is only true at high excitation (greater than $T_e = 0.6$ eV). For lower excitations, it tends to emphasize the tetrahedral character of the Ge atoms.

[2] A very low cooling rate is required to crystallize these materials compared to GeTe, which itself did not crystallize as seen in Chapter 4. It is therefore nearly impossible that the glasses did. HAADF-STEM experiments are planned to confirm this.

Although GeTe and these glasses are both disordered chalcogenide phases, the effects of photo-excitation are very different. In GeTe, it lead to out-of-equilibrium states assimilated to the melted phase for almost all properties analyzed. This is clearly not the case here. The liquid state possesses some features that are similar to that of the low-excited states (such as the proportion of tetrahedra), but there are some noticeable differences: for example the bonds lengths are longer in the liquid state. This difference in response between amorphous GeTe and these glasses is most probably due to their repective bond natures and optical band gaps. The glasses have a non negligible band gap whereas GeTe has a very small one. Moreover, *a*-GeTe is characterized by metavalent bonds, which are covalent delocalized bonds, while the glasses are "real" covalent materials, obeying the 8-N rule.

CONCLUSION AND PERSPECTIVES

Optimizing existing technologies requires to understand the underlying physics. In the case of resistive memory devices such as the crossbar architecture, which associates memory cells and selectors (both constituted of chalcogenide), the root is an electronic excitation. However, the essential of the mechanism is not understood: neither for the memory cells, nor for the selectors.

With this idea in mind, the excitation of four thin films of chalcogenide was investigated *via* experimental and simulation methods. Amorphous GeTe (*a*-GeTe), a protypical phase-change material used in memory cells, as well as three glasses, $Ge_{31}Se_{69}$ (GS), $Ge_{23}Se_{57}Sb_{20}$ (GSS) and $Ge_{23}Se_{53}Sb_{19}N_5$ (GSSN), candidates for OTS selectors applications, were pumped with a 30-fs laser of central wavelength of 800 nm, for various fluences. The first 9 picoseconds after excitation were probed *via* frequency-domain interferometry (FDI), an optical method that allows a femtosecond timescale resolution and a nanometric longitudinal resolution. The phase and reflectivity variations extracted from the FDI measurements enabled to retrieve not only the surface nature and dynamics, but also the dielectric properties of the thin films.
To complete these experimental results and understand the dynamics on a more local scale, *ab initio* molecular dynamics (AIMD) simulations were performed to reproduce the out-of-equilibrium states resulting from excitation.

With the help of these two methods combined, we were able to have a deeper understanding of the effects of excitation on those chalcogenide thin films. First, it should be noted that *a*-GeTe and the three glasses demonstrate an ultrafast response to the light excitation. In all cases, as soon as the energy has been deposited in the material, we measured a sudden change in dielectric properties, followed by a change of dynamics around 350 fs - 500 fs. However, as expected, this similar timescale for both types of materials does not mean that their responses in themselves are identical.

Amorphous GeTe undergoes first a non-thermal transition: in about 350 fs, the real part of the dielectric function, stabilizes at a saturation value (which does not really depend on the fluence applied). This non-thermal transition does not constitute the whole dynamics. After 1 picosecond, it is the imaginary part that shows a variation (though negligible compared to that of the real part). Given the timescale, we may attribute this to the electron-phonon coupling that comes into play. For fluences higher than 31 mJ/cm^2, this change is ε_i occurs with the concomitant development of a liquid phase of higher density. Indeed, the surface dynamics reveals that the material shrinks by up to 4 nm for the highest fluence of 80 mJ/cm^2. Overall, it was shown that fs-laser excitation lead to a transition between two amorphous states, but possessing different properties.

The AIMD out-of-equilibrium simulations revealed more information on the local scale mechanism. First, all observables: pair distribution functions (PDF), vibrational density of states (VDOS), distributions of angles,... lead to the fact that excitation almost essentially affects the Ge atoms. These latter show a change of local environment, from tetrahedral to octahedral sites. Furthermore, this transition passes by out-of-equilibrium excited states that are very similar to the liquid state in terms of structure and electronic properties, confirming the non-thermal behaviour observed during the experiments.

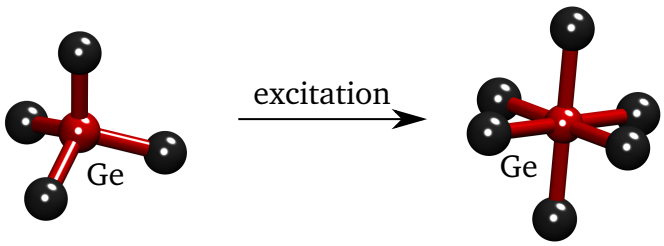

Figure 5.48 – *Change of local environment of the Ge atoms in GeTe upon excitation: they shift from tetrahedral to octahedral sites.*

In the case of the three chalcogenide glasses, though the main dynamics appears to be also on a very short timescale (below 500 fs), the discrepancy with *a*-GeTe is clear. First, the dielectric function is much more dependent on the fluence. There is still the same phenomenon of saturation on a longer timescale, but the final value is completely different if the impinging fluence is 30 or 76 mJ/cm^2 for example (for all three glasses). The most striking is for $Ge_{31}Se_{69}$, which demonstrates a raise of its real part when the fluence is low, but a drop when the fluence is high. Still, this latter behaviour can be explained *via* a model that takes into account the contribution of the band gap closure upon excitation. In the case of GS, the correction and the dependency of ε with wavelength explains the trends measured: the excitation induces a partial closure of the

band gap. The same model applied to GSS and GSSN is also consistent with the experiments, but only a negative variation can be obtained due to the dispersion behaviour of the refractive index.

Post-experiment phase-contrast microscopy revealed that, similarly to *a*-GeTe, the melting temperature of all three glasses has been reached for most fluences. For GS, we see proof of melting from $F = 81$ mJ/cm^{2}and $F = 68$ mJ/cm^2 for GSSN, and for the lowest fluence $F = 45$ mJ/cm^2 for GSS. However, this melting is not detected by our FDI measurements, which can be explained either by the fact that the electron-phonon coupling takes longer than the 9 ps probed, or that the liquid phase does not induce a change of volume/not detectable by the FDI.

The AIMD simulations revealed first that the three glasses had slightly different local environment already in the non-excited phase. GS is characterized by a majority of Ge atoms in tetrahedral environment (Ge^T), compared to GSS and GSSN which have respectively only about a third and a fifth of Ge^T. Upon low excitation ($T_e \leq 0.6$ eV) the out-of-equilibrium states generated are very similar to the non-excited phases. Only when the excitation applied is greater than 0.6 eV, the observables such as the angles or the bond lengths, show a really noticeable variation.

Comparing these observations with the results of *a*-GeTe, we hypothesize that it is the intrinsic nature of the materials that explains this discrepancy. In *a*-GeTe, Peierls distortion (though not as strong as in crystalline phase) induces short and long bonds, whose nature is different from the covalent network present in the glasses. Covalent bonds being stronger, the excitation required to break or just disturb the bonds is greater than in the case of GeTe. Moreover, GeTe is characterized by a very small optical band gap of 0.80 eV while for the glasses, it is 2-3 times larger, which makes them more difficult to excite.

Interestingly, if we look at the big picture, excitation of *a*-GeTe has resulted first in a non-thermal transition, that has been followed on the picosecond timescale by a thermal melting of the thin film, while excitation of the chalcogenide glasses has resulted in the closure of their band gap, leading to a more metallic character (and therefore conductive one also) but no change of volume has been measured experimentally on a short timescale. These two responses resemble greatly to what occurs in memory devices, phase-change materials in memory cells becoming far more conductive after a certain threshold voltage, and their transition to the other state when Joule heating is sufficient, and OTS selectors being able to undergo a large change of conductivity without much structural change. Instead of a purely electrical triggering, it is here a fs-light pulse that has induced the threshold switching observed in both types of materials.
Some phenomena observed in this thesis work cannot be explained very thoroughly, due to the complicated dynamics at play. However, it is fair to say that the results obtained here have permit-

ted a deeper understanding on the underlying mechanism of threshold switching in chalcogenide thin films.

This work opens then several directions of research: a first one is basically to study how these variations that we observe experimentally evolve depending on the probing wavelength. The imaginary part of dielectric function from simulation showed a node upon excitation at 532 nm, but this behaviour does not seem to occur on higher ones such as 630 nm for example.

As the excitation affects mostly Ge in *a*-GeTe, we could try to target the energy deposition and reduce the amount of this latter by exciting the Ge phonon modes resonantly with THz pulses. Another idea would be conducting time-resolved XANES experiments to follow the behaviour of each type of atoms.

RÉSUMÉ SUBSTANCIEL EN FRANÇAIS

Introduction

Stockage de données

Les sociétés modernes sont désormais basées sur un mode de vie complètement digital. Des interactions sociales à la paperasse administrative, toutes ces données ont besoin d'être stockées. La Datasphère Globale (incluant chaque bit d'information : des serveurs de stockage type clouds, serveurs d'entreprise et pcs/smartphones/...) s'évaluait à 33 Zettabits (ZB) en 2018. Les prédictions actuelles estiment que sa taille atteindra les 175 ZB en 2025 [1]. Cette expansion impressionnante s'accompagne de la hausse du niveau d'exigence : un temps d'accès toujours plus rapide, des capacités de stockage les plus larges possibles, à un prix concurrentiel. De quoi motiver les recherches pour un renouveau constant de ce type de stockage pour une optimisation perpétuelle.

En informatique, la hiérarchie des mémoires est souvent représentée sous forme d'une pyramide telle que celle de la Figure 49. Du sommet vers la base, les mémoires sont listées des plus rapides aux plus lentes. Mais on peut aussi la décrire en terme de coût par bit, qui va dans le même sens que le temps d'accès, ou bien selon les capacités de mémoire, cette fois dans le sens opposé. Au sommet se trouvent les *mémoires à accès aléatoire statiques* (SRAM : static random-access memory) et les mémoires CPU (cache et registres). C'est le type de mémoire le plus rapide, avec un temps de latence de 50 ns, mais les capacités de stockage sont limitées à environ 16 MB [2]. En second se positionnent les *mémoires à accès aléatoire dynamiques* (DRAM : dynamic random access memory), avec des capacités de stockages plus importantes : 64 GB par barre de RAM, mais contrebalancées par un temps d'accès doublé par rapport aux SRAM. Ces deux premiers types de mémoires sont caractérisées de *volatile*, *i.e.* elles ne préservent les données que si elles sont alimentées. Dès que l'alimentation est coupée, les données sont perdues. À la base de cette pyramide se trouvent les *disques à semiconducteurs* (SSD : solid state drive) ainsi que les *mémoires flash*, qui possèdent actuellement les capacités de stockage les plus élevées : 30 TB, mais le temps d'accès est aussi très élevé : il est multiplié par un factor 10^3. Il s'agit cette fois de *mémoires non-volatile*, capables de conserver les données longtemps après que le courant ait arrêté de les alimenter.

Le problème qui se pose est alors que l'on se retrouve avec deux types de mémoires très contrastées :

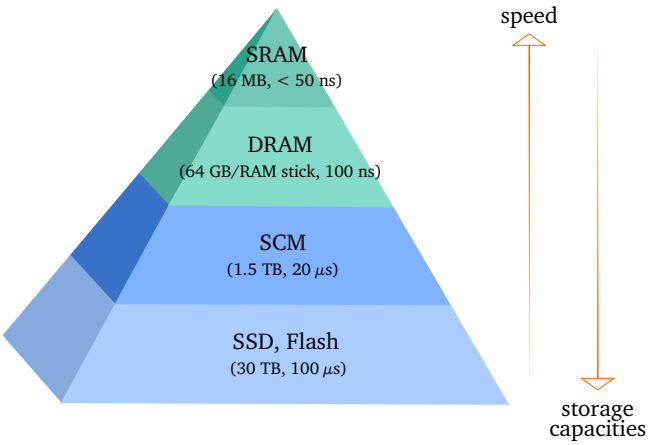

Figure 49 – *Hiérarchie des mémoires. Les mémoires non-volatiles sont en bleu (bas de la pyramide) tandis que les mémoires volatiles sont en vert (haut de la pyramide). Les valeurs de temps d'accès ainsi que les capacités de stockage proviennent de la référence [2].*

d'un côté un temps d'accès très court, mais associé à un caractère volatile et ne permettant qu'un stockage de données limité, et de l'autre des capacités de stockage conséquentes, persistante, mais dont la vitesse d'accès est très limitée.

Mémoires de classe de stockage (SCM : storage class memories)

Afin de combler le fossé entre ces deux extrêmes, les *mémoires de classe de stockage* (SCM : storage class memories) ont été développées avec des technologies émergentes [3]. Dans les SCM, la mémoire est persistante comme dans les dispositifs SSD, mais la latence offre un meilleur compromis, résultant en un cas intermédiaire dans la hiérarchie des mémoires avec des capacités de stockage d'environ 1.5 TB et des temps d'accès de l'ordre de 20 µs. Le but ultime est de développer une *mémoire universelle ultime*, basée sur le dévelopement de capacités neuromorphiques [4] : un seul élément mémoire serait alors requis pour gérer à la fois la partie stockage et la partie instructions/exécution [5].

L'architecture 3D d'un réseau de croisements (crossbar) a été developée et avec elle la commercialisation des *mémoires à accès aléatoire à changement de phase* (PCRAM : phase-change random access memories) avec le produit Optane^{TM} mis au point par Intel et Micron [6]. Cette technologie, appelée Xpoint ("cross"point en anglais), permet de contourner le problème de manque de place rencontré dans les dispositifs précédents lors de l'augmentation de la densité de stockage [7]. En effet ce problème était réglé majoritairement par la réduction de la taille des composants, ce qui a des limites, puisque les méthodes de fabrication (des transistors par exemple) sont elles-mêmes limitées par la taille des outils. Ajouter une dimension augmente la densité de stockage et ouvre la voie à un tout nouveau panel de mémoires, ayant des capacités accrues en terme de stockage, mais aussi en terme de fonctionnement.

La technologie "crossbar", représentée en Figure 50, consiste en un empilement de deux types d'éléments, qui ont des rôles distincts : les cellules mémoires et les sélecteurs. Chaque cellule mémoire encode un bit de donnée (un "0" ou un "1" en langage binaire informatique). Dans la pratique, ces états logiques correspondent à deux états que peut adopter la cellule mémoire : l'état

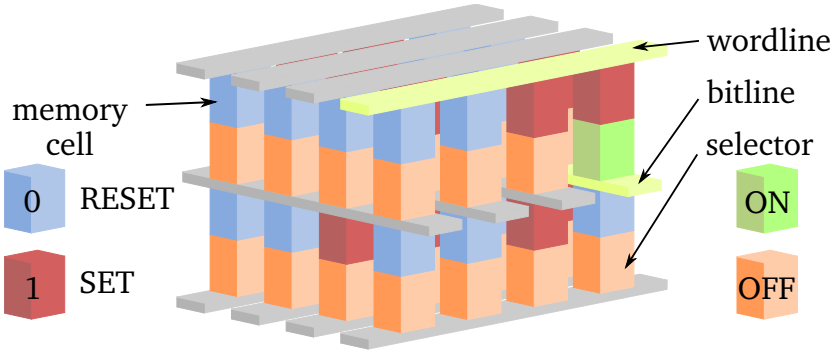

Figure 50 – *Technologie XPOINT. Il s'agit d'un empilement de cellules mémoire (bleu et rouge) et de sélecteurs (orange et vert). Une tension est appliquée sur une ligne de mot et une ligne de bit passe le sélecteur de son état OFF à à son état ON, ce qui induit le changement d'état de la cellule mémoire de "0" à "1" ou inversement par effet Joule.*

SET~"1", et l'état *RESET*~"0". Le passage entre les deux états s'effectue à l'échelle nanoseconde, et peut être inversé [8, 9]. Quant aux sélecteurs, leur rôle est de choisir quelle cellule mémoire spécifique écrire, lire ou effacer. Avant d'expliquer plus précisément le fonctionnement de cette technologie ainsi que le phénomène qui intervient, il est nécessaire de parler des matériaux qui constituent ces deux types d'éléments, et de leur remarquables propriétés : les chalcogénures.

Chalcogénures

Le terme de *chalcogénure* renvoie à des alliages semiconducteurs à base de S, Se, ou Te, des éléments chalcogène de la 16$^{\text{ième}}$ colonne du tableau périodique des éléments de Mendeleiev (voir Figure 51).
Leurs propriétés diverses en font des composants clés dans plusieurs domaines. Par exemple, leurs propriétés thermoélectriques [10, 11], ainsi que leurs propriétés non-linéaires [12, 13] en font des matériaux de choix pour des applications d'énergie et d'optique. Mais ils sont également largement employés dans le domaine d'intérêt de cette thèse : les applications de stockage de données. Les chalcogénures ont un long passé commun avec les mémoires. CDs, puis DVDs et Blu-rays [8], cette histoire commune se prolonge avec les technologies émergentes de type SCM [9].

Tout d'abord, ce sont leurs propriétés optiques et électriques hors-du-commun qui les rendent parfaitement appropriés pour des applications de stockage de données. Par exemple, le tellurure de germanium (GeTe), un chalcogénure typique, possède une réflectivité doublée dans sa phase crystalline par rapport à l'amorphe, et environ quatre ordres de grandeur en termes de conductivité. Cette particularité est peu commune parmi les semiconducteurs pour lesquels, bien que les propriétés soient différentes, ce n'est pas aussi marqué. Ce large contraste a été exploité dans les dispositifs mémoires, dans lequels il est crucial de pouvoir différencier les deux états logiques qui encodent les données. Les états "1" et "0" ont alors été associés à la phase cristalline et amorphe respectivement. Désormais, dans les architectures "crossbar", les cellules mémoires ne sont plus les seules à tirer parti de ces propriétés remarquables : comme il sera expliqué un peu plus loin, le contraste des propriétés électriques des verres de chalcogénure est également approprié pour les sélecteurs.

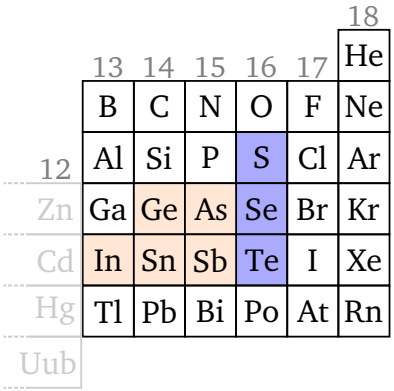

Figure 51 – *Zoom du tableau périodique des éléments de Mendeleiev sur les éléments principaux des chalcogénures. Les éléments colorés en violet S, Se et Te sont les trois chalcogènes utilisés pour les alliages tandis qu'en orange clair il s'agit des éléments électropositifs qui leur sont le plus souvent associés.*

Dans les mémoires, les chalcogénures sont présents sous trois phases : cristalline, amorphe, et vitreuse. Cependant, elles ne sont pas interchangeables. Il est donc important de les différencier pour prendre en compte tous les paramètres possibles lors de leur étude.

La phase cristalline est caractérisée par un ordre à longue portée. Elle est formée de la répétition d'un motif atomique, moléculaire ou bien ionique. La Figure 52 montre l'évolution de l'enthalpie H du système en fonction de la configuration atomique et de la temperature T [14]. La phase cristalline est formée lorsque la phase liquide est refroidie très lentement sous la température de cristallisation T_c et conduit à une configuration qui possède l'enthalpie la plus basse atteignable par le système. Plusieurs phases cristallines sont possibles pour un même composé (comme évoqué dans le Chapitre 1 pour GeTe). Ces phases ont des stabilités différentes, mais sont tout de même le type de phase le plus stable qui existe.

La réelle ambiguité se trouve dans la différence entre un état amorphe et vitreux, qui sont tous deux des phases désordonnées. Une première définition a été proposée en 1979 par Mott et Davis [15], définissant un verre comme une phase non crystalline obtenue à partir d'un liquide, en oppostion avec les autres phases amorphes obtenues à partir de phase vapeur/plasma. Une seconde définition suivit, et est désormais la plus couramment utilisée : Philips et Elliott [16, 17] ont classé les phases amorphes et vitreuses selon leur capacité à présenter ou non le phénomène de transition vitreuse. Lorsqu'un verre est refroidi sous la température de fusion du matériau, assez rapidement pour que la phase cristalline ne puisse pas être formée (généralement avec un taux de refroidissement de centaines de °C/s), un état désordonné métastable est alors atteint : un genre d'état liquide figé appelé un *verre* [18]. La transition vitreuse désigne la transition graduelle du verre vers un état liquide surfondu en le chauffant. Ce n'est pas une transition au sens thermodynamique, puisqu'il n'y a pas de discontinuité des propriétés physiques, mais le matériau passe d'un état vitreux dur et cassant à un état visqueux et caoutchouteux. La température de vitrification T_g est par conséquent difficle à déterminer précisément. Une valeur approchée peut être obtenue en utilisant la formule empirique reliant la valeur de T_g avec T_m tel que $T_g = 2/3T_m$ [19]. Tous les autres états refroidis et "figés", mais ne présentant pas cette transition, sont alors définis en tant qu'états *amorphes*.

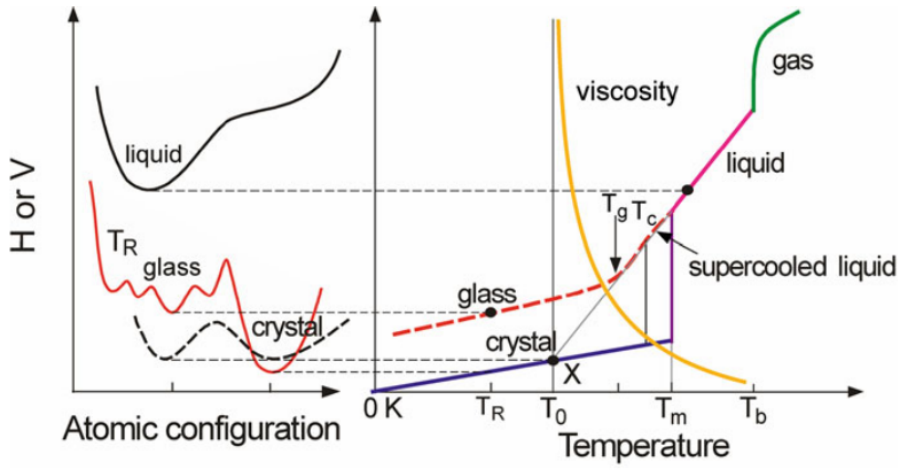

Figure 52 – *Schéma de l'enthalpie H et du volume V du système en fonction de la configuration atomique et de la température, repris de la référence [14].*
Les indices g, c, m, b et R désignent les températures de transition vitreuse, cristallisation, fusion et ébullition respectivement (T_0 : température hypothétique, non utilisée ici).

Les phases amorphes et vitreuses sont donc des phases métastables, correspondant à des minima locaux du paysage enthalpique. Comme pour la phase cristalline, il peut exister de nombreux états amorphes et vitreux, mais les états vitreux correspondent aux plus basses enthalpies.

Les chalcogénures présentent un contraste optique et électrique important, mais ce n'est pas la seule raison qui pousse à les utiliser dans les applications mémoires. Au long terme, encoder de l'information est utile, mais pouvoir le faire à haute fréquence, de manière réversible est encore mieux. Ceci est en fait possible, grâce au phénomène sous-jacent appelé *commutation à seuil* (*threshold switching*), qui prend effet sous deux formes.

Commutation à seuil (*threshold switching)*

L'effet de commutation à seuil a été présenté par Ovshinsky à la fin des années 60 [20]. En étudiant les courbes I-V (courant, tension) d'alliages semiconducteurs de Te-As-Si-Ge en phase amorphe, il mit en lumière une commutation reproduisible entre un état initial hautement résistif et un état conducteur lors de l'application d'une tension supérieure à une valeur seuil V_{th}.
Ce phénomène a par la suite été examiné plus en détails ce qui a conduit à deux conclusions. Premièrement, cette commutation peut être déclenchée à la fois par des impulsions électriques et lumineuses. Deuxièmement, le phénomène de commutation à seuil se produit de deux manières, permettant de catégoriser les matériaux selon la manifestation du phénomène (Figure 53).

1. Le premier type de commutation à seuil correspond a ce qu'avait rencontré Ovshinky, et qui a donc donné le nom de **commutation ovonique à seuil** (OTS : ovonic threshold switching[3]. Le phénomène OTS se produit entre un état initial amorphe de résistivité élevée (état OFF) qui passe à un autre état amorphe, cette fois de faible résistivité (état ON), lorsque la tension appliquée est supérieure à une valeur seuil. Il s'agit d'un effet volatile : dès que la tension

[3]le terme 'ovonique' provient de la contraction du chercheur Ov-shinsky, et des techniques d'électronique basées sur l'utilisation de couches mince de chalcogénures exploitant le phénomène de commutation à seuil.

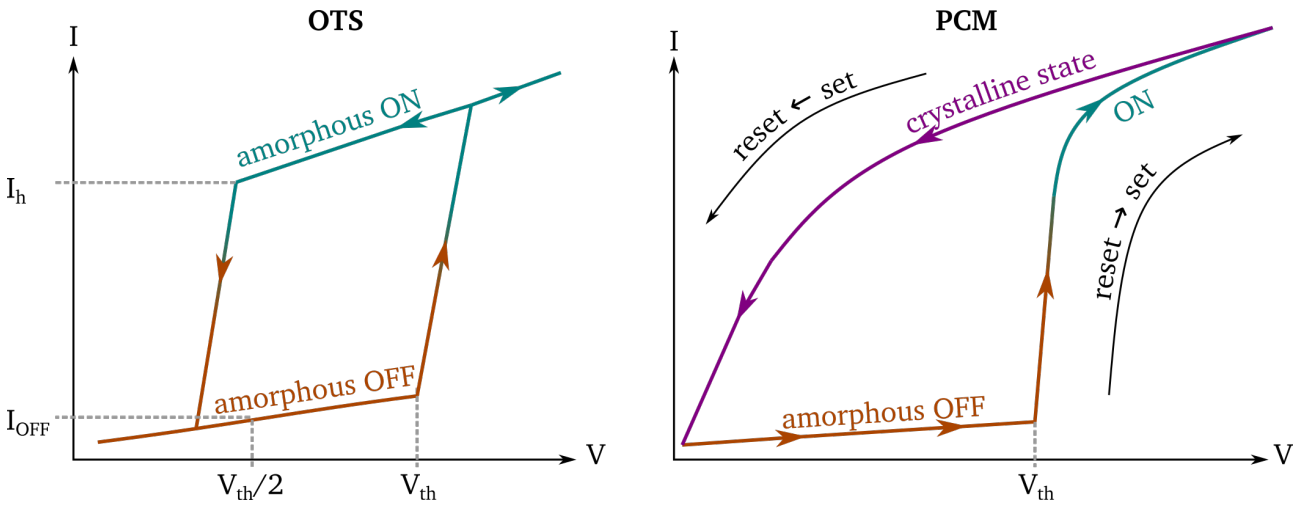

Figure 53 – *Schéma d'une réponse courant-tension (I-V) typique pour un matériau OTS (gauche) et PCM (droite).*

est coupée, le courant chute sous une valeur de *courant de maintien* I_h (holding current) et le matériau revient à son état OFF initial.

2. Le second type est le plus exploité dans les mémoires jusqu'à présent. Parfois appelé *commutation mémoire*, il s'agit de la transition permanente (non-volatile), mais réversible, entre l'état amorphe de résistivité élevée (RESET) et l'état cristallin conducteur (SET) rencontré dans les cellules mémoires, ce qui a conduit à l'appellation de matériaux **mémoires à changement de phase** (PCM) pour ceux qui appartiennent à cette catégorie.
   Les différences principales entre les OTS et les PCM sont la valeur de la tension de seuil V_{th} et la capacité du matériau à cristalliser après la commutation à seuil.
   Des matériaux autres que chalcogénures peuvent être des matériaux PCM, par exemple les alliages Ge-Sb, Ga-Sb ou InSb démontrent des propriétés PCM [21, 22]. Cependant, les alliages chalcogénures sont les plus aptes à répondres aux exigences attendues dans le domaine du stockage de données, à la fois pour les sélecteurs et les PCM.

Désormais il est possible de comprendre le mécanisme global dans les applications mémoires constituées de chalcogénures. Pour illustrer cette explication, l'écriture d'un bit est illustrée en Figure 54. Écrire un bit correspond à changer un état RESET (amorphe) en un état SET (cristallin). Les cellules mémoires sont composés d'un chalcogénure PCM, par conséquent cette transition s'effecture par le biais de la commutation à seuil citée plus haut. Une tension V est appliquée grâce à des barres de métal transverses pour sélectionner la colonne et la ligne de la cellule mémoire concernée (en jaune sur la Figure 54). Puisque les sélecteurs OTS et les cellules mémoires PCM sont empilés directement, le courant circule également dans ces sélecteurs, qui sont composés de verres de chalcogénures. Si la tension appliquée surpasse la tension seuil $V_{th,OTS}$, alors le sélecteur commute de l'état OFF à l'état ON. Le flux de courant qui était limité par l'état OFF du sélecteur est désormais plus important grâce à l'état ON conducteur. De manière similaire, les cellules mémoires PCM voient le flux de courant augmenter lorsque le sélecteur est activé. Lorsque la tension résultante devient plus importante qu'une certaine valeur seuil, l'état amorphe résistif initial (RESET) va alors passer à un état conducteur, renforçant l'effet Joule de chauffage. Cette hausse de température dans la cellule mémoire, telle que $T_g < T < T_m$ induit sa transition vers

l'état cristallin (SET).

Une fois le courant stoppé, le sélecteur s'échappe de cet état ON hors-équilibre et retrouve l'état stable initial OFF, tandis que la cellule mémoire persiste dans l'état SET. Pour effacer ce bit (transition inverse), un procédé similaire est mis en place. Dans ce cas, l'intensité de l'impulsion électrique est augmentée afin que la température de fusion T_m du matériau constituant la cellule mémoire soit atteinte, mais sa durée est limitée, entraînant un haut taux de refroidissement de la part des cellules froides voisines.

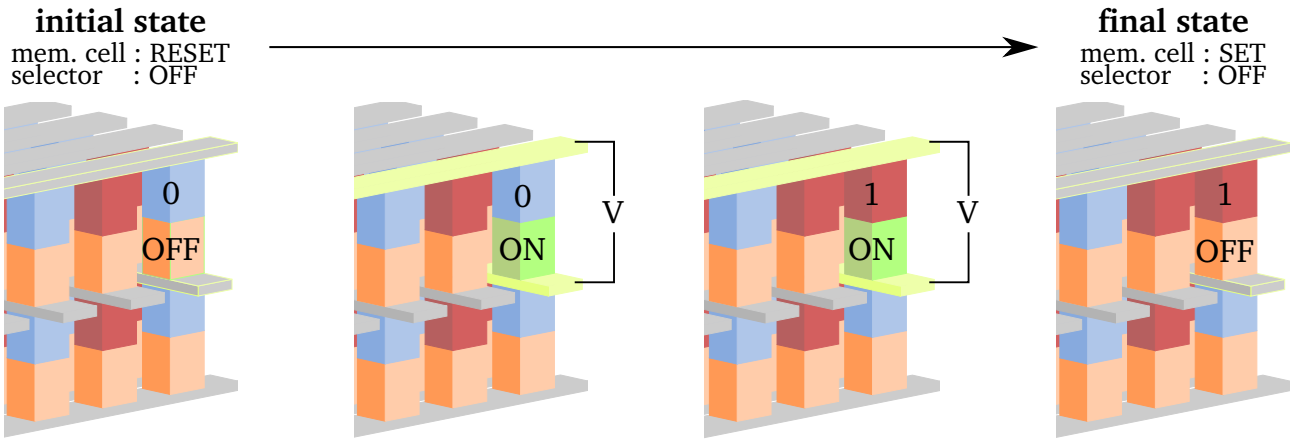

Figure 54 – *Schéma du processus d'écriture d'un bit dans un dispositif mémoire de type "crossbar".*

Les chalcogénures mémoires à changement de phase sont actuellement la meilleure option pour les cellules mémoires [8,9]. Les exigences concernant les matériaux utilisés dans les mémoires type réseau de croisements sont récapitulées dans le Tableau 3. Comme expliqué précédemment, les matériaux PCM présentent une transition réversible entre un état amorphe de faible réflectivité et résistivité élevée, et un état cristallin de réflectivité et conductivité élevées. Même avec le procédé limitant de cristallisation, cette transition ne prend que quelques centaines de nanosecondes. Quant aux autres propriétés, bien qu'elle ne soient pas aussi idéales qu'on le voudrait dans les PCMs, des solutions sont développées pour circonvenir aux problèmes rencontrés [9] : la rétention de données (stabilité de la phase amorphe au fil des années, aussi appelé *vieillissement*) peut être traité par le dopage du PCM par exemple (discuté dans le Chapitre 1), réduire la taille des cellules mémoire réduit la consommation de courant et la haute cyclabilité a été étudié en comparant différentes compositions de matériau. Les deux familles principales de PCM utilisées dans les mémoires sont les alliages Ge-Sb-Te (GST), avec les cas prototypiques des composés $Ge_2Sb_2Te_5$ et GeTe, ainsi les alliages Sb_2Te_3 dopé Ag/In (AIST), avec des compositions proches de $Ag_5In_5Sb_{60}Te_{30}$ pour les plus utilisés. Les deux familles ont été exploitées dans les dispositifs mémoires tels que les DVD-RW ou Blu-rays, mais les alliages GST sont les plus prometteurs, présentant une cristallisation plus rapide ainsi qu'un meilleur contraste entre les deux états logiques. Les composés GST sont donc désormais ceux principalement employés dans les mémoires.

Quant aux sélecteurs, les verres de chalcogénures OTS ont démontré un vrai potentiel [7,9,23,23], présentant une densité de courant élevée dans l'état ON, un courant de fuite I_{OFF} limitant la consommation électrique de cellules mémoires non sélectionnées, une stabilité thermique satisfaisante contre la cristallisation ainsi qu'une tension de seuil V_{th} compatible avec celles des

cellules mémoires prévenant le changement de phase d'élements mémoires qui ne sont pas au croisement ligne+colonne sélectionnées.

Cellules mémoires	• Contraste optique/électrique élevé entre les deux états encodeurs • Transition rapide entre ces deux états • Faible consommation de courant pour la transition • Au moins 10 ans de préservation des données • Une haute cyclabilité (au moins 10^6 cycles d'écriture/effacement)
Sélecteurs	• V_{th} limitant les transitions indésirables de cellules mémoires • Courant de maintien I_h compatible avec les cellules mémoires • Faible courant de fuite I_{OFF} • stabilité thermique contrant la cristallisation

Table 3 – *Propriétés nécessaires des matériaux constituant les cellules mémoires et les sélecteurs dans les mémoires "crossbar" [7–9].*

Mécanisme de la transition

Bien que les chalcogénures soient adaptés aux applications mémoires, il y a tout de même une marge d'amélioration. Le besoin d'optimisation des dispositifs mémoires, pour des capacités de stockage plus importantes ainsi qu'un temps d'accès réduit, a inspiré de nombreuses recherches. Outre la recherche de composés optimaux, des stimuli externes ont été investigués : impulsion laser [24–26], chauffage [27], champs électriques [28], pression [29–31]... Hormis le constat que les changements se produisent à une échelle locale, le mécanisme sous-jacent du phénomène de commutation à seuil n'a pas été clairement élucidé. La structure même des chalcogénures les plus usités tels que les phases amorphes de GeTe ou $Ge_2Sb_2Te_5$ sont encore sujettes à controverse [32–36].

Comme indiqué précédemment, améliorer les dispositifs mémoires ne s'est pas fait que par l'optimisation des composés. Un déclenchement électrique n'est pas le seul moyen d'induire la commutation à seuil. Des impulsions laser de diverses longueur d'ondes, intensités et surtout durées ont prouvé leur efficacité [37]. Le développement de sources optiques ultracourtes a permis l'usage commun de lasers femtosecondes en laboratoires, ouvrant la voie à l'étude de leur effet sur les PCMs de manière extensive. Réduire la durée des impulsions jusqu'à ce régime provoque de nouveaux phénomènes (détaillés dans le Chapitre 1), en particulier la génération d'états transitoires hors-équilibres pour lesquels la température électronique $T_e \neq T_i$ la température ionique. Le concept de transition non thermique est ainsi apparu et a été prouvé dans des semiconducteurs tel que Si, C,... [38–43]. Obtenir une phase possédant les propriétés de la phase liquide sans avoir besoin d'atteindre T_m est attractif pour des applications PCM, c'est pourquoi la possibilité d'une telle transition a été abordée puis observée dans des chalcogénures et composés PCM tels que GeSb [44] ou bien $Ge_2Sb_2Te_5$ [45]. La transposition de ce phénomène dans les dispositifs mémoires révolutionnerait le domaine, surmontant les limites de vitesses d'écritures et d'effacement actuelles imposés par la prédominance du phénomène (thermique) de chauffage.

Investigation de l'excitation électronique

Améliorer les dispositifs mémoires passe par la compréhension du mécanisme sous-jacent. Les transitions des cellules mémoires ainsi que des sélecteurs reposent sur la commutation à seuil, qui provient présumément d'une excitation électronique. Par ailleurs, les chalcogénures sont particulièrement sensibles aux techniques optiques de par leur propriétés contrastées. De ce fait, il paraît pertinent de s'intéresser aux effets de la lumière sous forme d'impulsions laser femtosecondes sur des couches minces de GeTe amorphe, un PCM largement étudié [46], et de trois verres de chalcogénures : $Ge_{31}Se_{69}$ (GS), $Ge_{23}Se_{57}Sb_{20}$ (GSS) and $Ge_{23}Se_{53}Sb_{19}N_5$ (GSSN), choisis pour leur potentiel en tant que sélecteur OTS [23, 47]. Bien qu'ils soient tous dans des phases désordonnées, ils n'appartiennent pas à la même catégorie (PCM *vs* OTS), leur réponse à une excitation électronique sera donc vraisemblablement différente.

Le chapitre 1 présente les techniques principales d'investigation ultrarapide des chalcogénures, puis les propriétés structurelles des verres de chalcogénure ainsi que des matériaux à changement de phase (centré sur GeTe) sont discutés. Le chapitre 2 présente les concepts de la théorie de la fonctionnelle de la densité (DFT) employée pour les simulations *ab initio* de dynamique moléculaire (AIMD) ainsi que le protocole permettant de générer les configurations initiales et leur excitation hors-équilibre. La dernière partie de ce chapitre détaille les méthodes d'analyse structurelles conduites par la suite. Le chapitre 3 explique la technique optique expérimentale utilisée dans cette étude, les informations que l'on peut tirer des mesures collectées ainsi que le montage permettant de faire ces mesures. Finalement, les chapitres 4 et 5 traitent des résultats obtenus par excitation respectivement de GeTe amorphe et verres de chalcogénures, obtenus à la fois expérimentalement et par des simulations.

1 Matériaux à changement de phase et verres chalcogénures

Les PCMs et OTS changent de phase à des échelles sub-picosecondes. Par ailleurs, ces transitions s'effectuent à une échelle locale. Il est donc nécessaire d'utiliser des techniques ayant des résolutions adaptées.

Techniques d'investigation ultra-rapide

L'excitation d'un semiconducteur par une impulsion laser sub-nanoseconde induit des procédés complètement différents de ceux résultants d'une excitation laser nanoseconde. La raison principale provient du couplage électron-phonon, qui s'évalue à l'échelle picoseconde. Par conséquent, pour des impulsions nanosecondes, les électrons et les ions ont le temps nécessaire pour retrouver un état d'équilibre tandis que ce n'est pas le cas pour des impulsions ps ou fs.

Ces mécanismes peuvent être classés selon les catégories suivantes : excitation des porteurs de charges (absorption simple photon et multiphotonique, absorption des électrons libres, ionisation par impact), thermalisation (interactions electron-electron, electrons-phonon), relaxation (recombinaison électron-trou, effet Auger, diffusion), effets structurels (phénomènes thermiques).

Ces phénomènes qui se produisent à des échelles femto/picosecondes pour la plupart, nécessitent des sondes adaptées. Les techniques principales utilisées pour l'étude (statique ou bien résolue en

temps) des chalcogénures sont présentées, telles que la réflectométrie, la spectroscopie Raman, la diffraction à rayons X (XRD), neutrons (ND) ou bien électrons (ED), le XANES ou encore l'EXAFS.

Ces techniques sont diverses mais complémentaires. Ce qui importe est de savoir ce qu'on mesure. En effet, la structure des composés GST a été longtemps débattue entre autres raisons parce que les sondes ne sont pas sensibles aux mêmes phénomènes. Les méthodes de diffraction moyenne sur la structure globale tandis que l'EXAFS est une sonde locale. Comme les matériaux GST présente un certain désordre, la structure locale mais n'est pas tout à fait équivalente à la structure globale.

Matériaux à changement de phase type Ge-Sb-Te

Les deux matériaux prototypiques de la famille des GST sont $Ge_2Sb_2Te_5$ et GeTe. Il a été montré que la structure locale de ces deux composants est similaire. Des différences quantitatives en termes de lacune, liaisons homopolaires distance interatomiques, mobilité atomique et structure électronique sont à noter, résultant de la présence de Sb dans $Ge_2Sb_2Te_5$, néanmoins ils sont tous deux caractérisés par les mêmes phénomènes : distortion de Peierls, nombre de coordination ne respectant pas la règle 8-N, une distribution radiale à longue portée similaire...

La phase cristalline de GeTe présente une transition paraélectrique entre le β-GeTe, une phase rhombohédrique présente à basse température de groupe d'espace $Fm\bar{3}m$ et la phase de haute température α-GeTe, une phase cubique de groupe d'espace $R3m$. Dans les applications mémoires, c'est la première qui intervient. Elle peut être décrite comme une phase cubique présentant un cisaillement le long de la direction [1,1,1] se caractérisant par un décentrement des atomes Ge et Te. Ce dernier résulte en des structures locales octaédriques distordues avec trois liaisons courtes et trois liaisons longues : un effet appelé *distortion de Peierls*.
C'est un phénomène induit par des effets électroniques. Le léger déplacement d'un atome induit l'ouverture d'un gap et permet une configuration plus stable énergétiquement parlant.

Bien que la structure du cristal soit désormais plutôt bien connue, la structure de l'amorphe est quant à elle toujours assez débattue, pour deux principales raisons : tout d'abord, les techniques de sonde les plus utilisées sont basées sur la diffraction, qui sont très limitées dans une phase amorphe puisqu'elle ne possède pas d'ordre à longue portée. Par ailleurs, bien que les simulations *ab initio* de dynamique moléculaire (AIMD) aient grandement aidé à élucider la structure des GST, les stuctures amorphes sont compliquées à générer : elles doivent ressembler au matériau réel, mais avec le moins d'atomes possibles car les capacités de calcul impliquent un temps conséquent de simulation. La nature intrinsèque de la phase amorphe induit également des difficultés : la technique la plus utilisée est la déposition par PVD (physical vapor deposition), résultant en une phase qualifiée de 'telle-que-déposée' (AD : as-deposited) tandis que les simulations sont basées en grande majorité sur la technique de "fusion-trempe" (MQ : melt-quench) par laquelle la boîte de simulation est chauffée au delà de la température de fusion du matériau, puis refroidie à avec une rampe de température très raide afin d'obtenir une phase amorphe. Cependant ces deux phases ne sont pas tout à fait équivalentes (vitesse de cristallisation, une phase AD contenant majoritairement des Ge tétraédriques tandis que la MQ est caractérisée par des Ge octaèdriques (distordus)).
De manière générale, la phase amorphe de GeTe est caractérisée par des liaisons homopolaires Ge-Ge de 2.47-2.60 Å, mais pas de Te-Te dans la première sphère de coordination. Les atomes de

Ge ont un nombre de coordination de 4, étant soit dans des sites tétraédriques (avec des angles proches de 110°), soit des octaèdres distordues lacunaires (angles ~ 90 °). Les atomes de Te ont eux une coordination de 2 et des angles caractéristiques proches de 90°. La température de fusion du composé GeTe stoechiométrique est estimée entre 825 K (couches minces de 2 nm) et 998 K (composé massique).

Verres chalcogénures

La configuration locale des verres chalcogénures a été majoritairement étudiée par le biais de multiples méthodes telles que XRD, ND, ED, Raman ou bien NMR. Une conclusion contre-intuitive pour des phases qualifiées de désordonnées, est la présence dans ces verres d'un réseau covalent, qui contribue à la présence d'anneaux constitués d'un large nombre d'atomes.
Contrairement à GeTe, les verres chalcogénures respectent la règle du 8-N et présentent des nombres de coordination de 4 pour Ge et 2 pour Se. Simulations et expériences ont révélé la présence d'une grande majorité de tétraèdres de type $GeSe_4$, connectés entre eux soit par une arête (ES : edge-sharing), soit par un sommet (CS : corner-sharing). Dans la première sphère de coordination, on trouve des liaisons Ge-Se ainsi que des liaisons homopolaires Se-Se mais quasiment pas de Ge-Ge. Avec l'addition de dopant Sb, des liaisons Sb-Se, Sb-Sb ainsi que des liaisons Ge-Sb sont formées. Ces deux dernières sont plutôt indésirables, car elles introduisent des défauts dans la bande interdite, ce qui est préjudiciable pour la rétention de données (vieillissement). Pour palier à ce problème, un dopage additionel avec de l'azote permet de former préférentiellement des liaisons Sb-N et Ge-N plutôt que Sb-Sb ou Ge-Sb. On dénote un caractère plutôt octaédrique dans ces composés bien que les tétraèdres de type CS et ES soient encore détectés.

Une transition ultra-rapide

Les transitions OTS et PCM s'effectuent sur des durées très courtes : de l'ordre de la nanoseconde. Afin de réduire ce temps plus encore, le concept de transition non-thermique a suscité de nombreuses recherches. Cette possibilité de pouvoir avoir les propriétés d'un liquide sans avoir à chauffer un matériau jusqu'à sa température de fusion serait révolutionnaire dans le domaine des mémoires, permettant d'outrepasser la limite de vitesse imposée par la transition thermique actuelle.

Le mécanisme de commutation à seuil n'est pas pour le moment pas élucidé. De nombreuses théories ont été proposées, telles que la théorie du retournement de parapluie, qui s'est avéré ne pas pouvoir expliquer des phénomènes découverts par la suite. On citera également la théorie des liaisons métavalentes, définies comme étant à la fois covalentes et délocalisées et seraient ainsi la clé de la rapidité de la transition. Actuellement, aucune théorie ne fait consensus que ce soit pour les PCM ou les OTS.

2 Simulations *ab initio* hors-équilibre

Théorie de la fonctionelle de la densité

Décrire un système de plusieurs atomes par le biais de la mécanique quantique est complexe. Il s'agit en effet de résoudre l'équation de Schödinger avec un grand nombre de degrés de libertés. L'approximation de Born-Oppenheimer séparant les contributions des noyaux et des électrons, bien que simplifiant le problème, ne le rend pas soluble si facilement tout de même. L'idée de la théorie de la fonctionnelle de la densité permit cela, en passant d'une fonction d'onde multi-électronique à la densité électronique, réduisant ainsi drastiquement le nombre de degrés de libertés. Celle-ci se base sur les théorèmes de Hohenberg et Kohn, stipulant que le potentiel les électrons déterminent les positions atomiques de manière unique, et décrivent ainsi toutes les propriétés du système. L'approche de Kohn et Sham complète le tableau, en montrant qu'il est possible d'exprimer l'énergie de l'état fondamental d'un système d'interactions comme étant celui d'un système isolé bien choisi. Toute différence entre les deux est englobée dans un seul terme, une fonctionnelle d'échange et corrélations. Il suffit donc de connaître cette fonctionnelle pour résoudre le problème facilement.

Evidemment ce n'est pas si simple, et seules des approximations permettent d'approcher ce terme. On présente ici l'approximation de densité locale consistant à considérer que les charges positives des noyaux sont réparties uniformément dans l'espace, et donc la densité électronique aussi. En second, l'approximation de gradient généralisé (GGA) regroupant de nombreuses fonctionnelles, y compris la PBE utilisée dans cette thèse. Pour ce type de fonctionnelle, les inhomogénéités du gaz d'électrons sont prises en compte d'une fonction dépendant du gradient de la densité. Finalement, les méta-GGA ainsi que les fonctionnelles hybrides sont évoquées. Ce sont les plus précises actuellement, alliant LDA et modèle de Hartree-Fock, elles permettent de palier au problème de calcul de gap rencontré dans les autres méthodes, mais nécessitent beaucoup plus de ressources.

Simulations hors-équilibre

La génération des boites de départ s'effectue selon la technique de fusion-trempe. Dans le cas de GeTe, dont la phase expérimentale que nous avons étudiée est une "as-deposited" et contient donc un très large nombre de tétraèdres par rapport à un fusion-trempé, la boite de départ est remplacée par une boite de SiTe, qui est un composé dans lequel les atomes de Si adoptent naturellement des environnements locaux tétraédriques. Ensuite les atomes de Si sont remplacées par des atoms de Ge, permettant ainsi d'obtenir une boite de simulation de GeTe possédant un large nombre de tétraèdres, et étant ainsi plus proche de des échantillons expérimentaux.

L'excitation se fait ensuite par le biais de l'application d'une fonction de Fermi-Dirac sur les électrons, avec une largeur de distribution assimilée à la température électronique T_e.

Afin de relier les simulations et les expériences, la variation relative de fonction diélectrique est considérée pour déterminer une température électronique permettant une comparaison. Cette dernière ne s'effectue pas sur n'importe quelles données, puisque nous ne voulons pas que des effets thermiques provenant du réseau ionique viennent fausser T_e. Nous considérons donc expérimentalement des temps très courts, inférieurs à la constante de couplage électron-phonon soit de l'ordre de la picoseconde. Ainsi le réseau doit encore être froid, ce qui permet de comparer

avec les simulations effectuées à $T_i = 300$ K.

Analyse structurale

Une fois les boites intéressantes déterminées, l'analyse de la structure s'effectue par le biais de plusieurs grandeurs : fonction diélectrique, densité d'états, fonction de corrélation de paires, nombres de coordinations, distribution angulaire, déplacement quadratique moyen, corrélation à 3-corps limitée en angles ainsi que densité vibrationnelle d'états sont donc présentés dans cette partie.

3 Interférométrie dans le domaine des fréquences

L'interférométrie dans le domaine des fréquences (FDI) est une technique optique, d'interférométrie comme son nom l'indique, qui a été dévelopée à l'origine en tant que diagnostic de plasmas. Mais son utilisation ne se limite pas à cela.

Le FDI est une technique pompe-sonde, où deux impulsions sondes séparées d'une durée fixe sont réfléchies sur un matériau tandis qu'une impulsion pompe, dont le délai varie par rapport à la seconde impulsion sonde déclenche un processus. Ici, la pompe dépose de l'énergie dans le matériau, le portant à un état excité. Etant réfléchies sur le matériau à deux moments avant et après excitations, les deux impulsions sondes sont modifiées par les réflectivités du matériau à ces deux instants, qui sont elles-mêmes différentes. En analysant l'interférogramme collecté en polarisation P et S simultanément pour chaque délai, les variations de réflectivité et de phase mesurées par le FDI peuvent être reliées à la dynamique de la surface ainsi qu'aux propriétés diélectriques. Il s'agit d'une technique basée sur des lasers femtosecondes, qui permet une résolution temporelle femtoseconde, et une résolution longitudinale nanométrique.

4 Dynamique de couches minces de GeTe amorphe sous excitation

Résultats expérimentaux de l'excitation de GeTe amorphe

La réponse de couches minces de GeTe amorphe excité par un laser femtoseconde de durée 50 fs FWHM et de longueur d'onde 800 nm est étudiée par FDI avec des impulsions sondes de 80 fs et de longueur d'onde 532 nm. Sur les 9 picosecondes sondées, on dénote une transition non thermique qui intervient en 300 fs, apparaissant dans les variation de fonction diélectrique, aboutissant à un état plus métallique. Pour les hautes fluences, cet état transitoire est suivi par le dévelopement d'une phase liquide de plus haute densité à partir d'1 ps, induisant ainsi une contraction du matériau jusqu'à 4 nm.
L'excitation de ce matériau déclenche ainsi la transition d'un premier état amorphe vers un second, donc les propriétés sont différentes.

Simulations *ab initio* de dynamique moléculaire de GeTe amorphe

Des simulations AIMD ont permis de comprendre les changements à une échelle locale : les simulations révèlent également une transition non-thermique. La VDOS, fonction de corrélation de paires, ou encore distribution des angles, ces analyses révèlent que les états hors-équilibres sont très similaires à l'état liquide.

Le scénario est donc le suivant : au début, l'état GeTe amorphe contient un grand nombre de tétraèdres. Lorsque la pompe excite l'échantillon, un changement d'ordre local s'opère pour GeTe vers des sites octahédriques. En moins de 300 fs cette transition non-thermique est achevée et abouti en une phase hors-équilibre dont la structure et les propriétés sont celles de la phase liquide de GeTe. Le couplage électron entrant en scène, le réseau ionique chauffe et atteint la température de fusion T_m. Bien que la structure ne change plus trop à partir de ce moment là, la propagation d'une phase liquide de haute densité entraine la contraction continue du matériau.

5 Dynamique de couches minces de verres chalcogénure sous excitation

Résultats expérimentaux de l'excitation de verres chalcogénures

L'excitation de trois verres de chalcogénures : $Ge_{31}Se_{69}$ (GS), $Ge_{23}Se_{57}Sb_{20}$ (GSS) and $Ge_{23}Se_{53}Sb_{19}N_5$ (GSSN) a été investiguée par FDI. Les mêmes paramètres laser que pour GeTe amorphe ont été utilisés.
Cette excitation entraine comme dans le cas de GeTe une transition de l'amorphe initial vers un autre état désordonné par le biais d'une phase liquide. Sur les 9 picosecondes sondées, on note une dynamique ultra-rapide qui intervient dès l'action de la pompe et induit une variation maximale en 400 - 500 fs pour les parties réelles et imaginaires des trois matériaux. Pour les trois matériaux, les résultats expérimentaux montrent que l'excitation induit une métallisation.

Simulations *ab initio* de dynamique moléculaire de verres chalcogénures

Bien que ne pouvant être que difficilement comparée avec les expériences à cause de la sous-estimation de la bande interdite dans les simulation, l'étude des états excités hors-équilibre a tout de même permis de voir la tendance vers un des sites octaédraux pour tous les types d'atomes, dans les trois verres. GS montre toutefois une tendance de ses atomes de Ge à former des tétraèdres sous excitation modérée.

Contrairement à GeTe amorphe, les effets de la photo-excitation n'induisent pas ici de transition non-thermique : les états hors équilibres possèdent certes des similarités avec le liquide, mais leurs différences sont trop marqués pour envisager de les assimiler. Cette différence de réponse provient probablement de la largeur de la bande interdite, ici beaucoup plus grande que dans GeTe. Par ailleurs, tandis que GeTe est caractérisé par des liaisons métavalentes, les verres possèdent des "vraies" liaisons covalentes, qui sont donc plus compliquées à briser.

Conclusion

Optimiser des technologies existantes requière de comprendre la physique des mécanismes sous-jacents. Dans le cas des mémoires résistives telles que celles présentant une architecture "crossbar" associant des cellules mémoires et sélecteurs composés tous deux de chalcogénures, la clé est à priori l'excitation électronique. Cependant, l'essentiel de ce mécanisme n'est connu ni pour les cellules mémoires, ni pour les sélecteurs.

Afin de contribuer à cette compréhension, l'excitation de quatre couches minces de chalcogénures a été investiguée par des méthodes expérimentales et des simulations. GeTe amorphe (*a*-GeTe), un matériau mémoire à changement de phase prototypique utilisé dans les cellules mémoires, ainsi que trois verres, $Ge_{31}Se_{69}$ (GS), $Ge_{23}Se_{57}Sb_{20}$ (GSS) and $Ge_{23}Se_{53}Sb_{19}N_5$ (GSSN), ayant un potentiel pour des applications de sélecteur OTS, ont été pompés par différentes fluences d'un laser de 30 fs à une longueur d'onde de 800 nm. Les premières neuf picoseconds après excitation ont été sondés par interférométrie dans le domaines des fréquences (FDI), une méthode optique permettant une résolution temporelle femtoseconde et une résolution longitudinale nanométrique. Les variations de phase et de réflectivité mesurées par le FDI permettent de retrouver non seulement la nature de la surface et sa dynamique, mais également les propriétés diélectriques du matériau sondé
Afin de compléter ces résultats expérimentaux et de comprendre la dynamique à une échelle locale, des simulations *ab initio* de dynamique moléculaire ont été conduites afin de reproduire les états hors-équilibre résultants de l'excitation.

Ces deux méthodes ont permis un approfondissement des connaissances des effets de l'excitation dans des couches minces de chalcogénures. Tout d'abord, on note la réponse ultra-rapide de *a*-GeTe et des trois verres suite à l'excitation laser. Tous montrent un changement soudain de propriétés diélectriques et un changement de dynamique en 350 -500 fs après la pompe. Cependant, comme attendu, cette échelle de temps similaire n'implique pas que leurs réponses soient identiques.

GeTe amorphe subit tout d'abord une transition non thermique : en 350 fs, la partie réelle de la fonction diélectrique se stabilise à une valeur de saturation, qui ne dépend pas vraiment de la fluence appliquée. Cette transition non-thermique ne constitue pas la dynamique entière. En effet, 1 picoseconde après excitation, la partie imaginaire montre une variation (bien que négligeable comparée à celle de la partie réelle), qui vu l'échelle de temps considérée peut être attribuée au couplage électron-phonon entrant en scène. Pour des fluences plus élevés que 31 mJ/cm^2, the changement de ε_i s'accompagne du dévelopement d'une phase liquide de haute densité. Il s'avère que les mesures FDI révèlent une contraction allant jusqu'à 4 nm du matériau pour la plus haute fluence. De manière générale, l'excitation laser fs a entrainé une transition entre deux états amorphes, mais ayant des propriétés différentes.
Les simulations AIMD hors-équilibre ont révélé sur la mécanisme à l'échelle locale. Tout d'abord, toutes les observables : fonction de corrélations de paires, densité vibrationnelle des états, distributions des angles... ont conduit au constat que l'excitation affecte essentiellement les atoms de Ge. Ces derniers montrent un changement d'environnement local, de sites tétraédriques vers des sites octaédriques. Par ailleurs, cette transition passe par des états excités transitoires hors-équilibre qui sont très similaires à la phase liquide en terme de structure et de propriétés électroniques,

confirmant le comportement non-thermique observé dans les expériences.

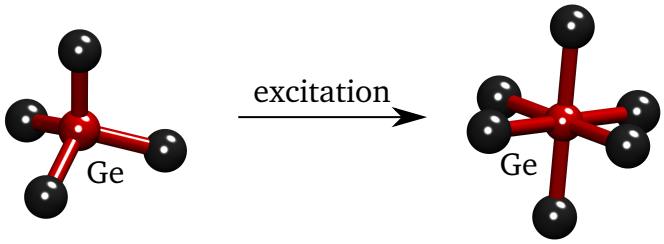

Figure 55 – *Changement d'environnement local des atomes de Ge lors de l'excitation de GeTe*

Dans le cas des verres de chalcogénures, bien que la dynamique principale prenne place également à une échelle de temps très courte, en dessous de 500 fs, la différence avec GeTe amorphe est flagrante. Premièrement, la fonction diélectrique dépend bien plus de la fluence. Le même phénomène de saturation est observé aux temps longs, mais la valeur résultante est complètement différentes si la fluence est 30 ou bien 76 mJ/cm^2, et ce pour les trois verres. Le résultat le plus frapant concerne $Ge_{31}Se_{69}$, qui montre une hausse de sa partie réelle lorsque la fluence est basse, mais une baisse lorsqu'on la fluence est élevée. Cependant, ceci peut-être expliqué par un modèle prenant en compte la contribution de fermeture de la bande interdite due à l'excitation. Dans le cas de GS, cettte correction et la dépendance de ε avec la longueur d'onde explique les tendances observées : l'excitation induit une fermeture partielle de bande interdite. Le même modèle appliqué à GSS et GSSN est également cohérent avec les expériences puisque seule une variation négative peut être obtenue.

La microscopie à contraste de phase effectuée post-expériences révèle que comme pour GeTe, la température de fusion des trois verres a été atteinte pour quasiment toutes les fluences : pour GS, des signes de fontes commencent à être distingués à partir de $F = 81$ mJ/cm^2, pour GSS la fluence la plus basse de $F = 45$ mJ/cm^2 présente déjà des structures de type empreinte digitale et pour $F = 68$ mJ/cm^2 la fusion de GSSN est observée.

Les simulations révèlent tout d'abord que les trois verres ont déjà des environnement quelque peu différents dans la phase initiale. GS est caractérisé par une majorité d'atomes Ge en environnement tétraédrique (Ge^T), comparé à GSS et GSSN qui ne possèdent qu'un tiers et un cinquième. Sous faible excitation (température électronique $T_e \leq 0.6$ eV), les états hors-équilibre résultant sont très similaires à ceux des phases non-excitées. Lorsque l'excitation dépasse 0.6 eV, les observables telles que les angles ou les longueurs de liaisons montrent une claire variation.

Par rapport à GeTe amorphe, nous supposons que c'est la nature intrinsèque des matériaux qui explique ces différences. Dans GeTe amorphe, la distortion de Peierls, bien que plus faible que dans le cristal, induit des liaisons longues et courtes dont la nature est différente du réseau covalent présent dans les verres. Les liaisons covalentes étant plus fortes, l'excitation requise pour rompre ou tout du moins perturber les liaisons est plus importante que dans le cas de GeTe avec ses liaisons de forces diverses. Par ailleurs, GeTe est caractérisé par une bande interdite de 0.80 eV tandis qu'elle est deux à trois fois plus élevée dans les verres, les rendant plus difficiles à exciter.

Il est intéressant de constater que si l'on regarde de manière globales ces phénomènes, l'excitation

de GeTe amorphe a déclenché à une transition non-thermique, suivie à l'échelle picoseconde de sa fonte thermique, tandis que pour les verres de chalcogénure, l'excitation a induit une fermeture paritelle de la bande interdite, conduisant à une phase plus métallique, mais aucun changement de volume n'a été été détecté expérimentalement aux temps courts. Ces deux réponses ressemblent clairement aux phénomènes rencontrés dans les applications mémoires, où les PCMs des cellules mémoires deviennent beaucoup plus conducteur quand la tension excède une valeur seuil, puis transitionnent vers un autre état lorsque l'effet Joule est assez important, tandis que les OTS sont capables de varier grandement leur conductivité, sans changement structurel flagrant. La différence est qu'ici ce n'est pas une excitation purement électrique, mais une impulsion lumineuse femtoseconde qui induit la commutation à seuil observée dans les deux types de matériau.
Certains des résultats de cette thèse ne peuvent pas être expliqués aussi pleinement que possible dû à la complexité de la dynamique en jeu. Cependant, il est plutôt juste de dire que ces résultats permettent une compréhension plus poussée du mécanisme sous-jacent de commutation à seuil présent dans les couches minces de chalcogénures.

Ce travail ouvre donc la voie à plusieurs directions de recherches : la première étant simplement d'étudier comme les variations observées évoluent selon la longueur d'onde sonde. Puisque la partie imaginaire de la fonction diélectrique est un noeud sous excitation à 532 nm, mais pas à 630 nm, il serait intéressant de comparer si la dynamique reste la même.
L'excitation affectant essentiellement les atomes de Ge dans GeTe, une autre idée serait d'exciter les modes de phonons résonants avec des impulsions THz, ou encore d'étudier les comportements précis de chaque atomes grâce à du XANES résolu en temps.

APPENDIX A

LATTICE REPRESENTATION

This appendix aims at giving a non-exhaustive list of properties of lattices and cells that are used in this thesis. While the lattice and basis consideration are crucial for the description of a crystal phase, they are also often used for the simulation of amorphous phases.

I Lattice description

Lattices are described thanks to a set of primitive lattice vectors $(\vec{a}_1, \vec{a}_2, \vec{a}_3)$. They are chosen such that a translation resulting from a linear combination of those such as $\boldsymbol{R} = n\vec{a}_1 + m\vec{a}_3 + p\vec{a}_3$ $(n, m, p \in \mathbb{Z})$ gives the same configuration as the initial one. This set of primitive lattice vectors defines the primitive unit cell, the smallest cell that still reflects all the symmetries of the crystal.

It may be convenient to work in the reciprocal space ($k-$space), with the so-called reciprocal lattice. This latter is just the Fourier transform of the direct space lattice. Any element of symmetry in direct space should still be found in the reciprocal space.
The corresponding primitive cell in reciprocal space is also defined by a set of vectors that are linked to the direct space ones. For $\boldsymbol{G} = m_1\vec{\boldsymbol{b}}_1 + m_2\vec{\boldsymbol{b}}_2 + m_3\vec{\boldsymbol{b}}_3$, with $(m_1, m_2, m_3 \in \mathbb{Z})$ the reciprocal lattice, we have :

$$\begin{aligned} \boldsymbol{b}_1 &= 2\pi \frac{\boldsymbol{a}_2 \times \boldsymbol{a}_3}{\boldsymbol{a}_1 \cdot (\boldsymbol{a}_2 \times a_3)} \\ \boldsymbol{b}_2 &= 2\pi \frac{\boldsymbol{a}_3 \times \boldsymbol{a}_1}{\boldsymbol{a}_1 \cdot (\boldsymbol{a}_2 \times \boldsymbol{a}_3)} \\ \boldsymbol{b}_3 &= 2\pi \frac{\boldsymbol{a}_1 \times \boldsymbol{a}_2}{\boldsymbol{a}_1 \cdot (\boldsymbol{a}_2 \times \boldsymbol{a}_3)} \end{aligned} \tag{A.1}$$

with the symbol '$\times$' begin the cross product and $\cdot$ the scalar product. The term $\boldsymbol{a}_1 \cdot (\boldsymbol{a}_2 \times \boldsymbol{a}_3)$ corresponds in fact to the volume of the primitive cell in real space.
In reciprocal space, it is the Brillouin zone (BZ) that defines the primitive cell.The formula A.1 implies that the symmetries encountered in real space will also appear in reciprocal space. A few high symmetry points are defined concerning the BZ : Γ is the center of the BZ, M the center of an edge, X the center of a face Γ point is the center of the BZ.

From these formula, we see that the lattice in the reciprocal space will keep its symmetries.

II Simulations with amorphous states

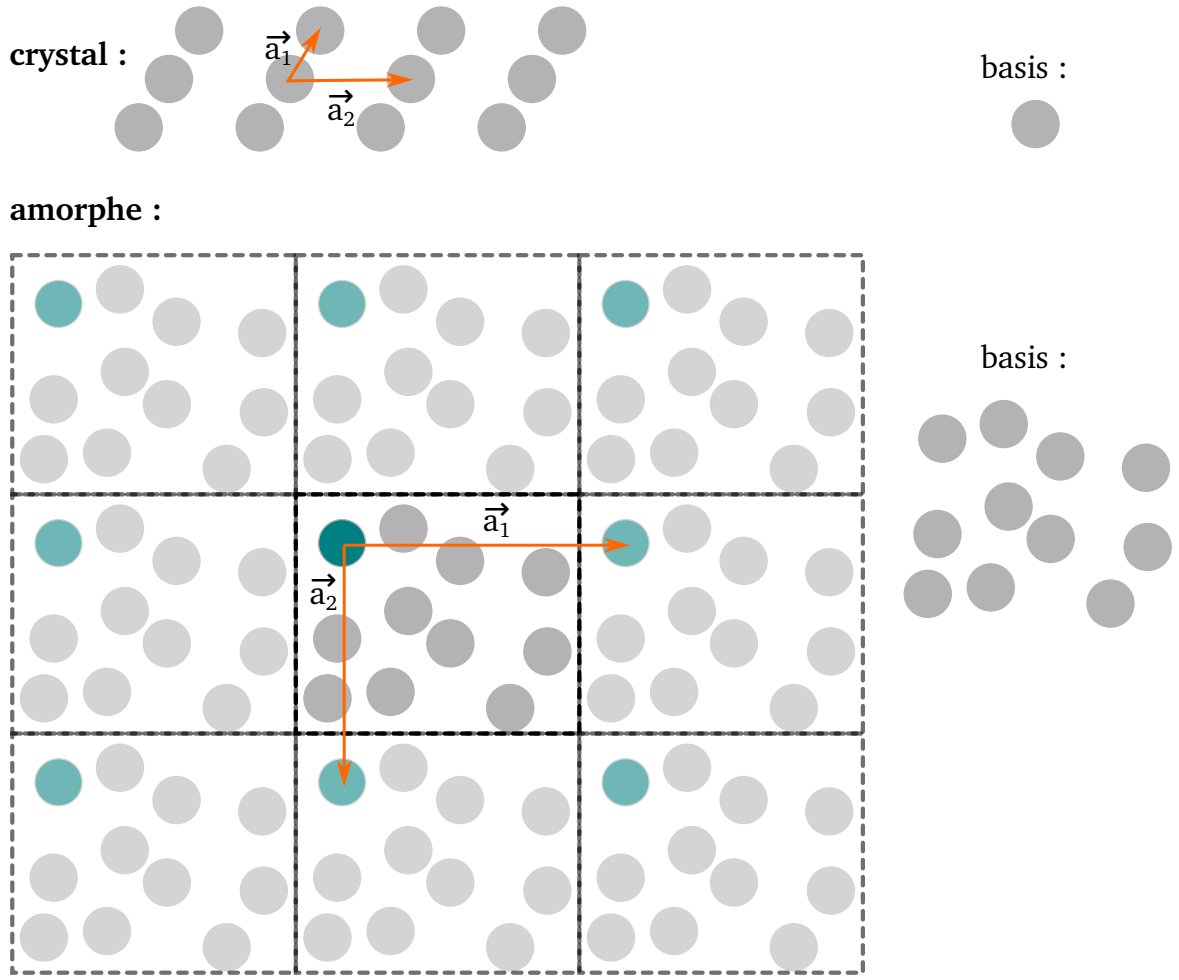

Figure A.1 – *Crystal vs amorphous state in simulations*

In simulation, a set of vector $(\vec{c}_1, \vec{c}_2, \vec{c}_3)$ should be given, along with the coordinates of the atoms in the initial state. For a crystal, this is not an issue, $(\vec{a}_1, \vec{a}_2, \vec{a}_3)$ are used.
In the case of an amorphous state, the question is raised : how to describe a structure with a minimum of atoms, and has no symmetry ? In practice, the solution is to find a simulation cell that has enough atoms to reflects properly the overall properties of the real material, but still low enough to reduce at maximum the computation time. As in Figure A.1, what we do is considering a pseudo-cubic cell, that comprises all the atoms. The pseudo-basis corresponding to this state is then all the atoms rather than just one as in the case of a crystal.
With this cubic cell, we can work similarly as in a crystal state. Of course the symmetry does not exist here. But we can still define a Γ point in reciprocal space that corresponds to the center of the BZ and enables to do the calculations.

Periodic boundaries conditions (PBC)

A real material contains far too many atoms to be simulated just as such with the actual computer capacities. The way around it is to consider only a small portion of it, which is small enough to be simulated in a decent amount of time, but still large enough to represent accurately the properties of the corresponding real material.
In practice in simulations, the coordinates for each direction are updated at each iteration step with a function f defined as :

$$f(x_i, L_i) = \begin{cases} x_i + L_i, & x < -L_i/2 \\ x_i - L_i, & x \geq L_i/2 \\ x \quad \text{otherwise.} \end{cases} \tag{A.2}$$

with L_i the size of the simulation cell in the i direction.

APPENDIX B

OPTICAL CONVENTIONS AND DRUDE MODEL

I Choice of convention

The convention for the complex refractive index N as well as the dielectric function ε are dictated by that of the electric field E of the laser. In this thesis, we chose :

$$\vec{E} = \vec{E_0} e^{-i\left[\omega t - \vec{k}\cdot\vec{r}\right]} \tag{B.1}$$

E_0 is the amplitude of the field, ω and $\vec{k}$ the radial frequency and wavevector of the laser respectively. We consider the complex refractive index $N = Re(N) + i\ Im(N)$, Re and Im designating the real and imaginary part respectively.
Introducing the light speed c, the wavevector k can be expressed using N such that :

$$k = \frac{\omega}{c} N = \frac{\omega}{c} \left[Re(N) + i\ Im(N)\right] \tag{B.2}$$

Therefore, the electric field can now be written as:

$$E = E_0 e^{-i\omega t + i\frac{\omega}{c} r (Re(N) + i Im(N))} = E_0 e^{-i\omega t + i\frac{\omega}{c} r\ Re(N)} \underbrace{\boxed{e^{-i\frac{\omega}{c} Im(N) r}}}_{0 \text{ when } r \to \infty} \tag{B.3}$$

As the electric field should be finite, it implies that the boxed term should tend to zero as r tend to $+\infty$. As a consequence, $Im(N)$ is positive.
The relationship with absorption can be cleared by comparing with the Beer-Lamber law, with α the absorption coefficient ($\in \mathbb{R}$) :

$$I(r) = I_0 e^{-\alpha(r)} \tag{B.4}$$

The intensity derived from the electric field is $I = EE^*$, so we have the following deductions :

$$I = |E_0|^2 e^{-2\frac{\omega}{c} r\ Im(N)} = I_0 e^{-\alpha r} \Rightarrow \alpha = 2\frac{\omega}{c} Im(N) \tag{B.5}$$

In order to have absorption in our material when it is irradiated, α must be positive, which implies that $Im(N)$ is also positive. The imaginary part of the refractive index, called the extinction coefficient is usually chosen as belonging to $\mathbb{R}^+$, so we can choose the following convention to describe our sytem :

$$\boxed{N = n + i\kappa} \qquad \text{with } n, \kappa \in \mathbb{R}^+ \tag{B.6}$$

The two conventions $\varepsilon = \varepsilon_r \pm i\ \varepsilon_i$ are possible, but don't refer to the same situation as per the initial convention that we have chosen. The complex refractive index N is linked to the dielectric function such that $N^2 = \varepsilon$ whatever the convention.

$$N^2 = n^2 + 2n\kappa\ i - \kappa^2 \Rightarrow \begin{cases} Re(\varepsilon) = n^2 - \kappa^2 \\ Im(\varepsilon) = 2n\kappa \end{cases} \tag{B.7}$$

n and κ being in $\mathbb{R}^+$, the imaginary part of ε evolves in the same way as κ. As $\kappa \propto \alpha$, then $Im(\varepsilon) \propto \alpha$. This implies that :

- for the convention $\varepsilon = \varepsilon_r - i\ \varepsilon_i$, absorption is characterized by ε_i <0
- if ε is defined such that $\varepsilon = \varepsilon_r + i\varepsilon_i$, it is ε_i >0 that implies absorption

Recapitulative

$$\boxed{\begin{aligned} E &= E_0 e^{-i\left(\omega t - \vec{k}\vec{r}\right)} \\ N &= n + i\kappa \\ \varepsilon &= \varepsilon_r + i\ \varepsilon_i \end{aligned}} \tag{B.8}$$

II Drude model

To describe the variation in dielectric function due to free carriers in the conduction band, a Drude model is often used. It is based on the hypothesis that the motion of the ions in the material is completely negligible compared to that of the electrons, and that the electrons constitute a non-interacting gas.
The Maxwell equations state that :

$$\vec{\nabla} \times \vec{B} = \mu_0 \vec{j} + \frac{\varepsilon_\infty}{c^2} \frac{\partial \vec{E}}{\partial t} \tag{B.9}$$

with j the current density and ε_∞ the high frequency limit of the dielectric function.
As $\vec{E} = \vec{E_0} e^{-i\left(\omega t - \vec{k}\cdot\vec{r}\right)}$, $\partial E/\partial t = -i\omega E$. Moreover, as $j = \sigma E$, with σ the conductivity, it yields :

$$\begin{aligned} \vec{\nabla} \times \vec{B} &= \mu_0 \sigma \vec{E} - i\frac{\omega}{c^2} \varepsilon_\infty \vec{E} \\ &= -i\frac{\omega}{c^2} \left(\varepsilon_\infty + i\frac{\sigma}{\varepsilon_0 \omega} \right) \vec{E} \end{aligned} \tag{B.10}$$

From which the Drude dielectric function can be identified

$$\varepsilon^D = \varepsilon_\infty + i\frac{\sigma}{\varepsilon_0 \omega} \tag{B.11}$$

The second step consists in expressing the conductivity σ. In order to do that, we consider the equation of motion of an electron in an electric field :

$$m\frac{d\vec{v}}{dt} = -e\vec{E} - mv\vec{v} \tag{B.12}$$

with m the mass of the electron, $\vec{v}$ its velocity, v the collision frequency.
Its velocity $\vec{v}$ must have the same time dependency as the electric field : $\vec{v} = v_0 e^{-i\omega t}$. From B.12, the relation between v and E is then deduced to be :

$$\vec{v} = -\frac{e}{m}\frac{1}{v - i\omega}\vec{E} \tag{B.13}$$

Using $\vec{j} = -ne\vec{v}$, with n the density of charge carriers, and $j = \sigma E$, we identify

$$\sigma = \frac{ne^2}{m}\frac{1}{v - i\omega} \tag{B.14}$$

It allows to express fully the dielectric function, with $\omega_p = \sqrt{\frac{ne^2}{m\varepsilon_0}}$ the plasma frequency :

$$\boxed{\varepsilon^D = \varepsilon_\infty - \frac{\omega_p^2}{\omega^2}\frac{1}{1 + i\frac{v}{\omega}}} \tag{B.15}$$

APPENDIX C

SUPPLEMENTARY DATA ON GERMANIUM TELLURIUM

I Tauc plot for the band gap determination

To determine the band gap of a material, several methods are possible. One of them is the fitting of a Tauc plot [66, 286–290]. The Tauc model links the energy E to the quantity αE (with α the absorption coefficient) under the form:

$$\alpha E = B(E - E_g)^m with m = \begin{cases} 1/2\text{: direct allowed transitions} \\ 3/2\text{: direct forbidden transitions} \\ 1/2\text{: indirect allowed transitions} \\ 3\text{: indirect forbidden transitions} \end{cases} \tag{C.1}$$

In our case, $m = 2$, with gives $(\alpha E)^{1/2} = B(E - E_g)$. Fitting with a $f = ax + b$ function then allows to retrieve E_g.

II External pressure - map

All the *ab initio* molecular dynamics simulations were performed in the canonical ensemble (NVT). In order to keep the volume constant, an external pressure in applied on the simulation cell at each time step. If the material tries to expand, external forces are increased to constraint this expansion and keep the volume wanted. On the contrary if the material tends to shrink, negative external forces are applied to get the correct volume.
With the five cases picked for the comparison data, the simulation also give a tendency of shrinkage, with a negative external pressure needed.

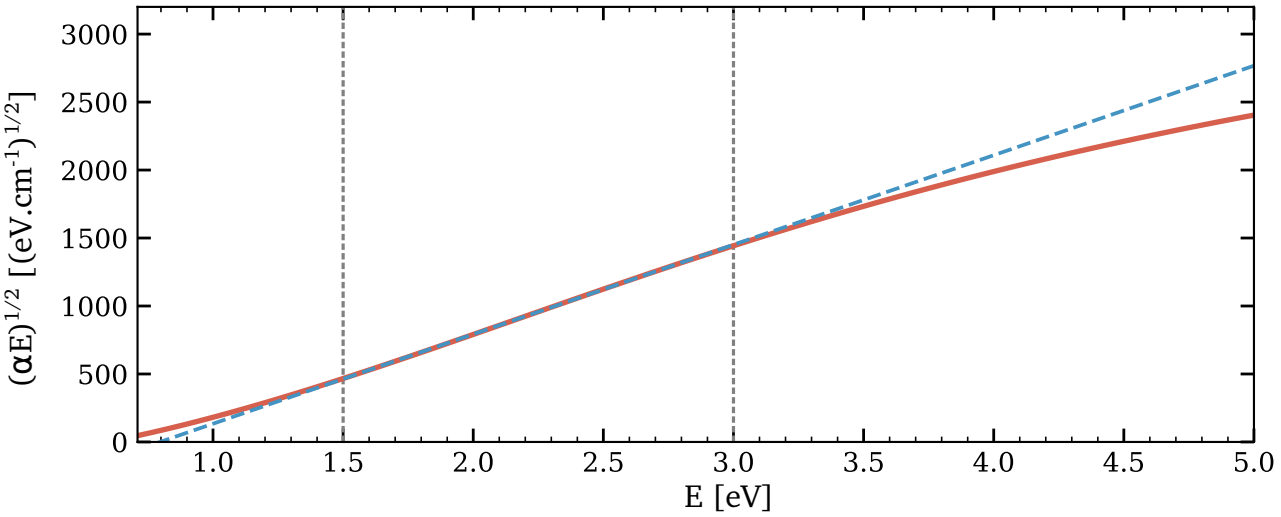

Figure C.1 – *Tauc plot with ellipsometry data for GeTe. We find* $E_g = 0.80 \pm 0.01$ *eV.*

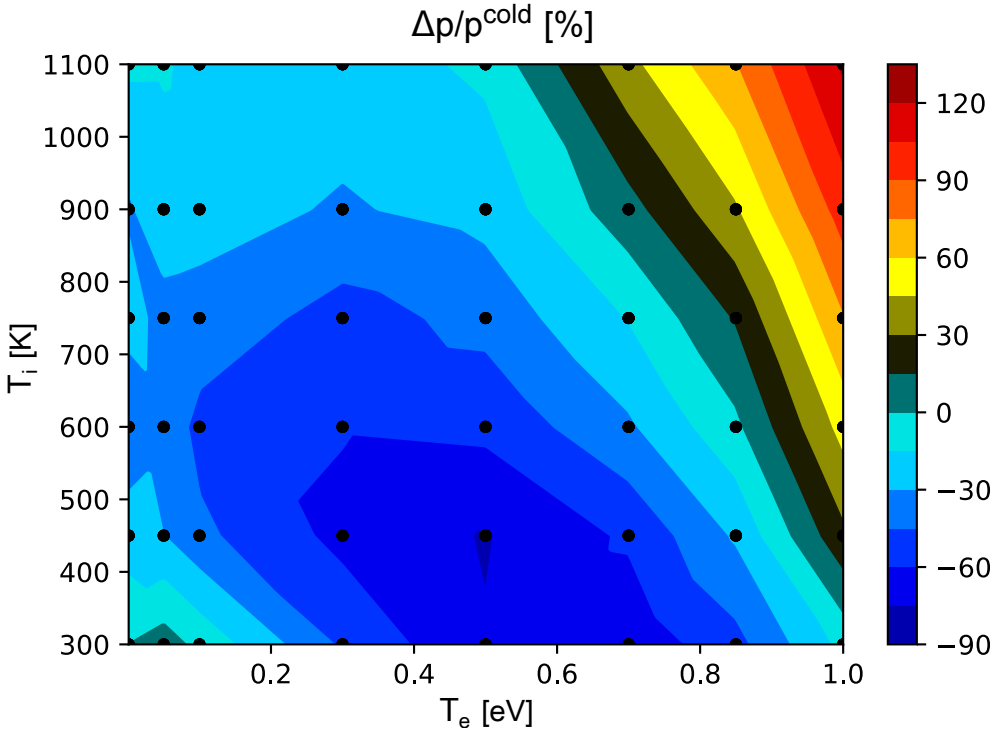

Figure C.2 – *External pressure in [kB] as a function of* T_e *and* T_i *for GeTe, averaged on the last 5 picoseconds of the simulation.*

III Dielectric function - map

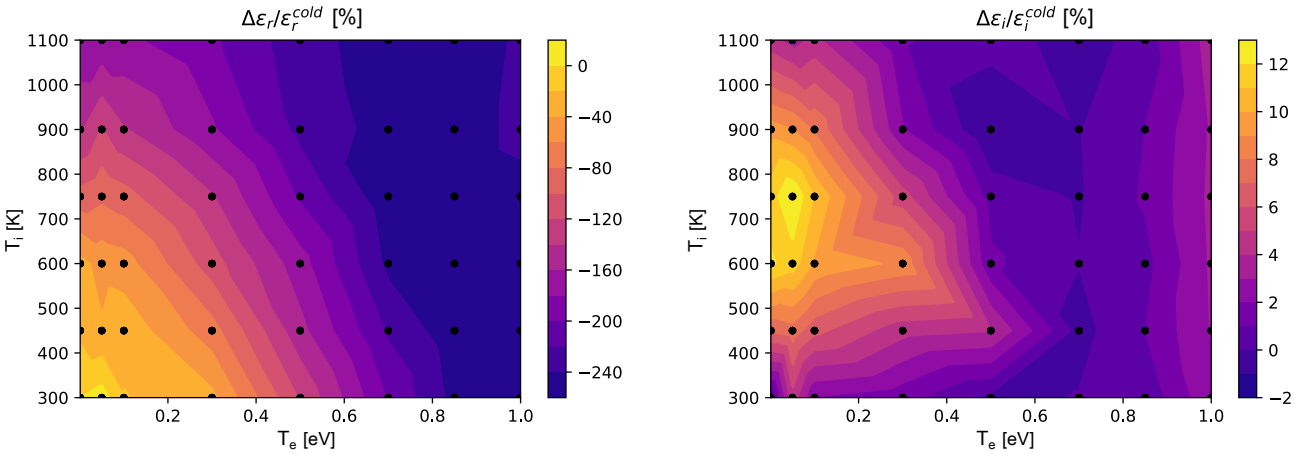

Figure C.3 – *maps of relative variation of the dielectric function of GeTe at 532 nm*

IV ALTBC

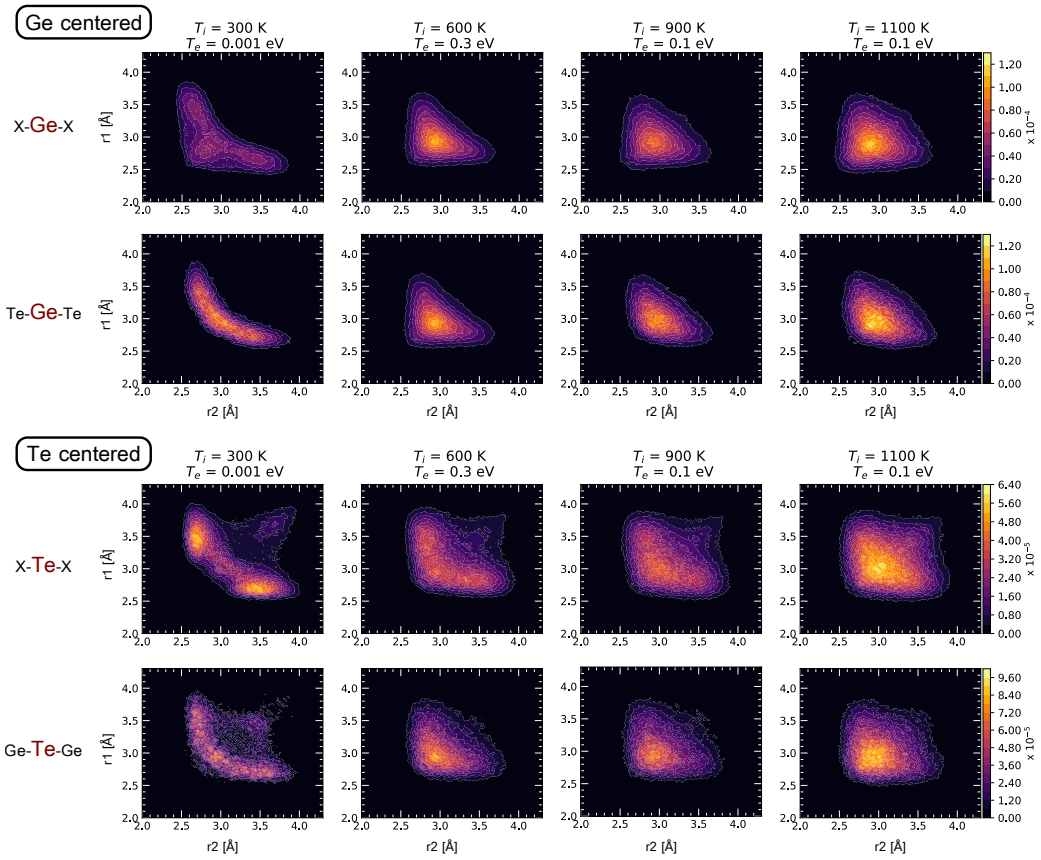

Figure C.4 – *ALTBC of GeTe computed for Ge (top) and Te (bottom). X-Ge-X indicates that all bonds (within the angle constraint condition) was taken into account for the Ge calculation (the same goes for Te).*

V Pair distribution function

The pair distribution functions of all the pairs of T_e, T_i are shown here. Overall highly excited states as well as liquid states are much less structured.

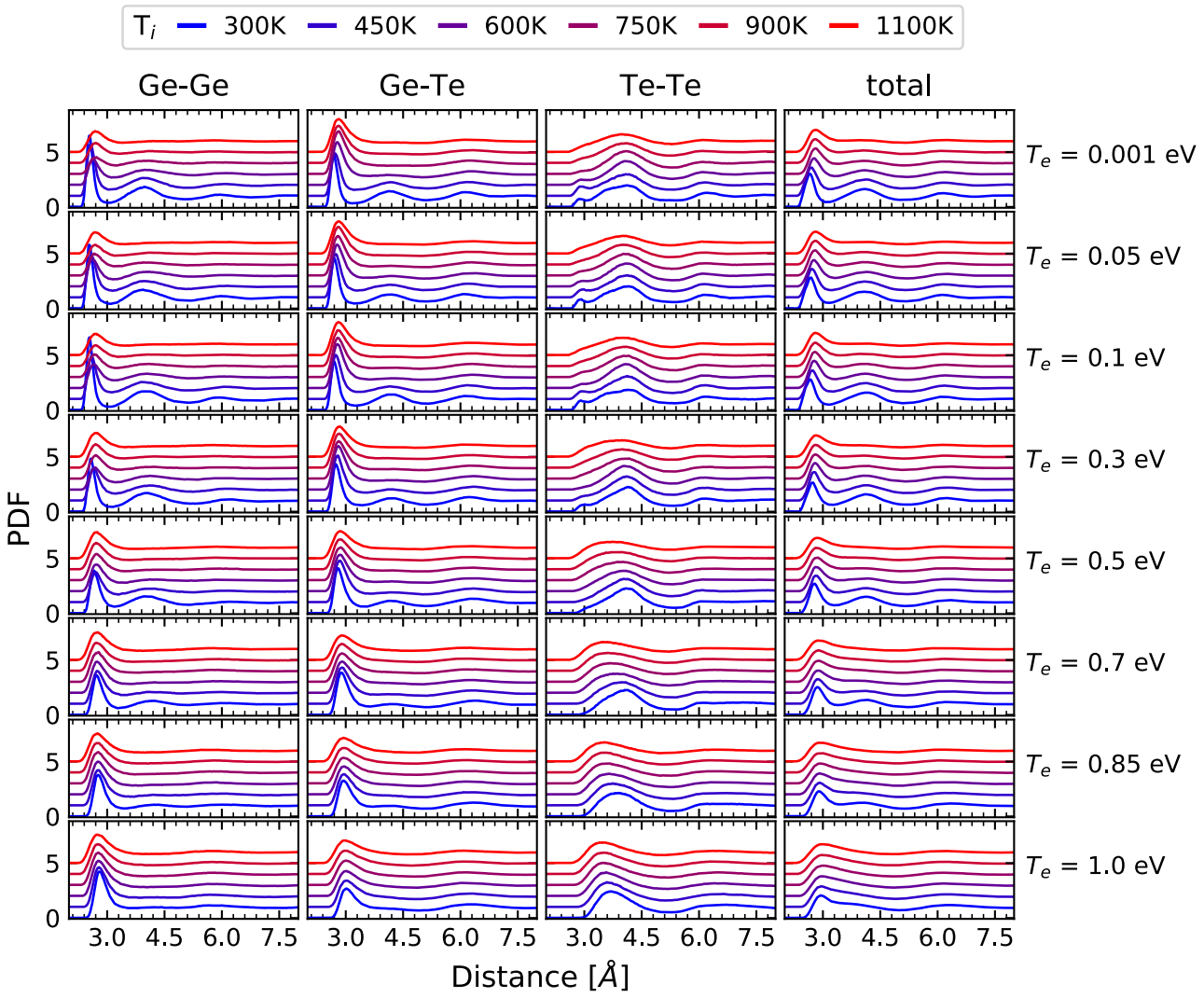

Figure C.5 – *Pair distribution function of all the (T_i - T_e) pairs simulated for GeTe*

APPENDIX D

SUPPLEMENTARY DATA - CHALCOGENIDE GLASSES

I External pressure

All the *ab initio* molecular dynamics simulations were performed in the canonical ensemble (NVT). In order to keep the volume constant, an external pressure in applied on the simulation cell at each time step. If the material tries to expand, external forces are increased to constraint this expansion and keep the volume wanted. On the contrary if the material tends to shrink, negative external forces are applied to get the correct volume.

This constraint is rather well tolerated in most cases, but what we see in the case of the high excitations of GS and GSS for T_i = 300 K is a large increase of the external pressure, which means that it is difficult to restrain the need of expansion of the material.

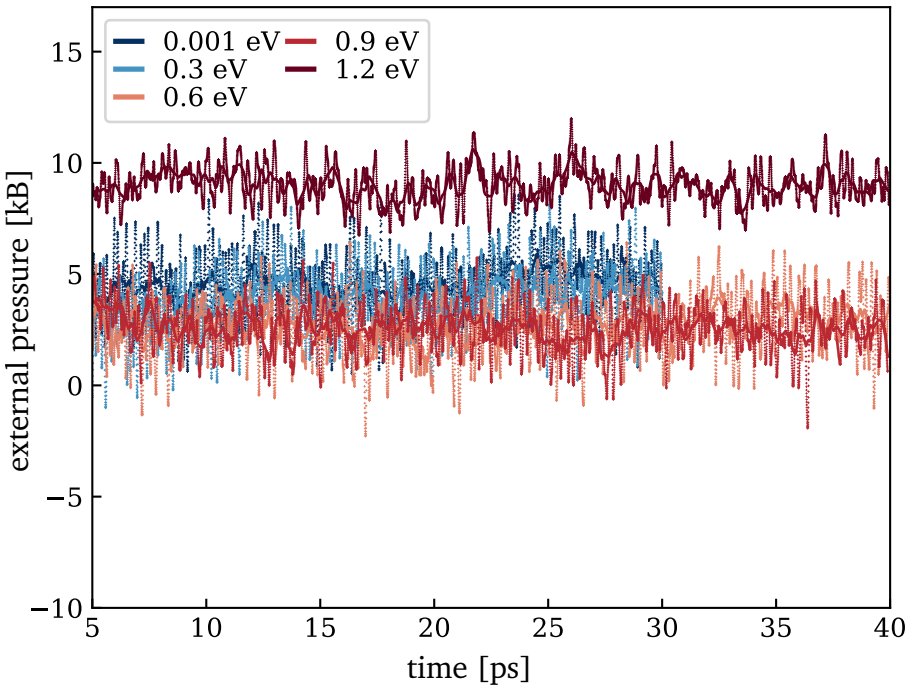

Figure D.1 – *External pressure on GS to maintain a constant volume during MD simulation, T_i = 300 K. For T_e = 1.2 eV, a large increase of external pressure is seen, which means that the simulation is having a hard time keeping a constant volume for this case.*

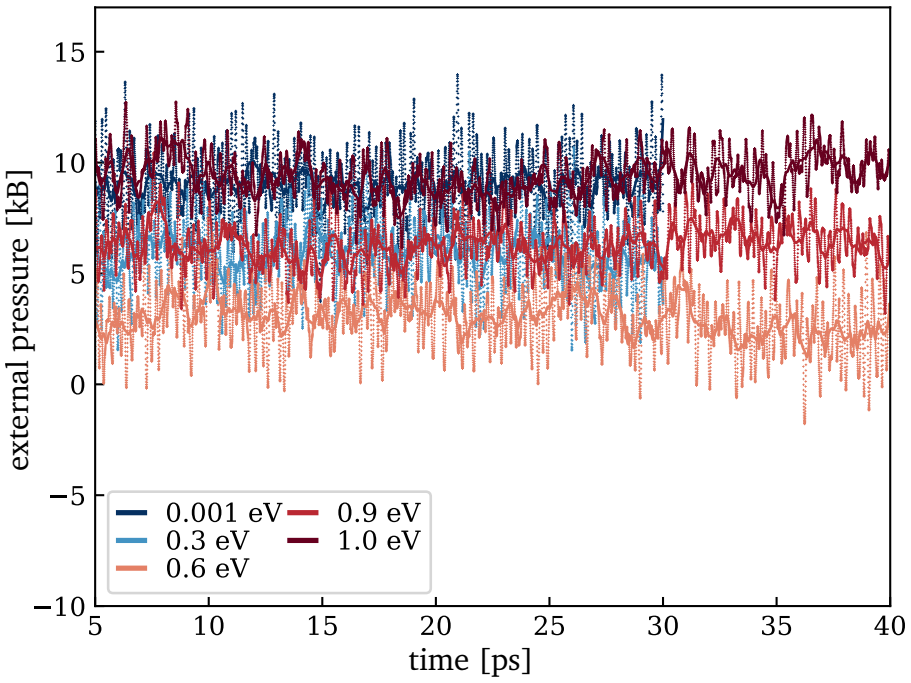

Figure D.2 – *External pressure on GSS to maintain a constant volume during MD simulation, T_i = 300 K. The pressure corresponding to the highest excited state is the same as for the non-excited state, but it is more the tendency from T_e = 0.6 eV that is important. For the cases of an electronic temperature of T_e = 0.9 eV and 1.0 eV, we see clear steps in external pressure compared to the case of T_e = 0.6 eV.*

II Pair distribution function - Cut-off r_{cut}

Table D.1 – *Cut-offs of glassy GS from simulation*

Ti - Te	300 K - 0.001 eV	300 K - 0.3 e V	300 K - 0.6 eV	300 K - 0.9	1200 K - 0.1 eV
r_{cut} [Å]	2.92	2.92	3.01	3.15	3.10

Table D.2 – *Cut-offs of glassy GSS from simulation*

Ti Te	300 K 0.001 eV	300 K 0.3 eV	300 K 0.6 eV	300 K 0.9 eV	300 K 1.0 eV	1200 K 0.1 eV
r_{cut} [Å]	3.08	3.22	3.31	3.35	3.40	3.13

Table D.3 – *Cut-offs of glassy GSSN from simulation*

Ti - Te	300 K - 0.001 eV	300 K - 0.3 e V	300 K - 0.6 eV	300 K - 0.9	1200 K - 0.1 eV
r_{cut} [Å]	3.04	3.04	3.12	3.17	3.12

III Diffusion coefficient

The diffusion coefficients of GS, GSS and GSSN were extracted for the fitting of their mean squared displacement (MSD) curves using Equation 2.53. For GSS and GSSN, the non/low-excited states demonstrate a "caged-like" behaviour for which the fitting is not possible.

T_i - T_e	D_{Ge} [cm^2/s]	D_{Se} [cm^2/s]
300 K - 0.001 eV	3.8×10^{-7}	4.6×10^{-7}
300 K - 0.3 eV	1.2×10^{-6}	1.4×10^{-6}
300 K - 0.6 eV	1.6×10^{-6}	2.6×10^{-6}
300 K - 0.9 eV	5.6×10^{-6}	7.0×10^{-6}
1200 K - 0.1 eV	8.1×10^{-5}	1.0×10^{-4}

Table D.4 – *Diffusion coefficients of GS from simulations*

T_i - T_e	D_{Ge} [cm^2/s]	D_{Se} [cm^2/s]	D_{Sb} [cm^2/s]
300 K - 0.001 eV	-	-	-
300 K - 0.3 eV	4.9×10^{-7}	3.8×10^{-7}	3.7×10^{-7}
300 K - 0.6 eV	1.6×10^{-6}	1.4×10^{-6}	1.6×10^{-6}
300 K - 0.9 eV	4.0×10^{-6}	3.2×10^{-6}	5.0×10^{-6}
300 K - 1.0 eV	6.4×10^{-6}	5.8×10^{-6}	9.3×10^{-6}
900 K - 0.08 eV	1.6×10^{-5}	1.5×10^{-5}	1.4×10^{-5}

Table D.5 – *Diffusion coefficients of GSS from simulations*

T_i - T_e	D_{Ge} [cm^2/s]	D_{Se} [cm^2/s]	D_{Sb} [cm^2/s]	D_N [cm^2/s]
300 K - 0.001 eV	-	-	-	-
300 K - 0.3 eV	-	-	-	-
300 K - 0.6 eV	2.2×10^{-6}	2.6×10^{-6}	2.2×10^{-6}	1.5×10^{-6}
300 K - 0.9 eV	4.3×10^{-6}	4.5×10^{-6}	5.2×10^{-6}	2.3×10^{-6}
1200 K - 0.1 eV	4.7×10^{-5}	5.5×10^{-5}	4.9×10^{-5}	3.1×10^{-5}

Table D.6 – *Diffusion coefficients of GSSN from simulations*

IV Excited dielectric function

The dielectric function of the excited state resulting from a pumping using sub-picosecond pulses can be expressed using the Equation 5.4. The result for GS is given in the Chapter 5, Figure 5.10. In the Figure D.3 and D.4, this model was applied to GSS and GSSN respectively. The effective mass of the holes m_h^* and of the electrons m_e^* were estimated using mobility measurements from Reference [14] in glassy $GeSe_2$ giving $\mu_e = 0.2$ cm^2/V/s and $\mu_h = 0.04$ cm^2/V/s.

The response of the two materials is very similar. However, it is different from the one exhibited by GS. Here the real part does not show any increase, whatever the parameters. As it was stated in the Chapter 5, the dispersion relation of the dielectric function with the energy is what must cause the peculiar behaviour of GS.

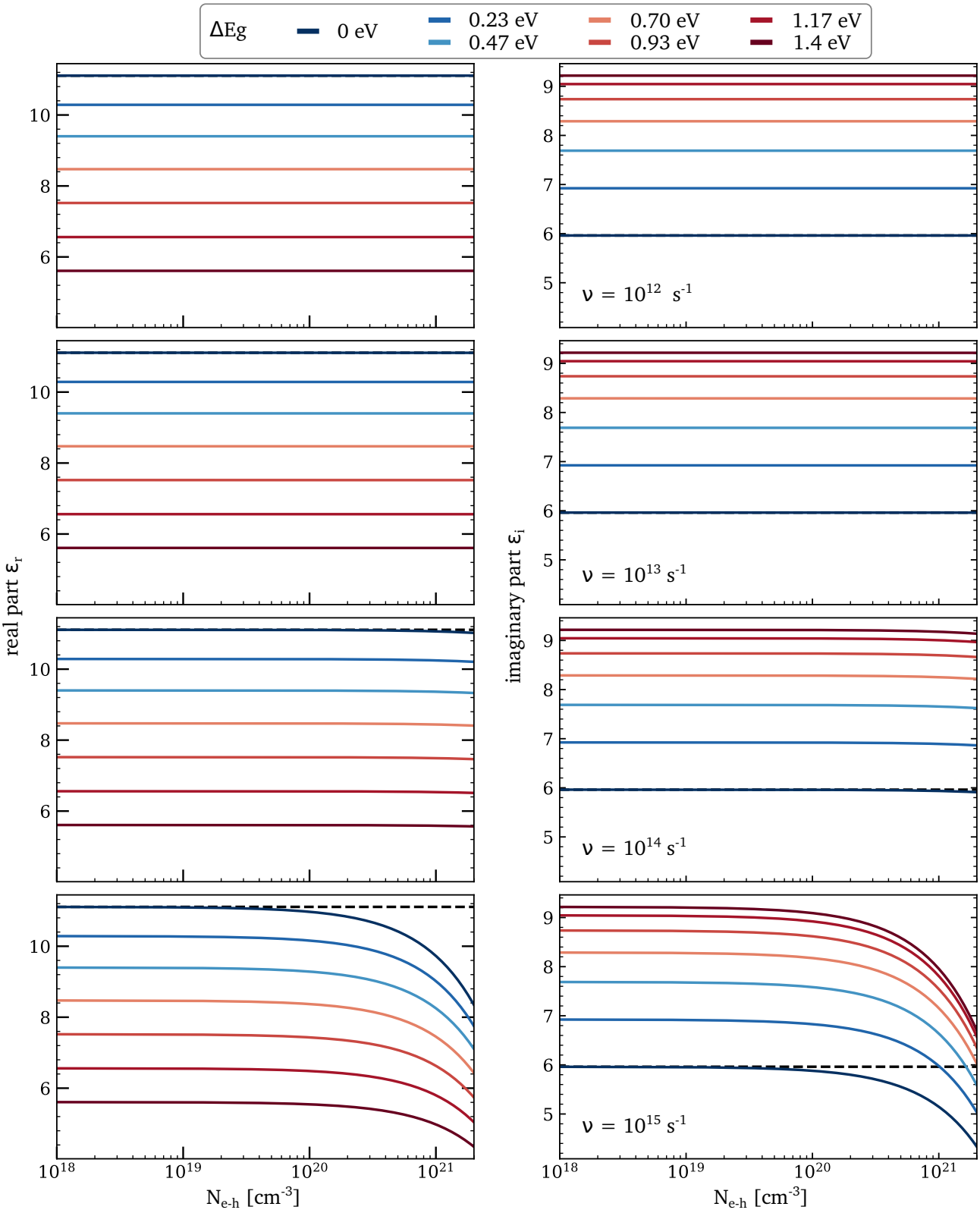

Figure D.3 – *Excited dielectric function at 532 nm for GSS. The horizontal dotted line shows the value of* $\varepsilon^{cold}(532\ nm) = 11.11 + 5.96i$.

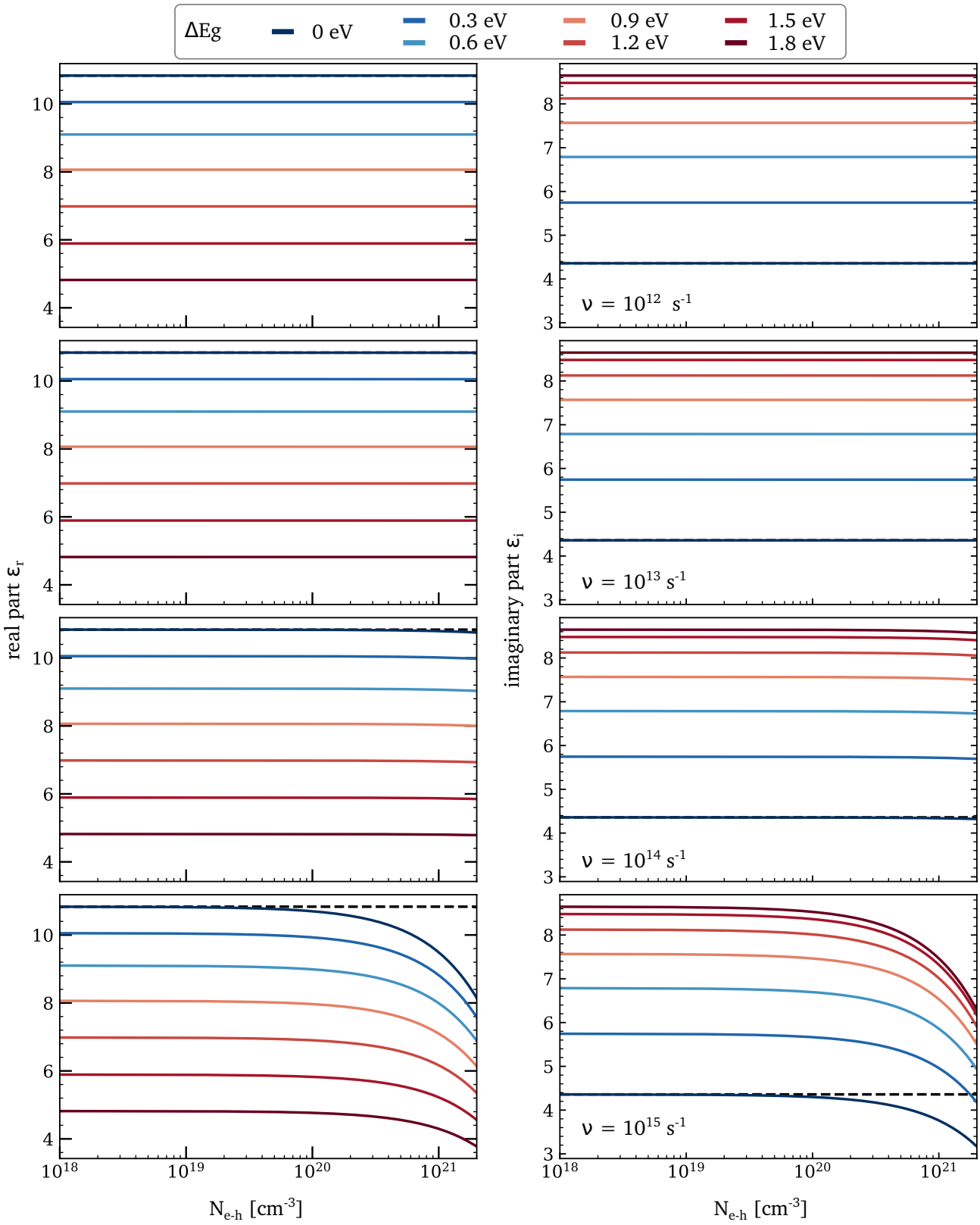

Figure D.4 – *Excited dielectric function at 532 nm for GSSN. The horizontal dotted line shows the value of* ε^{cold}*(532 nm) = 10.83 + 4.36i.*

V Tauc plot

To determine the band gap of the glasses, we fitted the data with a Tauc plot [66, 286–290]. The Tauc model links the energy E to the quantity αE (with α the absorption coefficient) under the form:

$$\alpha E = B(E - E_g)^m with m = \begin{cases} 1/2\text{: direct allowed transitions} \\ 3/2\text{: direct forbidden transitions} \\ 1/2\text{: indirect allowed transitions} \\ 3\text{: indirect forbidden transitions} \end{cases} \tag{D.1}$$

In our case, $m = 2$, with gives $(\alpha E)^{1/2} = B(E - E_g)$. Fitting with a $f = ax + b$ function would then retrieve E_g.

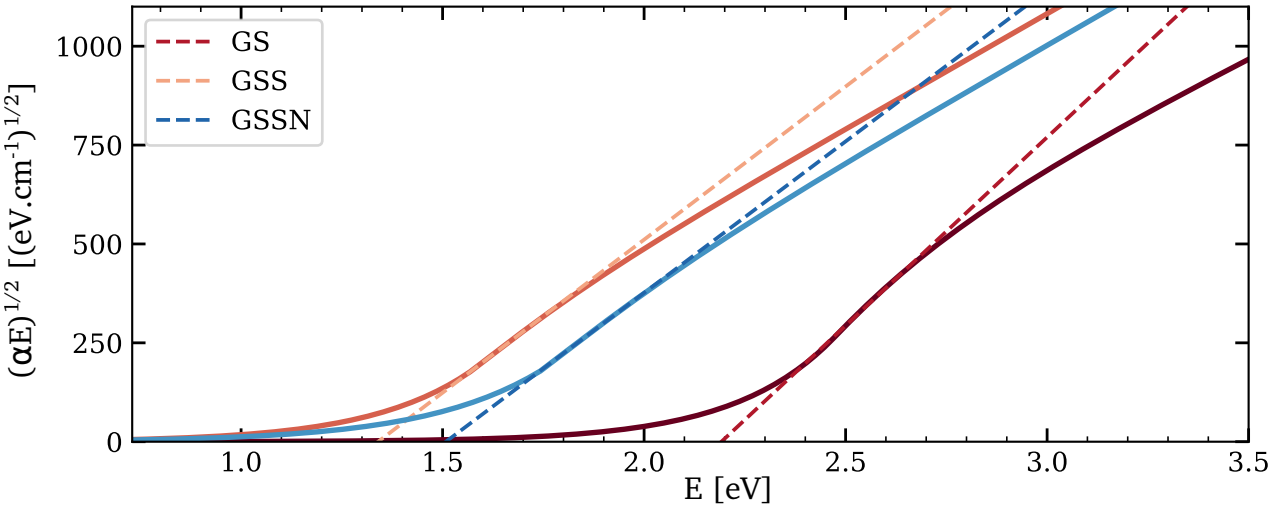

Figure D.5 – *Tauc model*

BIBLIOGRAPHY

[1] D. Reinsel, J. Gantz, J. Rydning, The Digitization of the World from Edge to Core, Technical report, **2018**.

[2] G. Kranz, Storage Class Memory, https://searchstorage.techtarget.com/definition/storage-class-memory, **2021**.

[3] G. W. Burr, B. N. Kurdi, J. C. Scott, C. H. Lam, K. Gopalakrishnan, R. S. Shenoy, *IBM Journal of Research and Development* **2008**, *52*, 4.5 449.

[4] G. W. Burr, R. M. Shelby, A. Sebastian, S. Kim, S. Kim, S. Sidler, K. Virwani, M. Ishii, P. Narayanan, A. Fumarola, L. L. Sanches, I. Boybat, M. Le Gallo, K. Moon, J. Woo, H. Hwang, Y. Leblebici, *Advances in Physics: X* **2017**, *2*, 1 89.

[5] J. von Neumann, *IEEE Annals of the History of Computing* **1993**, *15*, 4 27.

[6] T. Billy, Intel Launches Optane Memory M.2 Cache SSDs For Consumer Market, **2017**.

[7] G. W. Burr, R. S. Shenoy, K. Virwani, P. Narayanan, A. Padilla, B. Kurdi, H. Hwang, *Journal of Vacuum Science & Technology B, Nanotechnology and Microelectronics: Materials, Processing, Measurement, and Phenomena* **2014**, *32*, 4 040802.

[8] M. Wuttig, N. Yamada, *Nature Materials* **2007**, *6*, 11 824.

[9] P. Noé, C. Vallée, F. Hippert, F. Fillot, J.-Y. Raty, *Semiconductor Science and Technology* **2018**, *33*, 1 013002.

[10] C. Han, Q. Sun, Z. Li, S. X. Dou, *Advanced Energy Materials* **2016**, *6*, 15 1600498.

[11] Y. Shi, C. Sturm, H. Kleinke, *Journal of Solid State Chemistry* **2019**, *270* 273.

[12] A. Zakery, S. R. Elliott, *Journal of Non-Crystalline Solids* **2003**, *330*, 1 1.

[13] S. Dai, Y. Wang, X. Peng, P. Zhang, X. Wang, Y. Xu, *Applied Sciences* **2018**, *8*, 5 707.

[14] K. Tanaka, K. Shimakawa, *Amorphous Chalcogenide Semiconductors and Related Materials*, Springer New York Dordrecht Heidelberg London, **2011**.

[15] N. Mott, E. Davis, *Electronic Processes in On-Crystalline Materials*, Clarendon Oxford, 2nd edition edition, **1979**.

[16] J. C. Phillips, *Journal of Non-Crystalline Solids* **1980**, *35–36* 1157.

[17] S. Elliott, *Physics of Amorphous Materials*, Longman Scientific & Technical ; New York : Wiley, 2nd edition edition, **1990**.

[18] P. G. Debenetti, F. H. Stillinger, *Nature Insight Review Articles* **2001**, *410* 259.

[19] W. Kauzmann, *Chemical Reviews* **1948**, *43*, 2 219.

[20] S. R. Ovshinsky, *Physical Review Letters* **1968**, *21*, 20 1450.

[21] R. M. Shelby, S. Raoux, *Journal of Applied Physics* **2009**, *105*, 10 104902.

[22] S. Raoux, A. K. König, H.-Y. Cheng, D. Garbin, R. W. Cheek, J. L. Jordan-Sweet, M. Wuttig, *physica status solidi (b)* **2012**, *249*, 10 1999.

[23] A. Verdy, F. d'Acapito, J.-B. Dory, G. Navarro, M. Bernard, P. Noé, *physica status solidi (RRL) – Rapid Research Letters* **2020**, *14*, 5 1900548.

[24] W. Zhang, R. Mazzarello, M. Wuttig, E. Ma, *Nature Reviews Materials* **2019**, *4*, 3 150.

[25] M. Behrens, A. Lotnyk, J. W. Gerlach, M. Ehrhardt, P. Lorenz, B. Rauschenbach, *ACS Applied Materials & Interfaces* **2019**.

[26] H. Tanimura, S. Watanabe, T. Ichitsubo, *Advanced Functional Materials* **2020**, *30*, 31 2002821.

[27] K. S. Andrikopoulos, S. N. Yannopoulos, G. A. Voyiatzis, A. V. Kolobov, M. Ribes, J. Tominaga, *Journal of Physics: Condensed Matter* **2006**, *18*, 3 965.

[28] P. Zalden, M. J. Shu, F. Chen, X. Wu, Y. Zhu, H. Wen, S. Johnston, Z.-X. Shen, P. Landreman, M. Brongersma, S. W. Fong, H.-S. P. Wong, M.-J. Sher, P. Jost, M. Kaes, M. Salinga, A. von Hoegen, M. Wuttig, A. M. Lindenberg, *Physical Review Letters* **2016**, *117*, 6 067601.

[29] A. Pawbake, C. Bellin, L. Paulatto, K. Béneut, J. Biscaras, C. Narayana, D. J. Late, A. Shukla, *Physical Review Letters* **2019**, *122*, 14 145701.

[30] C. Bellin, A. Pawbake, L. Paulatto, K. Béneut, J. Biscaras, C. Narayana, A. Polian, D. J. Late, A. Shukla, *Physical Review Letters* **2020**, *125*, 14 145301.

[31] C. Yildirim, M. Micoulaut, P. Boolchand, I. Kantor, O. Mathon, J.-P. Gaspard, T. Irifune, J.-Y. Raty, *Scientific Reports* **2016**, *6*, 1 27317.

[32] M. Wuttig, V. L. Deringer, X. Gonze, C. Bichara, J.-Y. Raty, *Advanced Materials* **2018**, *30*, 51 1803777.

[33] J.-Y. Raty, M. Schumacher, P. Golub, V. L. Deringer, C. Gatti, M. Wuttig, *Advanced Materials* **2019**, *31*, 3 1806280.

[34] T. H. Lee, S. R. Elliott, *Advanced Materials* **2020**, *32*, 28 2000340.

[35] T. H. Lee, S. R. Elliott, *physica status solidi (RRL) – Rapid Research Letters* **2021**, *15*, 3 2000516.

[36] M. Micoulaut, H. Flores-Ruiz, A. Pradel, A. Piarristeguy, *physica status solidi (RRL) – Rapid Research Letters* **2021**, *15*, 3 2000490.

[37] J. Solis, C. Afonso, *Applied Physics A: Materials Science & Processing* **2003**, *76*, 3 331.

[38] C. V. Shank, R. Yen, C. Hirlimann, *Physical Review Letters* **1983**, *50*, 6 454.

[39] A. Rousse, C. Rischel, S. Fourmaux, I. Uschmann, S. Sebban, G. Grillon, P. Balcou, E. Förster, J. P. Geindre, P. Audebert, J. C. Gauthier, D. Hulin, *Nature* **2001**, *410*, 6824 65.

[40] C. W. Siders, *Science* **1999**, *286*, 5443 1340.

[41] M. Frumar, A. P. Firth, A. E. Owen, *Journal of Non-Crystalline Solids* **1995**, *192–193* 447.

[42] D. H. Reitze, H. Ahn, M. C. Downer, *Physical Review B* **1992**, *45*, 6 2677.

[43] S. V. Govorkov, T. Schröder, I. L. Shumay, P. Heist, *Physical Review B* **1992**, *46*, 11 6864.

[44] K. Sokolowski-Tinten, J. Solis, J. Bialkowski, J. Siegel, C. N. Afonso, D. von der Linde, *Physical Review Letters* **1998**, *81*, 17 3679.

[45] L. Waldecker, T. A. Miller, M. Rudé, R. Bertoni, J. Osmond, V. Pruneri, R. E. Simpson, R. Ernstorfer, S. Wall, *Nature Materials* **2015**, *14*, 10 991.

[46] A. Redaelli, editor, *Phase Change Memory*, Springer International Publishing, Cham, **2018**.

[47] P. Noé, A. Verdy, F. d'Acapito, J.-B. Dory, M. Bernard, G. Navarro, J.-B. Jager, J. Gaudin, J.-Y. Raty, *Science Advances* **2020**, *6*, 9 eaay2830.

[48] P. Martinez, I. Papagiannouli, D. Descamps, S. Petit, J. Marthelot, A. Lévy, B. Fabre, J.-B. Dory, N. Bernier, J.-Y. Raty, P. Noé, J. Gaudin, *Advanced Materials* **2020**, *32*, 38 2003032.

[49] A. Grolleau, F. Dorchies, N. Jourdain, K. Ta Phuoc, J. Gautier, B. Mahieu, P. Renaudin, V. Recoules, P. Martinez, L. Lecherbourg, *Physical Review Letters* **2021**, *127*, 27 275901.

[50] W. Wełnic, A. Pamungkas, R. Detemple, C. Steimer, S. Blügel, M. Wuttig, *Nature Materials* **2006**, *5*, 1 56.

[51] S. K. Sundaram, E. Mazur, *Nature Materials* **2002**, *1*, 4 217.

[52] B. Rethfeld, D. S. Ivanov, M. E. Garcia, S. I. Anisimov, *Journal of Physics D: Applied Physics* **2017**, *50*, 19 193001.

[53] A. Kaiser, B. Rethfeld, M. Vicanek, G. Simon, *Physical Review B* **2000**, *61*, 17 11437.

[54] W. Maes, K. De Meyer, R. Van Overstraeten, *Solid-State Electronics* **1990**, *33*, 6 705.

[55] S. I. Anisimov, B. L. Kapeliovich, T. L. Perel'man, *Zh. Eksp. Teor. Fiz.* **1974**, *66*, 2 375.

[56] T. J. Derrien, T. Sarnet, M. Sentis, T. E. Itina, *Journal of Optoelectronics and Advanced Materials* **2010**, *12*, 3 610.

[57] T. Shin, S. W. Teitelbaum, J. Wolfson, M. Kandyla, K. A. Nelson, *The Journal of Chemical Physics* **2015**, *143*, 19 194705.

[58] Z. Lin, L. V. Zhigilei, V. Celli, *Physical Review B* **2008**, *77*, 7 075133.

[59] B. Holst, V. Recoules, S. Mazevet, M. Torrent, A. Ng, Z. Chen, S. E. Kirkwood, V. Sametoglu, M. Reid, Y. Y. Tsui, *Physical Review B* **2014**, *90*, 3 035121.

[60] T. A. Miller, M. Rudé, V. Pruneri, S. Wall, *Physical Review B* **2016**, *94*, 2 024301.

[61] J. Siegel, W. Gawelda, D. Puerto, C. Dorronsoro, J. Solis, C. N. Afonso, J. C. G. de Sande, R. Bez, A. Pirovano, C. Wiemer, *Journal of Applied Physics* **2008**, *103*, 2 023516.

[62] J. P. Callan, A. M.-T. Kim, C. A. D. Roeser, E. Mazur, J. Solis, J. Siegel, C. N. Afonso, J. C. G. de Sande, *Physical Review Letters* **2001**, *86*, 16 3650.

[63] K. Shportko, S. Kremers, M. Woda, D. Lencer, J. Robertson, M. Wuttig, *Nature Materials* **2008**, *7*, 8 653.

[64] M. Konishi, H. Santo, Y. Hongo, K. Tajima, M. Hosoi, T. Saiki, *Applied Optics* **2010**, *49*, 18 3470.

[65] F. Deneuville, Ph.D. thesis, Bordeaux, **2013**.

[66] J.-B. Dory, C. Castro-Chavarria, A. Verdy, J.-B. Jager, M. Bernard, C. Sabbione, M. Tessaire, J.-M. Fédéli, A. Coillet, B. Cluzel, P. Noé, *Scientific Reports* **2020**, *10*, 1 11894.

[67] A. V. Kolobov, P. Fons, A. I. Frenkel, A. L. Ankudinov, J. Tominaga, T. Uruga, *Nature Materials* **2004**, *3*, 10 703.

[68] A. A. Bunaciu, E. gabriela Udriştioiu, H. Y. Aboul-Enein, *Critical Reviews in Analytical Chemistry* **2015**, *45*, 4 289.

[69] H. Weber, M. Schumacher, P. Jóvári, Y. Tsuchiya, W. Skrotzki, R. Mazzarello, I. Kaban, *Physical Review B* **2017**, *96*, 5 054204.

[70] M. Wuttig, D. Lüsebrink, D. Wamwangi, W. Wełnic, M. Gilleßen, R. Dronskowski, *Nature Materials* **2007**, *6*, 2 122.

[71] P. Jost, H. Volker, A. Poitz, C. Poltorak, P. Zalden, T. Schäfer, F. R. L. Lange, R. M. Schmidt, B. Holländer, M. R. Wirtssohn, M. Wuttig, *Advanced Functional Materials* **2015**, *25*, 40 6399.

[72] P. Zalden, F. Quirin, M. Schumacher, J. Siegel, S. Wei, A. Koc, M. Nicoul, M. Trigo, P. Andreasson, H. Enquist, M. J. Shu, T. Pardini, M. Chollet, D. Zhu, H. Lemke, I. Ronneberger, J. Larsson, A. M. Lindenberg, H. E. Fischer, S. Hau-Riege, D. A. Reis, R. Mazzarello, M. Wuttig, K. Sokolowski-Tinten, *Science* **2019**, *364*, 6445 1062.

[73] M. Fabian, N. Dulgheru, K. Antonova, A. Szekeres, M. Gartner, *Advances in Condensed Matter Physics* **2018**, *2018* 1.

[74] Ashcroft, Mermin, *Solid State Physics*, Saunders College Publishing, **1976**.

[75] P. H. Fuoss, P. Eisenberger, W. K. Warburton, A. Bienenstock, *Physical Review Letters* **1981**, *46*, 23 1537.

[76] M. T. M. Shatnawi, C. L. Farrow, P. Chen, P. Boolchand, A. Sartbaeva, M. F. Thorpe, S. J. L. Billinge, *Physical Review B* **2008**, *77*, 9 094134.

[77] S. Kohara, K. Kato, S. Kimura, H. Tanaka, T. Usuki, K. Suzuya, H. Tanaka, Y. Moritomo, T. Matsunaga, N. Yamada, Y. Tanaka, H. Suematsu, M. Takata, *Applied Physics Letters* **2006**, *89*, 20 201910.

[78] P. Jóvári, I. Kaban, W. Hoyer, R. G. Delaplane, A. Wannberg, *Journal of Physics: Condensed Matter* **2005**, *17*, 10 1529.

[79] T. Chattopadhyay, J. X. Boucherle, H. G. vonSchnering, *Journal of Physics C: Solid State Physics* **1987**, *20*, 10 1431.

[80] P. S. Salmon, I. Petri, *Journal of Physics: Condensed Matter* **2003**, *15*, 16 S1509.

[81] J. Y. Raty, V. V. Godlevsky, J. P. Gaspard, C. Bichara, M. Bionducci, R. Bellissent, R. Céolin, J. R. Chelikowsky, P. Ghosez, *Physical Review B* **2002**, *65*, 11 115205.

[82] C. Bergman, C. Bichara, J. P. Gaspard, Y. Tsuchiya, *Physical Review B* **2003**, *67*, 10 104202.

[83] P. Jóvári, A. Piarristeguy, R. Escalier, I. Kaban, J. Bednarčik, A. Pradel, *Journal of Physics: Condensed Matter* **2013**, *25*, 19 195401.

[84] I. Petri, P. S. Salmon, H. E. Fischer, *Physical Review Letters* **2000**, *84*, 11 2413.

[85] M.-V. Coulet, D. Testemale, J.-L. Hazemann, J.-P. Gaspard, C. Bichara, *Physical Review B* **2005**, *72*, 17 174209.

[86] E. Matsubara, S. Okada, T. Ichitsubo, T. Kawaguchi, A. Hirata, P. F. Guan, K. Tokuda, K. Tanimura, T. Matsunaga, M. W. Chen, N. Yamada, *Physical Review Letters* **2016**, *117*, 13.

[87] J. J. Rehr, R. C. Albers, *Reviews of Modern Physics* **2000**, *72*, 3 621.

[88] F. Dorchies, V. Recoules, *Physics Reports* **2016**, *657* 1.

[89] W. Zhou, M. Paesler, D. E. Sayers, *Physical Review B* **1991**, *43*, 3 2315.

[90] P. Fons, H. Osawa, A. V. Kolobov, T. Fukaya, M. Suzuki, T. Uruga, N. Kawamura, H. Tanida, J. Tominaga, *Physical Review B* **2010**, *82*, 4 041203.

[91] D. A. Baker, M. A. Paesler, G. Lucovsky, S. C. Agarwal, P. C. Taylor, *Physical Review Letters* **2006**, *96*, 25 255501.

[92] P. Noé, C. Sabbione, N. Castellani, G. Veux, G. Navarro, V. Sousa, F. Hippert, F. d'Acapito, *Journal of Physics D: Applied Physics* **2016**, *49*, 3 035305.

[93] A. V. Kolobov, M. Krbal, P. Fons, J. Tominaga, T. Uruga, *Nature Chemistry* **2011**, *3*, 4 311.

[94] M. Krbal, A. V. Kolobov, P. Fons, J. Tominaga, S. R. Elliott, J. Hegedus, A. Giussani, K. Perumal, R. Calarco, T. Matsunaga, N. Yamada, K. Nitta, T. Uruga, *Physical Review B* **2012**, *86*, 4.

[95] T. Siegrist, P. Jost, H. Volker, M. Woda, P. Merkelbach, C. Schlockermann, M. Wuttig, *Nature Materials* **2011**, *10*, 3 202.

[96] P. Fons, T. Matsunaga, A. V. Kolobov, M. Krbal, J. Tominaga, N. Yamada, *physica status solidi (b)* **2012**, *249*, 10 1919.

[97] P. Fons, A. V. Kolobov, M. Krbal, J. Tominaga, K. S. Andrikopoulos, S. N. Yannopoulos, G. A. Voyiatzis, T. Uruga, *Physical Review B* **2010**, *82*, 15 155209.

[98] J. Akola, R. O. Jones, *Physical Review B* **2007**, *76*, 23 235201.

[99] E. Steigmeier, G. Harbeke, *Solid State Communications* **1970**, *8*, 16 1275.

[100] K. M. Rabe, J. D. Joannopoulos, *Physical Review B* **1987**, *36*, 12 6631.

[101] T. Chatterji, S. Rols, U. D. Wdowik, *Frontiers of Physics* **2019**, *14*, 2 23601.

[102] H. Wiedemeier, P. A. Siemers, *Zeitschrift für anorganische und allgemeine Chemie* **1977**, *431*, 1 299.

[103] J.-P. Gaspard, *Comptes Rendus Physique* **2016**, *17*, 3 389.

[104] B. R. Judd, *Canadian Journal of Physics* **1974**, *52*, 11 999.

[105] R. E. Peierls, *Quantum Theory of Solids*, Oxford university press edition, **1955**.

[106] J.-P. Gaspard, A. Pellegatti, F. Marinelli, C. Bichara, *Philisophical Magazine B* **1998**, *77*, 3 727.

[107] M. Fowler, Electrons in One Dimension : The Peierls Transition, **2-28-07**.

[108] P. W. Anderson, P. A. Lee, M. Saitoh, *Solid State Communications* **1973**, *13*, 5 595.

[109] J. Akola, R. O. Jones, *physica status solidi (b)* **2012**, *249*, 10 1851.

[110] S. Raoux, H.-Y. Cheng, M. A. Caldwell, H.-S. P. Wong, *Applied Physics Letters* **2009**, *95*, 7 071910.

[111] R. De Bastiani, E. Carria, S. Gibilisco, M. G. Grimaldi, A. R. Pennisi, A. Gotti, A. Pirovano, R. Bez, E. Rimini, *Physical Review B* **2009**, *80*, 24 245205.

[112] J. Akola, J. Larrucea, R. O. Jones, *Physical Review B* **2011**, *83*, 9.

[113] J. Y. Raty, W. Zhang, J. Luckas, C. Chen, R. Mazzarello, C. Bichara, M. Wuttig, *Nature Communications* **2015**, *6*, 1 7467.

[114] Y. Maeda, M. Wakagi, *Japanese Journal of Applied Physics* **1991**, *30*, Part 1, No. 1 101.

[115] J. R. Stellhorn, S. Hosokawa, W.-C. Pilgrim, N. Blanc, N. Boudet, H. Tajiri, S. Kohara, *physica status solidi (b)* **2016**, *253*, 6 1038.

[116] M. Micoulaut, A. Piarristeguy, H. Flores-Ruiz, A. Pradel, *Physical Review B* **2017**, *96*, 18 184204.

[117] J. van Eijk, Ph.D. thesis, **2010**.

[118] G. E. Ghezzi, J. Y. Raty, S. Maitrejean, A. Roule, E. Elkaim, F. Hippert, *Applied Physics Letters* **2011**, *99*, 15 151906.

[119] J. Akola, R. O. Jones, *Physical Review Letters* **2008**, *100*, 20 205502.

[120] J. Hegedüs, S. R. Elliott, *Nature Materials* **2008**, *7*, 5 399.

[121] S. Raoux, R. M. Shelby, J. Jordan-Sweet, B. Munoz, M. Salinga, Y.-C. Chen, Y.-H. Shih, E.-K. Lai, M.-H. Lee, *Microelectronic Engineering* **2008**, *85*, 12 2330.

[122] C. Bichara, M. Johnson, J. Y. Raty, *Physical Review Letters* **2005**, *95*, 26 267801.

[123] Y. Kawakita, Y. Kato, S. Tahara, H. Fujii, S. Takeda, K. Maruyama, *Journal of Non-Crystalline Solids* **2007**, *353*, 18 1999.

[124] C. Otjacques, J.-Y. Raty, J.-P. Gaspard, Y. Tsuchiya, C. Bichara, *École thématique de la Société Française de la Neutronique* **2011**, *12* 233.

[125] Y.-X. Zhou, H.-Y. Zhang, V. L. Deringer, W. Zhang, *physica status solidi (RRL) – Rapid Research Letters* **2020**, 2000403.

[126] S. Wei, P. Lucas, C. A. Angell, *MRS Bulletin* **2019**, *44*, 9 691.

[127] M. Micoulaut, M.-V. Coulet, A. Piarristeguy, M. R. Johnson, G. J. Cuello, C. Bichara, J.-Y. Raty, H. Flores-Ruiz, A. Pradel, *Physical Review B* **2014**, *89*, 17 174205.

[128] Y. Tsuchiya, *Journal of the Physical Society of Japan* **1991**, *60*, 1 227.

[129] P. G. Debenedetti, *Journal of Physics : Condensed Matter* **2003**, *15* R1669.

[130] S. Sen, R. L. Andrus, D. E. Baker, M. T. Murtagh, *Physical Review Letters* **2004**, *93*, 12 125902.

[131] J. Y. Raty, V. Godlevsky, P. Ghosez, C. Bichara, J. P. Gaspard, J. R. Chelikowsky, *Physical Review Letters* **2000**, *85*, 9 1950.

[132] K. Chebli, J. Saiter, J. Grenet, A. Hamou, G. Saffarini, *Physica B: Condensed Matter* **2001**, *304*, 1-4 228.

[133] G. C. Sosso, J. Behler, M. Bernasconi, *physica status solidi (b)* **2012**, *249*, 10 1880.

[134] P. Zalden, A. von Hoegen, P. Landreman, M. Wuttig, A. M. Lindenberg, *Chemistry of Materials* **2015**, *27*, 16 5641.

[135] D. Lencer, M. Salinga, B. Grabowski, T. Hickel, J. Neugebauer, M. Wuttig, *Nature Materials* **2008**, *7*, 12 972.

[136] K. Maruyama, M. Inui, S. Takeda, S. Tamaki, Y. Kawakita, *Physica B: Condensed Matter* **1995**, *213–214* 558.

[137] N. Ramesh Rao, P. S. R. Krishna, S. Basu, B. A. Dasannacharya, K. S. Sangunni, E. S. R. Gopal, *Journal of Non-Crystalline Solids* **1998**, *240*, 1 221.

[138] E. Bychkov, C. J. Benmore, D. L. Price, *Physical Review B* **2005**, *72*, 17 172107.

[139] R. W. Fawcett, C. N. J. Wagner, G. S. Cargill, *Journal of Non-Crystalline Solids* **1972**, *8–10* 369.

[140] O. Uemura, Y. Sagara, T. Satow, *physica status solidi (a)* **1974**, *26*, 1 99.

[141] J. C. Malaurent, J. Dixmier **1980**, 6.

[142] M. M. Hafiz, F. H. Hammad, N. A. El-Kabany, *Physica B: Condensed Matter* **1993**, *183*, 4 392.

[143] Y. Wang, E. Ohata, S. Hosokawa, M. Sakurai, E. Matsubara, *Journal of Non-Crystalline Solids* **2004**, *337*, 1 54.

[144] P. Tronc, M. Bensoussan, A. Brenac, C. Sebenne, *Physical Review B* **1973**, *8*, 12 5947.

[145] S. Sugai, *Physical Review B* **1987**, *35*, 3 1345.

[146] X. Feng, W. J. Bresser, P. Boolchand, *Physical Review Letters* **1997**, *78*, 23 4422.

[147] Y. Wang, O. Matsuda, K. Inoue, O. Yamamuro, T. Matsuo, K. Murase, *Journal of Non-Crystalline Solids* **1998**, *232–234* 702.

[148] S. Onari, K. Matsuishi, T. Arai, *Journal of Non-Crystalline Solids* **1985**, *77–78* 1121.

[149] E. Gulbrandsen, H. B. Johnsen, M. Endregaard, T. Grande, S. Stølen, *Journal of Solid State Chemistry* **1999**, *145*, 1 253.

[150] B. Bureau, J. Troles, M. Le Floch, P. Guénot, F. Smektala, J. Lucas, *Journal of Non-Crystalline Solids* **2003**, *319*, 1 145.

[151] P. Lucas, E. A. King, O. Gulbiten, J. L. Yarger, E. Soignard, B. Bureau, *Physical Review B* **2009**, *80*, 21 214114.

[152] S. Sen, Z. Gan, *Journal of Non-Crystalline Solids* **2010**, *356*, 28 1519.

[153] E. L. Gjersing, S. Sen, R. E. Youngman, *Physical Review B* **2010**, *82*, 1 014203.

[154] M. Micoulaut, A. Kachmar, M. Bauchy, S. Le Roux, C. Massobrio, M. Boero, *Physical Review B* **2013**, *88*, 5 054203.

[155] K. Arne, *Acta Chemica Scandinavica* **1964**, *18* 2379.

[156] J.-Y. Raty, P. Noé, *physica status solidi (RRL) – Rapid Research Letters* **2020**, *14*, 5 1900581.

[157] C. Yildirim, J.-Y. Raty, M. Micoulaut, *The Journal of Chemical Physics* **2016**, *144*, 22 224503.

[158] P. S. Salmon, *Journal of Non-Crystalline Solids* **2007**, *353*, 32 2959.

[159] C. Massobrio, A. Pasquarello, *Journal of Physics: Condensed Matter* **2007**, *19*, 41 415111.

[160] S. Bordas, M. T. Clavaguera-Mora, B. Legendre, *Thermochimica Acta* **1982**, *56*, 2 161.

[161] A. B. Gokhale, R. Abbaschian, *Bulletin of Alloy Phase Diagrams* **1990**, *11*, 3 257.

[162] H. Okamoto, *Journal of Phase Equilibria* **2000**, *21*, 3.

[163] J. Barták, P. Koštál, V. Podzemná, J. Shánělová, J. Málek, *The Journal of Physical Chemistry B* **2016**, *120*, 32 7998.

[164] S. Martinková, J. Barták, P. Koštál, J. Málek, H. Segawa, *The Journal of Physical Chemistry B* **2017**, *121*, 33 7978.

[165] K. Maruyama, M. Misawa, M. Inui, S. Takeda, Y. Kawakita, S. Tamaki, *Journal of Non-Crystalline Solids* **1996**, *205–207* 106.

[166] W. A. Crichton, M. Mezouar, T. Grande, S. Stølen, A. Grzechnik, *Nature* **2001**, *414*, 6864 622.

[167] I. V. Karpov, M. Mitra, D. Kau, G. Spadini, Y. A. Kryukov, V. G. Karpov, *Journal of Applied Physics* **2007**, *102*, 12 124503.

[168] P. Fantini, S. Brazzelli, E. Cazzini, A. Mani, *Applied Physics Letters* **2012**, *100*, 1 013505.

[169] F. Zipoli, D. Krebs, A. Curioni, *Physical Review B* **2016**, *93*, 11 115201.

[170] D. Ielmini, M. Boniardi, A. L. Lacaita, A. Redaelli, A. Pirovano, *Microelectronic Engineering* **2009**, *86*, 7 1942.

[171] M. Wimmer, M. Kaes, C. Dellen, M. Salinga, *Frontiers in Physics* **2014**, *2* 75.

[172] M. Le Gallo, A. Athmanathan, D. Krebs, A. Sebastian, *Journal of Applied Physics* **2016**, *119*, 2 025704.

[173] D. Krebs, T. Bachmann, P. Jonnalagadda, L. Dellmann, S. Raoux, *New Journal of Physics* **2014**, *16*, 4 043015.

[174] J. Luckas, A. Piarristeguy, G. Bruns, P. Jost, S. Grothe, R. M. Schmidt, C. Longeaud, M. Wuttig, *Journal of Applied Physics* **2013**, *113*, 2 023704.

[175] M. Durandurdu, D. A. Drabold, N. Mousseau, *Physical Review B* **2000**, *62*, 23 15307.

[176] Y. Pan, F. Inam, M. Zhang, D. A. Drabold, *Physical Review Letters* **2008**, *100*, 20 206403.

[177] S. Gabardi, S. Caravati, G. C. Sosso, J. Behler, M. Bernasconi, *Physical Review B* **2015**, *92*, 5 054201.

[178] K. Kim, J.-C. Park, J.-G. Chung, S. A. Song, M.-C. Jung, Y. M. Lee, H.-J. Shin, B. Kuh, Y. Ha, J.-S. Noh, *Applied Physics Letters* **2006**, *89*, 24 243520.

[179] Z. Sun, J. Zhou, H.-J. Shin, A. Blomqvist, R. Ahuja, *Applied Physics Letters* **2008**, *93*, 24 241908.

[180] Y. M. Lee, H. J. Shin, S. J. Choi, J. H. Oh, H. S. Jeong, K. Kim, M. C. Jung, *Current Applied Physics* **2011**, *11*, 3 710.

[181] A. V. Kolobov, P. Fons, B. Hyot, B. André, J. Tominaga, Y. Tamenori, H. Yoshikawa, K. Kobayashi, *Applied Physics Letters* **2012**, *100*, 6 061910.

[182] J.-Y. Raty, P. Noé, G. Ghezzi, S. Maîtrejean, C. Bichara, F. Hippert, *Physical Review B* **2013**, *88*, 1.

[183] G. Betti Beneventi, L. Perniola, V. Sousa, E. Gourvest, S. Maitrejean, J. C. Bastien, A. Bastard, B. Hyot, A. Fargeix, C. Jahan, J. F. Nodin, A. Persico, A. Fantini, D. Blachier, A. Toffoli, S. Loubriat, A. Roule, S. Lhostis, H. Feldis, G. Reimbold, T. Billon, B. De Salvo, L. Larcher, P. Pavan, D. Bensahel, P. Mazoyer, R. Annunziata, P. Zuliani, F. Boulanger, *Solid-State Electronics* **2011**, *65–66* 197.

[184] E. Cho, Y. Youn, S. Han, *Applied Physics Letters* **2011**, *99*, 18 183501.

[185] W. Zhou, L. Wu, X. Zhou, F. Rao, Z. Song, D. Yao, W. Yin, S. Song, B. Liu, B. Qian, S. Feng, *Applied Physics Letters* **2014**, *105*, 24 243113.

[186] G. Wang, Q. Nie, X. Shen, R. P. Wang, L. Wu, J. Fu, T. Xu, S. Dai, *Applied Physics Letters* **2012**, *101*, 5 051906.

[187] Y. Zhu, Z. Zhang, S. Song, H. Xie, Z. Song, X. Li, L. Shen, L. Li, L. Wu, B. Liu, *Materials Research Bulletin* **2015**, *64* 333.

[188] B. Huang, *physica status solidi (b)* **2015**, *252*, 2 431.

[189] J. Solis, C. N. Afonso, S. C. W. Hyde, N. P. Barry, P. M. W. French, *Physical Review Letters* **1996**, *76*, 14 2519.

[190] H. Jeschke, Ph.D. thesis, Freien Universität Berlin, **2000**.

[191] D. H. Auston, J. A. Golovchenko, P. R. Smith, C. M. Surko, T. N. C. Venkatesan, *Applied Physics Letters* **1978**, *33*, 6 539.

[192] J. A. Van Vechten, R. Tsu, F. W. Saris, *Physics Letters A* **1979**, *74*, 6 422.

[193] D. von der Linde, N. Fabricius, *Applied Physics Letters* **1982**, *41*, 10 991.

[194] J. M. Liu, H. Kurz, N. Bloembergen, *Applied Physics Letters* **1982**, *41*, 7 643.

[195] A. V. Kolobov, P. Fons, J. Tominaga, *physica status solidi (b)* **2014**, *251*, 7 1297.

[196] M. Hada, W. Oba, M. Kuwahara, I. Katayama, T. Saiki, J. Takeda, K. G. Nakamura, *Scientific Reports* **2015**, *5*, 1 13530.

[197] R. Gu, T. Perrault, V. Juvé, G. Vaudel, M. Weis, A. Bulou, N. Chigarev, A. Levchuk, S. Raetz, V. Gusev, Z. Cheng, H. Bhaskaran, P. Ruello, *Physical Review Applied* **2021**, *16*, 1 014055.

[198] X.-B. Li, X. Q. Liu, X. D. Han, S. B. Zhang, *physica status solidi (b)* **2012**, *249*, 10 1861.

[199] X.-B. Li, X. Q. Liu, X. Liu, D. Han, Z. Zhang, X. D. Han, H.-B. Sun, S. B. Zhang, *Physical Review Letters* **2011**, *107*, 1 015501.

[200] C. Lang, S. A. Song, D. N. Manh, D. J. H. Cockayne, *Physical Review B* **2007**, *76*, 5 054101.

[201] B. Huang, J. Robertson, *Physical Review B* **2010**, *81*, 8.

[202] W. H. Zachariasen, *Journal of the American Chemical Society* **1932**, *54*, 10 3841.

[203] G. Lucovsky, R. M. White, *Physical Review B* **1973**, *8*, 2 660.

[204] M. Zhu, O. Cojocaru-Mirédin, A. M. Mio, J. Keutgen, M. Küpers, Y. Yu, J.-Y. Cho, R. Dronskowski, M. Wuttig, *Advanced Materials* **2018**, *30*, 18 1706735.

[205] I. Ronneberger, Z. Zanolli, M. Wuttig, R. Mazzarello, *Advanced Materials* **2020**, *32*, 29 2001033.

[206] J.-Y. Raty, M. Wuttig, *Journal of Physics D: Applied Physics* **2020**, *53*, 23 234002.

[207] J. Hempelmann, P. C. Müller, P. M. Konze, R. P. Stoffel, S. Steinberg, R. Dronskowski, *Advanced Materials* **2021**, *33*, 37 2100163.

[208] H. Nakashima, H. Nakatsuji, *The Journal of Chemical Physics* **2007**, *127*, 22 224104.

[209] M. Born, R. Oppenheimer, *Annalen der Physik* **1927**, *389*, 20 457.

[210] B. H. Bransden, C. J. Joachain, *Physics of Atoms and Molecules*, Pearson Education, second edition, **2003**.

[211] Fermi, *Rendiconti dell Accademia Nazionale dei Lincei* **1927**, *6*, 602-607 32.

[212] L. H. Thomas, *Mathematical Proceedings of the Cambridge Philosophical Society* **1927**, *23*, 5 542.

[213] P. Hohenberg, W. Kohn, *Physical Review* **1964**, *136*, 3B B864.

[214] W. Kohn, L. J. Sham, *Physical Review* **1965**, *140*, 4A A1133.

[215] J. P. Perdew, A. Zunger, *Physical Review B* **1981**, *23*, 10 5048.

[216] T. Yanai, D. P. Tew, N. C. Handy, *Chemical Physics Letters* **2004**, *393*, 1-3 51.

[217] J. P. Perdew, K. Burke, Y. Wang, *Physical Review B* **1996**, *54*, 23 16533.

[218] J. P. Perdew, K. Burke, M. Ernzerhof, *Physical Review Letters* **1996**, *77*, 18 3865.

[219] J. Heyd, G. E. Scuseria, M. Ernzerhof, *The Journal of Chemical Physics* **2003**, *118*, 18 8207.

[220] R. Martin, *Electronic Structure : Basic Theory and Practical Methods*, Cambridge University Press, **2004**.

[221] D. M. Ceperley, B. J. Alder, *Physical Review Letters* **1980**, *45*, 7 566.

[222] D. Ceperley, *Physical Review B* **1978**, *18*, 7 3126.

[223] J. P. Perdew, A. Ruzsinszky, G. I. Csonka, O. A. Vydrov, G. E. Scuseria, L. A. Constantin, X. Zhou, K. Burke, *Physical Review Letters* **2008**, *100*, 13 136406.

[224] B. Hammer, L. B. Hansen, J. K. Nørskov, *Physical Review B* **1999**, *59*, 11 7413.

[225] R. Armiento, A. E. Mattsson, *Physical Review B* **2005**, *72*, 8 085108.

[226] L. J. Sham, M. Schlüter, *Physical Review Letters* **1983**, *51*, 20 1888.

[227] R. W. Godby, M. Schlüter, L. J. Sham, *Physical Review Letters* **1986**, *56*, 22 2415.

[228] L. J. Sham, M. Schlüter, *Physical Review B* **1985**, *32*, 6 3883.

[229] T. Van Voorhis, G. E. Scuseria, *The Journal of Chemical Physics* **1998**, *109*, 2 400.

[230] J. P. Perdew, S. Kurth, A. Zupan, P. Blaha, *Physical Review Letters* **1999**, *82*, 12 2544.

[231] P. J. Stephens, F. J. Devlin, C. S. Ashvar, C. F. Chabalowski, M. J. Frisch, *Faraday Discussions* **1994**, *99* 103.

[232] G. Kresse, J. Furthmüller, *Computational Materials Science* **1996**, *6*, 1 15.

[233] G. Kresse, J. Furthmuller, *Physical Review B* **1996**, *54*, 16 1169.

[234] J. Hafner, *Journal of Computational Chemistry* **2008**, *29*, 13 2044.

[235] Davidson, *Methods in Computational Molecular Physics*, volume 113 of *NATO Advanced Study Institute, Series C*, Plenum new-york edition, **1983**.

[236] M. P. Teter, M. C. Payne, D. C. Allan, *Physical Review B* **1989**, *40*, 18 12255.

[237] P. Pulay, *Chemical Physics Letters* **1980**, *73*, 2 393.

[238] D. M. Wood, A. Zunger, *Journal of Physics A: Mathematical and General* **1985**, *18*, 9 1343.

[239] M. C. Payne, M. P. Teter, D. C. Allan, T. A. Arias, J. D. Joannopoulos, *Reviews of Modern Physics* **1992**, *64*, 4 1045.

[240] D. R. Hamann, M. Schlüter, C. Chiang, *Physical Review Letters* **1979**, *43*, 20 1494.

[241] D. Vanderbilt, *Physical Review B* **1990**, *41*, 11 7892.

[242] P. E. Blöchl, *Physical Review B* **1994**, *50*, 24 17953.

[243] G. Kresse, D. Joubert, *Physical Review B* **1999**, *59*, 3 1758.

[244] R. Car, M. Parrinello, *Physical Review Letters* **1985**, *55*, 22 2471.

[245] T. D. Kühne, M. Krack, F. R. Mohamed, M. Parrinello, *Physical Review Letters* **2007**, *98*, 6 066401.

[246] J. Hutter, M. Iannuzzi, F. Schiffmann, J. VandeVondele, *Wiley Interdisciplinary Reviews: Computational Molecular Science* **2014**, *4*, 1 15.

[247] J. VandeVondele, M. Krack, F. Mohamed, M. Parrinello, T. Chassaing, J. Hutter, *Computer Physics Communications* **2005**, *167*, 2 103.

[248] S. Goedecker, M. Teter, J. Hutter, *Physical Review B* **1996**, *54*, 3 1703.

[249] K. Lee, É. D. Murray, L. Kong, B. I. Lundqvist, D. C. Langreth, *Physical Review B* **2010**, *82*, 8 081101.

[250] P. Giannozzi, S. Baroni, N. Bonini, M. Calandra, R. Car, C. Cavazzoni, D. Ceresoli, G. L. Chiarotti, M. Cococcioni, I. Dabo, A. Dal Corso, S. de Gironcoli, S. Fabris, G. Fratesi, R. Gebauer, U. Gerstmann, C. Gougoussis, A. Kokalj, M. Lazzeri, L. Martin-Samos, N. Marzari, F. Mauri, R. Mazzarello, S. Paolini, A. Pasquarello, L. Paulatto, C. Sbraccia, S. Scandolo, G. Sclauzero, A. P. Seitsonen, A. Smogunov, P. Umari, R. M. Wentzcovitch, *Journal of Physics: Condensed Matter* **2009**, *21*, 39 395502.

[251] A. V. Kolobov, P. Fons, J. Tominaga, M. Hase, *The Journal of Physical Chemistry C* **2014**, *118*, 19 10248.

[252] C. Lian, S. B. Zhang, S. Meng, *Physical Review B* **2016**, *94*, 18 184310.

[253] X.-P. Wang, X.-B. Li, N.-K. Chen, J. Bang, R. Nelson, C. Ertural, R. Dronskowski, H.-B. Sun, S. Zhang, *npj Computational Materials* **2020**, *6*, 1 1.

[254] N. D. Mermin, *Physical Review* **1965**, *137*, 5A A1441.

[255] M. Gajdoš, K. Hummer, G. Kresse, J. Furthmüller, F. Bechstedt, *Physical Review B* **2006**, *73*, 4 045112.

[256] S. Le Roux, P. Jund, *Computational Materials Science* **2010**, *49*, 1 70.

[257] C. Bichara, A. Pellegatti, J.-P. Gaspard, *Physical Review B* **1993**, *47*, 9 5002.

[258] U. R. Pedersen, Ph.D. thesis, Roskilde University, **2009**.

[259] E. Bévillon, J. P. Colombier, V. Recoules, H. Zhang, C. Li, R. Stoian, *Physical Review B* **2016**, *93*, 16 165416.

[260] M. Hase, P. Fons, K. Mitrofanov, A. V. Kolobov, J. Tominaga, *Nature Communications* **2015**, *6*, 1 8367.

[261] V. Recoules, J. Clérouin, G. Zérah, P. M. Anglade, S. Mazevet, *Physical Review Letters* **2006**, *96*, 5 055503.

[262] P.-K. Lai, S.-T. Lin, *Journal of Computational Chemistry* **2015**, *36*, 8 507.

[263] T. Róg, K. Murzyn, K. Hinsen, G. R. Kneller, *Journal of Computational Chemistry* **2003**, *24*, 5 657.

[264] J. P. Geindre, A. Mysyrowicz, A. D. Santos, P. Audebert, A. Rousse, G. Hamoniaux, A. Antonetti, F. Falliès, J. C. Gauthier, *Optics Letters* **1994**, *19*, 23 1997.

[265] F. Deneuville, B. Chimier, D. Descamps, F. Dorchies, S. Hulin, S. Petit, O. Peyrusse, J. J. Santos, C. Fourment, *Applied Physics Letters* **2013**, *102*, 19 194104.

[266] C. Fourment, B. Chimier, F. Deneuville, D. Descamps, F. Dorchies, G. Duchateau, M.-C. Nadeau, S. Petit, *Physical Review B* **2018**, *98*, 15.

[267] K. Widmann, G. Guethlein, M. E. Foord, R. C. Cauble, F. G. Patterson, D. F. Price, F. J. Rogers, P. T. Springer, R. E. Stewart, A. Ng, T. Ao, A. Forsman, *Physics of Plasmas* **2001**, *8*, 9 3869.

[268] P. Antici, S. N. Chen, L. Gremillet, T. Grismayer, P. Mora, P. Audebert, J. Fuchs, *Review of Scientific Instruments* **2010**, *81*, 11 113302.

[269] C. A. Brebbia, editor, *Electromagnetic Applications*, Springer Berlin Heidelberg, Berlin, Heidelberg, **1989**.

[270] A. Lévy, P. Audebert, R. Shepherd, J. Dunn, M. Cammarata, O. Ciricosta, F. Deneuville, F. Dorchies, M. Fajardo, C. Fourment, D. Fritz, J. Fuchs, J. Gaudin, M. Gauthier, A. Graf, H. J. Lee, H. Lemke, B. Nagler, J. Park, O. Peyrusse, A. B. Steel, S. M. Vinko, J. S. Wark, G. O. Williams, D. Zhu, R. W. Lee, *Physics of Plasmas* **2015**, *22*, 3 030703.

[271] N. Fedorov, S. Beaulieu, A. Belsky, V. Blanchet, R. Bouillaud, M. De Anda Villa, A. Filippov, C. Fourment, J. Gaudin, R. E. Grisenti, E. Lamour, A. Lévy, S. Macé, Y. Mairesse, P. Martin, P. Martinez, P. Noé, I. Papagiannouli, M. Patanen, S. Petit, D. Vernhet, K. Veyrinas, D. Descamps, *Review of Scientific Instruments* **2020**, *91*, 10 105104.

[272] D. Strickland, G. Mourou, *Optics Communications* **1985**, *56*, 3 219.

[273] G. Cerullo, S. De Silvestri, *Review of Scientific Instruments* **2003**, *74*, 1 1.

[274] G. Ghosh, *Optics Communications* **1999**, *163*, 1-3 95.

[275] W. Sellmeier, *Annalen der Physik und Chemie* **1871**, *219* 272.

[276] C. Rullière, T. Amand, X. Marie, *Femtosecond Laser Pulses*, Springer New York, second edition, **2005**.

[277] S. Caravati, M. Bernasconi, T. D. Kühne, M. Krack, M. Parrinello, *Applied Physics Letters* **2007**, *91*, 17 171906.

[278] J. Akola, R. O. Jones, *Physical Review B* **2009**, *79*, 13 134118.

[279] J.-Y. Raty, C. Otjacques, J.-P. Gaspard, C. Bichara, *Solid State Sciences* **2010**, *12*, 2 193.

[280] E. Chason, T. M. Mayer, *Critical Reviews in Solid State and Materials Sciences* **1997**, *22*, 1 1.

[281] R. Berthier, N. Bernier, D. Cooper, C. Sabbione, F. Hippert, P. Noé, *Journal of Applied Physics* **2017**, *122*, 11 115304.

[282] M. Krbal, A. V. Kolobov, P. Fons, K. Nitta, T. Uruga, J. Tominaga, *Pure and Applied Chemistry* **2019**, *91*, 11 1769.

[283] J.-B. Dory, These de doctorat, Bourgogne Franche-Comté, **2019**.

[284] A. S. Ferlauto, G. M. Ferreira, J. M. Pearce, C. R. Wronski, R. W. Collins, X. Deng, G. Ganguly, *Journal of Applied Physics* **2002**, *92*, 5 2424.

[285] G. E. Jellison, F. A. Modine, *Applied Physics Letters* **1996**, *69*, 3 371.

[286] M. Dongol, A. F. Elhady, M. S. Ebied, A. A. Abuelwafa, *Optical Materials* **2018**, *78* 266.

[287] J. Tauc, R. Grigorovici, A. Vancu, *physica status solidi (b)* **1966**, *15*, 2 627.

[288] M. Olivier, P. Němec, G. Boudebs, R. Boidin, C. Focsa, V. Nazabal, *Optical Materials Express* **2015**, *5*, 4 781.

[289] C. Vigreux, A. Piarristeguy, R. Escalier, S. Ménard, M. Barillot, A. Pradel, *physica status solidi (a)* **2014**, *211*, 4 932.

[290] A. Mendoza-Galván, E. García-García, Y. V. Vorobiev, J. González-Hernández, *Microelectronic Engineering* **2000**, *51–52* 677.

[291] P. Němec, J. Přikryl, V. Nazabal, M. Frumar, *Journal of Applied Physics* **2011**, *109*, 7 073520.

[292] T. Ju, J. Viner, H. Li, P. C. Taylor, *Journal of Non-Crystalline Solids* **2008**, *354*, 19 2662.

[293] J.-Y. Raty, *physica status solidi (RRL) – Rapid Research Letters* **2019**, *13*, 4 1800590.

[294] M. Upadhyay, S. Murugavel, M. Anbarasu, T. R. Ravindran, *Journal of Applied Physics* **2011**, *110*, 8 083711.

[295] G. S. Varma, M. S. R. N. Kiran, D. V. S. Muthu, U. Ramamurty, A. K. Sood, S. Asokan, *Journal of Non-Crystalline Solids* **2012**, *358*, 23 3103.

[296] P. Martinez, V. Blanchet, D. Descamps, J.-B. Dory, C. Fourment, I. Papagiannouli, S. Petit, J.-Y. Raty, P. Noé, J. Gaudin, *Advanced Materials* **2021**, *33*, 41 2102721.

[297] K. V. Mitrofanov, P. Fons, K. Makino, R. Terashima, T. Shimada, A. V. Kolobov, J. Tominaga, V. Bragaglia, A. Giussani, R. Calarco, H. Riechert, T. Sato, T. Katayama, K. Ogawa, T. Togashi, M. Yabashi, S. Wall, D. Brewe, M. Hase, *Scientific Reports* **2016**, *6*, 1 20633.

[298] A. Hilton, D. Hayes, *Journal of Non-Crystalline Solids* **1975**, *17*, 3 339.

[299] D. Palima, J. Glückstad, *Contemporary Physics* **2010**, *51*, 3 249.

[300] Y.-X. Tong, Q.-H. Zhang, L. Gu, *Chinese Physics B* **2018**, *27*, 6 066107.

[301] G. C. Sosso, J. Behler, M. Bernasconi, *physica status solidi (a)* **2016**, *213*, 2 329.

[302] N. Medvedev, Z. Li, B. Ziaja, *Physical Review B* **2015**, *91*, 5 054113.

[303] M. Inui, A. Koura, Y. Kajihara, S. Hosokawa, A. Chiba, K. Kimura, F. Shimojo, S. Tsutsui, A. Q. R. Baron, *Physical Review B* **2018**, *97*, 17 174203.

[304] B. J. Price, J. Padur, N. S. Robson, *Advances in X-Ray Analysis* **1990**, *34* 193.

[305] K. Jackson, A. Briley, S. Grossman, D. V. Porezag, M. R. Pederson, *Physical Review B* **1999**, *60*, 22 R14985.

[306] T. Halenkovič, J. Gutwirth, P. Němec, E. Baudet, M. Specht, Y. Gueguen, J.-C. Sangleboeuf, V. Nazabal, *Journal of the American Ceramic Society* **2018**, *101*, 7 2877.

[307] J. H. Lee, J. H. Yi, W. H. Lee, Y. G. Choi, *Journal of Non-Crystalline Solids* **2017**, *456* 27.

[308] J. Bonse, G. Mann, J. Krüger, M. Marcinkowski, M. Eberstein, *Thin Solid Films* **2013**, *542* 420.

[309] N. Bowden, S. Brittain, A. G. Evans, J. W. Hutchinson, G. M. Whitesides, *Nature* **1998**, *393*, 6681 146.

[310] K. Sokolowski-Tinten, D. von der Linde, *Physical Review B* **2000**, *61*, 4 2643.

[311] V. Fiorentini, A. Baldereschi, *Physical Review B* **1995**, *51*, 23 17196.

[312] S. Bhosle, K. Gunasekera, P. Boolchand, M. Micoulaut, *International Journal of Applied Glass Science* **2012**, *3*, 3 205.

Dynamique ultra-rapide dans les matériaux à changement de phase et verres chalcogénures

Résumé : Les chalcogénures sont constitués d'un alliage de Te, S ou Se, avec un élément électropositif tel que Ge, In ou Ag. Composants clés dans les mémoires, notamment avec le développement des architectures 3D Xpoint par Intel, ils sont également prometteurs pour de futures applications synaptiques d'intelligence artificielle. Leurs remarquables propriétés optiques et électriques les rendent parfaitement adaptés pour les applications de stockage de données. Tout d'abord, ils possèdent un grand contraste optique et électrique entre leur phase amorphe et cristalline : pour GeTe, un chalcogénure typique utilisé dans les dispositifs mémoires, la réflectivité de la phase cristalline vaut le double de celle de la phase amorphe, et plusieurs ordres de grandeur séparent les résistivités de ces deux phases. Par ailleurs, le phénomène de commutation à seuil (threshold switching), similaire à un effet transistor, permet une transition très rapide, réversible, qui peut être aussi rapide que quelques centaines de picosecondes sous l'excitation d'une impulsion laser ou électrique. Cette commutation à seuil s'effectue sous deux formes, qui définissent deux sous-catégories de chalcogénures. Dans le premier cas, il s'agit d'une transition permanente (non volatile) entre une phase amorphe et une phase cristalline, qui caractérise les matériaux 'mémoires à changement de phase' (PCM). Dans le second cas, une transition non-permanente est déclenchée entre un premier état amorphe très résistif et un second de faible résistivité, définissant les matériaux commutateurs ovoniques à seuil (OTS). Les deux procédés étant déclenchés par une excitation électronique, l'interaction des chalcogénures PCM avec des impulsions laser ultra-courtes a suscité beaucoup d'intérêt dans le but d'atteindre une transition non-thermique qui dépasserait les vitesses actuelles dans les dispositifs mémoires, restreintes par des procédés thermiques.
L'interférométrie dans le domaine des fréquences, une technique pompe-sonde avec une résolution temporelle sub-picoseconde ainsi qu'une résolution longitudinale nanométrique, a permis de sonder la dynamique ultra-rapide des états hors-équilibre résultant de l'irradiation par un laser pompe de 30 fs, à 800 nm, de couches minces de GeTe amorphe, un PCM typique, ainsi que trois verres de type Ge-Sb-Se-N, candidats pour des applications OTS. Cette méthode permet de retrouver les propriétés diélectriques, mais également d'identifier la nature et la dynamique de la surface. En complément, des simulations ab initio hors-équilibre de dynamique moléculaire (AIMD) ont permis une compréhension plus poussée des résultats expérimentaux.
Ces résultats révèlent que le GeTe photo-excité subit une transition amorphe-amorphe, avec quelques subtilités. En 300 fs, une transition non-thermale est détectée, et aboutit à un état hors-équilibre dont la structure est très similaire à la phase liquide. À l'échelle picoseconde, le couplage électron-phonon induit une transition thermique pour les hautes excitations, accompagnée du développement d'une phase liquide et de la contraction du matériau. Cette dynamique affecte principalement les atomes de Ge, qui passent de sites locaux tétraédriques à octaédriques.
Les verres chalcogénures démontrent une réponse différente à l'excitation laser. Tout d'abord, la fonction diélectrique dépend beaucoup plus de l'intensité laser. Ensuite, bien qu'une phase liquide apparaisse, cette phase est très différente des états hors-équilibre. Il est tout de même intéressant de noter qu'à la fois pour GeTe et les verres chalcogénures, l'environnement local des atomes de Ge tend à devenir octahédrique sous l'effet de l'excitation.
Ces résultats permettent une nouvelle perception des états excités des chalcogénures, intervenant dans les deux procédés hors-équilibre notables des mémoires : transition des matériaux mémoires à changement de phase, ainsi que le phénomène de commutation à seuil sous l'effet d'un champ statique.

Mots-clés : laser femtoseconde, interférométrie dans le domaine des fréquences, simulation *ab initio*, matériau à changement de phase, commutation ovonique à seuil, chalcogénure

Ultrafast dynamics in phase-change materials and chalcogenide glasses

Abstract: Chalcogenide are materials made of Te, S or Se alloyed with an electropositive element such as Ge, In or Ag. Key-components in memories with the development of the 3D X-point cross-bar structure by Intel, they are now prospective candidates for future artificial intelligence synaptic devices. Their outstanding optical and electrical properties that make them well-suited for data storage applications. First, they demonstrate a high optical and electrical contrast between their crystalline and amorphous state : in Germanium Telluride, a prototypical chalcogenide used in memory devices, the reflectivity of the crystalline state is the double of the amorphous state and several orders of magnitude separate the resistivities of these two phases. Second, the threshold switching phenomenon, similar to a transistor effect, allows a very fast transition, reversible, which can be as fast as hundreds of picoseconds upon electronic excitation of the material using a light or an electrical pulse. This threshold switching occurs in two ways, which define two sub-categories of chalcogenides. In the first case, a permanent (non-volatile) transition is seen between an amorphous and a crystalline phase. This characterizes the so-called 'Phase-Change Memory' (PCM) materials. In the second case, a non-permanent transition is triggered between an initial highly resistive amorphous phase and another amorphous phase of low resistivity, defining the 'Ovonic Threshold Switching' (OTS) materials. As both processes are triggered by electronic excitation, the interaction of chalcogenide PCM with ultra-short light pulse has attracted significant attention in the hunt for a possible non-thermal transition that would overcome the actual thermal "speed limits" in memory devices.
Thin films of amorphous GeTe, a well-known PCM material, and three selenide chalcogenide glasses (Ge-Sb-Se-N alloys) candidates for OTS applications, were pumped at 800 nm by 30-fs laser pulses in order to trigger out-of-equilibrium states. Frequency-domain interferometry (FDI), a pump-probe technique that allows for a sub-picosecond time resolution and nanometric longitudinal resolution was used to investigate the resulting ultrafast dynamics. This method not only retrieves the evolution of the dielectric properties, but also the surface nature and dynamics. Complementary out-of-equilibrium ab initio molecular dynamics (AIMD) simulations were conducted to get a deeper understanding of the experimental results.
Experiment and simulations reveal that photo-excited GeTe undergoes an amorphous - amorphous transition, with some subtleties on a closer look. We measure a non-thermal transition occuring within 300 fs, leading to an out-of-equilibrium state that is structurally speaking very similar to the liquid phase. On the picosecond timescale, the electron-phonon coupling drives a thermal transition for high irradiation intensity leading to the development of a liquid phase and a shrinkage of the film. This whole dynamics mainly affects the Ge atoms, switching from tetrahedral local sites to octahedral sites.
Chalcogenide glasses respond differently to the laser impingement. First, we see a higher dependency of the dielectric functions to the laser intensity. Second, though a liquid state is also appearing due to thermal effect, this liquid state is found to be very different from the early-times out-of-equilibrium states. However, it is interesting to note that in both GeTe and chalcogenide glasses, the local environment of the Ge atoms tends to octahedral sites upon excitation.
These experimental and theoretical results shed a new light on the optically highly excited states in chalcogenide materials involved in both important processes in non-equilibrium conditions : phase-change materials transitions in memory device and ovonic threshold switching phenomenon induced by static field.

Keywords: femtosecond lasers, frequency-domain interferometry, *ab initio* simulation, phase-change material, ovonic threshold switching, chalcogenide

---

CEntre des Lasers Intenses et Applications
UMR 5107 Université de Bordeaux, 33400 Talence, France.